Vol. 189 No. 1, November 15, 1986 ISSN 0003-2670

Special Issue
MODERN METHODS OF POLYMER CHARACTERIZATION

ANALYTICA CHIMICA ACTA

International journal devoted to all branches of analytical chemistry

ELSEVIER

ANALYTICA CHIMICA ACTA

International journal devoted to all branches of analytical chemistry
Revue internationale consacrée à tous les domaines de la chimie analytique
Internationale Zeitschrift für alle Gebiete der analytischen Chemie

PUBLICATION SCHEDULE FOR 1986

	J	F	M	A	M	J	J	A	S	O	N	D
Analytica Chimica Acta	179	180	181	182	183	184	185	186	187	188	189/1 189/2	190/1 190/2

Scope. *Analytica Chimica Acta* publishes original papers, short communications, and reviews dealing with every aspect of modern chemical analysis both fundamental and applied.

Submission of Papers. Manuscripts (three copies) should be submitted as designated below for rapid and efficient handling:

Papers from the Americas to: Professor Harry L. Pardue, Department of Chemistry, Purdue University, West Lafayette, IN 47907, U.S.A.

Papers from all other countries to: Dr. A. M. G. Macdonald, Department of Chemistry, The University, P.O. Box 363, Birmingham B15 2TT, England. Papers dealing particularly with computer techniques to: Professor J. T. Clerc, Universität Bern, Pharmazeutisches Institut, Baltzerstrasse 5, CH-3012 Bern, Switzerland.

Submission of an article is understood to imply that the article is original and unpublished and is not being considered for publication elsewhere. Upon acceptance of an article by the journal, authors will be asked to transfer the copyright of the article to the publisher. This transfer will ensure the widest possible dissemination of information.

Information for Authors. Papers in English, French and German are published. There are no page charges. Manuscripts should conform in layout and style to the papers published in this Volume. Authors should consult Vol. 170 for detailed information. Reprints of this information are available from the Editors or from: Elsevier Editorial Services Ltd., Mayfield House, 256 Banbury Road, Oxford OX2 7DH (Great Britain).

Reprints. Fifty reprints will be supplied free of charge. Additional reprints (minimum 100) can be ordered. An order form containing price quotations will be sent to the authors together with the proofs of their article.

Advertisements. Advertisement rates are available from the publisher.

Subscriptions. Subscriptions should be sent to: Elsevier Science Publishers B.V., Journals Department, P.O. Box 211, 1000 AE Amsterdam, The Netherlands. Tel: 5803 911, Telex: 18582.

Publication. *Analytica Chimica Acta* appears in 13 volumes in 1986. The subscription for 1986 (Vols. 179–191) is Dfl. 2730.00 plus Dfl. 312.00 (p.p.h.) (total approx. US $1192.94). All earlier volumes (Vols. 1–178) except Vols. 23 and 28 are available at Dfl. 231.00 (US $90.59), plus Dfl. 15.00 (US $5.88) p.p.h., per volume.

Our p.p.h. (postage, packing and handling) charge includes surface delivery of all issues, except to subscribers in the U.S.A., Canada, Japan, Australia, New Zealand, P.R. China, India, Israel, South Africa, Malaysia, Thailand, Singapore, South Korea, Taiwan, Pakistan, Hong Kong, Brazil, Argentina and Mexico, who receive all issues by air delivery (S.A.L. — Surface Air Lifted) at no extra cost. For the rest of the world, airmail and S.A.L. charges are available upon request.

Claims for issues not received should be made within three months of publication of the issues. If not they cannot be honoured free of charge.

For further information, or a free sample copy of this or any other Elsevier Science Publishers journal, readers in the U.S.A. and Canada can contact the following address: Elsevier Science Publishing Co. Inc., Journal Information Center, 52 Vanderbilt Avenue, New York, NY 10017, U.S.A., Tel: (212) 916-1250.

0003-2670/86/$03.50

Printed in The Netherlands

ANALYTICA CHIMICA ACTA
VOL. 189 (1986)

ANALYTICA CHIMICA ACTA

International journal devoted to all branches of analytical chemistry

ELSEVIER Amsterdam–Oxford–New York–Tokyo

Anal. Chim. Acta, Vol. 189 (1986)

0003-2670/86/$03.50

PRINTED IN THE NETHERLANDS

SPECIAL ISSUE

MODERN METHODS OF POLYMER CHARACTERIZATION

CONTENTS

Special Issue on Modern Methods of Polymer Characterization

Preface

Analytical chemistry and polymer science are two of the more vibrant fields of chemistry today. To a large extent, they have developed independently, yet there are substantial areas of overlap to provide incentive for increased communication among practitioners of both disciplines. The principle domain of intersection is polymer characterization, where the word characterization is broadly defined. The traditional views of qualitative and quantitative analysis are not the issues for synthetic polymers, where one usually has a very good idea of the identity of the chemical species, and of their relative amounts. Rather, a distinguishing feature of polymers is the fact that no two molecules of the same chemical formula need have the same chemical structure and physical properties; characterization then becomes the science of distinguishing one structure from another. Important characteristics range from the basic, such as molecular weight and molecular weight distribution, through the subtleties of single-chain structure, such as copolymer composition and distribution, tacticity and sequence distribution, and degree of long-chain branching, to the complexities of bulk polymer architecture, including cross-link density, phase-separated domain size, and degree of crystallinity. Such a broad range of chemical and physical properties continues to stimulate development and application of an equally diverse set of experimental techniques.

The papers in this special issue have been collected and selected with the main purpose of fostering increased communication between the two disciplines. Thus, the papers illustrate the kinds of issues which are exciting in polymer characterization today. No attempt has been made to provide an exhaustive survey of the field, nor even a proportionally representative one; such a collection would be enormous. Nevertheless, several features of the polymer/analytical chemistry interface emerge. For example, some of the experimental techniques employed are fundamentally very familiar to analytical chemists concerned with "small molecules": chromatography, infrared and fluorescence spectroscopy, and nuclear magnetic resonance. Others, such as scattering and conformational dynamics experiments, are perhaps less so; they are tailored to exploit the most basic polymeric feature, that of large spatial correlations accompanied by relatively slow intramolecular rearrangements. Even when the instrumental technique is not foreign, the specific application may well be. For example, the five papers on nuclear magnetic resonance address five completely different issues, and all are concerned with inherently polymeric properties. Whether a given technique is familiar or not, the same questions apply: how can signal-to-noise be optimized, how can sensitivity and detection limits be improved, are the data subject to interferences? The answers to these questions frequently transcend the size of the

analyte molecule, and thus analysts of any stripe should find something of interest and value in these pages.

Timothy P. Lodge
Department of Chemistry,
University of Minnesota,
Minneapolis,
MN 55455,
U.S.A.

Analytica Chimica Acta, 189 (1986) 1—15
Elsevier Science Publishers B.V., Amsterdam — Printed in The Netherlands

COMPARISON OF POLYMER RESOLUTION IN THERMAL FIELD-FLOW FRACTIONATION AND SIZE-EXCLUSION CHROMATOGRAPHY

JUDY J. GUNDERSON and J. CALVIN GIDDINGS*
Department of Chemistry, University of Utah, Salt Lake City, Utah 84112 (U.S.A.)
(Received 14th April 1986)

SUMMARY

A comparison of the resolving power of thermal field-flow fractionation (thermal FFF) and size-exclusion chromatography (SEC) has been made by the experimental operation of a high-resolution system from each category. For the experimental systems used, the measured resolution for thermal FFF was found to be higher than that for SEC for three different binary polymer mixtures. Only for a single low-molecular-weight mixture falling outside the optimal operating range of thermal FFF did SEC show better resolution. The experimental resolution values were broken down into selectivity and column efficiency parameters. While selectivity was easily obtained, column efficiency required a correction for polydispersity effects. With the polydispersity correction made on the basis of thermal FFF data, true resolution values were calculated to replace the apparent or experimental resolution levels. Overall, the corrected resolution values showed that thermal FFF had a significant advantage over SEC. Prospects for future advances in these two techniques are discussed.

Size-exclusion chromatography (SEC) and thermal field-flow fractionation (thermal FFF) are two of the most powerful methods available for characterizing the molecular weight distribution of polymers [1, 2]. Although the separation mechanisms are quite different, the elution volume of a given polymer series in each system with fixed operating conditions is a unique function of molecular weight. Once the elution volume/molecular weight relationship (calibration) has been established, the molecular weight distribution of a polymer sample can be determined.

The accuracy of the molecular weight distribution acquired from SEC or thermal FFF experiments is related to the resolving power of the system used. This study compares the resolving power of the two techniques, which contrast sharply in a number of important respects: in the origin of the separation effect, in elution order, in the kinds of experimental manipulations possible, and in the factors underlying resolution. With respect to the latter, SEC is a highly efficient method in which the eluting zones are quite sharp, but the technique has low selectivity. By comparison, thermal FFF is very selective but presently has relatively low efficiency. In this paper, experimentally determined resolution values are examined in terms of these two key factors, selectivity and efficiency, for each system.

0003-2670/86/$03.50

Previous comparisons of thermal FFF and SEC have been based largely on theoretical factors [1, 3]. However, in order to get a proper perspective on comparative resolution and on the distinctly different performance characteristics of the two systems, it is useful to present experimental data in which the two systems are operated under comparable circumstances and produce separations in similar periods of time. Such a comparison is made in this paper. However, the paper goes beyond empirical comparisons by relating these experimental results to the theoretical underpinnings of the methods to show how different resolution values arise.

An experimental comparison at this stage is particularly useful because both thermal FFF and SEC systems have improved in recent years. Better packing materials and packing methods characterize present SEC columns. A popular commercial column was chosen to illustrate the performance characteristics of SEC. Thermal FFF, while subjected to far less development effort than SEC, has also undergone dramatic improvement. The principal gain has arisen from the capability of assembling thinner channel systems without a loss of channel uniformity. Channels of 0.0030-in. (76-μm) thickness are now standard in this laboratory; such a channel system was used for the present study.

Size-exclusion chromatography is a well known technique that utilizes differential partitioning into a porous matrix to separate molecules according to size [2, 4]. Thermal FFF is less well known and therefore a longer discussion of the separation mechanism is given. Field-flow fractionations are done in a thin, ribbon-like channel, with an external field or gradient applied across the channel faces [5]. The flow of a Newtonian fluid between parallel plates results in a parabolic or near-parabolic flow profile. The flow velocity next to the walls of the channel is zero while the maximum velocity occurs in the middle of the channel. The applied external field must be of such a nature as to interact significantly with the sample molecules, forcing them to migrate towards one wall. The migration of molecules towards this "accumulation" wall is balanced by diffusion away from the wall, resulting in a steady-state distribution of sample. Different levels of interaction with the applied field for different species results in the formation of distributions or layers of different thicknesses near the wall. Once formed, the sample layers are carried downstream by the steady flow of carrier liquid through the channel. Species that form the most compact layers against the wall are displaced more slowly than species forming diffuse layers because the velocity profile of the carrier, as noted, is parabolic, with the slowest flow near the wall. Thus, separation is accomplished [1].

The applied "field" in thermal FFF is a temperature gradient. It has been shown that thermal FFF is applicable to a wide variety of polymers including polystyrene [6, 7], polymethylmethacrylate, polyisoprene, polytetrahydrofuran [8], polyethylene, polypropylene [9], and, in unpublished work, branched-chain polystyrenes. Polymers of molecular weight greater than 10^7 have been separated by thermal FFF without difficulty [10]. The practical

lower limit for molecular weight is about 2000, although polymers of molecular weight lower than 1000 have been retained slightly [11]. The practical range of molecular weights for a given run depends on the temperature drop, ΔT, between the channel walls; fortunately, ΔT can be readily varied to meet specific needs.

THEORY

Retention

Retention in thermal FFF. The distribution of the sample near the wall in a thermal FFF system is characterized by the nondimensional parameter, λ, which is defined as the mean thickness, l, of the solute zone divided by the channel thickness, w. The mean thickness is a function of the temperature gradient and of the transport coefficients of the sample [6]:

$$1/l = (D_T/D + \gamma)\, dT/dx \tag{1}$$

where D_T is the thermal diffusion coefficient, D is the normal diffusion coefficient, γ is the thermal expansion coefficient, and dT/dx is the applied temperature gradient.

The extent to which a sample is retained in the channel is specified by its retention ratio, R, equal to the displacement velocity of the sample relative to that of the fluid carrier. The parameter, R, is related to λ for a parabolic flow profile [6] by

$$R = V^0/V_r = 6\lambda[\coth(2\lambda)^{-1} - 2\lambda] \tag{2}$$

where V^0 is the volume of the channel and V_r is the retention volume or the volume necessary to elute the sample. This equation is only correct to a first approximation for thermal FFF because of the influence of the applied temperature gradient, which causes variations in the fluid viscosity across the channel. The variable viscosity leads to departures from parabolic flow. These departures have been examined and corrections applied [12].

Retention in SEC. In liquid chromatographic methods other than SEC, the sample is positively retained by the column packing and elutes after the inert or unretained solvent peak. Field-flow fractionation works also by inducing positive retention. However, in SEC the sample elutes before the solvent peak because it is partially excluded from the pores of the column packing. If it is assumed that the sample does not interact with the column packing, the retention volume of a sample can be approximated as

$$V_r = V_0 + KV_i \tag{3}$$

where V_0 is the interstitial liquid volume, V_i is the internal pore volume and K (generally less than unity) is the entropy-controlled solute distribution coefficient which expresses the ratio of concentration of solute in the pores to that in the interstitial liquid [2, 4].

Resolution

The resolution of two adjacent peaks is defined [2, 3] as

$$R_s = \Delta V_r / 4\bar{\sigma}_v \tag{4}$$

where ΔV_r is the difference in the retention volumes of the two peaks and $\bar{\sigma}_v$ is the average standard deviation measured in volume units. It has been shown [1] that the resolution as a function of efficiency and selectivity is approximated by

$$R_s = (N^{1/2}/4)\,[\mathrm{d}\ln V_r/\mathrm{d}\ln M]\,(\Delta M/M) \tag{5}$$

where N is the average number of plates, $[\mathrm{d}\ln V_r/\mathrm{d}\ln M]$ is the selectivity, ΔM is the difference in molecular weight of the two samples, and M is the average molecular weight. The absolute values are indicated for the derivative term because it may be positive as in FFF or negative as in SEC.

When the same mixture is injected into both SEC and thermal FFF systems, the term $\Delta M/M$ is the same for both cases and Eqn. 5 can be converted to a resolution ratio which expresses the relative R_s values of the two systems

$$R_s(\mathrm{FFF})/R_s(\mathrm{SEC}) = N^{1/2}(\mathrm{FFF})S(\mathrm{FFF})/N^{1/2}(\mathrm{SEC})S(\mathrm{SEC}) \tag{6}$$

where the selectivity ($[\mathrm{d}\ln V_r/\mathrm{d}\ln M]$) is represented by the symbol S. It is clear from this expression that selectivity and efficiency (N) are the parameters of major importance in describing column performance. The product, $(1/4)N^{1/2}S$, has been termed the fractionating power [3].

EXPERIMENTAL

The basic thermal FFF system has been described elsewhere [6]. In the present case, the channel consists of two copper-zirconium alloy (Amzirc, Viking Metals, Verdi, NV) bars with highly polished chrome-plated faces clamped together over a sheet of Mylar from which the channel space was cut. The channel is rectangular with 45° tapered ends. The channel volume, V^0, is approximately 0.75 ml. The channel is 0.003-in. (0.0762-mm) thick, 2.0 cm in breadth and 45 cm in length between the inlet and the outlet ports located at the apices of the tapered ends. The top bar was heated by two 1.5-kW cartridge heaters. The heat input was controlled by two variable transformers. The bottom bar was milled to accommodate the flow of cold water which acts as a heat sink. Both bars had small holes, regularly spaced, drilled to within 0.8 mm of the surface for temperature measurement by a type-J thermocouple thermometer.

The column was pressurized to approximately 100 psi, allowing the system to be run with the hot wall near or above the normal boiling point of the carrier. The hot wall in these experiments was kept at 72°C while the cold wall was held at 22°C.

The SEC column was a commercial Ultrastyragel column (Waters Chromatography Div., Millipore Corp.). The column is 30 cm long and has an inner

diameter of 7.8 mm. The particle diameter is 7 μm and the "pore size" is reported as 10^4 nm. The column is described as applicable over the molecular-weight range from 50×10^3 to 4000×10^3.

Spectrophotometric-grade tetrahydrofuran was used as carrier. The SEC flow rate was fixed at the recommended level of 1.0 ml min^{-1}. The flow rate of the thermal FFF system was then varied so that the time necessary to run each sample mixture was approximately the same in the two systems. The same or at least comparable auxiliary equipment was also used for both separation units. A Waters model 6000A pump was used for solvent delivery. The channel effluent from each column was detected by an Altex u.v. detector (Berkeley, CA). A two-pen Goertz Metrawatt recorder (Nürnberg, F.R.G.) monitored the outputs of the detectors.

Five different polymer samples, with molecular weights of 50, 100, 233, 411 and 600×10^3 dalton, were used for calibration and for preparing mixtures. Each mixture was composed of two polystyrene standards. The polystyrene standards were obtained from Pressure Chemical Co. (Pittsburgh, PA) except for the 411×10^3 sample which was from Mann Research Labs (New York, NY). The standards had reported polydispersities of 1.06 or less, except for the 411×10^3 and 600×10^3 standards which had reported polydispersities of 1.10. The 411×10^3 standard was found to have a molecular weight of 350×10^3 dalton via the calibration curves for both systems. Sample concentrations were 1 mg ml^{-1} and injections of 10 μl were made via a sampling valve.

Resolution values were calculated from measurements of retention volume and standard deviation obtained from single sample runs. The standard deviation was evaluated from the peak width at half height.

RESULTS AND DISCUSSION

Because the present purpose is the evaluation and comparison of the output of thermal FFF and SEC systems, the substantial difference encountered in comparing thermal field-flow fractograms and size-exclusion chromatograms must be emphasized again. This difference, the result of the divergent fundamental characteristics of the two systems, can lead to significant misconceptions and erroneous conclusions if not carefully considered.

The contrast in the output of the two systems is illustrated in Fig. 1, where the fractogram and the chromatogram for the polymers with molecular weights 233×10^3 and 411×10^3 are superimposed. Although the key parameter, resolution R_s is very close in the two cases (0.79 for thermal FFF and 0.65 for SEC), little else is similar. Particularly, component peaks in SEC are much narrower, but as the above resolution values show, it is erroneous to assume that the narrower peaks translate automatically into higher resolution.

Part of the difference in the fractograms originates in the opposite elution

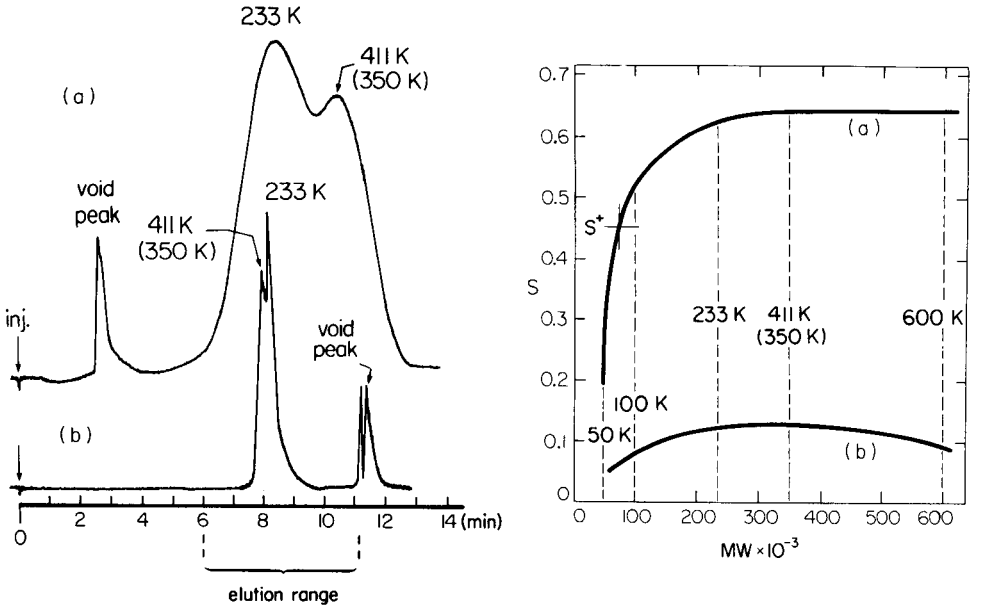

Fig. 1. Contrast between thermal FFF (a) and SEC (b) is illustrated by the partial resolution of polystyrene samples with molecular weights of 233 × 10^3 and reported 411 × 10^3 (measured 350 × 10^3). Experimental conditions: for SEC, the flow rate was 1.0 ml min^{-1}; for thermal FFF, wall temperatures were as specified under Experimental and flow rate was 0.3 ml min^{-1}.

Fig. 2. Selectivity, S, as a function of polystyrene molecular weight in the range 50—600 × 10^3 dalton for thermal FFF (curve a) and SEC (curve b). The thermal FFF plot is for a 50°C temperature drop.

orders; high-molecular-weight components emerge last in thermal FFF and first in SEC method. However, a factor of even more substantial importance is the volume-confined chromatogram in which all peaks must fit into an elution volume range (and the corresponding time range) equal to the pore volume of the column, in contrast to the more open-ended thermal FFF system in which peaks can be eluted over a volume range many times larger than the channel volume. The peaks crowded into this relatively narrow elution range in SEC (illustrated in Fig. 1) tend to be quite narrow, as they must in order to provide good resolution in such a confined region. Thermal FFF peaks tend to be broader, but the increased elution space permits their wider distribution and thus allows high resolution based on different considerations. A wider relative spacing between peaks is related to higher selectivity, which will be discussed next. The contrast in peak width is described by column efficiency factors, which will be described below.

Selectivity

The selectivity, S, represents the fractional change in elution volume relative to the fractional increment in molecular weight (see Eqn. 5). It is thus clearly a measure of how far apart various polymer samples are distributed along the elution volume axis.

The selectivity will vary with elution position, i.e., with retention. The theoretical nature of this dependence has been elucidated [3]. In this paper, selectivity curves are constructed based on experimental data. The experiments for thermal FFF were run at a constant temperature gradient so that the selectivity (as in SEC) is a function only of molecular weight. The dependence on molecular weight for each system was determined by measuring the tangent to the experimentally determined V_r vs. MW calibration curve at various molecular weights and calculating S. The resulting selectivity curves for both systems are shown in Fig. 2. It is seen that the selectivity of the SEC system is relatively constant over the molecular-weight range of interest, whereas the selectivity of the thermal FFF system increases sharply with molecular weight after which it levels off to a constant value. The thermal FFF system has about 5-fold the maximum selectivity of the SEC system. Equation 6 shows that in order to achieve the same resolution in the two systems, the SEC system must have 5^2 (or 25) times as many plates as the thermal FFF system.

Clearly, if selectivity in any part of the required range of molecular weight drops too low relative to its maximum value, resolving power is sacrificed and new conditions (a different temperature gradient in thermal FFF) or a new column (as in SEC) should be used to restore resolution. The effective operating range (e.g., 50 000 to 4 000 000 for the present column) specified for different SEC systems simply reflects an acceptable selectivity range. For thermal FFF, where selectivity changes rather abruptly, we consider the effective operating range as that for which selectivity remains at or above the value $S^+ = S_{max}/2^{1/2}$, where S_{max} is the S value of the upper plateau (≈ 0.63) shown in Fig. 2. When S falls below S^+, at least twice the number of plates is needed to maintain the resolution achievable at S_{max}. Furthermore, the number of plates in an FFF system tends to fall substantially as S drops, thus emphasizing the importance of maintaining high S values near or above S^+. The location of S^+ on the selectivity curve for thermal FFF is illustrated in Fig. 2. The value of S^+ corresponds to a retention ratio of 0.53 for a system described by Eqn. 2. Fortunately, the position of S^+ along the molecular weight scale is not absolute; it can be shifted left (to lower molecular weights) by an increase in the temperature drop, ΔT, applied across the channel.

Efficiency

While the calculation of selectivity from experimental data is straightforward, the acquisition of meaningful efficiency or plate-height data is indirect and subject to considerable error. The problem, greatly magnified in systems of high efficiency and/or selectivity, is that sample polydispersity

contributes an unwanted term to peak broadening and thus to plate height. This spurious contribution must be subtracted in order to arrive at a plate-height value representing the column processes alone. This subtraction is subject to considerable error because of the lack of reliable data on the polydispersities of narrow polystyrene samples. However, it has been found that good estimates of polydispersities can be made directly from the thermal FFF data [13, 14], allowing correction for the polydispersity term to be made with reasonable accuracy.

The measured efficiency of a column (SEC or thermal FFF) is represented by the number of theoretical plates, calculated [2] from

$$N = 5.54\,(t_r/w_{1/2})^2 = L/H \tag{7}$$

where t_r is the retention time of the peak, $w_{1/2}$ is the peak width at half-height in time units, L is the column length and H is the plate height. The plate height is a sum of several contributions which, for the moment, are represented in the simple form

$$H = H_c + H_p \tag{8}$$

where H_c represents the column contribution and H_p accounts for band-broadening caused by polydispersity. Extracolumn contributions to zone dispersion are assumed negligible. When Eqn. 8 is substituted into Eqn. 7, N acquires a relationship to the two constituent N values, one that would be observed with column effects acting alone ($N_c = L/H_c$) and the other with polydispersity acting alone ($N_p = L/H_p$), of the following form

$$1/N = 1/N_c + 1/N_p \tag{9}$$

For an evaluation of true column efficiency and true column resolution, N_c must be used in all equations in place of N. Therefore, the term containing N_p must be subtracted or otherwise accounted for.

The polydispersity contribution of narrow polymer fractions to plate height can be approximated [13, 14] by

$$H_p = LS^2\,(\mu - 1) \tag{10}$$

where μ is the polydispersity expressed by the ratio $\bar{M}_w/\bar{M}_n$. When Eqn. 10 is used in conjunction with Eqn. 9 and the latter is solved for the desired quantity $1/N_c$, then

$$1/N_c = (1/N) - S^2(\mu - 1) \tag{11}$$

This equation shows that if reliable data can be obtained for selectivity and polydispersity, the true (or column) plate number N_c can be isolated and subsequently used to obtain a true resolution or resolution ratio by means of Eqns. 5 and 6.

While it is impossible to obtain true resolution values or the ratio of such values for different systems without a polydispersity correction, it can be shown generally that if the observed resolution (i.e., the experimental resolu-

tion found with polydisperse samples) is higher for one system than for another, then the true resolution will likewise be higher for that system than for the other system. This observation is confirmed by substituting Eqn. 11 into Eqn. 6, which yields

$$\frac{R_s(\mathrm{FFF})}{R_s(\mathrm{SEC})} = \left[\frac{1}{N_c(\mathrm{SEC})S^2(\mathrm{SEC})} + (\mu - 1)\right]^{1/2} \Big/ \left[\frac{1}{N_c(\mathrm{FFF})S^2(\mathrm{FFF})} + (\mu - 1)\right]^{1/2} \quad (12)$$

This equation shows that the intrinsic or true resolution ratio, found when $\mu = 1$, will gradually degrade to unity as μ increases but will stay either greater or less than unity over the entire range of variation of μ. Whether or not this ratio is greater or less than unity depends upon the relative magnitudes of the N_cS^2 term, representing the intrinsic level of resolution or fractionating power.

Resolution

Because empirical resolution measurements indicate the qualitative relationship between true resolution values in any two systems, as shown above, it becomes possible to look more broadly at resolution measurements to indicate the relative effectiveness of the present thermal FFF and SEC systems. Figures 3 and 4 show the results obtained with two different polymer pairs. (Note that different time scales are used for the two systems in order to

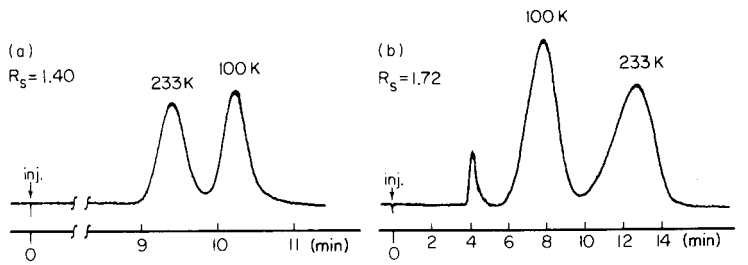

Fig. 3. Separation of polystyrene samples with molecular weights 100 × 10^3 and 233 × 10^3 by SEC (curve a) and thermal FFF (curve b). Experimental conditions as for Fig. 1, except that the flow rate for thermal FFF was 0.2 ml min^{-1}.

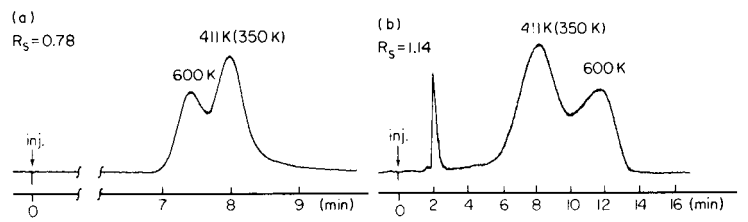

Fig. 4. Separation of polystyrene samples with molecular weights 411 × 10^3 reported (measured 350 × 10^3) and 600 × 10^3 by SEC (curve a) and thermal FFF (curve b). Experimental conditions as for Fig. 1 except that the flow rate for thermal FFF was 0.4 ml min^{-1}.

make the results more directly comparable.) Figure 3 represents the rather easy fractionation of two polymers that differ by over a factor of 2 in molecular weight (100 and 233 × 10^3). The resolution in the thermal FFF system is observed to be slightly higher, 1.72 compared to 1.40. The relative advantage of thermal FFF is somewhat improved in Fig. 4, where thermal FFF shows a resolution of 1.14 compared to 0.78 for SEC.

Outside the effective operating range of thermal FFF, i.e., below S^+ in Fig. 2, the advantage of this method is obviously lost. This is shown in Fig. 5, which compares the resolution of the 50 × 10^3 and 100 × 10^3 polymers in the two systems. The lower resolution for thermal FFF, 0.59 as compared to 0.80, reflects inferior operation below S^+. However, the operating range above S^+ can be easily changed to meet special needs, as has been indicated. Thus, if one encountered a practical resolution problem in this low-molecular-weight range, the temperature drop, ΔT, could be increased to extend the molecular-weight operating range and to restore thermal FFF resolution back to its normal values.

Correction of resolution for polydispersity

Relative resolution values are only roughly indicated by the experimental fractograms and chromatograms. The true resolution ratio can only be ob-

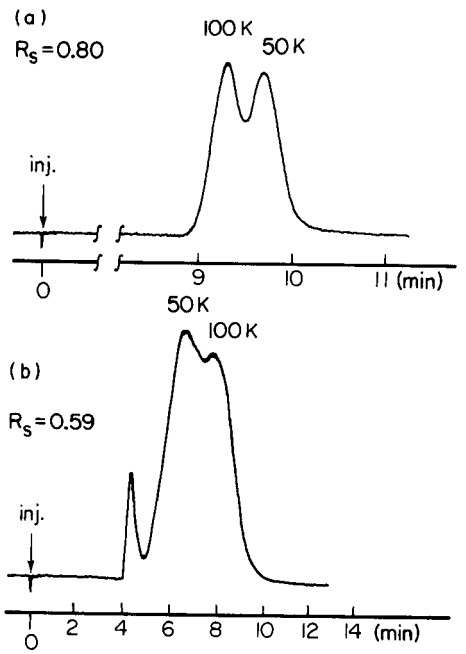

Fig. 5. Separation of polystyrene samples with molecular weights 50 × 10^3 and 100 × 10^3 by SEC (curve a) and thermal FFF (curve b). Experimental conditions as for Fig. 1 except that the flow rate for thermal FFF was 0.2 ml min^{-1}.

tained by correcting for polydispersity. The polydispersity of each sample can be calculated from the thermal FFF results by taking measured plate-height values and subtracting the estimated column dispersion contributions [13, 14]. For this, the experimental plate height will be assumed to be composed of the sum of the contributions

$$H = H_c + H_p = H_n + H_r + H_p \tag{13}$$

where the column contribution, H_c, is expressed as the sum of H_n, the nonequilibrium contribution, and H_r, the relaxation contribution. The term H_p, as used in Eqn. 8, is the polydispersity contribution.

The nonequilibrium contribution arises from the action of the nonuniform flow profile in displacing regions of the sample zone unequally along the channel. The plate height contribution attributed to nonequilibrium is described [13] by $H_n = \chi w^2 \langle v \rangle / D$, where D is the diffusion coefficient, $\langle v \rangle$ is the average linear fluid velocity, and χ is a complicated function of λ increasing as λ^3 when λ is small. (This rapid increase of χ with λ, corresponding to an increase in χ with a decrease in molecular weight, is responsible for the loss of efficiency in the low-molecular-weight range noted earlier.)

The contribution related to the initial establishment of the sample distribution is described as a relaxation effect. During the time required for the sample to relax to its equilibrium distribution, it is subjected to a wide range of longitudinal velocities. The relaxation contribution to plate height [13] is

$$H_r = n(17/140L)\,[w^2 \lambda \langle v \rangle / D]^2 \tag{14}$$

where n is the number of relaxation processes, usually assumed to be one.

The polydispersity contribution, the last term in Eqn. 13, was given earlier by Eqn. 10. Because both H_n and H_r can be calculated from the last two equations, H_p can be obtained by subtracting these two terms from the experimental H as shown by Eqn. 13.

TABLE 1

Experimental retention ratio and plate-height measurements from thermal FFF, with calculated contributions to the plate height and resulting polydispersity (μ) values for polystyrene standards[a]

Molecular weight (10^3 dalton)	R_{exp}	H_{exp} (cm)	H_n (cm)	H_r (cm)	H_p (cm)	μ
50	0.670	0.358	0.264	0.023	0.071	1.018
100	0.501	0.279	0.203	0.013	0.063	1.006
233	0.300	0.208	0.106	0.010	0.092	1.005
350	0.235	0.186	0.066	0.009	0.111	1.006
600	0.157	0.177	0.031	0.008	0.138	1.008

[a]Conditions: cold wall temperature $T_c = 22°C$; hot wall temperature $T_H = 72°C$; flow rate 0.1 ml min^{-1}.

Table 1 shows the measured plate height, the calculated contributions due to nonequilibrium and relaxation, and the residual polydispersity contribution of H_p evaluated from Eqn. 13. Table 1 also includes the polydispersity (μ) values which are calculated from H_p by using Eqn. 10. (The fact that μ values are much lower than the commonly reported value 1.06 has been confirmed in a more exhaustive study [14].) With these μ values and the S values from Fig. 2, the true plate count, N_c, of each system can be calculated from Eqn. 11 and compared to the experimentally measured values of N as shown in Table 2. The polydispersity correction for efficiency is generally larger in thermal FFF than in SEC because of the higher selectivity of thermal FFF.

The true resolving power of each system can be calculated by using the corrected plate counts from Table 2. These are compared to the experimentally determined resolution values in Table 3. The results confirm a higher resolving power for thermal FFF than for SEC for all but the lowest molecular weight mixture studied. The results of Table 3 can be examined in terms of the relative importance of selectivity and efficiency via Eqn. 6. Table 4 gives ratios of selectivity, true plate count, and true resolution for thermal FFF relative to SEC. These results indicate that although SEC is a

TABLE 2

Experimentally measured average plate counts, N, and true plate counts N_c corrected for polydispersity for polystyrene mixtures[a]

Molecular weight (10^3 dalton)	Plate count for SEC		Plate count for FFF	
	Exp. (N)	True (N_c)	Exp. (N)	True (N_c)
50/100	5459	7126	144	202
100/233	4486	5971	188	302
233/350	3135	4411	229	475
350/600	1980	2492	248	942

[a]The experimental conditions for each mixture are given in the corresponding legends to Figs. 1, 3, 4, and 5.

TABLE 3

Experimentally measured resolution for polystyrene mixtures and true resolution corrected for polydispersity

Molecular weight (10^3 dalton)	Experimental R_s		True R_s	
	SEC	FFF	SEC	FFF
50/100	0.80	0.59	0.91	0.71
100/233	1.40	1.72	1.73	2.13
233/350	0.65	0.79	0.84	1.38
350/600	0.78	1.14	0.79	2.54

TABLE 4

Selectivity S, corrected plate count N_c, and corrected resolution R_s ratios for polystyrene mixtures

Molecular weight (10^3 dalton)	$\frac{S(\text{FFF})}{S(\text{SEC})}$	$\frac{N_c(\text{FFF})}{N_c(\text{SEC})}$	$\frac{R_s(\text{FFF})}{R_s(\text{SEC})}$
50/100	4.61	0.0283	0.78
100/233	5.45	0.0506	1.23
233/350	5.04	0.1077	1.65
350/600	5.25	0.3780	3.23

highly efficient method, the greater selectivity of thermal FFF produces a greater resolving power for this technique for all mixtures studied except that of lowest molecular weight. This result stems from the fact that resolution varies linearly with selectivity and only as the square root of the efficiency; thus the selectivity tends to be the dominating factor for the determination of resolution. The higher resolving power of thermal FFF means that thermal FFF will give information about the molecular weight distribution of a polymer that is more accurate than that available from SEC, for the experimental conditions studied.

CONCLUSIONS

In this study, an attempt has been made to evaluate thermal FFF relative to SEC by choosing two high-resolution experimental systems and comparing them under conditions where elution times are similar. By fixing the experimental conditions for these systems, it has been possible to reduce the comparison to numerical values representing relative resolution values. It has also been possible to extract from the experimental data the parameters which serve as an underpinning for resolution, namely, selectivity and column efficiency. This analysis shows that thermal FFF has an advantage in selectivity while SEC has an advantage in efficiency. Because selectivity has a higher order effect on resolution than does column efficiency, the resultant resolution is shown to be greater for thermal FFF than for SEC as long as conditions do not stray outside the normal ranges of operation.

It is not implied that the results found here are universally applicable. Both techniques can be operated under different conditions yielding different results. Also, both are subject to further improvement. In the case of SEC, where optimization has already been pursued at great length, further improvements in column efficiency can be expected as a consequence of ongoing work. However, because of the thoroughness of past efforts, the gains may not be large unless new approaches are found. The search for increased performance in SEC is likely to be hampered by the relative inflexibility of the technique. Resolution is not in general strongly influenced by flow vel-

ocity, carrier solvent, temperature, or by any other readily controllable parameter. Size-exclusion systems cannot be programmed except by extreme means [15]. The principal flexibility left to the discretion of the operator is therefore that of substituting one column system for another. Here, optimization can be pursued by varying column length, column diameter, packing material, and by linking together segments of columns having different packing materials. For example, the use of packing materials with different pore sizes will extend the range of operation of a system, but by way of trade-off it will decrease the selectivity [3].

Thermal FFF is far more flexible than SEC. While column (channel) systems could be linked together and their lengths varied, all the benefits of these efforts can be achieved far more easily by using a fixed-column system and varying experimental conditions. In thermal FFF, resolution and speed are both highly sensitive to operating conditions. Both temperature gradient and flow velocity have profound effects on performance. In addition, both temperature gradient and flow velocity can be varied (programmed) in the course of the run in order to significantly expand the normal operating range.

While broad guidelines have been established for the optimization of thermal FFF, the experimental pursuit of optimization is in its infancy. Barring unforeseen obstacles, substantial gains can be expected. Some of the approaches in this direction are clearly forecast by theory [7, 16]. For major improvements in both resolution and speed, theory suggests that the channel thickness should be further reduced and that the temperature drop across the channel should be increased. The flow velocity can be increased or decreased depending upon whether one wishes to emphasize increased speed or increased resolution. As noted before, the applicable range of molecular weight can be increased by judicious programming approaches.

While both SEC and thermal FFF are subject to improvements which will affect their relative efficacy, it is emphasized that the two systems separate on the basis of different physicochemical parameters, and in this sense are complementary to one another. For example, the thermal diffusion process underlying the thermal FFF method is sensitive to both polymer type and molecular size. Thus the combination of the two methods may prove to be more effective than either system alone in characterizing mixed polymeric systems such as polymer blends and copolymers [17].

This material is based on work supported by the National Science Foundation under grant CHE82-18503.

REFERENCES

1 J. C. Giddings, Pure Appl. Chem., 51 (1979) 1459.
2 W. W. Yau and J. J. Kirkland, Modern Size-Exclusion Liquid Chromatography, Wiley, New York, 1975.
3 J. C. Giddings, Y. H. Yoon and M. N. Myers, Anal. Chem., 47 (1975) 126.
4 J. C. Giddings, E. Kucera, C. P. Russell and M. N. Myers, J. Phys. Chem., 72 (1968) 4397.

5 J. C. Giddings, Sep. Sci. Technol., 19 (1984) 831.
6 J. C. Giddings, K. D. Caldwell and M. N. Myers, Macromolecules, 9 (1976) 106.
7 J. C. Giddings, M. Martin and M. N. Myers, J. Chromatogr., 158 (1978) 419.
8 J. C. Giddings, M. N. Myers and J. Janca, J. Chromatogr., 186 (1979) 261.
9 S. L. Brimhall, M. N. Myers, K. D. Caldwell and J. C. Giddings, Sep. Sci. Technol., 16 (1981) 671.
10 Y. S. Gao, K. D. Caldwell, M. N. Myers and J. C. Giddings, Macromolecules, 18 (1985) 1272.
11 J. C. Giddings, L. K. Smith and M. N. Myers, Anal. Chem., 47 (1975) 2389.
12 J. J. Gunderson, K. D. Caldwell and J. C. Giddings, Sep. Sci. Technol., 19 (1984) 667.
13 M. Martin, M. N. Myers and J. C. Giddings, J. Liq. Chromatogr., 2 (1979) 147.
14 M. E. Schimpf, M. N. Myers and J. C. Giddings, J. Appl. Polym. Sci., in press.
15 J. C. Giddings and K. Dahlgren, Sep. Sci., 5 (1970) 717.
16 J. C. Giddings, Sep. Sci., 8 (1973) 567.
17 J. J. Gunderson and J. C. Giddings, Macromolecules, 19 (1986) 2618.

Analytica Chimica Acta, 189 (1986) 17—25
Elsevier Science Publishers B.V., Amsterdam — Printed in The Netherlands

DETERMINATION OF END GROUPS AS A FUNCTION OF MOLECULAR SIZE FOR ALIPHATIC POLYESTERS BY DERIVATIZATION OF END GROUPS AND SIZE-EXCLUSION CHROMATOGRAPHY WITH INFRARED DETECTION

SADAO MORI

Department of Industrial Chemistry, Faculty of Engineering, Mie University, Tsu, Mie 514 (Japan)

(Received 29th January 1986)

SUMMARY

End groups of poly(ethyleneglycol sebacate) having number average molecular weights less than 2500 were characterized as a function of molecular size by derivatizing end groups separately to form 3,5-dinitrobenzoyl and *p*-nitrobenzyl esters. A hydroxyl end group was reacted with 3,5-dinitrobenzoyl chloride (DNBC) and a carboxyl end group was reacted with *O*-(*p*-nitrobenzyl)-*N,N'*-diisopropyl isourea (PNBD). After separation of these derivatized polyesters by size-exclusion chromatography, the effluent was monitored by using a highly sensitive infrared detector. Concentrations of polyesters were monitored at 1740 cm^{-1} for a carbonyl group in the main chain, polyesters derivatized with DNBC at 1560 cm^{-1} for a hydroxyl end group (characteristic absorption band for the nitro group of DNBC), and polyesters derivatized with PNBD at 1537 cm^{-1} for a carboxyl end group (a characteristic absorption band for the nitro group of PNBD). By this technique, three types of polyesters having different end groups were characterized: a diol-type polyester, a mixture of polyesters of a diol type and a mono-ol/monocarboxyl type, and a mixture of polyesters of a dicarboxyl type and a mono-ol/monocarboxyl type.

Polyesters made from ethyleneglycol and organic dibasic acids have both hydroxyl and carboxyl end groups, of which ratios vary with the molar ratio of the starting materials. Equal quantities of the starting materials result ideally in the formation of mono-ol(hydroxyl)/monocarboxyl polyesters which have a hydroxyl group at one end and a carboxyl group at the other. With increasing amounts of ethylene glycol in the reaction vessel, for example, the ratio of hydroxyl end groups in polyesters increases and ultimately diol-type polyesters which have a hydroxyl group at both ends are produced. Therefore, polyesters are generally mixtures with three different end groups (i.e., diol, dicarboxyl, and mono-ol/monocarboxyl).

Polyethyleneglycol terephthalate is a well known synthetic polyester fibre. Aliphatic polyesters such as polyethyleneglycol adipate or sebacate are used to produce ester-type polyurethane. In order to regulate the reaction ratio of isocyanate with polyesters, the end group distribution as a function of molecular weight must be known as well as the types of end groups and their contents. So far, this approach has not been reported.

0003-2670/86/$03.50

Oligomers can be separated into individual molecular sizes by high-performance size-exclusion chromatography (SEC) [1, 2]. However, it is not easy to estimate the types of end groups of separated oligomers by the usual detection techniques for high-performance liquid chromatography. In the work described here, characterization of end groups as a function of molecular size for oligoethyleneglycol sebacate (OEGS) having an average molecular weight of less than 2500 was attempted by attaching infrared-sensitive functional groups to these end groups. First, size-exclusion chromatograms of OEGS were obtained by using a highly sensitive infrared detector [3] at 1740 cm^{-1}, which is the characteristic absorption band for a carbonyl group. Then OEGS was subjected to derivatization with 3,5-dinitrobenzoyl chloride (DNBC) to form the 3,5-dinitrobenzoyl ester with the hydroxyl end group and size-exclusion chromatograms of this sample were obtained at 1740 cm^{-1} and 1560 cm^{-1} which is the characteristic absorption band for a 3,5-dinitrobenzoyl group (strictly, the nitro group). Finally, OEGS was reacted with *O*-(*p*-nitrobenzyl)-*N*,*N*′-diisopropyl isourea (PNBD) to form *p*-nitrobenzyl esters with the carboxyl end group and size-exclusion chromatograms of this sample were obtained at two absorption bands. By this method, concentrations of main chains as well as hydroxyl and carboxyl end groups can be estimated as a function of molecular weight.

EXPERIMENTAL

Sample preparation

A mixture of ethyleneglycol and sebacic acid of specified molar ratio was heated at 160°C until production of water ceased and then the reaction was continued at 200—230°C under reduced pressure (20—30 mm Hg) for 3—6 h. The reaction product was washed with methanol to remove unreacted materials and dried. The content of end groups was determined as the acid value for a carboxyl end group and the hydroxyl value for a hydroxyl end group and was expressed as mass (mg) of KOH per gram of sample. The acid value (C) was determined by dissolving a sample in pyridine and titrating the solution with a potassium hydroxide solution [4]. A hydroxyl value (A) was obtained by dissolving the sample in pyridine, adding acetic anhydride to the solution to acetylate hydroxyl end groups (by heating on a steam bath for 45 min) and titrating the solution with ethanolic sodium potassium solution after decomposition of the excess of acetic anhydride to acetic acid with water [5]. A blank value (B) was determined similarly and the hydroxyl value was calculated from $B + C - A$. The number average molecular weight, $\bar{M}_n$, was calculated from $2 \times 56.1 \times 1000 \times$ (acid value + hydroxyl value).

Derivatization

Hydroxy end groups were derivatized with DNBC to form the 3,5-dinitrobenzoyl ester:

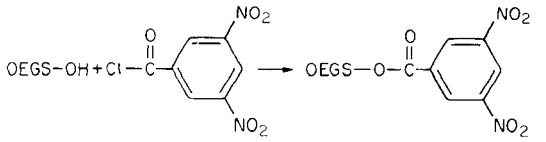

Portions (30 mg) of OEGS and 60 mg of DNBC were dissolved in anhydrous benzene to which several drops of triethylamine were added and the mixture was heated at 70°C for 1 h. The reaction solution was then washed with 0.2 M HCl, water, 1 M KOH, and water in that order. Benzene in the solution was removed at room temperature under reduced pressure and the residue was redissolved in 5 ml of chloroform to give a sample solution for SEC.

Carboxyl end groups were treated with PNBD to form *p*-nitrobenzyl ester [6]:

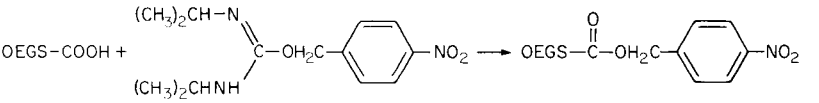

Portions (5 mg) of OEGS and 20 mg of PNBD were dissolved in 4 ml of chloroform. The reaction vessel was sealed and the reaction solution was heated at 70°C for 3 h in a water bath. After the reaction, the volume of chloroform was reduced to 2 ml at room temperature under reduced pressure and the residue was used as the sample solution for SEC.

Size-exclusion chromatography

The apparatus was a Jasco TROROTAR high-performance liquid chromatograph (Japan Spectroscopic Co., Hachioji, Tokyo 192, Japan) equipped with a Jasco high-sensitivity infrared detector (Model HPIR-100). Two Shodex A802 columns (8-mm i.d. × 50 cm) (Showa Denkko Co., Minato-ku, Tokyo 105) were used. The mobile phase was chloroform at a flow rate of 1 ml min^{-1}. The injected volume of sample solution was 0.1 or 0.25 ml.

Wavenumber settings on the infrared detector were 1740 cm^{-1} for carbonyl groups, 1560 cm^{-1} for the dinitrobenzoyl nitro groups, and 1537 cm^{-1} for the *p*-nitrobenzyl nitro groups. Calibration graphs for carbonyl groups and two end groups were constructed by using the following compounds: adipic acid dimethyl ester for the carbonyl groups, 3,5-dinitrobenzoyl methyl ester for the DNB nitro groups, and *p*-nitrobenzyl acetyl ester for the PNB nitro groups. Because the absorptivities of carbonyl groups attached to DNB and PNB were different from those of the other carbonyl groups in the chain, some correction was required. For this purpose, DNB and PNB stearyl esters were synthesized and used in the preparation of calibration graphs for the carbonyl groups.

RESULTS AND DISCUSSION

Acid and hydroxyl values of oligoethyleneglycol sebacate (OEGS) samples are listed in Table 1. Samples 2 and 3 contain more hydroxyl end groups than carboxyl end groups, indicating that some of the OEGS samples are of the diol type. In contrast, sample 5 must contain a dicarboxyl-type OEGS; this sample had a strong absorption band corresponding to carbonyl groups at 1740 cm^{-1}. The range 1500–1600 cm^{-1} was transparent and the detection of absorption by nitro groups was not affected by the OEGS absorption. This was confirmed by SEC with the detector in this range; no response was obtained.

The OEGS samples can be classified into three groups according to the types of end groups: diol, dicarboxyl, and mono-ol/monocarboxyl. Each group has different ratios of carbonyl to hydroxyl end groups, and of carbonyl to carboxyl end groups. Classifications and ratios are shown in Table 2.

TABLE 1

Characterization of OEGS samples

Sample no.	End group (mg KOH/g OEGS)		$\bar{M}_n$
	Acid value (COOH)	Hydroxyl value (OH)	
2	25.2	92.5	960
3	6.3	40	2430
5	75	24	1130

TABLE 2

Classification and ratios of carbonyl groups to end groups of OEGS

(S^a:—O—C(=O)—$(CH_2)_8$—C(=O)—; G^b:—O—CH_2CH_2—)

n^c	Type	Ratios	
		(C=O/OH End)	(C=O/COOH End)
1	HOOC—S—G—OH	2	2
	HO—G—S—G—OH	1	X
	HOOC—S—G—S—COOH	X	2
2	HOOC—S—G—S—G—OH	4	4
	HO—G—S—G—S—G—OH	2	X
	HOOC—S—G—S—G—S—COOH	X	3
3	HOOC—S—G—S—G—S—G—OH	6	6
	HO—G—S—G—S—G—S—G—OH	3	X
	HOOC—S—G—S—G—S—G—S—COOH	X	4

[a]Monomer unit of sebacic acid. [b]Monomer unit of ethylene glycol. [c]Degree of polymerization.

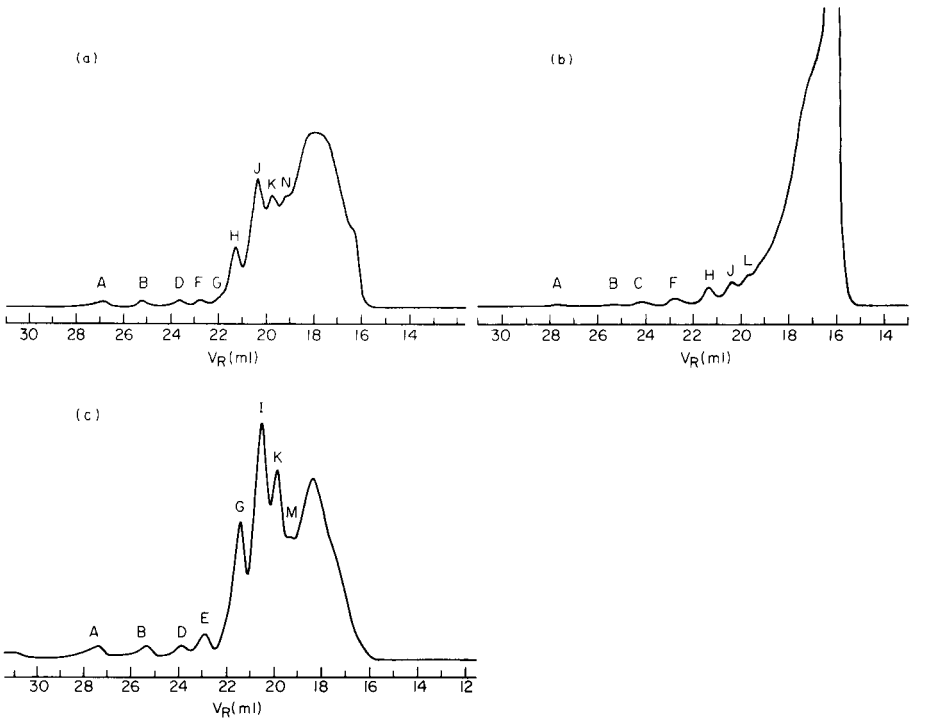

Fig. 1. Chromatograms of OEGS samples (C=O monitored). Sample: (a) no. 2; (b) no. 3; (c) no. 5. Conditions: wavenumber setting 1740 cm^{-1}; attenuation 0.04 AFS; sample concentration 0.5%; injected volume 0.1 ml. The peak at V_R = 16.0 ml on (b) went completely off-scale.

When these values are known, the types of end groups and the degree of polymerization can be estimated.

Size-exclusion chromatographic effluents of OEGS samples 2, 3 and 5 were monitored at 1740 cm^{-1} to detect carbonyl groups. The chromatograms are shown in Fig. 1. Peaks marked A—N are oligomers with smaller molecular weights and were identified as shown in Tables 3—5 and in the following paragraphs. Size-exclusion chromatograms of sample 3 derivatized with DNBC (DNB-OEGS) are shown in Fig. 2. Peaks after V_R = 30 ml in Fig. 2(a) and V_R = 27 ml in Fig. 2(b) are due to the derivatization reagents. The PNB derivative showed the same chromatogram as the unreacted OEGS at 1740 cm^{-1} and no response was obtained at 1537 cm^{-1}, indicating that sample 3 had no carboxyl end group.

Concentrations of the carbonyl group and the DNB end group at each peak or retention volume of the chromatograms in Fig. 2(a, b) are summarized in Table 3. The carbonyl concentration obtained from the chromatogram in Fig. 2(a) includes the concentration of carbonyl derived from the DNB end group. The latter concentration must be subtracted from the total

TABLE 3

Characterization of OEGS sample 3[a]

V_R (ml)	C=O (nmol)	DNB (nmol)	Net C=O (nmol)	C=O/DNB ratio	Identification (n)	Peak
26.5	7	3.5	3.5	1	1 diol	B
24.4	12	4	8	2	2 diol	F
22.9	15	4	11	2.8	3 diol	H
21.9	25	5	20	4	4 diol	J
21.2	37	6	31	5.2	5 diol	L
20.5	42	6	36	6	6 diol	
20.2	57	7	50	7.1	7 diol	
19.9	72	8	64	8	8 diol	
19.6	85	8.5	76.5	9	9 diol	
19.3	99	9	90	10	10 diol	
19.1	114	9.5	104.5	11	11 diol	
19.0	132.5	10.2	122.3	12	12 diol	
18.5	225	12	213	17.8		
18.0	305	12.5	292.5	23.4		
17.5	327	11	316	28.7		

[a]Identified as a diol type.

TABLE 4

Characterization of OEGS sample 2[a] with combined data for DNB and PNB derivatives

V_R (ml)			Net C=O[b]	DNB[b]	PNB[b]	Total end[b]	C=O/ total end	n	Identi-fication[c]	Peak
DNB-OEGS (Fig. 3a)	PNB-OEGS (Fig. 4a)	OEGS (Fig. 1a)								
	24.5		17.5	0	7.6	7.6	2.3			
	23.8	23.8	14	0	8.8	8.8	1.6	1	Dicarboxy	D
24.5	22.2	22.7	36	12	4.5	16.5	2.2	2	Mono 54%	F
23.0	21.2	21.3	50	8	3.7	11.7	4.3	3	Mono 63%	H
22.0	20.2	20.4	150	20	7.4	27.4	5.5	4	Mono 54%	J
21.3	19.5	19.7	208	25.3	10.1	35.4	5.9	5	Mono 72%	L
20.7	19.0	19.2	172	15.3	7.4	22.7	7.6	6	Mono 65%	
19.5	17.7	17.8	274	16	8.6	24.6	11.1	(9.3)	Mono 72%	

[a]Assumed to be mainly diol type (X) but including mono-ol/monocarboxyl type. [b]Given as nanomoles. [c]$Y/(2X + Y)$ = (mole of PNBD)/(mole of DNBC), where $Y = 1 - X$.

value of carbonyl concentration to obtain the net carbonyl concentration. The ratio of the net carbonyl concentration to the DNB concentration corresponds to the ratio of carbonyl groups in the main chain to hydroxyl end groups as shown in Table 2. From this ratio, each peak was identified as a diol type OEGS (see Table 3); n means the degree of polymerization, e.g., HO—G—(—S—G—)$_n$—OH.

TABLE 5

Characterization of OEGS sample 5[a] with combined data for DNB and PNB derivatives

V_R (ml)			Net C=O[b]	DNB[b]	PNB[b]	Total end[b]	C=O/ total end	n	Identification[c]	Peak
DNB-OEGS	PNB-OEGS	OEGS								
	24.6		14		4.1	4.1	3.4			
	23.9	23.9	42		26.2	26.2	1.6	1	Dicarboxy	D
24.3 / 23.4	22.0	22.9	84	5	26	31	2.7	2	Mono 32%	E
22.8 / 22.5	21.0	21.4	196	3	33.5	36.5	5.3	3	Mono 16%	G
21.8	20.2	20.6	156	9	21.7	30.7	5.1	4	Mono 58%	I
21.1	19.5	19.8	159	10.8	18.5	29.3	5.4	5	Mono 74%	K
19.5	18.2	18.4	180	7.5	11.9	19.4	9.3	(9.3)	Mono 77%	

[a]Assumed as mainly dicarboxyl-type (X) but including mono-ol/monocarboxyl type. [b]Given as nanomoles. [c]$Y/(2X + Y)$ = (mole of DNBC)/(mole of PNBD).

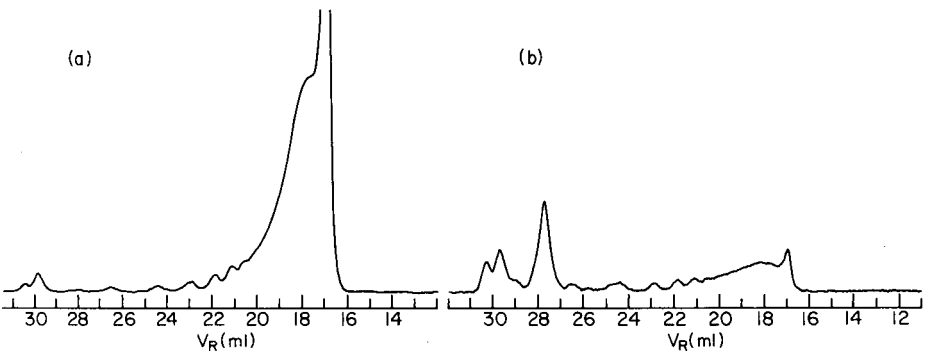

Fig. 2. Chromatograms of DNB-OEGS sample 3. (a) C=O monitored under the same conditions as in Fig. 1; the peak at V_R = 17 ml went completely off-scale. (b) NO_2 group monitored; wavenumber 1560 cm^{-1}, attenuation 0.02 AFS, sample concentration 0.5%, injected volume 0.1 ml.

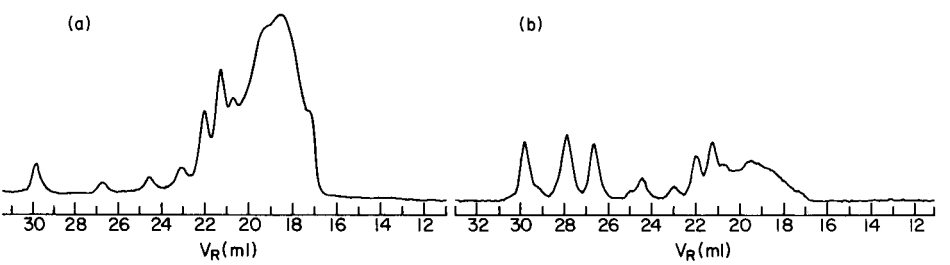

Fig. 3. Chromatograms of DNB-OEGS sample 2. (a) C=O monitored under the conditions given in Fig. 1. (b) NO_2 group monitored under the conditions given for Fig. 2(b).

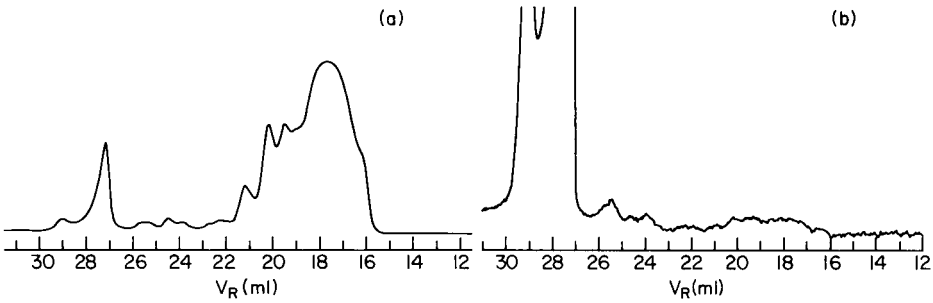

Fig. 4. Chromatograms of PNB-OEGS sample 2. (a) C=O monitored under the conditions given in Fig. 1. (b) NO_2 group monitored; wavenumber 1537 cm^{-1}, attenuation 0.01 AFS, sample concentration 0.25%, injected volume 0.25 ml.

Once sample 3 had been identified as a diol-type OEGS (a hydroxyl group attached to both ends), retention volumes of the diol-type OEGS were established, and subsequent characterization was simplified. Figure 3 shows the size-exclusion chromatograms, with detection of carbonyl and nitro groups, for OEGS sample 2 derivatized with DNBC. Figure 4 shows the analogous chromatograms for the PNB derivative. The DNB derivative eluted 1—1.5 ml later than the relevant underivatized OEGS and the PNB derivative eluted near the underivatized OEGS. Peaks eluting after 26.5 ml in Fig. 3 and after 25 ml in Fig. 4 are presumed to originate from the derivatizing reagents and not from the OEGS sample. From normalized chromatograms of Figs. 3 and 4, concentrations of the carbonyl groups in the main chain, the DNB (hydroxyl) end group, and the PNB (carboxyl) end group were calculated. These results are summarized in Table 4. The OEGS sample 2 was assumed to consist of both a diol-type OEGS (mole fraction X) and a mono-ol/monocarboxyl-type OEGS (mole fraction Y). The values of X and Y were calculated from $Y/(2X + Y)$ = (mole of PNB end)/(mole of DNB end), where $Y = 1 - X$. From these results, OEGS sample 2 appears to contain 50—70% mono-ol/monocarboxyl-type oligomers. The peak at V_R = 23.8 ml is assumed to be a monomeric dicarboxyl-type oligoester. The peak at V_R = 24.5 ml in Fig. 4(a) and Fig. 4(b) was not identified because it did not appear in the chromatogram of underivatized OEGS.

Chromatograms of the DNB and PNB derivatives of OEGS sample 5 are shown in Fig. 5. Retention volumes of each peak for this sample are slightly different from those for samples 2 and 3. Peaks appearing after 26.5 ml in Fig. 5(a) and after 25 ml in Fig. 5(b) are presumed to be due to the reagents. Similar treatment as for Figs. 3 and 4 was applied and the results are listed in Table 5. Sample 5 was assumed to be a mixture of dicarboxyl-type OEGS (mole fraction X) and mono-ol/monocarboxyl-type OEGS (mole fraction Y) and the values of X and Y were calculated from $Y/(2X + Y)$ = (mole of DNB end)/(mole of PNB end). The content of mono-ol/monocarboxyl-type OEGS was between 16 and 77%. Peak A in Fig. 1 was assumed to be a monomeric mono-ol/monocarboxyl-type OEGS. Peak C was not identified.

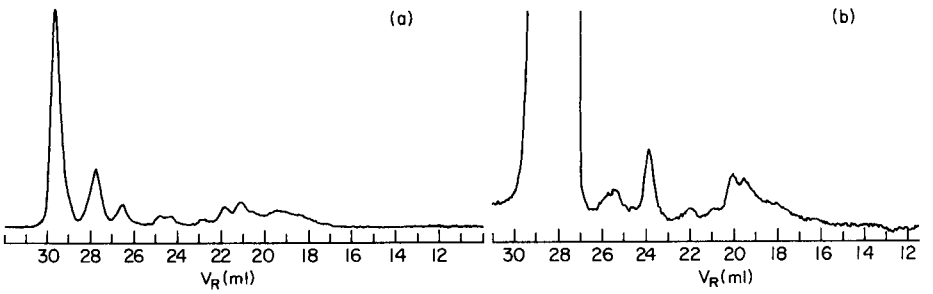

Fig. 5. Chromatograms for the OEGS sample 5 with nitro group monitoring. (a) The DNB derivative under the conditions given for Fig. 2(b). (b) The PNB derivative under the conditions given for Fig. 4(b).

REFERENCES

1 S. Mori, Anal. Chem., 50 (1978) 1639.
2 S. Mori and A. Yamakawa, J. Liq. Chromatogr., 3 (1980) 329.
3 S. Mori, A. Wada, F. Kaneuchi, A. Ikeda, M. Watanabe and K. Mochizuki, J. Chromatogr., 246 (1982) 215.
4 P. Fijolka, I. Lenz and F. Runge, Makromol. Chem., 23 (1957) 60.
5 C. L. Ogg, W. L. Porter and C. O. Willits, Ind. Eng. Chem., Anal. Ed., 17 (1945) 394.
6 D. R. Knapp and S. Krueger, Anal. Lett., 8 (1975) 603.

Analytica Chimica Acta, 189 (1986) 27—40
Elsevier Science Publishers B.V., Amsterdam — Printed in The Netherlands

TIME-RESOLVED INFRARED SPECTROSCOPIC STUDY OF THE ORIENTATION BEHAVIOR OF LIQUID CRYSTALLINE MOLECULES IN THE PRESENCE OF AN ELECTRIC FIELD

A. KAITO[a], Y. K. WANG and S. L. HSU*

Department of Polymer Science and Engineering, University of Massachusetts, Amherst, Massachusetts 01003 (U.S.A.)

(Received 8th May 1986)

SUMMARY

Time-resolved Fourier-transform infrared spectroscopy is used to follow the changes induced by electric field in molecular orientation of a 4-n-pentyl-4′-cyanobiphenyl (5CB) liquid crystal. At an electric field strength greater than 600 V cm^{-1}, the long axis of a 5CB molecule orientates to the direction of the electric field. The orientation function, however, saturates at a field strength greater than 1000 V cm^{-1}. The relaxation time of the rise and decay processes was in the range of 0.04—0.24 s and decreased with increasing field strength. The orientation/relaxation process is discussed on the basis of the motion of liquid crystal domains.

Molecular alignment in liquid crystals induced by an external electric field has been extensively investigated along with its application to electro-optical devices. Details regarding the rate and the degree of molecular orientation in the presence of an applied field are of particular importance because they are responsible for the anisotropic properties of liquid crystals. The n-alkyl derivatives of 4-cyanobiphenyl are well suited for the study of field-induced molecular orientation, because they are chemically stable and easily form nematic liquid crystals at relatively low temperatures. The orientational distribution function of n-alkyl cyanobiphenyl liquid crystals has been investigated by means of birefringence [1], infrared spectroscopy [2], fluorescence [3], Raman scattering [4, 5], and two-photon dichroism [6]. Attenuated-total-reflectance infrared spectroscopy has been applied to the observation of molecular reorientation of a nematic 4-n-pentyl-4′-cyanobiphenyl (5CB) under an external electric field [7]; the structure is shown below with definition of molecular axes.

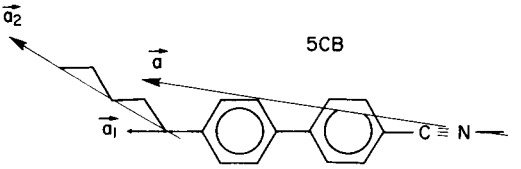

[a]Permanent address: Research Institute for Polymers and Textiles, 1-1-4 Yatabe-Higashi, Tsukuba, Ibaraki 305, Japan.

0003-2670/86/$03.50

The particular advantage of using vibrational spectroscopy for structural characterization is the ability to characterize selectively the local conformation or molecular packing. If the transition moments are well defined, it is possible to interpret the orientation of individual functional groups by measuring the absorption of polarized incident radiation. In electro-optical applications of molecular liquid crystals, the dynamics of structural change are among the most important information needed to interpret the direct relationship between structure and property. Yet, it is in this area that most spectroscopic measurements fail. Most of the experiments in vibrational spectroscopic studies suffer because short time-dependent phenomena cannot be measured conveniently. Fourier-transform infrared spectroscopy (F.t.i.r.) has proven to be an extremely useful characterization tool. However, it has been applied only to the observation of events that are stationary in time, or at least stationary with respect to the measurement time. The multiplex characteristic (the ability to measure all spectral elements) of the interferometer together with the high energy throughput, provide F.t.i.r. with a substantial gain in signal-to-noise ratio for a given measurement time, compared to a dispersive instrument. Therefore, the use of F.t.i.r. to study time-dependent phenomena is feasible. Simultaneous measurements of band shape, position, and relative intensity are retained.

It is still impractical, if not impossible, for the interferometer to follow mechanically the rapid structural changes that can occur on the millisecond time scale. Therefore, in this laboratory, several time-resolved techniques have been developed [8, 9] with considerable flexibility in the time-resolution achievable, to capture and analyze the structural changes such as molecular alignment induced by an external electric field. Structural changes on the order of a millisecond or less can be measured with confidence. A quantitative description of the orientation of individual structural units associated with 4-n-pentyl-4′-cyanobiphenyl (5CB) liquid crystals has been derived. The orientation and the subsequent relaxation of the structural units in the presence of an electric field has been measured by the time-resolved technique. The results are reported in this paper.

EXPERIMENTAL

4-n-Pentyl-4′-cyanobiphenyl (5CB) was used as received from commercial sources. The various phases associated with this sample have been characterized previously [10]. A sample cell was designed around the liquid cell generally used for solution studies. This cell is shown schematically in Fig. 1. Although the gap between the gold electrodes is designed to be small (ca. 1 mm) in order to obtain a sufficiently high electric field, a sufficiently high level of transmittance can still be achieved for quite acceptable signal/noise ratio.

A strip of paper 1 mm wide was put on the middle of a KBr disk surface before it was coated with gold electrodes by vacuum evaporation. The

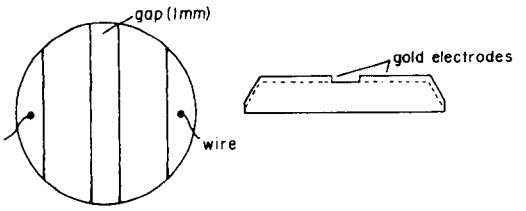

Fig. 1. Schematic diagram of the cell used.

thickness of the electrodes, and therefore, the thickness of the 5CB layer was controlled by the heating current and the evaporating time, and ensured that the absorbance of the measured bands was below 1.2. Soft electric wires were connected to the electrodes with electrically-conductive resin. Two drops of 5CB were placed in the gap and then covered by another KBr disk.

The time-resolved technique has been adequately described [8, 9]. In this particular experiment, an electric field of 600, 800, 1000, or 2000 V cm^{-1} was periodically applied to the sample for 0.37 or 0.62 s, and then turned off for an equivalent amount of time before the electric field was re-applied. An external microprocessor was used to correlate this external event to the interferometer movement [11]. An IBM Model-98 vacuum Fourier-transform spectrometer was used for all experiments. Polarized radiation was obtained by the use of a Molectron wire grid polarizer. All spectra were kept to a resolution of 2 cm^{-1}. Generally, 50 scans for each time period were sufficient to obtain spectra of sufficient signal/noise ratio for further examination. The details of the data-acquisition procedure and the subsequent construction of interferograms to obtain high time resolution is described elsewhere [11]. Time resolution of 10 ms was found to be sufficient to follow the structural changes induced by the electric field in 5CB's. The external microprocessor used to monitor and control the phase relationship between the external

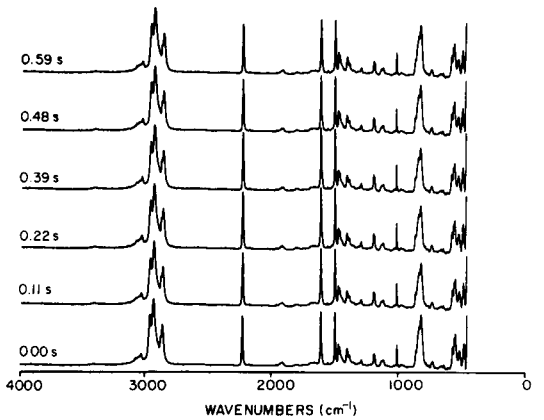

Fig. 2. A series of representative time-resolved infrared spectra. Polarizer is parallel to the electric field; E = 1000 V cm^{-1}. Spectra were measured at the time intervals noted on the spectra.

event and the interferometer movement is not critical; any model with a parallel interface board suffices. In this particular case, a California Computer System microprocessor was used. The polarized spectra obtained with the time-resolved technique have a sufficiently high signal/noise ratio for examination. A representative series with time resolution of 10 ms is shown in Fig. 2.

THEORETICAL ASPECTS

Polarized infrared absorption measurements allow the orientation function of individual functional groups in 5CB to be studied by measuring the second moment of the orientation function, f, which can be expressed as

$$f = (D - 1)(D_0 + 2)/(D + 2)(D_0 - 1) \quad (1)$$

where the dichroic ratio, D, is the relative absorbance for mutually perpendicular polarization of the incident infrared radiation. The reference axis for the polarized measurements is generally defined in the laboratory. Because the transition moment of individual vibrations cannot be easily defined, a reference axis is usually needed in the molecule. In polymers, the vector connecting translationally equivalent groups is generally given at this axis. In virtually all experiments of interest, these two axes coincide. The D_0 in the second-moment expression is then given by $D_0 = 2\cot^2\alpha$, where α is the angle between the transition moment and defined molecular axis.

The orientation of the methylene sequence in 5CB relative to the rest of the molecule is of considerable interest. The orientation function of this flexible part is expressed as f_{ms}. The transition-moment direction of symmetric stretching vibration of each CH_2 unit is assumed to be a bisector of HCH angle, while that for methylene asymmetric stretching is perpendicular to the CCC plane. Because the energy between the *gauche* and the *trans* conformation is not high (nearly 500 cal mol^{-1}), it is not expected that the conformation of the methylene sequences will maintain in these experiments the planar zigzag form observed in the crystalline state; instead it needs to be expressed as a statistical distribution. Then the effective transition moments associated with various localized methylene vibrations must also be statistically averaged, excluding the extremely high energy conformation $-gg'-$

TABLE 1

Transition moment direction

Group	Vibration	$\cos^2\alpha$[a]
Cyanobiphenyl	C≡N stretching	1.0
Terminal methyl	Methyl asym. str.	0.0
Methylene sequence	Methylene sym. str.	0.11436
Methylene sequence	Methylene asym. str.	0.10960

[a] α is the angle between transition moment direction and the molecular axis in each group.

contribution, as in the procedure proposed by Flory [12]. The averaged transition moment direction in each vibration is summarized in Table 1. In the present analysis, f_{ms} is defined in terms of an axis, a_2, connecting the α-carbon to the terminal carbon, the position of which is evaluated in terms of the statistically averaged conformation discussed above. The orientation of the rigid part, represented by the cyanobiphenyl group, is evaluated with reference to the central axis, a_1 (see formula). Because the terminal methyl group has well-defined vibrations with respect to the skeletal plane of the methylene sequences, a third orientation function, f_{tm}, is defined.

The angle between the long axis of the cyanobiphenyl group and the methylene sequence depends on the conformation of the methylene sequence, and was found to be 52° for the statistically averaged conformation. In these experiments, it is important to express the orientation functions defined relative to these two structurally important axes separately. The relative orientation function is an important parameter. Thus a third axis, a, is defined; it connects the N of the cyanobiphenyl group to the terminal carbon of the methylene sequence (see formula).

As shown in Fig. 3, the axis a', representing a_1 or a_2 is at an angle γ with respect to a. The angles θ and θ' are the angles of a and a', respectively, measured from the z axis defined in the laboratory (electric field direction). The azimuthal angle, ω, represents the rotation of a' about a. The axis a' tends to be directed at the positive direction of the z axis at $\omega = 0$.

The angles θ', θ γ, and ω satisfy the equation

$$(\cos^2\theta')_{av} = [(\sin\theta \sin\gamma \cos\omega + \cos\theta \cos\gamma)^2]_{av} \quad (2)$$

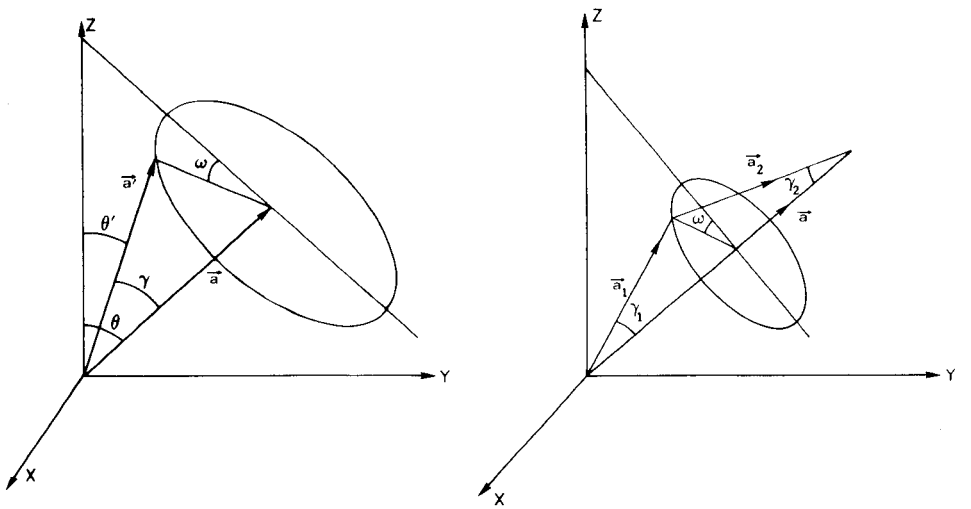

Fig. 3. Definition of molecular axes and angles θ, θ', γ, and ω.

Fig. 4. Spacial distribution of the molecular axis of the entire molecule, $\vec{a}$, the long axis of cyanobiphenyl group, $\vec{a}_1$, and the axis of the methylene sequence, $\vec{a}_2$.

where the average is taken over the orientation of axes a and a'. The value of $(\cos\omega)_{av}$ depends on θ, and from symmetry considerations is zero at $\theta = 0$ and π. Therefore, $(\cos\omega)_{av}$ can be expanded in a series of $\sin n\theta$:

$$(\cos\omega)_{av} = \sum_{n=1} f_{\omega}^{n} \sin n\theta \tag{3}$$

By substituting Eqn. 3 into Eqn. 2 and neglecting the higher-order terms, one obtains

$$(\cos^2\theta')_{av} = (\sin^2\theta)_{av} \sin^2\gamma/2 + (\cos^2\theta)_{av} \cos^2\gamma + \\ + 4(\sin^2\theta \cos^2\theta)_{av} \sin\gamma \cos\gamma f_{\omega}^{2} + \ldots \tag{4}$$

Equation 4 can then be expressed as

$$f_{\theta}' = f_{\theta} f_{\gamma} + 6(\sin^2\theta \cos^2\theta)_{av} \sin\gamma \cos\gamma f_{\omega}^{2} + \ldots \tag{5}$$

where f_{θ}' and f_{θ} are the second moments of orientation distribution functions of the axes a' and a, respectively: $f_{\theta}' = [3(\cos^2\theta')_{av} - 1]/2$, $f_{\theta} = [3(\cos^2\theta)_{av} - 1]/2$, and $f_{\gamma} = [3\cos^2\gamma - 1]/2$. When f_{ω}^{2} is positive, the axis a' tends to be parallel to the z axis, rather than the x-y plane. The negative value of f_{ω}^{2} stands for the reverse situation.

From Eqn. 5 the orientation function of the axis a_1, which corresponds to f_{cb} is expressed as

$$f_{cb} = f_{\theta} f_{\gamma_1} + 6(\sin^2\theta \cos^2\theta)_{av} \sin\gamma_1 \cos\gamma_1 f_{\omega}^{2} \tag{6}$$

where γ_1 is the angle between the axes a_1 and a. The azimuthal angle, ω, for the axis a_2 is as defined in Fig. 4. This means that the value of orientation functions, f_{ω}^{2}, of the axes a_1 and a_2 are equal in magnitude but opposite in sign. Therefore, the orientation function of the axis a_2 is given by

$$f_{ms} = f_{\theta} f_{\gamma_2} - 6(\sin^2\theta \cos^2\theta)_{av} \sin\gamma_2 \cos\gamma_2 f_{\omega}^{2} \tag{7}$$

where γ_2 is the angle between the axes a_2 and a.

From Eqns. 6 and 7, the orientation functions f_{θ} and f_{ω} can be deduced as follows:

$$f_{\theta} = (f_{cb} \sin\gamma_2 \cos\gamma_2 + f_{ms} \sin\gamma_1 \cos\gamma_1)/(f_{\gamma_1} \sin\gamma_2 \cos\gamma_2 + f_{\gamma_2} \sin\gamma_1 \cos\gamma_1) \tag{8}$$

$$f_{\omega}^{2} = (f_{\gamma_2} f_{cb} - f_{\gamma_1} f_{ms})/6(\sin^2\theta \cos^2\theta)_{av} (f_{\gamma_1} \sin\gamma_2 \cos\gamma_2 + f_{\gamma_2} \sin\gamma_1 \cos\gamma_1) \tag{9}$$

The values of f_{γ_1}, f_{γ_2}, $\sin\gamma_1 \cos\gamma_1$, and $\sin\gamma_2 \cos\gamma_2$ were calculated by averaging over conformations of the methylene sequence. The value of f_{θ} can be calculated from Eqn. 8, while Eqn. 9 contains another unknown factor $(\sin^2\theta \cos^2\theta)_{av}$, which can be expressed as

$$(\sin^2\theta \cos^2\theta)_{av} = (\cos^2\theta)_{av} - (\cos^4\theta)_{av}. \tag{10}$$

Although the value of $(\cos^2\theta)_{av}$ can be calculated from the value of f_θ which is derived from Eqn. 9, the relationship between $(\cos^4\theta)_{av}$ and $(\cos^2\theta)_{av}$ depends on the choice of orientation distribution function. In this work, the orientation distribution function proposed for affine deformation [13] was used for the evaluation of the $(\cos^4\theta)_{av}/(\cos^2\theta)_{av}$ relationship.

RESULTS AND DISCUSSION

The infrared absorption spectrum of 5CB in the region of 2750—3150 cm^{-1} is shown in Fig. 5. The absorption bands of C—H stretching vibrations were assigned by reference to the assignments for n-paraffins [14, 15]; the results are shown in Table 2. The intensity of each absorption band was obtained by the least-squares curve-fitting method. The combination band is strongly overlapping with the methylene asymmetric stretching vibration, suggesting that intensity of the combination band is borrowed from the methylene asymmetric stretching vibration. It is difficult to resolve these two bands with accuracy by the least-squares curve-fitting method. In this work, the intensity of the combination band was added to that of the methylene asymmetric stretching vibration after the curve-fitting had been done.

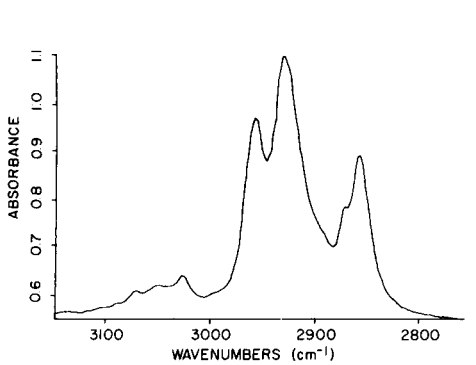

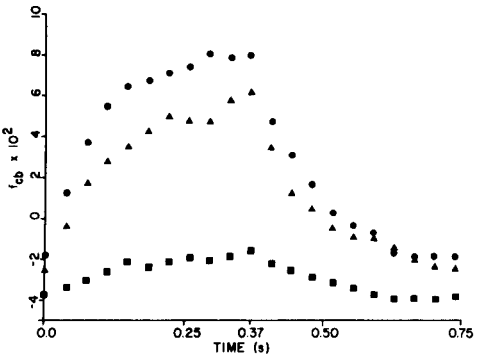

Fig. 5. Infrared absorption spectrum of 5CB in the 2750—3150 cm^{-1} region.

Fig. 6. Orientation function of cyanobiphenyl group as a function of time: (•) 1000 V cm^{-1}; (▲) 800 V cm^{-1}; (■) 600 V cm^{-1}.

TABLE 2

Infrared spectral assignment

ν (cm^{-1})	Assignment	ν (cm^{-1})	Assignment
2226	C≡N stretching	2929	Methylene asym. str.
2856	Methylene sym. str.	2958	Methyl asym. str.
2872	Methyl sym. str.	3050	C—H str. of biphenyl rings
2908	Combination band of methylene deformation		

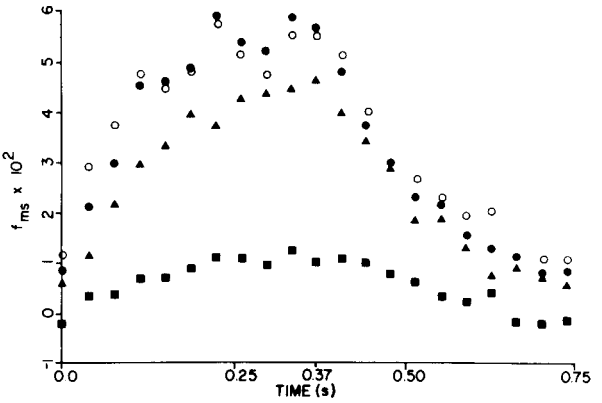

Fig. 7. Orientation function of methylene sequence as a function of time: (○, ●) 1000 V cm^{-1}; (▲) 800 V cm^{-1}; (■) 600 V cm^{-1}. (○) Calculated from methylene symmetric stretching vibration; (●, ▲, ■) calculated from methylene asymmetric stretching vibration.

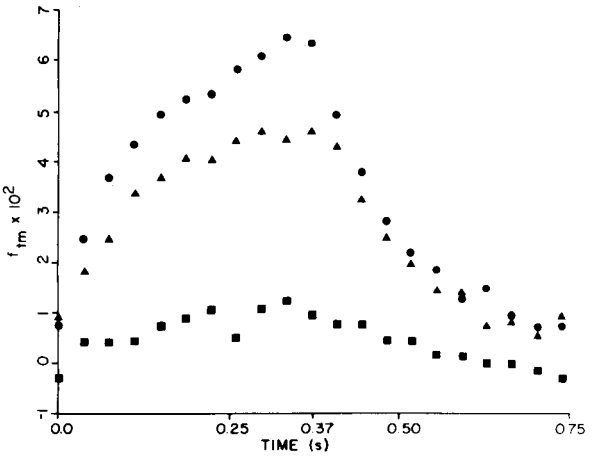

Fig. 8. Orientation function of methyl group as a function of time: (●) 1000 V cm^{-1}; (▲) 800 V cm^{-1}; (■) 600 V cm^{-1}.

The time dependence of the orientation functions, f_{cb}, f_{ms}, and f_{tm} is derived from the individual dichroic ratios measured and shown in Figs. 6—8. In this experiment, the electric field was present for 0.0—0.37 s and absent for 0.37—0.74 s. In the initial state, the cyanobiphenyl group tended to be orientated perpendicular to the direction of the electric field; the methyl and methylene groups showed nearly random or slightly parallel orientation. The initial orientation was induced by the wall effect of the sample cell [16]. The orientation function increased with application of the electric field and showed approximately an exponential decay on the removal of the electric field. As shown in Fig. 7, the orientation function, f_{ms}, calculated from the methylene symmetric stretching vibration is in good agreement with that

obtained from methylene asymmetric stretching vibration, which indicates the validity of the present analysis, including the curve resolution of the spectrum, the calculation of the transition moment direction, and the choice of molecular axes. The orientation functions, f_{ms} and f_{tm}, showed quite similar behavior to each other in their absolute value, time dependence, and field-strength dependence. In contrast, the orientation function, f_{cb}, responded to the electric field more sensitively than f_{ms} and f_{tm}. The electric-field-induced orientation was dependent on the strength of the electric field. At 600 V cm^{-1}, the electric field induced only very weak orientation, whereas the orientational response increased greatly with an increase in field strength to 800—1000 V cm^{-1}.

The orientation function, f_θ, of the entire molecule is shown in Fig. 9. The orientation function increased on applying the electric field and the rise was approximated by an exponential function of time; the function also showed an exponential decay after the electric field had been removed:

$$f_\theta = C\,[1 - \exp(-t/\tau_r)] \text{ and } f_\theta = C' \exp(-t/\tau_d)$$

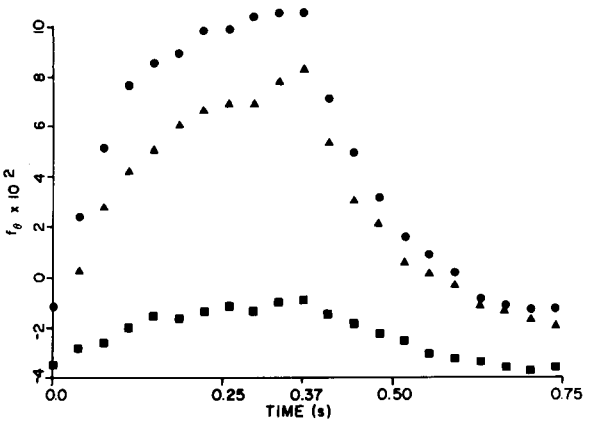

Fig. 9. Orientation function of the long axis of the entire molecule, $\vec{a}$ as a function of time. Symbols as in Fig. 8.

TABLE 3

Rise time, decay time, and orientation function

E (V cm^{-1})	τ_r (s)	τ_d (s)	Δf^a
2000	0.048	<0.1	0.11
1000	0.095	0.126	0.118
800	0.129	0.119	0.103
600	0.134	0.232	0.026

[a]Difference between maximum and minimum orientation functions.

In these equations, τ_r and τ_d represent the relaxation times of the rise and decay processes. The values of τ_r and τ_d are presented in Table 3 along with the difference between maximum and minimum orientation functions, Δf. The time dependence of the orientation function was also investigated at an electric field of 2000 V cm^{-1} and at a longer period of electric field switching (1.24 s). The result is included in Table 3. The values of τ_r and τ_d decreased with increasing field strength. The response to the electric field was faster at a higher electric field. The value of Δf increased steeply with increase in the field strength from 600 V cm^{-1} to 800 V cm^{-1}, and saturated at the electric field higher than 1000 V cm^{-1}.

The orientation function, f_ω^2, is shown in Figure 10. The values of f_ω^2 are concerned with the azimuthal angle, ω, which represents the rotation of the axes a_1 and a_2 around the molecular axis, a of the entire molecule. The case in which the molecular axis a is inclined from the z axis by a certain angle less than $\pi/2$ is considered (Fig. 4). As the value of f_ω^2 becomes negative, there is a larger population of the molecules at $\pi/2 < \omega < 3\pi/2$ than at $-\pi/2 < \omega < \pi/2$. The negative value of f_ω^2 represents the situation in which the inclination angle of the methylene sequence from the direction of electric field (z axis) tends to be smaller and that of the cyanobiphenyl group tends to increase relative to the random distribution of the azimuthal angle, $\omega(f_\omega^2 = 0)$. This orientational structure exists irrespective of the presence of the external electric field and is interpreted as originating from the wall effects of the sample cell. A wall-induced birefringence has been reported for 5CB and other liquid crystalline molecules [16]. The wall-induced orientation would depend on the details in the sample preparation and the history of sample flow. The value of f_ω^2 is changed little with time and electric field, suggesting that the molecules are not rotated by the external field and that the axis, $\vec{a}$, is an axis of orientation of the entire molecule.

Theoretical analysis has been applied to the deformation induced by the electric field in nematic liquid crystals [17, 18]. Our results will be discussed for two cases which are shown in Fig. 11. Here, $\vec{E}$ and $\vec{L}$ are the electric field

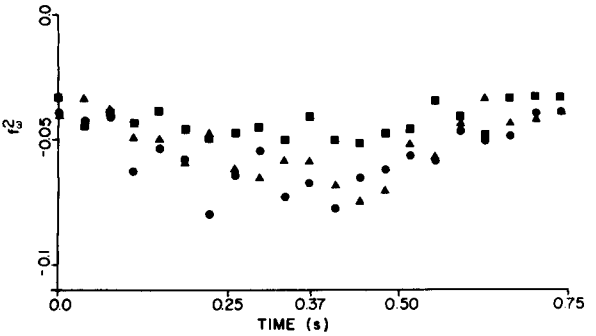

Fig. 10. Orientation function, f_ω^2, as a function of time. Symbols as in Fig. 8.

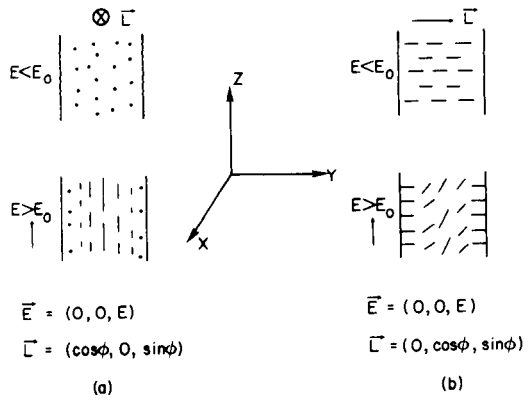

Fig. 11. Illustration of molecular alignment above and below threshold electric field: (a) optical axis is parallel to wall at $E < E_0$; (b) optical axis is perpendicular to wall at $E < E_0$.

and the optical axis, respectively, and the angle ϕ represents the angle of deflection. In case (a), the nematic director is parallel to the surface of the cell, whereas the initial direction of the nematic director is perpendicular to the surface of the cell in case (b). In both cases, the electric field is applied perpendicular to the initial direction of the nematic director. In order to deform nematic liquid crystals, electric energy is required to overcome the elastic energy that would be stored in the material by deformation. This means that there is a threshold value of the electric field in which the electric energy is balanced with the elastic one. The threshold fields E_0 for cases (a) and (b) are given [17, 18], respectively, by

$$E_0 = (\pi/X_0)\,(k_{22}/\epsilon_0 \Delta\epsilon)^{1/2} \text{ and } E_0 = (\pi/X_0)\,(k_{33}/\epsilon_0 \Delta\epsilon)^{1/2}$$

where k_{22} and k_{33} are the twist and bend elastic constants, respectively, and $\Delta\epsilon$ is the anisotropy of dielectric constants. In this work, infrared spectra were measured at a cell length $x_0 = 5\,\mu$m. For $k_{22} = 1.1$—0.5×10^{-6} dyne [19], $k_{33} = 4.0$—1.1×10^{-6} dyne [19], and $\Delta\epsilon = 11.5$ [20], values of E_0 were 400—600 V cm^{-1} and 600—1100 V cm^{-1}, for cases (a) and (b), respectively. These values agree fairly well with the electric field strength at which the orientation function starts to increase. Although the entire system of 5CB liquid crystals is nearly isotropic in the absence of an electric field, some portions of the nematics are distributed as in cases (a) and (b). When the electric field exceeds the threshold value, orientation of the nematic director takes place in a way that is shown in Fig. 11.

Another theoretical approach to the orientation induced by an electric field was done on the basis of Boltzmann distribution [21, 22]. When the orientation is caused by the permanent dipole, the orientation function is expressed as

$$f = [3(\cos^2\theta)_{av} - 1]/2$$

$$\text{where } (\cos^2\theta)_{av} = \int_0^{\pi} \cos^2\theta \exp(-\mu E\cos\theta/kT)\sin\theta\,d\theta \Big/ \int_0^{\pi} \exp(-\mu E\cos\theta/kT)\sin\theta\,d\theta$$

If the induced dipole is the driving force of orientation, then

$$(\cos^2\theta)_{av} = \int_0^{\pi} \cos^2\theta \exp(\Delta\alpha E\cos^2\theta/kT)\sin\theta\,d\theta \Big/ \int_0^{\pi} \exp(\Delta\alpha E\cos^2\theta/kT)\sin\theta\,d\theta$$

where $\Delta\alpha$ is the anisotropy of the polarizability tensor. Figure 12 shows the plots of the orientation function as a function of μ and $\Delta\alpha$ at a constant electric field of 1000 V cm^{-1}. In order to achieve $f = 0.1$, $\mu = 1.6 \times 10^4$ Debye or $\Delta\alpha = 2.6 \times 10^{-15}$ cm^3 are required. It cannot be established whether the electric dipole is the permanent type or an induced one. However, these values are much higher than those of a 5CB molecule (μ = 4.1 Debye [23], $\Delta\alpha = 1.1$—1.8×10^{-23} cm^3 [24]).

Dielectric relaxation studies in nematic mixtures of 5CB and its analogs have been reported [25, 26]. The dielectric-loss peak caused by a single molecular process was observed in the frequency range of 10^4—10^7 Hz [25, 26] at room temperature. The relaxation time observed in this work (0.04– 0.23 s) is, however, much longer than that expected from the dielectric relaxation experiments.

These results suggest that a mechanism other than a single molecular process participates in the orientation relaxation process of the 5CB liquid

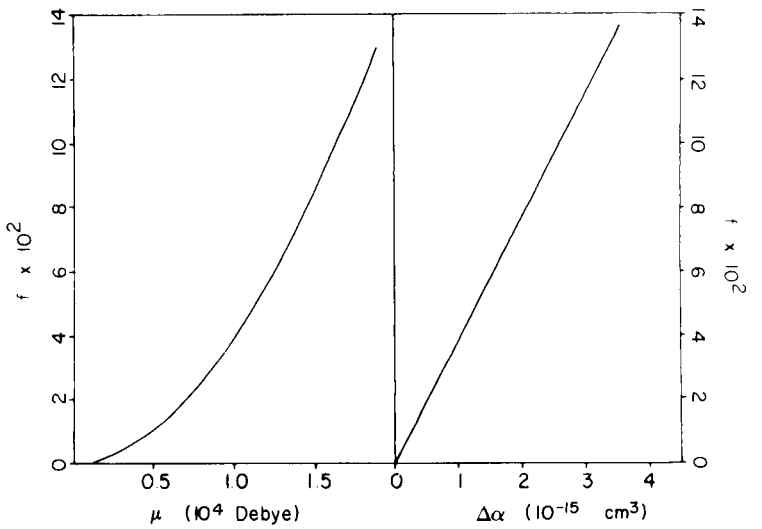

Fig. 12. Orientation function calculated on the basis of Boltzmann distribution as a function of (a) permanent dipole moment and (b) anisotropy of polarizability tensor. Electric field and temperature are 1000 V cm^{-1} and 298 K, respectively.

crystal. Generally, liquid crystals appear in multidomain structures. In each domain, molecules are uni-axially aligned, forming an ordered structure. If the molecules are highly orientated in the domain, each domain has a huge permanent dipole and/or a huge anisotropy of polarizability tensor. If an external electric field is applied, the charges accumulated at the boundaries of the domain interact with the external field which causes a torque on the liquid crystal domains. The relaxation time measured in this work is much longer than that of the single molecular process. This is because the mobility of the liquid crystal domains is lower than that of individual molecules. As a consequence, the orientation/relaxation process of the 5CB nematic liquid is interpreted as motion of liquid crystal domains induced by the electric field.

Conclusions

Time-resolved infrared spectroscopy was used to follow the orientational behavior of liquid crystalline molecules. The technique is shown to be useful for the study of orientation and relaxation processes in liquid crystals.

In the initial state, there is a wall-induced orientation in which the methylene sequence tends to be parallel to the direction of the electric field and the cyanobiphenyl group favors the perpendicular orientation. With application of an external electric field, the molecular axis of 5CB molecules line up with the direction of the electric field. As the strength of the electric field increased above 600 V cm^{-1}, molecular orientation starts to take place. The threshold electric field found was in agreement with that predicted from the elastic constants. With further increasing field strength above 1000 V cm^{-1}, the orientation function saturated.

The orientation/relaxation process of the 5CB liquid crystal cannot be attributed to a single molecular process, but is reasonably explained by the motion of liquid-crystal domains.

We gratefully acknowledge the National Science Foundation, Grant DMR 8407539, for support of this research.

REFERENCES

1 M. S. Sen, R. Brahma, S. K. Roy, D. K. Mukherjee and S. B. Roy, Mol. Cryst. Liq. Cryst., 100 (1983) 327.
2 N. Kirov, M. Sabeva and H. Ratajczak, Adv. Mol. Relaxation Interaction Processes, 22 (1982) 145.
3 Z. Salamon and A. Skibiński, Mol. Cryst. Liq. Cryst., 90 (1983) 205.
4 K. Miyano, Phys. Lett. A, 63A(1) (1977) 37.
5 S. Kobinata, Y. Nakajima, H. Yoshida and S. Maeda, Mol. Cryst. Liq. Cryst., 66 (1981) 67.
6 S. D. Durbin and Y. R. Shen, Phys. Rev. A, 30 (1984) 1419.
7 A. Hatta, Mol. Cryst. Liq. Cryst., 74 (1981) 195.
8 D. J. Burchell, J. E. Lasch, R. J. Farris and S. L. Hsu, Polym., 23 (1982) 965.
9 J. E. Lasch, D. J. Burchell, T. Masoaka and S. L. Hsu, Appl. Spectrosc., 38 (1984) 351.
10 G. W. Gray, K. J. Harrison and J. A. Nash, Electron. Lett., 9 (1973) 130.

11 S. E. Molis, W. J. MacKnight and S. L. Hsu, Appl. Spectrosc., 38 (1984) 529.
12 P. J. Flory, Statistical Mechanics of Chain Molecules, Interscience, New York, 1969.
13 V. O. Kratky, Kolloid-Z., 64 (1933) 213.
14 R. G. Snyder and J. H. Schachtschneider, Spectrochim. Acta, 19 (1963) 85.
15 J. H. Schachtschneider and R. G. Snyder, Spectrochim. Acta, 19 (1963) 117.
16 K. Miyano, Phys. Rev. Lett., 43 (1979) 51.
17 H. Gruler, T. J. Scheffer and G. Meier, Z. Naturforsch., Teil A, 27 (1972) 966.
18 W. Helfrich, Mol. Cryst. Liq. Cryst., 21 (1973) 187.
19 H. Hakemi, E. F. Jagodzinski and D. B. DuPré, J. Chem. Phys., 78 (1983) 1513.
20 P. G. Cummins, D. A. Dunmur and D. A. Laidler, Mol. Cryst. Liq. Cryst., 30 (1975) 109.
21 C. T. O'Konski, K. Yoshioka and W. H. Orttung, J. Phys. Chem., 63 (1959) 1558.
22 K. Yoshioka, J. Chem. Phys., 79 (1983) 3482.
23 H. J. Coles and B. R. Jennings, Mol. Phys., 36 (1978) 1661.
24 J. P. Parneix and A. Chapoton, Acta Phys. Pol. A, 54 (1978) 667.
25 E. I. Ryumtsev, S. G. Polushin, A. P. Kovshik and P. V. Adomenas, Sov. Phys. Crystallogr., 24 (1979) 314.
26 H. R. Zeller, Phys. Rev. A, 23 (1981) 1434.

Analytica Chimica Acta, 189 (1986) 41—56
Elsevier Science Publishers B.V., Amsterdam — Printed in The Netherlands

TIME-RESOLVED DETECTION OF X-RAY SCATTERING FOR STUDIES OF RELAXATION PHENOMENA

S. SUEHIRO, K. SAIJO, Y. OHTA[a], T. HASHIMOTO* and H. KAWAI[b]
Department of Polymer Chemistry, Kyoto University, Kyoto 606 (Japan)
(Received 8th April 1986)

SUMMARY

An instrument for time-resolved detection of small-angle and wide-angle x-ray scattering is described. The apparatus consists of a 12-kW rotating-anode x-ray generator, a linear position-sensitive detector, a two-parameter multichannel analyzer to record the time-dependence of x-ray scattering patterns, a servo-controlled hydraulic sample deformation device, a temperature-controlled environmental chamber, a programmable function generator, a programmable timer and a microcomputer. The programmable function generator is used to control the mechanical or thermal stimulus on the sample under variable conditions and to synchronize the x-ray data acquisition with the stimulus. The environmental chamber allows temperature control of the sample between —100 and 300°C. Two experimental methods, involving transient and oscillatory experiments, for time-resolved studies with this apparatus are discussed. Experimental studies on kinetics of oriented crystallization of cross-linked polybutadiene and on lamellar deformation of tubular-extruded poly(1-butene) films are presented as typical applications of time-resolved x-ray scattering technique.

In recent years, wide-angle and small-angle x-ray scattering methods have proved to be extremely powerful tools in polymer fields, providing information on internal structures of materials from the atomic level to the supermolecular level, i.e., from a few ångstrom to 100 nm in size.

The time-dependent structural change can be followed by real-time measurements of x-ray scattering to elucidate structural mechanisms of relaxation phenomena in polymeric systems. Extensive studies on the viscoelastic properties of semicrystalline polymers were made by Stein and co-workers [1—3] and Kawai and co-workers [4—7] by doing simultaneous measurements of dynamic mechanical properties and wide-angle x-ray scattering (w.a.x.s). They studied the time-dependence of crystallite orientations and crystal deformations by making real-time measurements of x-ray diffraction intensity from a sample under rapid stretching or cyclic elongation, and discussed underlying mechanisms of viscoelasticity of semicrystalline polymers. Such studies are time-consuming because they require many repetitive measurements to detect a small change in x-ray intensity resulting from

[a,b]Present addresses: [a]Research Center, Toyobo Co. Ltd., Katata, Ohtsu, Shiga 520-02, Japan; [b]Hyogo University of Education, Yashiro-cho, Kato-gun, Hyogo 673-14, Japan.

0003-2670/86/$03.50

structural changes in a sample. Real-time measurements of small-angle x-ray scattering (s.a.x.s.) were almost impossible because the number of scattered photons per unit time is even smaller for s.a.x.s.

However, by remarkable advancements in position-sensitive detectors (PSD) and associated electronics, and high flux x-ray sources, such as synchrotron radiation and rotating-anode x-ray generators, it is now feasible to study the kinetics of formation, dissolution and deformation of internal structures by using small-angle as well as wide-angle x-ray scattering.

Recently, developments in experimental techniques and apparatus for time-resolved studies of s.a.x.s. measurements have been made, such as a sample deformation device [8] and a fast x-ray data-acquisition system [9] for the 10-m s.a.x.s. camera [10] at the U.S. Oak Ridge National Laboratory, and a time-resolved s.a.x.s. apparatus developed by Hashimoto et al. [11].

In order to conduct the above-mentioned kinetic studies by means of x-ray scattering, instrumentation must involve three important functions, namely, the capability to apply programmably-variable mechanical, thermal or electrical stimulus to the sample, to acquire the data on the x-ray scattering intensity distribution in synchronization with the applied stimulus, and to record simultaneously the responses of sample in terms of various physical properties, such as stress or strain during the x-ray measurement. Such an instrument will be used for a wide variety of experiments in studying crystallization kinetics [12] and deformation mechanisms of crystalline polymers, and phase transition in multicomponent polymer systems, such as polymer blends and block copolymers [13–15]. It will also be valuable in various fields in materials science as well as polymer science.

This paper describes recent instrumental developments for time-resolved detection of x-ray scattering. The fundamental techniques underlying such studies are also discussed. Some experimental results on time-dependent structural changes in polymeric systems are presented as typical applications of the technique.

EXPERIMENTAL

Instrumentation

The basic concept of the present instrumentation is that the time-dependence of the stimulus applied to a sample can be set arbitrarily, and a time-resolved recording of an x-ray scattering profile can be obtained in synchronization with the applied stimulus, with simultaneous measurements of the time responses of various physical properties of the sample. The rate and the functional form of the stimulus can be fully automated with a programmable function generator. Thus, a wide variety of experiments can be done, e.g., the sample excitation could be a single step, a multiple step, sinusoidal, or superimposed sinusoidal function having multiple frequency components.

Currently, the stimulus can be either thermal or mechanical. Experiments possible include temperature-jump (T-jump) or temperature-drop (T-drop)

experiments, experiments under programmed temperature conditions, experiments under constant stress or constant strain, transient experiments with a single-shot high-speed elongation, and oscillatory experiments with a sinusoidal elongation or load. Furthermore, the present instrument can easily support electric, magnetic or other kinds of stimuli, simply by providing driving units for those stimuli.

The system consists of a 12-kW rotating-anode x-ray generator (Rigaku Denki, Ru-a), a sample-deformation device and a data-acquisition system. The data-acquisition system as well as the sample-deformation device are the most important in time-resolved x-ray detection. A block diagram of this part is shown in Fig. 1. It consists of a linear position-sensitive detector (PSD), a multichannel analyzer (MCA), an analog interface, a function generator and a hydraulic sample-deformation device, a programmable timer, and a microcomputer. Details of each component are described below.

X-ray detector. The detector is a linear PSD (a multicathode delay line, position-sensitive proportional counter; Rigaku Denki) having a gold-plated tungsten anode wire, and is filled with 90% argon/10% methane. It has an effective active area of 50 mm long and a thickness of the drift field of 11 mm. The maximum total count rate of the detector is 20 000 events s^{-1}. The spatial resolution was determined as a Gaussian resolution function with a standard deviation of 60 μm [16].

The position of an incident x-ray photon is measured as a time delay between the two output pulses at both ends of the delay line in the detector. The maximum time delay is 0.8 μs. The time delay is converted to a pulse height by a time-to-amplitude converter (Model 2043 TAC; Canberra

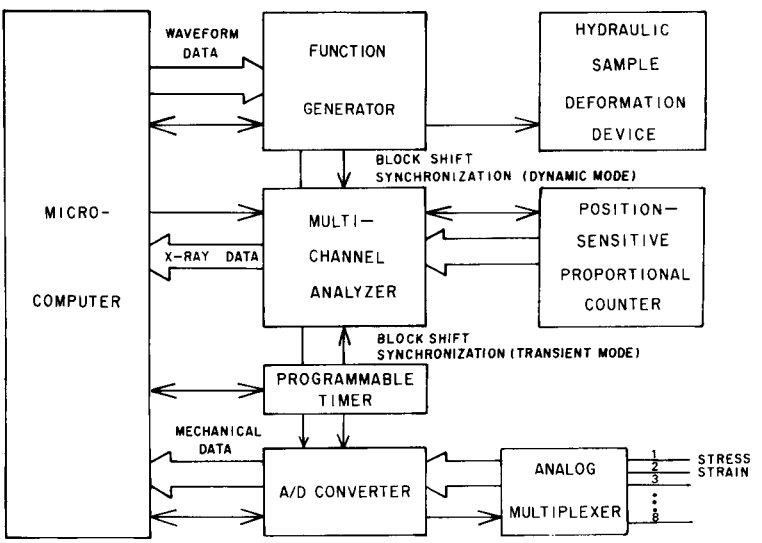

Fig. 1. Block diagram of the sample-deformation and data-acquisition system for time-resolved detection of x-ray scattering.

Industries) and the pulse height is converted to a digital number by a fast analog-to-digital converter (TN-1213A ADC; Tracor Northern). The resulting digital number is transferred to the MCA for data recording.

Multichannel analyzer. The two-parameter MCA (Rigaku Denki) having 16K words of histogramming memory is used. The MCA either increments or decrements the content of its memory at a certain location of the currently selected block, which corresponds to the incident position of the x-ray photon. This is called 'histogramming' and is a basic function of an MCA. The increment mode is the normal operation mode and the decrement mode can be used to subtract background. One word consists of 20 bits, hence up to 1048575 events of x-ray incidence can be recorded in each word. The histogramming cycle takes place within 4 μs, and the total dead-time including the time required for the position encoding is ca. 10 μs. Therefore, ca. 11 000 events s^{-1} can be processed with a statistical counting loss of 10%. This means that a relatively uniform scattering pattern of 256 position points, under the condition of the total count rate being 11 000 events s^{-1}, can be recorded in 10 s with 5% statistical counting error at each position. For a time-resolved study, several such memory blocks are required to record the time-dependent variation of an x-ray scattering profile. The histogramming memory can be divided into memory blocks in five different ways. It can record N time-slices of M positions, where possible combinations of N and M are: 16,1024; 32,512; 64,256; 128,128; and 256,64.

Two synchronization signals for the time-resolved data acquisition are provided. The switching between the consecutive memory blocks (i.e., the block shifting) is synchronized with the mechanical or the thermal stimulus on the sample by using the BLOCK SHIFT pulse provided by the programmable function generator or the programmable timer. The time required for the memory block switching is less than 1 μs. After N block shifts starting from the first block, the switching is routed back to the first block. The PHASE ZERO pulse forces the switching to the first block at any time. Thus repetitive data accumulation can be synchronized with the cyclic stimulus.

The content of the MCA memory is transferred to the microcomputer by the byte-serial data transfer. Start and stop of the MCA data collection and clearing the MCA memory are controlled either by the microcomputer or manually at the front panel. The x-ray data collection can be monitored by the real-time CRT display.

Deformation device. Figure 2 shows the block diagram of the hydraulic sample-deformation device. The actuator driven by the hydraulic pump provides a controlled load to the specimen. The flow rate of the oil is 30 cm^3 s^{-1}. The maximum load and the maximum displacement are 490 N and $\pm$7.5 mm, respectively, and the operating frequency is between 0 and 60 Hz. At frequencies higher than 4 Hz, the maximum displacement decreases with frequency to the ultimate value of $\pm$0.5 mm at 60 Hz. The displacement of the actuator (i.e., the sample deformation) is measured by a linear variable differential transformer (LVDT) and a strain amplifier. The maximum dis-

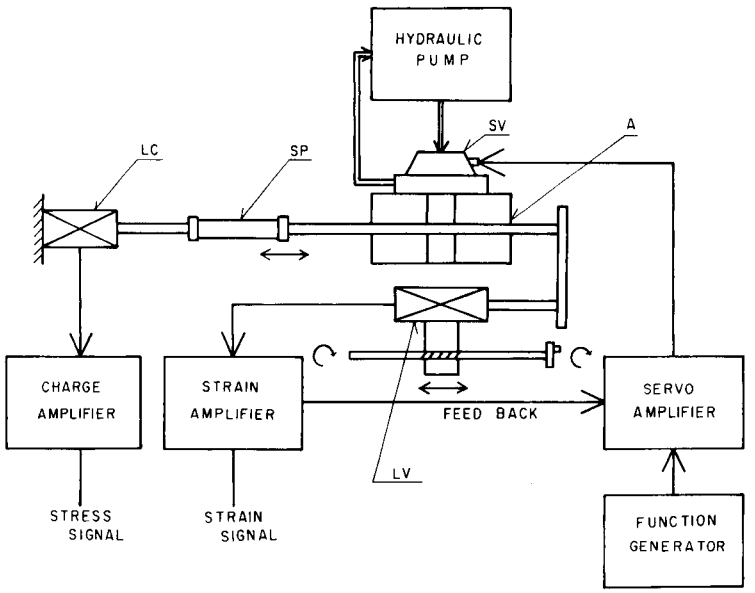

Fig. 2. Schematic diagram of the servo-controlled hydraulic sample deformation device. SP, Sample; LC, piezoelectric stress sensor; SV, servovalve; A, actuator; LV, linear variable differential transformer.

placement of the LVDT is ±8 mm. The signal of the strain amplifier is fed back to the servoamplifier in order to control the sample deformation to follow exactly the preprogrammed output of the function generator by controlling the oil flow at the servovalve. The frequency range of the servoamplifier is from 0 to 1 kHz. The nonlinearity and the maximum output drift are 0.5% and 1%, respectively. The stress on the sample is detected by a piezoelectric stress sensor (Type 9203; Kistler Instrumente, Winterthur, Switzerland) and amplified with a charge amplifier (Type 5001; Kistler Instrumente). The stress sensor allows the maximum load of 588 N, and has a resolution of 1 mN, nonlinearity of 1% and resonant frequency of 27 kHz. The charge amplifier has nonlinearity of 0.05% and maximum leakage current of 0.03 pA. The stress signal can also be fed back to the servoamplifier instead of the strain signal for the case in which the stress is determined by the function generator. The advantage of the servo-controlled system is that either the strain or the stress of the sample can be controlled in a flexible way.

Figure 3 shows a schematic drawing of the deformation device for s.a.x.s. studies. One of sample clamps is connected with the stress sensor. The stress sensor itself is fixed at the end of the support. The other clamp is connected with the actuator. The actuator assembly can be moved horizontally along the guide G which is attached to the support, in order to provide the static strain of the sample. The support can be rotated around the center of the sample by rotating the screw S2, to permit time-resolved s.a.x.s. measurements at various azimuthal angles.

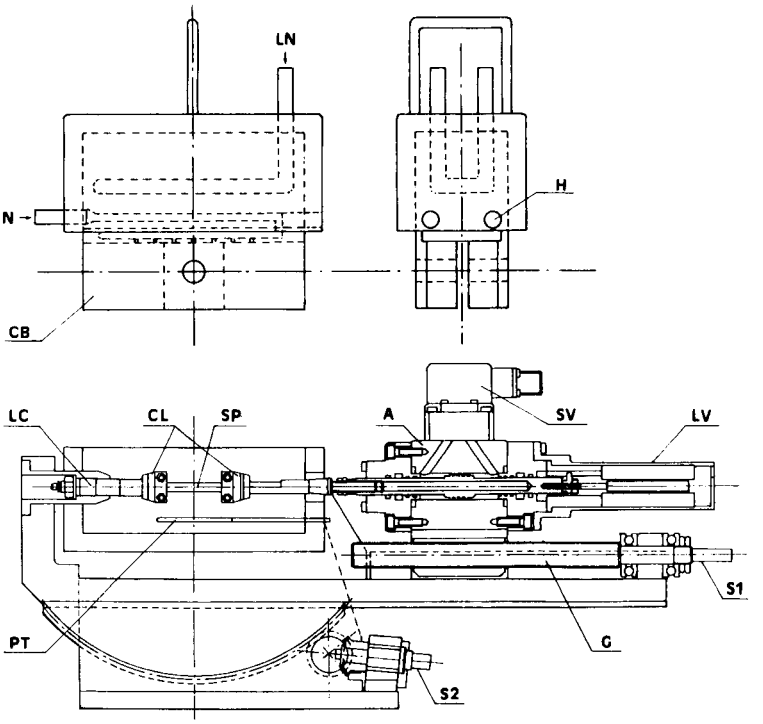

Fig. 3. Schematic drawing of the sample-deformation device with the temperature-controlled sample chamber. SP, Sample; CL, clamp; LC, piezoelectric stress sensor; A, actuator; SV, servovalve; LV, linear variable differential transformer; PT, Pt thermometer; S1 and S2, adjustment screws for static strain and drawing direction of the sample, respectively; G, supporting guide; H, heater; CB, copper block; LN, liquid N_2; N, N_2 gas.

Environmental chamber. A schematic drawing of the sample chamber is shown in the upper half of Fig. 3. It is made from a copper block, and has two heating elements and a channel of liquid nitrogen. The temperature of the sample can be controlled at a constant value between −100 and 300°C, within an accuracy of ±0.5°C.

Function generator. The programmable function generator is a specially designed module to produce an excitation waveform to the specimen. It contains 1K word memory of 12 bits, a 12-bit digital-to-analog converter (DATEL DAC-DG12B), an address counter and a frequency control register. The DAC has 0—10 V peak-to-peak analog output. The rate of the output function can be selected by changing the clock frequency which advances the address counter. This is accomplished by loading an appropriate number in the frequency control register. The clock frequency can be set as $10^6 \times 2^{-k}$ Hz, where k is the content of the frequency control register and must be an integer number between 0 and 23. Because it takes 1024 clock periods to output one cycle of the waveform, the range of the repeating frequency of the function generator is from 0.00012 to 977 Hz.

Besides the function output, two digital signals, PHASE ZERO and BLOCK SHIFT, are generated. These signals provide a phase reference in x-ray and analog data acquisition and are used by the MCA and the microcomputer. The PHASE ZERO pulse is generated when the address counter reaches zero, and the BLOCK SHIFT is generated every $1/N$ period, where N is switch-selectable as 8, 16, 32 and 64. After writing an appropriate excitation waveform in the memory and setting the frequency control register, the function generator can be brought into a 'free-running' mode and will then continuously output the waveform and give the PHASE ZERO and the BLOCK SHIFT pulses without any support of the computer.

Timer. The programmable timer is used to control the 'transient-mode' experiment. It has a presettable 16-bit timer and generates the timing pulse at intervals between 1 and 65536 periods of the time base. The time base can be selected as 10 ms, 100 ms, 1 s or 10 s; thus it provides a timing signal having a duration between 10 ms and ca. 1 week, with more than 4-digit accuracy. It is used to fix the PRESET TIME, the duration of each x-ray sampling, and the PAUSE TIME, the interval between two samplings, and to select the next memory block of the MCA by triggering the MCA with the BLOCK SHIFT pulse. The length of the next PRESET TIME can be preset during the pause period via the computer and the next PAUSE TIME can be preset likewise. With this feature, for example, it is possible to sample x-ray data at equal intervals in logarithmic time scale. This is particularly useful when the intensity of the scattered x-ray shows exponential increase or decrease after a stepwise stimulus has been exerted on the sample.

Analog data acquisition. Responses of various physical properties of the sample other than the x-ray scattering are usually obtained as analog signals. Such quantities (e.g., stress and strain) can be sampled in synchronization with the x-ray data acquisition. The BLOCK SHIFT pulse from the function generator (in the oscillatory mode) or from the programmable timer (in the transient mode) is available as an analog sampling signal (see Fig. 1). One of 8 analog signals (currently only two signals, stress and strain, are used) can be selected by an analog multiplexer (Analog Devices AD7501) and converted to a digital value by a 12-bit analog-to-digital converter (Analog Devices AD574) in ca. 35 μs. Analog data acquisition is accomplished by software control.

Computer. A microcomputer (M223 Mark II, Sord Computer Systems) based on an 8-bit microprocessor (Z80A, Zilog) is used. It has 64 kbyte of random access memory (RAM), two RS232 serial ports, two 5.25-in. double-density floppy disk drives and a dot-matrix printer. The interface between the computer and the various devices such as the MCA is furnished on two S-100 bus modules.

Software. The software for this system falls into three categories: FORTRAN-callable assembler subroutines, data-acquisition programs, and data-processing programs. Data-acquisition and data-processing programs should be written in high-level languages such as FORTRAN or C because

those programs must be interactive and easy to modify according to changes of experimental needs. However, in most cases, assembler programs are needed to control hardware modules. One reasonable solution to this problem is to prepare FORTRAN-callable hardware-control assembler subroutines which can be called by FORTRAN-coded data-acquisition programs.

Assembler subroutines provide various control methods for the hardware modules, among which are MCAINI for initializing the MCA interface, MCTL for controlling the MCA functions, PRESET for programming the MCA operation modes, MCREAD for MCA data transfer, MCDISP for the real-time display of one memory block of the MCA, FGCTL for start/stop control of the function generator, FREQWT for setting the clock frequency of the function generator, and WTFG for writing the waveform memory of the function generator.

The menu-driven data-acquisition program, FGADC, was written in FORTRAN, which provides complete control for the oscillatory measurements: loading the cosine curve in the waveform memory of the function generator, changing the frequency of the output function, start/stop x-ray data acquisition, analog data acquisition and data transfer from the MCA. Data-processing programs, FTXIS and FTENK, were also written in FORTRAN; the former is for the x-ray data evaluation and the latter is for the evaluation of the stress and strain data. Both programs involve Fourier expansion of the raw data.

Time-resolved data acquisition

A time-resolved experiment can be either single-shot or repetitive. A single-shot, or transient, experiment typically measures time-response functions of a sample in the time domain. In contrast, a repetitive measurement is typically done to obtain response functions in the frequency domain by applying an oscillatory load to the sample. Such experiments are here called oscillatory experiments. A repetitive experiment may also be a repetition of a single-shot experiment in order to increase the signal-to-noise ratio.

Transient experiment. Figure 4A shows a schematic diagram illustrating the principle of the transient mode. In this example, the strain of the sample is increased in a very short period at time t; then the x-ray scattering profile and the stress on the sample are recorded as illustrated in the bottom half of the figure. The timing charts of the measurement are shown. The PHASE ZERO signal generated by the timer triggers the measurement. On accepting this signal, the MCA clears the block counter, consequently the first memory block is selected, and the x-ray intensity profile is accumulated for a certain time period, which is given by the PRESET TIME. With the arrival of the next BLOCK SHIFT signal from the timer, the next memory block is selected and the x-ray sampling is again activated.

As described above, the number and the size of the memory blocks can be chosen in several ways so that one can select the best combination of the number of time-slices and the number of resolving points along the scattering

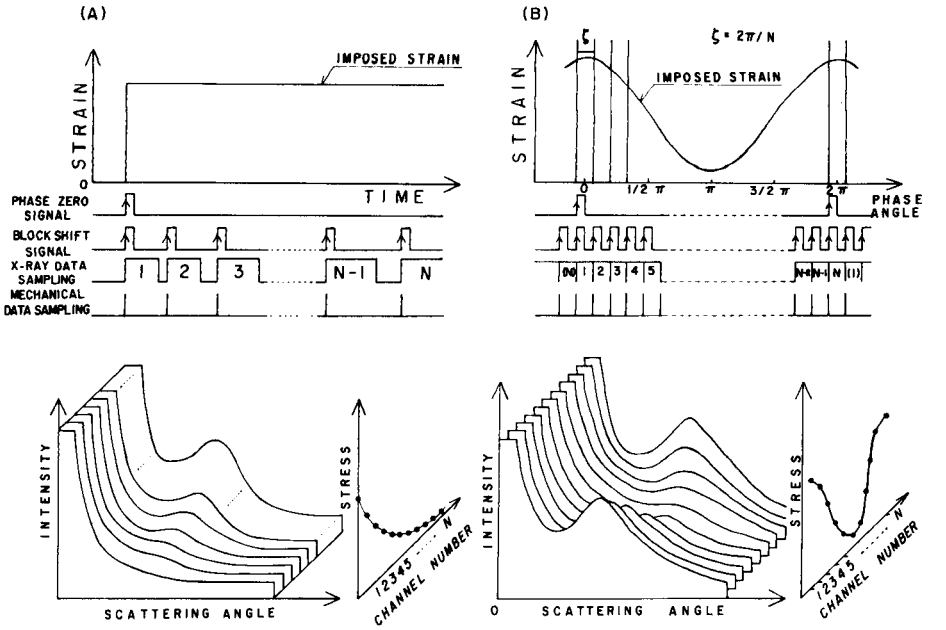

Fig. 4. Schematic diagrams illustrating general principles: (A) the transient experiment; (B) the oscillatory experiment using sinusoidal elongation.

angle for the experimental needs. The stress data are sampled by the computer and stored in the computer memory synchronously with the BLOCK SHIFT signal. The PRESET TIME and the PAUSE TIME can be varied arbitrarily by the computer during the course of the measurement as described before. After a preset period of data sampling, the content of the MCA is transferred to the computer and processed with the stress data.

Oscillatory experiment. Figure 4B illustrates the principle of the oscillatory experiment. In this mode, a cyclic excitation is applied to the specimen and the time-sliced x-ray and mechanical data acquisition can be repeated over many cycles of oscillation. A sinusoidal strain is assumed in Fig. 4B. The PHASE ZERO signal is generated by the function generator at the zero phase point of the cosine curve. As soon as this signal is received, the MCA selects the first memory block and the x-ray scattering at the first phase interval of the strain is accumulated in the first memory block. On receiving the next BLOCK SHIFT signal from the function generator, the second memory block is selected and activated immediately for the data acquisition of x-ray scattering profile for the second phase interval of the strain. Analog data sampling is done simultaneously. With the next PHASE ZERO signal, the data acquisition returns to the first memory block where the input intensity data are added to the previous intensity data. In this way one can accumulate the data corresponding to the scattering profile at each phase interval of the stimulus over a suitable number of cycles to gain good counting statistics.

Unlike the transient mode, this mode assumes no pause time between samplings and equal intervals between BLOCK SHIFT signals, the interval being a multiple of 1/1024 of a period. Hence the data are accumulated at N equally-divided intervals, N normally being 64.

Once the oscillatory measurement is started, the x-ray data-acquisition continues endlessly. Therefore software to count the number of cycles and to stop the measurement is necessary. The mechanical data, e.g., stress and strain, are sampled and stored in computer memory also by software control. Upon completion, the content of the MCA memory is transferred to the microcomputer, and Fourier expansion is performed to obtain Fourier coefficients of the x-ray intensity at every scattering angle and the mechanical data.

In-phase and out-of-phase components of the dynamic variation of x-ray intensity are obtained as first-order Fourier coefficients. From these, one can calculate the amplitude and the phase of the linear-response component of the x-ray intensity. As x-ray data are measured in synchronization with the timing signal produced by the function generator, phase correction must be done to get the true phase relationship between the x-ray intensity and the applied strain. This is accomplished by subtracting the phase delay of the strain signal with respect to the timing signal of the function generator from the estimated phase angle obtained by the Fourier expansion of the raw data. The phase delay of the strain with respect to the output of the function generator arises mainly from the delayed response of the hydraulic system. This phase delay is determined from the first-order Fourier coefficients of the strain data by correcting other phase delays caused by the LVDT and the strain amplifier. The linear responses of the stress or other physical properties can be calculated in a similar way. Furthermore, nonlinear response of the internal structure can be evaluated by using higher-order Fourier coefficients of x-ray intensity.

This mode is quite useful to follow processes with short time scales, because the total duration of the measurement can be far longer than the time scale of the physical process of interest, in contrast to the one-shot transient experiment.

RESULTS AND DISCUSSION

Orientated crystallization of cross-linked polybutadiene rubber

The kinetics of oriented crystallization were studied by following changes of s.a.x.s. and w.a.x.s. profiles with time during isothermal crystallization at given draw ratio (λ in the range 2 to 3.5) and crystallization temperature (T_c in the range -30 to -10°C). This study represents a typical example of transient experiments.

The polymer studied was cross-linked polybutadiene rubber with high *cis*-1,4 content (99%) supplied by Assoreni, San Donato Milanese (Italy). Polybutadiene rubber has a cross-link density of 10^{-4} mol cm^{-3} and a number-average molecular weight between cross-links of 9000.

The samples were uniaxially stretched at room temperature at given draw ratios, which were not high enough to induce crystallization at room temperature. Then the samples were cooled to a given crystallization temperature. Details on these studies on the equilibrium state of orientated crystallization have been presented elsewhere [12]. The s.a.x.s. patterns were two-point patterns oriented in the draw direction, indicating crystallization into regularly packed lamellar crystallites with their normals parallel to the draw direction. The w.a.x.s. results indicated uniaxial orientation of the crystallites with their chain axes parallel to the draw direction.

Figure 5 shows typical time evolution of w.a.x.s. profiles along the equator (the direction perpendicular to the draw direction) during isothermal crystallization at $T_c = -10°C$ and $\lambda = 2.0$. Each profile was measured with 50-s exposure to x-rays. It is clearly seen that the diffracted intensity from crystallites slowly increases with time. From such data one can estimate x-ray crystallinity, X_c, as a function of time. Such fundamental information is of importance in understanding the mechanism and kinetics of the orientated crystallization.

Figure 6 shows typical time evolution of s.a.x.s. profiles along the meridian during isothermal crystallization at $T_c = -10°C$ and $\lambda = 3.0$. Each profile was measured with 10-s exposure to x-rays. Clearly, the scattering maximum appears after the onset of crystallization and the position of the maximum shifts remarkably toward larger scattering angle. The excess scattering profiles

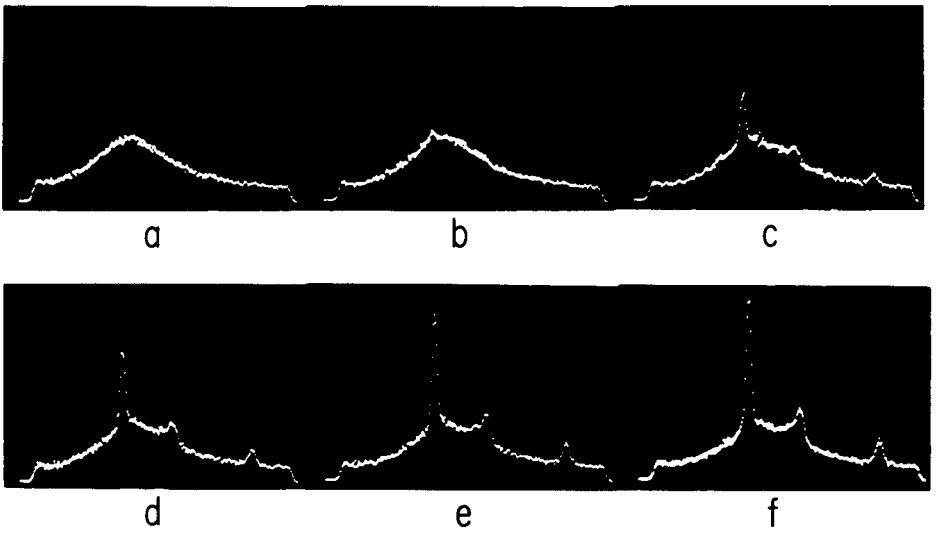

Fig. 5. Typical change in w.a.x.s. profiles with time along the equator (the direction perpendicular to draw direction) during isothermal crystallization of stretched and cross-linked polybutadiene; the draw ratio and crystallization temperature were 2.0 and −10°C, respectively. (a) 50 s; (b) 450 s; (c) 950 s; (d) 1300 s; (e) 2200 s; (f) 4050 s after onset of the isothermal crystallization.

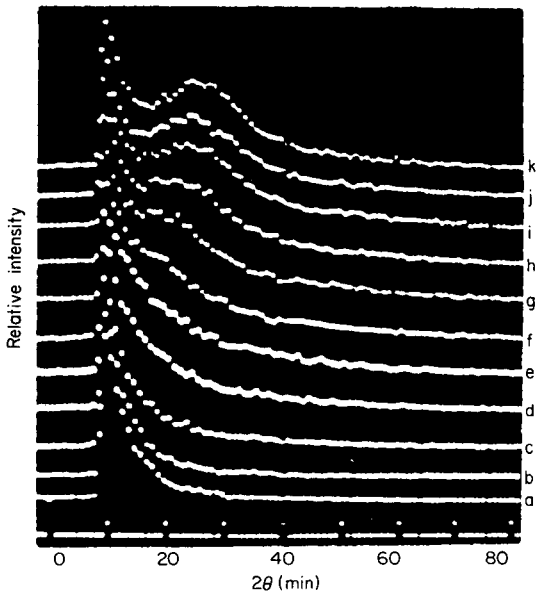

Fig. 6. Typical change in s.a.x.s. profiles with time along the meridian during isothermal crystallization of the stretched and cross-linked polybutadiene; the draw ratio and crystallization temperature were 3.0 and −10°C, respectively. (a) 10 s; (b) 100 s; (c) 150 s; (d) 200 s; (e) 250 s; (f) 310 s; (g) 445 s; (h) 695 s; (i) 1205 s; (j) 2015 s; (k) 3025 s after onset of the isothermal crystallization. The profiles have been shifted vertically for clarity.

caused by crystallization were obtained by subtracting the scattering intensity of the molten rubbers from s.a.x.s. profiles at given time. From such real-time s.a.x.s. data, one can estimate (1) long spacing, L, (2) lamellar thickness, D, and (3) integrated intensity, Q_r, of the excess scattering intensity which depends on $(\rho_c - \rho_a)$, the electron density difference between crystalline and amorphous regions and ϕ_c, the volume fraction of lamellar crystallites in the one-dimensional assembly.

Figure 7 summarizes various structural parameters as a function of time during the isothermal crystallization at $\lambda = 3.0$ and $T_c = -10°C$, where σ/σ_0 is the stress relaxation during crystallization, with σ_0 being the stress before crystallization. One interesting feature of the results is that the lamellar thickness, D, remains essentially independent of time whereas L decreases significantly. The decrease of L occurs in parallel with increase of Q_r. The other interesting feature is that the increase of the w.a.x.s. crystallinity, X_c, generally lags with the increase of the s.a.x.s. integrated intensity, Q_r. This time lag is smaller for higher supercooling. This seems to indicate that a perfection of crystal lattice is built up by local rearrangements of atoms or molecules with a time lag to formation of periodic electron-density fluctuations. Detailed discussion of these results about crystallization kinetics will be described elsewhere.

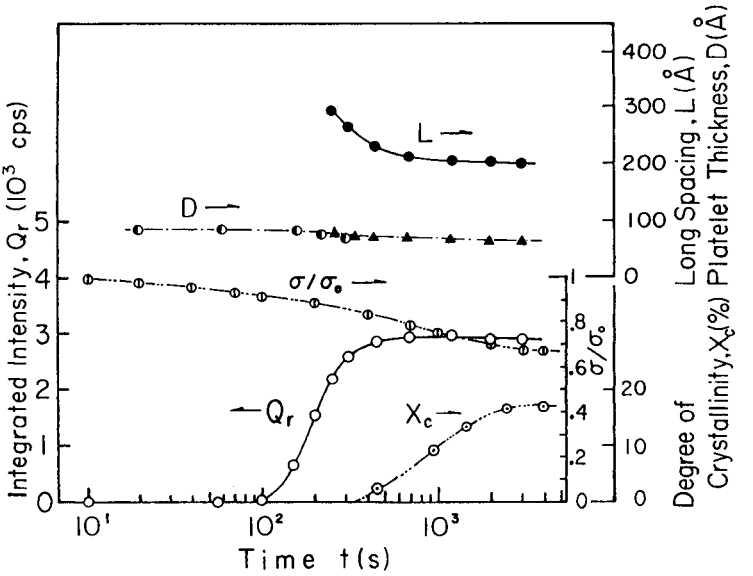

Fig. 7. Variations of L, D, Q_r, σ/σ_0 and X_c with time during isothermal crystallization at a draw ratio of 3.0 and a crystallization temperature of −10°C.

Dynamic lamellar deformation of tubular-extruded poly(1-butene) films

In this section, a typical application of oscillatory s.a.x.s. measurements in studying dynamics of polymer deformation is presented. Samples used are tubular-extruded films of a semicrystalline polymer, poly(1-butene). The films have stacked lamellar structure [17], the stacks of crystalline lamellae are mainly oriented with their normals parallel to the extrusion direction. The s.a.x.s. patterns of the samples are the typical two-point patterns reflecting this internal structure. Upon stretching along the extrusion direction, the interlamellar spacing, L, increases and a large increase of the scattering intensity occurs because of the decrease in density and the change of volume fraction $(1 - \phi_c)$ of the interlamellar noncrystalline region.

The temperature-dependence of the dynamic Young's modulus of the sample measured at a frequency of 1.9 Hz clearly showed a dispersion at ca. −30°C, i.e., the storage modulus, E', decreases with increasing temperature and the loss modulus, E'', shows a distinct peak at ca. −30°C. An interesting question is how this mechanical response is correlated with the response of the internal lamellar structure. In order to get information concerning this, the dynamic variation of the s.a.x.s. intensity profile under sinusoidal elongation of the sample was measured. The optical geometry of the dynamic s.a.x.s. experiment is illustrated in Fig. 8. The specimen is deformed along the direction of the extrusion, by applying a dynamic strain of 2% superimposed on the pre-stretching (static) strain of 7%. The two-point s.a.x.s. pattern appears along the meridional direction, accordingly the PSD is placed parallel to the stretching direction.

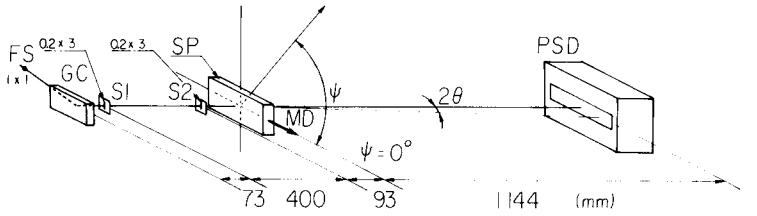

Fig. 8. Optical geometry of time-resolved s.a.x.s. experiment. FS, Focal spot; GC, graphite monochromator; S1, S2, slits; SP, specimen; MD, machine direction; PSD, position-sensitive detector.

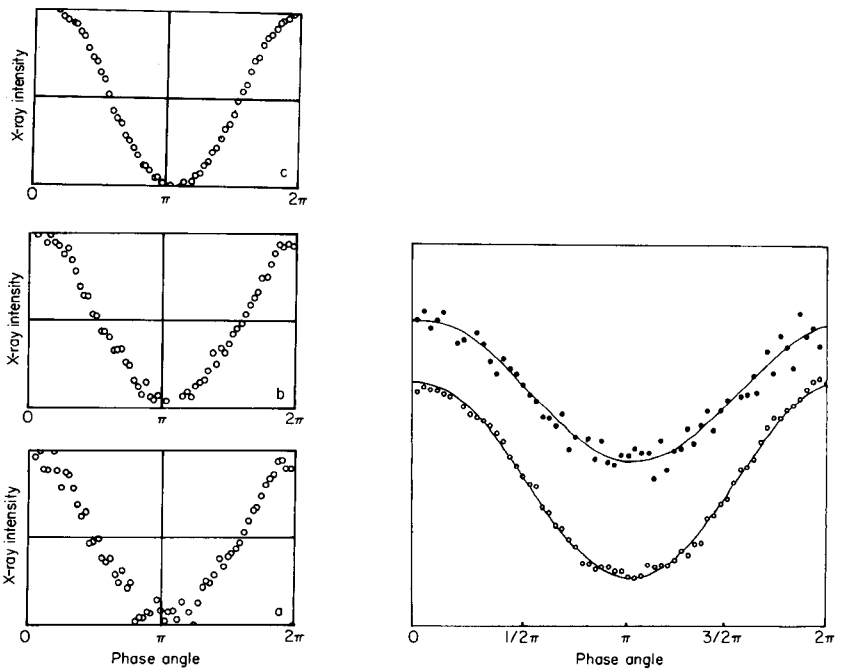

Fig. 9. Variation of accumulated s.a.x.s. intensity with phase angle of sample elongation, obtained after 200 (a), 800 (b) and 3200 (c) cycles of sinusoidal elongation at −20°C and 1.9 Hz.

Fig. 10. Variations of peak position (•) and integrated intensity (○) of s.a.x.s. at −20°C and 1.9 Hz, with phase angle of strain.

In Fig. 9, the variation of the s.a.x.s. intensity measured at a Bragg angle, where a peak maximum appears, under sinusoidal deformation of the sample is plotted against the phase angle of the sinusoidal signal ($\Delta\lambda \cos \omega t$) of the function generator. The measurement was done at −20°C, near the temperature of the maximum E'', and a frequency of 1.9 Hz, where the sample exhibits viscoelastic dispersion. The figure shows that the s.a.x.s. intensity

varies as a result of the elongational deformation of the sample, and that there is a linear relationship between the intensity and the sample strain. The figure also demonstrates clearly the effect of data accumulation. With an increasing number of accumulation cycles, better counting statistics are observed. This particular example shows that 3200 cycles is enough to give satisfactory results; after 3200 cycles, Fig. 9 shows clearly that the x-ray intensity lags behind the sinusoidal signal in this example. Quantitative evaluation of the linearity of the response and the phase delay can be conducted by calculating the in-phase and out-of-phase components of the first-order and the higher-order Fourier coefficients of the dynamic variation of the x-ray intensity. However, to get information on the internal structure, further measurements of the scattering intensity are necessary.

Variation of the peak position in the scattering intensity distribution with the applied strain can be obtained by calculating the center of the scattering peak, $\theta_0 = \int \theta I(\theta) \mathrm{d}\theta / \int I(\theta) \mathrm{d}\theta$, at every phase angle of the strain. Variation of the integrated scattering intensity can be also calculated at every such phase angle. Figure 10 represents the variations of the peak position and the integrated intensity thus determined. The results show sinusoidal variations of the scattering peak and the integrated intensity with the external strain, indicating that the long spacing and the s.a.x.s. intensity vary linearly with sample deformation.

The dynamic long spacing, ΔL^*, and the dynamic s.a.x.s. intensity, ΔQ_r^*, are calculated by Fourier expansion of these data. The dynamic long spacing correlates with the dynamic variation of the mean lamellar separation and the dynamic s.a.x.s. intensity results from dynamic variation of electron-density fluctuation in the sample. These data provide fundamental knowledge about the relation between the mechanical response of the lamellar structure and the relaxation phenomena of crystalline polymers, which will be discussed elsewhere in detail.

Conclusion

The technique for the time-resolved detection of x-ray scattering is quite important in studying the dynamics of the internal-structure response in polymeric materials to applied external stimuli. For example, the technique can be applied to study the kinetics of phase transition and molecular or structural origin of the relaxation phenomena.

This work was supported by a Grant-in-Aid for Scientific Research (449012) from the Ministry of Education, Science and Culture, Japan. The authors are grateful to Professor A. Ziabicki for providing the cross-linked polybutadiene samples and for his scientific stimulation.

REFERENCES

1 T. Kawaguchi, T. Ito, H. Kawai, D. Keedy and R. S. Stein, Macromolecules, 1 (1968) 126.

2 A. Tanaka, E. P. Chang, B. Delf, I. Kimura and R. S. Stein, J. Polym. Sci. Polym. Phys. Ed., 11 (1973) 1891.
3 R. J. Cembrola, T. Kyu, R. S. Stein, S. Suehiro and H. Kawai, J. Polym. Sci. Polym. Phys. Ed., 21 (1983) 329.
4 S. Suehiro, T. Yamada, H. Inagaki, T. Kyu, S. Nomura and H. Kawai, J. Polym. Sci. Polym. Phys. Ed., 17 (1979) 763.
5 S. Suehiro, T. Yamada, T. Kyu, K. Fujita, T. Hashimoto and H. Kawai, Polym. Eng. Sci., 19 (1979) 929.
6 K. Fujita, H. Niwa, S. Nomura and H. Kawai, J. Polym. Sci. Polym. Phys. Ed., 21 (1983) 1713.
7 H. Kawai, S. Suehiro, T. Kyu and A. Shimomura, Polym. Eng. Rev., 3 (1983) 109.
8 P. Young, T. Kyu, S. Suehiro, J. S. Lin and R. S. Stein, J. Polym. Sci. Polym. Phys. Ed., 21 (1983) 881.
9 R. W. Hendricks, P. A. Seeger, J. W. Sheer and S. Suehiro, Nucl. Instrum. Methods, 201 (1982) 261.
10 R. W. Hendricks, J. Appl. Crystallogr., 11 (1978) 15.
11 T. Hashimoto, S. Suehiro, M. Shibayama, K. Saijo and H. Kawai, Polym. J., 13 (1981) 501.
12 T. Hashimoto, K. Saijo, M. Kość, H. Kawai, A. Wasiak and A. Ziabicki, Macromolecules, 18 (1985) 472.
13 T. Hashimoto, Y. Tsukahara and H. Kawai, Macromolecules, 14 (1981) 708.
14 T. Hashimoto, K. Kowsaka, M. Shibayama and S. Suehiro, Macromolecules, 19 (1986) 750.
15 T. Hashimoto, K. Kowsaka, M. Shibayama and H. Kawai, Macromolecules, 19 (1986) 754.
16 M. Fujimura, T. Hashimoto and H. Kawai, Mem. Fac. Eng. Kyoto Univ., 43 (1981) 224.
17 T. Hashimoto, A. Todo, Y. Tsukahara and H. Kawai, Polymer, 20 (1979) 636.

Analytica Chimica Acta, 189 (1986) 57—67
Elsevier Science Publishers B.V., Amsterdam – Printed in The Netherlands

DEPOLARIZED LIGHT-SCATTERING SPECTROSCOPY AND POLYMER CHARACTERIZATION

G. D. PATTERSON* and D. J. RAMSAY
Department of Chemistry, Carnegie-Mellon University, Pittsburgh, PA 15213 (U.S.A.)
P. J. CARROLL
AT and T Bell Laboratories, Murray Hill, NJ 07974 (U.S.A.)
(Received 14th April 1986)

SUMMARY

Light scattering has long been established as a technique for measuring the molecular weight and radius of gyration of polymer molecules. Depolarized light scattering can be studied accurately with lasers. The theory of static and dynamic depolarized light-scattering spectroscopy is presented and illustrated with two examples of novel particles in solution. From the static intensity measured as a function of angle, the length of rod-like molecules can be evaluated. More complicated geometrical measures are obtained in the general case. From the dynamic light scattering, the translational self-diffusion coefficient and the rotational diffusion coefficient are obtained. These quantities can be interpreted in terms of a major semi-axis length and an axial ratio for the molecule or particle by using the Perrin equations.

Light scattering has long been established as a method for determining the molecular weight of polymers in solution [1, 2]. The incident light is characterized by a well defined intensity I_i, wavelength λ, and direction. The incident wavelength and direction define an incident wavevector $\vec{q}_i$ with magnitude $2\pi/\lambda$ in a vacuum. The scattered light observed at angle θ in the scattering plane defined by the incident and scattered light is also characterized by an intensity I_s and wavevector, $\vec{q}_s$. A quantity called the scattering vector is defined as $\vec{q} = \vec{q}_s - \vec{q}_i$. The intensity of scattered light is measured as a function of concentration c and scattering angle θ. For a polymer solution, the intensity is measured relative to that for the pure solvent. The excess intensity of scattered light caused by fluctuations of polymer concentration in the thermodynamic (low angle) limit is proportional to $ckT/(\partial\pi/\partial c)$ where k is the Boltzmann constant, T the temperature, and π the osmotic pressure. In the limit of infinite dilution, $(\partial\pi/\partial c)$ is proportional to kT/M, where M is the molecular weight of the polymer. The excess scattered intensity divided by the concentration is extrapolated to zero scattering angle and infinite dilution and the molecular weight is proportional to the intercept.

For polymers that are large enough, the radius of gyration R_g can be found from the angular dependence of the excess scattered intensity in the limit of

0003-2670/86/$03.50

infinite dilution. The angular dependence can be described by a function $P(\theta)$ [3]. In the low-angle limit

$$P(\theta) = 1 - 1/3\, R_g^2 q^2 \tag{1}$$

where $q = (4\pi n/\lambda) \sin(\theta/2)$ is the magnitude of the scattering vector in the medium and n is the refractive index of the medium. A wealth of data relating the radius of gyration of polymer molecules to their molecular weight has been collected by using arc lamps as light sources [4].

The advent of laser sources has made possible two types of advances in the use of light scattering to characterize polymers: both depolarized scattered light and the dynamics of polymer solutions by photon correlation spectroscopy can be studied. If the incident light is polarized in the vertical direction (V) with respect to the scattering plane, then scattered light observed with an analyzer set in the horizontal position (H) (in the scattering plane) is called depolarized or HV scattering. The excess depolarized intensity of polymer solutions is often very weak, but it can now be detected and analyzed. In the simplest case, the excess polarized (VV) light scattering from polymer solutions is due to concentration fluctuations. Analysis of the time dependence of the scattered intensity yields the mutual diffusion coefficient, D_m. In the limit of infinite dilution, the mutual-diffusion coefficient is equal to the self-diffusion coefficient, D_0. The self-diffusion coefficient is given by $D_0 = kT/6\pi\eta R_h$, where η is the solvent viscosity and R_h is the hydrodynamic radius of the polymer molecule. The behavior of the self-diffusion coefficient in polymer solutions has been thoroughly reviewed recently [5]. In the present paper, the use of depolarized light scattering is examined for the characterization of polymers in solution. Both total intensity and dynamic light scattering are considered.

DEPOLARIZED LIGHT SCATTERING

When a molecule is placed in an electric field E, a dipole moment μ is induced in the molecule. The relation between the field and the dipole moment involves the polarizability tensor α for the molecule: $\mu = \alpha E$. The polarizability tensor can be divided into a mean scalar part, $\bar{\alpha} = (1/3)\, Tr\, \alpha$, and a symmetric traceless part, $\hat{\alpha} = \alpha - \bar{\alpha}\mathbf{E}_3$, where $\mathbf{E}_3$ is the unit tensor and Tr denotes the trace. The quantity $\hat{\alpha}$ is called the optical anisotropy tensor. The depolarized scattered intensity I_{HV} is proportional to the quantity, $\gamma^2 = 3/2\, Tr\, \hat{\alpha}\hat{\alpha}$.

The value of γ^2 depends on the composition and structure of the molecule. One model that allows γ^2 to be calculated for any molecule is to assign an anisotropy tensor to each chemical bond in the molecule and to sum the bond tensors to obtain a molecular anisotropy tensor [6]. Although this model is not rigorous and certainly not universally valid, it has been successfully applied to polymers [7]. Polymer molecules can adopt many different conformations. There will be a different value of γ^2 for each conformation.

Thus, the quantity observed for polymers is the mean-squared optical anisotropy $\langle\gamma^2\rangle$, where the brackets denote an average over all the conformations of the molecule. Theoretical techniques for evaluating such averages have been highly developed [8]. Measurements of $\langle\gamma^2\rangle$ can then be used to infer the average conformation of the polymer molecule.

When the polymer molecules become sufficiently large, the depolarized intensity is a function of scattering angle just like the polarized scattering caused by concentration fluctuations. The fundamental relation that governs the depolarized intensity is given by

$$S_{HV}(q) = \sum_{j,k} \langle \hat{\alpha}^j_{yz} \hat{\alpha}^k_{yz} \exp(i\vec{q}\vec{r}_{jk}) \rangle$$

where j and k refer to bonds in the molecule, $\vec{r}_{jk}$ is the vector from bond j to bond k, and $\hat{\alpha}_{yz}$ is the yz component of the anisotropy tensor in the laboratory frame of reference. The direction of scattered light defines the x-direction and the scattering plane is the xy plane. This expression has been evaluated for flexible chain polymers in the low q region [9, 10]. The term in q^2 depends on averages over terms involving both $\hat{\alpha}^j_{yz}$ and $\vec{r}_{jk}$. The major difficulty in the calculations involves averaging over the orientation of the molecule in the laboratory frame of reference. Measurements of the angular dependence of the excess depolarized intensity in flexible polymer solutions are still scarce. In this paper, measurements of the angular dependence of the excess depolarized intensity are reported for two systems that are not simple flexible polymers.

Another type of polymer that can be treated theoretically is the rigid rod polymer. The chain can be viewed as a linear pearl necklace with a polarizability tensor assigned to each pearl. If the rod has a length, L, and the quantity $x = qL$ is defined, the polarized scattering caused by the mean scalar polarizability can be considered. The angular dependence of the scattered intensity is given by

$$S(q) = (2/x)\int_0^x (\sin z/z)dz - (2\sin x/x)^2$$

One complicating factor is that the VV intensity is not entirely due to the mean scalar polarizability. For rod molecules, there will be a significant contribution to the VV scattering from optical anisotropy. The HV scattering is entirely due to optical anisotropy. If the angular dependence of the HV scattering can be calculated, then it is possible to infer L in a less complicated fashion.

The angular dependence of the excess HV scattered intensity for a rod molecule can be expressed [11, 12] as

$$S_{HV}(\theta) = \gamma^2[(1/2)Y(x) - (3/4)X(x) - (1/4)\cos\theta Z(x)]$$

where

$$X(x) = (\sin x/x^5) - (\cos x/x^4) + (\sin x/2x^3) + (\cos x/2x^2) - (4/3x^2) + (1/2x)\int_0^x (\sin z/z)\mathrm{d}z$$

$$Y(x) = (\sin x/x^3) - (2/x^2) + (\cos x/x^2) + (1/x)\int_0^x (\sin z/z)\mathrm{d}z$$

$$Z(x) = (5\sin x/x^5) - (5\cos x/x^4) + (\sin x/2x^3) + (\cos x/2x^2) - (8/3x^2) + (1/2x)\int_0^x (\sin z/z)\mathrm{d}z$$

A typical plot of $S_{HV}(\theta)$ vs. θ is shown in Fig. 1. The value of $S_{HV}(\theta)$ displays a minimum for sufficiently large values of θ. The value of θ at the minimum has been calculated as a function of L and the results are shown in Fig. 2. If the rod is too short there will be no minimum for the values of qL obtainable with light scattering. If the rod is longer than 5 μm, it will be very difficult to determine the exact value of L because the angle at the minimum changes very little with length for long rods.

Further information about the particle can be obtained from the dynamic light scattering. The intensity is measured as a function of time and the intensity correlation function $C(t) = \langle I(t)I(0)\rangle/\langle I\rangle^2$ is calculated. This correlation function is related to the normalized function for electric field relaxation $\phi(t)$ by $C(t) = 1 + A\phi^2(t)$ where the coefficient A depends entirely on experimental details. The normalized function for electric field relaxation is equal to the normalized relaxation function for whatever process gives rise to the light scattering. In the simplest case of light scattering by isotropic particles observed in the VV geometry, the relaxation function is given by

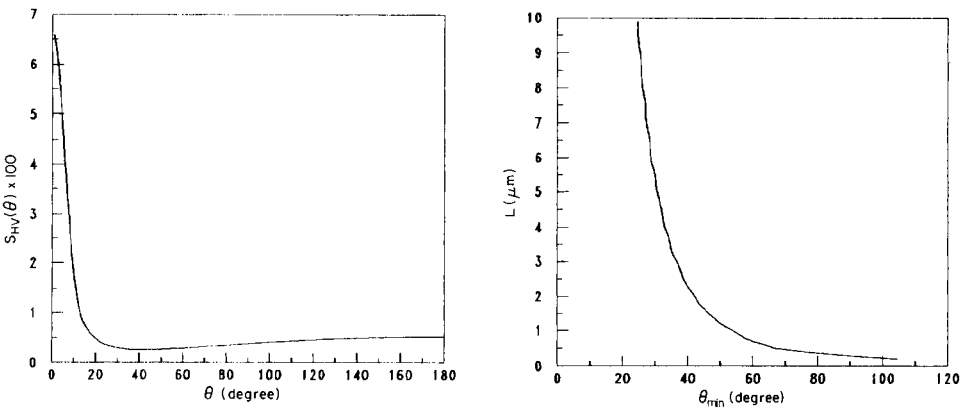

Fig. 1. Typical plot of the depolarized scattering function $S_{HV}(\theta)$ vs. θ for a rod with L = 2 μm, λ = 514.5 nm, and n = 1.5.

Fig. 2. The rod length L is plotted against the angle θ_{min} at which $S_{HV}(\theta)$ reaches a minimum. The incident wavelength and refractive index are the same as for Fig. 1.

$\phi(t) = \exp(-D_0 q^2 t)$. In the simplest case for depolarized light scattering, the relaxation function decays with a rate given by $D_0 q^2 + 6\Theta$, where Θ is the rotational diffusion coefficient. By measuring the relaxation function as a function of q, both D_0 and Θ can be obtained. These quantities have been calculated for generalized ellipsoids as a function of the axial ratios by Perrin [13]. If the particle is characterized by a major semi-axis of length a and an axial ratio $\rho = b/a$, then the translational diffusion coefficient is given by

$$D_0 = kT\,G(\rho)/6\pi\eta a$$

and the rotational diffusion coefficient by

$$\Theta = (3kT/16\pi\eta a^3)[(2-\rho^2)G(\rho) - 1]/(1-\rho^4)$$

where the function $G(\rho)$ is given by

$$G(\rho) = \langle \ln\{[1 + (1-\rho^2)^{1/2}]/\rho\}\rangle/(1-\rho^2)^{1/2}$$

for the prolate ($\rho < 1$) case and

$$G(\rho) = [\tan^{-1}(\rho^2 - 1)^{1/2}]/(\rho^2 - 1)^{1/2}$$

for the oblate ($\rho > 1$) case. The two equations for D_0 and Θ can then be solved simultaneously for a and ρ.

When static and dynamic light-scattering data are combined, the overall shape of particles in solution can be obtained. By using depolarized light scattering, even axial ratios can be calculated. This technique has not yet been routinely exploited, but it has proven to be very useful in the examples to be reported in this paper.

EXPERIMENTAL

Light-scattering spectroscopy is now a highly developed technique. Incident light is routinely obtained from a laser. Although a He/Ne laser is sufficient for most work that measures only the scattered intensity, dynamic light scattering is best done with a more intense source. The scattered intensity depends on the fourth power of the incident light frequency (or the inverse fourth power of the wavelength). The He/Ne laser line routinely used is 632.8 nm. The argon ion laser has become the laser of choice for most light-scattering spectroscopy. The two strongest emission lines for the argon ion laser are 488.0 nm and 514.5 nm. Not only is the incident power level much higher, but also the scattering efficiency is much better because of the higher frequency. If the incident light is absorbed by the sample it may be desirable to use an incident wavelength where absorption is at a minimum. But the use of resonance enhancement [14] allows very dilute solutions to be studied. When a longer wavelength is required a krypton ion laser offers substantially more power than a He/Ne laser at red wavelengths. The laser used here is a Spectra-Physics Model 2020 argon ion laser operated at 514.5 nm. The incident intensity is actively stabilized by a feedback loop to the laser power

supply. This avoids the need to measure the scattered intensity with a ratio scheme that detects both the incident intensity and the scattered intensity simultaneously.

In addition to controlling the incident intensity, the incident polarization must be adjusted. The output polarization of the laser was changed externally with a double Fresnel rhomb polarization rotator to be vertical with respect to the scattering plane. When necessary, the incident beam polarization was improved with a Glan laser polarizer with extinction greater than 10^5:1. In order further to increase the power density in the sample, the incident light is usually focussed with a final lens. This produces an incident beam with a diameter in the range 100—500 μm. In the present experiments, the laser beam was not focussed, because the intense absorption by the particles in solution would lead to thermal defocussing. The lower power density prevented defocussing of the incident laser beam and the large diameter beam allowed the maximum scattering volume to be observed consistent with the coherence area of the scattered light.

Light-scattering spectroscopy can be done under a very wide range of sample conditions. Samples at temperatures from 4 K to 600 K and at pressures from 1 bar to 3 kbar have been studied. For the experiments reported here, the solutions were studied at 293.15 K. The solutions were contained in cylindrical cells of 1-cm diameter. The cells were immersed in a vat containing an index-matching fluid to minimize stray scattering from the cell itself. The incident light passed through the cell, out of the vat, and into a light trap. Another common design is to incorporate the light trap in the vat to avoid the rear-window reflection problem. The entrance and exit windows of the vat were flat to avoid flare at low angles. The vat fluid was toluene, but any fluid with a refractive index near 1.47 would do. Although light scattering is now a mature technique, considerable research is still devoted to cell and vat design.

One of the most vexing problems associated with light scattering is the optical clarification of the sample. Dust particles interfere with the observation of the intrinsic light scattering from the solvent or the solution. When all the components in the solution are small, the solution can be clarified by direct filtration with micropore (0.2-μm pore size) filters. When the solute particles are large or fragile, clarification is often accomplished by centrifugation. In the present experiments, the solutions were prepared with filtered solvent. The large size and unique chemical properties of the solute precluded direct filtration of the solutions. Because of the intense resonance scattering by the solute particles, scattering by other particles was not observed with the same level of sensitivity as that used to study the solute particles.

The light scattered at angle θ was collected with a light-scattering goniometer. The one used here was a Brookhaven Instruments Model 240M. The size of the scattering volume is defined by a pinhole and two lenses. The scattering solid angle is defined by another aperture. In order to do photon correlation spectroscopy, the scattering volume and solid angle must be small

enough that the coherence properties of the light are maintained. The coefficient A defined above depends on these variables. The scattered light is passed through an analyzer polarizer when depolarized light scattering is observed. Because the polarized scattering can be very intense for polymer solutions, it is important to use a very good polarizer in the scattered beam to isolate only the depolarized component. The scattered light is detected with a photomultiplier tube. Although modern photomultiplier tubes are very good, they are not perfect. The first problem is dark current; the increase in intensity caused by dark current can easily be corrected for the integrated intensity, but there is no time to correct for it during dynamic light scattering. The dark current can be minimized by using a small photocathode area. The second problem is after-pulsing: when a photon strikes the photocathode, an electron is ejected and amplified by a series of dynodes. There is a finite probability that another electron will be ejected by the first dynode within a short period after the initial photoelectron strikes it. This produces apparent correlations at short times (<1 μs). This artifact must be minimized to obtain good data at short times, but even with the best photomultipliers, data obtained at short times must be excluded from further treatment. The photocurrent is converted to a train of emitter-coupled logic (ECL) pulses and counted with a photon counter. If only the integrated intensity is required, the total number of counts is recorded over an appropriate time interval. If dynamic light scattering is being examined, the number of photons during a small time interval is counted and the intensity correlation function is calculated. This is done with a digital correlator. The one used here was a Brookhaven Instruments Model 2020 digital correlator with 256 delay channels. The delay channels could be divided into four groups with different sample times. This allowed data over four decades in time to be collected simultaneously. Sample times from 100 ns to 1 s could be chosen. A dramatic example of a light-scattering correlation function is shown in Fig. 3. Data were collected over seven decades in time for a nonexponential decay. This illustrates the power of the four sample-time correlator with 256 channels.

Although the simple theory predicts that the relaxation function is a single exponential decay, real data often depart from this ideal case. The most obvious reason is that there will be a distribution of molecular sizes in any real sample. The problem of polydispersity has been the subject of much research [14, 15]. The relaxation function can be represented as

$$\phi(t) = \int_0^\infty G(\Gamma) \exp(-\Gamma t) d\Gamma$$

where $G(\Gamma)$ is the distribution of decay rates. One approach is to use an empirical distribution function characterized by a minimum number of parameters (usually two) to fit the data. Then any moment can be calculated in terms of the parameters of the empirical distribution function. In the present work, the average decay rate was obtained by fitting the observed relaxation function with a log normal distribution of decay rates and calculating the

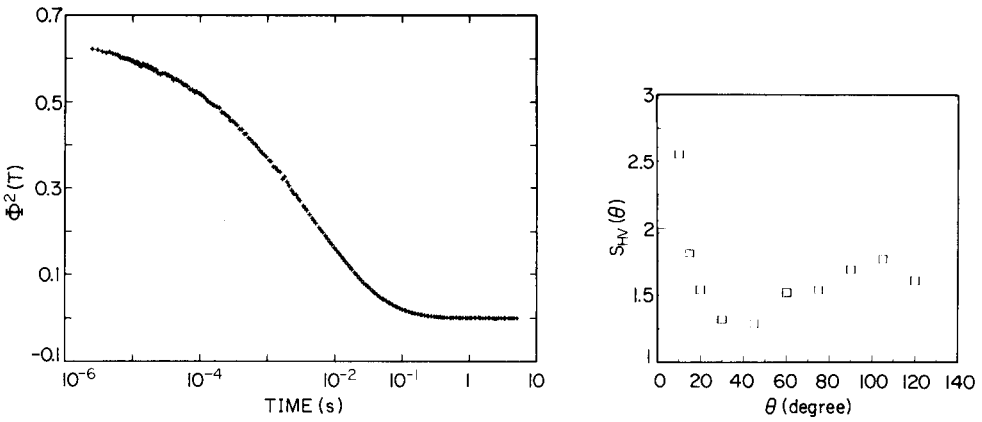

Fig. 3. A light-scattering relaxation function, $\phi^2(t)$, obtained over seven decades in time. The sample was a liquid near its glass transition.

Fig. 4. Excess depolarized intensity, $S_{HV}(\theta)$, in arbitrary units from a solution of $Li_2Mo_6Se_6$ plotted vs. scattering angle, θ. The intensity exhibits a minimum near 40°.

average. Another standard method for obtaining the average decay rate is to plot the log of the relaxation function against time and calculate its initial slope using the method of cumulants [16]. The initial slope is equal to the average decay rate. The former method was more robust on a routine basis, even though it has no theoretical justification as does the method of cumulants. If the data depart substantially from a single exponential decay, an actual discrete inversion of the data is routinely used to obtain the distribution of decay rates directly [17]. The data obtained in the present experiments were never of sufficient quality to justify an inversion. The primary importance of the present results is that they represent one of the few successful attempts to use depolarized Rayleigh scattering to characterize particles in solution.

RESULTS AND DISCUSSION

In order to use light scattering as a technique for evaluating single particle properties, the particles must be dispersed in a solvent. The two examples that follow are novel cases of particles in solution. The first system discussed is a polymer of $Li_2Mo_6Se_6$ dissolved in propylene carbonate [18]. In the solid state, this material forms black crystals with highly anisotropic properties. The high absorptivity persists in solution. Consequently, the concentration of polymer was kept very low ($<10^{-7}$ g ml^{-1}). The use of very low concentrations can introduce an additional component in the correlation function because of fluctuations in the number of particles in the scattering volume [11]. While this effect is always present, it is usually too small to observe. In the present experiments, the scattering volume was maximized to

help avoid this problem. The light scattering was still very intense because of resonance enhancement. The incident power level was kept very low in order to avoid local heating of the solution. Excessive power levels are easily detectable as thermal lensing of the incident light exiting from the sample.

The depolarized light scattering from this sample was similar in magnitude to the excess polarized scattering. This makes this system a good candidate for extracting information from the depolarized scattering. The depolarized scattering from pure propylene carbonate is very weak. It is generally important to choose a solvent with a low depolarized intensity so that the excess scattering is a significant fraction of the total. The excess depolarized intensity (in arbitrary units) is plotted against the scattering angle in Fig. 4. There is a very strong dependence of the intensity on angle and the data exhibits a minimum. From the value of θ at the minimum, a value of L can be inferred from calculations of $S_{HV}(\theta)$ for different values of L/λ. The value of L is near 2 μm with a range of uncertainty from 1.5 to 4 μm. The precision of this result is not good, but it serves to support the results obtained from dynamic light scattering. The existence of rod-like molecules in this size range in solution was confirmed by transmission electron microscopy [18].

Although the data are consistent with a picture of 2-μm rods in solution, static light scattering alone cannot prove that this is true. The intensity data at angles higher than the minimum are not in good accord with a fully linear molecule of negligible width. Thus, the molecules may have some degree of curvature or the discrepancy may be due to other unknown causes. The use of dynamic light scattering provides additional evidence for the overall shape of the molecule in solution. The average decay rate, $\langle\Gamma\rangle$, is plotted against q^2 in Fig. 5. The data are linear over two orders of magnitude. From the slope

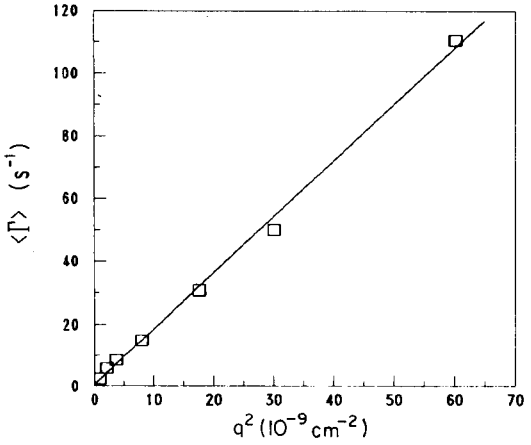

Fig. 5. Average decay rate, $\langle\Gamma\rangle$, plotted vs. q^2 for the depolarized scattering from the same solution. From the slope, the translational self-diffusion coefficient is calculated to be $D_0 = 1.8 \pm 0.1 \times 10^{-9}$ cm^2 s^{-1}. From the intercept, the rotational diffusion coefficient is $\Theta = 0.1 \pm 0.1$ s^{-1}.

and intercept, it is calculated that the self-diffusion coefficient is equal to $1.8 \pm 0.1 \times 10^{-9}$ cm^2 s^{-1} and the rotational diffusion coefficient is equal to 0.1 ± 0.1 s^{-1}. This is a very small value of the rotational diffusion coefficient. The Perrin equations were solved simultaneously for a and ρ using the measured values of D_0 and Θ. The viscosity of propylene carbonate at 293.15 K is 2.79 cP. Because the relative uncertainty for Θ was large, it was assumed that D_0 was known exactly and Θ was varied from 0.01 to 0.3. Values of $\Theta < 0.05$ gave unacceptably large values for a. Because $a = L/2$, values of $a > 2$ μm would not be expected. Also, for $\Theta < 0.05$, values of $\rho < 0.01$ were calculated. Although this is not impossible for this system, it would require that these chains be very stiff. The values of a and ρ for $\Theta = 0.1$ s^{-1} were $a = 1.9$ μm and $\rho = 0.02$. If a is fixed at 1 μm ($L = 2$ μm), then Θ would need to be 0.3 s^{-1} and $\rho = 0.20$. If the predicted upper limit, $\Theta = 0.2$ s^{-1}, is used, the calculated parameters are $a = 1.3$ μm and $\rho = 0.10$. The dynamic light-scattering results favor a chain that is longer than $L = 2.5$ μm. The axial ratio is characteristic of a rod-like structure with $\rho < 0.1$. The chain is not a perfectly rigid rod, but the lengths evaluated by static and dynamic light scattering are similar. The axial ratio is an effective value for the actual chain modeled as an ellipsoid, but it is small enough to conclude that the chain is reasonably stiff.

Polyacetylene is normally a black intractable powder [19] or a black insoluble mat of fibrils [20]; this is not the most promising candidate for a light-scattering study. Bates and Baker [21] devised a way to solubilize polyacetylene by grafting it onto polyisoprene. The product was stable in solution, but it was uncertain what actually was in solution. The results of this study have been reported [22]. The polyisoprene was characterized by itself in toluene. Although the refractive index increment for polyisoprene in toluene is very low, it was large enough to give a measurable result. The hydrodynamic radius was $R_h = 160 \pm 10$ Å. For a flexible coil polymer, the radius of gyration R_G is typically 1.5 times the hydrodynamic radius. When the graft copolymer was studied, the concentration was kept very low to avoid the intense absorption by the polyacetylene. The angular dependence of the excess intensity indicated that a structure larger than the carrier polymer was involved. The intensity was analyzed by using Eqn. 1 and an apparent radius of gyration of 350 ± 70 Å was calculated. Virtually all the scattered intensity came from the polyacetylene part of the particle because of the strong resonance enhancement. This meant that the length evaluated from the angular dependence of the intensity did not necessarily reflect the overall size of the particle. If it was assumed that the particle in solution was a single polyacetylene rod with a polyisoprene head, then the measured R_G value implies a rod length of 1200 Å ($L = R_G (12)^{1/2}$).

The dynamic depolarized light scattering was the key to understanding the nature of the particle in solution. The average decay rate was measured as a function of angle. It was linearly dependent on q^2. The translational diffusion coefficient was inferred from the slope to be $3.45 \pm 0.15 \times 10^{-8}$ cm^2 s^{-1}.

The value of the decay constant at $q = 0$ implied that the rotational diffusion constant was $153 \pm 20\ s^{-1}$. From these two results, an axial ratio $\rho = 0.4 \pm 0.1$ and a major semi-axis length of 1800 ± 200 Å were inferred. It was concluded that the particle in solution must be a micellar aggregate with a polyacetylene core. Isolated polyacetylene molecules would be expected to be very rod-like.

These two examples illustrate the power of depolarized light scattering to study the nature of particles in solution. The particles need not be assumed to be spherical. Both the overall size and the axial ratio can be obtained under normal conditions. The use of both static and dynamic light scattering further strengthens the method.

REFERENCES

1 D. McIntyre and F. Gornick (Eds.), Light Scattering from Dilute Polymer Solutions, Gordon and Breach, New York, 1964.
2 P. J. Flory, Principles of Polymer Chemistry, Cornell University Press, Ithaca, 1953.
3 C. Tanford, Physical Chemistry of Macromolecules, John Wiley, New York, 1961.
4 M. B. Huglin (Ed.), Light Scattering from Polymer Solutions, Academic Press, New York, 1972.
5 M. Tirrell, Rubber Chem. Technol., 57 (1984) 523.
6 M. V. Volkenstein, Configurational Statistics of Polymeric Chains, Interscience, New York, 1963.
7 G. D. Patterson and P. J. Flory, J. Chem. Soc. Faraday Trans. II, 68 (1972) 1098.
8 P. J. Flory, Statistical Mechanics of Chain Molecules, Interscience, New York, 1969.
9 K. Nagai, Polym. J., 3 (1972) 67.
10 G. D. Patterson, Macromolecules, 7 (1974) 220.
11 B. J. Berne and R. Pecora, Dynamic Light Scattering, Wiley-Interscience, New York, 1976.
12 P. Horn, Ann. Phys., 10 (1955) 386.
13 F. Perrin, J. Phys. Radium, 7 (1936) 1.
14 R. Pecora (Ed.), Dynamic Light Scattering, Plenum, New York, 1985.
15 B. E. Dahneke (Ed.), Measurement of Suspended Particles by Quasi-Elastic Light Scattering, Wiley-Interscience, New York, 1983.
16 D. E. Koppel, J. Chem. Phys., 57 (1972) 4814.
17 P. J. Carroll and G. D. Patterson, J. Chem. Phys., 82 (1985) 9.
18 J. M. Tarascon, F. J. DiSalvo, C. H. Chen, P. J. Carroll, M. Walsh and L. Rupp, J. Solid State Chem., 58 (1985) 290.
19 G. Natta, G. Mazzanti and P. Corradini, Atti Accad. Naz. Lincei. Rend. Cl. Sci., 25 (1958) 3.
20 H. Shirakawa and S. Ikeda, Polym. J., 2 (1971) 231.
21 F. S. Bates and G. L. Baker, Macromolecules, 16 (1983) 704.
22 F. L. VanNice, F. S. Bates, G. L. Baker, P. J. Carroll and G. D. Patterson, Macromolecules, 17 (1984) 2626.

Analytica Chimica Acta, 189 (1986) 69—87
Elsevier Science Publishers B.V., Amsterdam — Printed in The Netherlands

ZERO-ANGLE DEPOLARIZED LIGHT SCATTERING OF A COLLOIDAL POLYMER

PAUL S. RUSSO*, MARY J. SAUNDERS and L. MARK DeLONG

Macromolecular Studies Group, Louisiana State University, Baton Rouge, LA 70803 (U.S.A.)

SCOTT KUEHL and KENNETH H. LANGLEY

Departments of Physics and Astronomy, and Polymer Science and Engineering, University of Massachusetts, Amherst, MA 01003 (U.S.A.)

ROBERT W. DETENBECK

Department of Physics, University of Vermont, Burlington, VT 05405 (U.S.A.)

(Received 14th April 1986)

SUMMARY

The potential of zero-angle depolarized scattering for measuring the size distributions of optically anisotropic particles is considered. To illustrate the method, an analysis of Fluon, a teflon latex suspension, is presented. Homodyne correlation functions having signal-to-noise characteristics every bit as good as conventional unpolarized finite-angle measurements enabled confident application of a smoothed exponential sampling algorithm to obtain the decay rate distribution, which was converted to a size distribution with certain approximations. The size distribution obtained from light scattering agrees well with that from electron microscopy.

In the analytical chemistry of polymers, the pertinent questions are often concerned not with identification or determination but rather with molecular size and degrees of polydispersion and aggregation. Techniques used to answer questions of the latter type can be grouped according to whether or not measurement perturbs the solution. Most methods do alter the solution slightly. Examples are simple capillary viscometry, which imposes shear, and molecular-exclusion chromatography, which imposes bulk flow, shear and the presence of a complex gel matrix. In contrast, light-scattering methods impose on the measured sample almost no artificiality (apart from a very slight thermal heating in some unusual cases). Even though light scattering is a profoundly weak effect relying on very small spontaneous fluctuations in concentration, one can easily obtain not only the average intensity and its distribution with scattering angle, which together provide average molecular weight and average size information, but also the time-correlation function of the scattered light [1—3], which contains information about the distribution of sizes and molecular weights. This paper demonstrates the potential of zero-angle depolarized dynamic light scattering for sizing of

0003-2670/86/$03.50

optically anisotropic particles/polymers. It is convenient to begin with a discussion of more conventional, non-polarized finite-angle dynamic light-scattering measurements.

CONVENTIONAL DYNAMIC LIGHT SCATTERING FOR PARTICLE SIZING

In a typical application, a vertically polarized laser is focused onto a carefully cleaned polymer solution, and the light scattered through an angle θ into approximately one coherence area [3] lying in the horizontal plane is detected by a phototube, without regard to the polarization sense of the scattered light. This is called the Uv-geometry (U being the unpolarized detection and v the vertically polarized incident light). The intensity fluctuations reflect alternating constructive and destructive interferences as the molecules in the detected volume undergo diffusive motion, thus changing their distances to the detector. On a very long time-scale, these fluctuations appear random. However, they are not totally random; if two intensities separated by a very short time interval are measured, they are found to be similar, i.e., correlated. Thus, the intensity fluctuations have a finite lifetime, inversely related to the polymer diffusion coefficient. In order to characterize the intensity fluctuations, the time autocorrelation function, $G^{(2)}(\tau)$, is introduced:

$$G^{(2)}(\tau) = \lim_{T\to\infty} (1/2T) \int_{-T}^{T} I(t)I(t+\tau)\,dt \tag{1}$$

The parenthesized superscript 2 indicates a second-order correlation function involving intensities. Superscript 1 would indicate a correlation function of the electric field. When τ approaches zero, $I(t) \approx I(t+\tau)$, so the above integral clearly represents the average of the squared intensity, $\langle I^2 \rangle$. As τ becomes very large, $I(t)$ no longer has any relation to $I(t+\tau)$, so the above integral yields $\langle I \rangle^2$, which must be less than $\langle I^2 \rangle$. Thus, correlation functions decay with τ, and it can be shown [1] that, for monodisperse samples, the decay is usually exponential. Most experiments are now done in a homodyne mode, meaning that there is no direct, unscattered light from the laser (no "local oscillator" signal) added to the scattered light. Then, in the usual case, the correlation function has the form:

$$G^{(2)}(\tau) = B(1 + f|g^{(1)}(\tau)|^2) \tag{2}$$

where B is the baseline, and f is an instrumental coherence factor ranging from 0 to 1, which essentially gives the maximum ratio of useful signal to baseline. The fundamental quantity of interest is $g^{(1)}(\tau)$, the normalized (indicated by lower-case g) electric field autocorrelation function. It is related to the normalized second-order correlation function $g^{(2)}(\tau) = 1 + |g^{(1)}(\tau)|^2$. In most instances the particle is not very large compared to q^{-1} where q is the magnitude of the scattering vector: $q = (4\pi n/\lambda_0)\sin(\theta/2)$, with n the solution refractive index, θ the scattering angle, and λ_0 the in vacuo wavelength of the incident light. For a monodisperse sample, $g^{(1)}(\tau) = \exp(-q^2 D\tau)$, where

D is the mutual diffusion coefficient. When extrapolated to zero concentration (indicated by superscript zero), D is related to the hydrodynamic radius, R_h, by the Stokes—Einstein relation:

$$D^0 = kT/6\pi\eta_0 R_h \tag{3}$$

where η_0 is the solvent viscosity and kT is the thermal energy.

For polydisperse samples having a near-continuous distribution, $g^{(1)}(\tau)$ can be expressed as a virtual continuum of exponential decays:

$$g^{(1)}(\tau) = \int_0^\infty A(\Gamma)\exp(-\Gamma\tau)\,d\Gamma \tag{4}$$

where $\Gamma = q^2D(M, c)$, $D(M, c)$ being a mutual diffusion coefficient dependent on concentration and molecular weight, and the $A(\Gamma)$ representing scattering amplitudes, proportional to polymer concentration, molecular weight and scattering form factor:

$$A(\Gamma) \approx cMP(qR_g) \tag{5}$$

where $P(qR_g)$ is the factor ($0 \leqslant P(qR_g) \leqslant 1$) by which light scattered through a scattering vector, q, from a polymer with molecular weight M and radius of gyration [4] $R_g = R_h/X$ is reduced by intramolecular interference compared to its intrinsic value at $q = 0$ (i.e., $\theta = 0$). If the experiment can be done at sufficiently low concentrations, extrapolated thereto, or if the concentration dependence of D for various M is known, then molecular weight distributions can be obtained by the following steps: (1) inverse Laplace transformation of Eqn. 4 to obtain the function $A(\Gamma)$ (most Laplace inversion routines produce a subset $[A(\Gamma)]$, i.e., a discrete set of Γ and $A(\Gamma)$); (2) conversion of the $[\Gamma]$ to diffusion coefficients using $\Gamma = q^2D$, to hydrodynamic radii R_h using Eqn. 3, and to molecular weights using $D^0 = \alpha M^{-\gamma}$, where α and γ are either taken from the literature [5, 6] or measured directly from fractionated samples; (3) use of tables or explicit equations [7] to compute $P(qR_g)$ by assuming a shape for the polymer (e.g., Gaussian coil) and using a hydrodynamic draining factor X (tabulated for a variety of polymers [5]) to obtain R_g from R_h; and (4) given $P(qR_g)$ and M, solution of Eqn. 5 for the relative concentrations to obtain the molecular weight distribution, c vs. M, or the size distribution, c vs. R_g or R_h.

The algorithm given, or its equivalent, is applicable to a wide variety of macromolecules, including those which are difficult to separate by molecular-exclusion chromatography because of aggressive solvents, adsorption or excessive size [8, 9]. It is presented here as background and to assist in the development of the main objective, zero-angle depolarized scattering, a somewhat more specialized particle-sizing method which is applicable to a less encompassing, but still broad, variety of polymers and colloids.

ZERO-ANGLE DEPOLARIZED SCATTERING

Scattering is the re-radiation of light from an induced dipole, μ, established in the particle (polymer) by the incident electric-field vector, **E**. If μ is always parallel to **E**, then the particle is said to be optically isotropic, whatever its geometric shape; thus optically isotropic means that the dipole moment induced by the incident electric field is given by a scalar polarizability, α: $\mu = \alpha \mathbf{E}$.

Many interesting polymers and particles, however, display optical anisotropy, requiring a tensorial treatment for the polarizability: $\mu = \underline{\alpha}\, \mathbf{E}$. When an optically anisotropic sample is placed between crossed polars, there will be a small amount of depolarized light, as the tensor has the effect of producing an induced dipole which may have an instantaneous component parallel to the analyzer. As the particle rotates, $\underline{\alpha}$ varies (in the laboratory frame of reference) so the strength of the depolarized signal fluctuates. Hence, rotational motion can be detected by depolarized correlation experiments. The commonest configuration is Hv (where H is the detection of the horizontal component of scattered light and v is the vertically polarized incident light).

As changes in the polarizability of the particle as it undergoes rotation are detected, one must consider how these are related to the rotational modes of the particle. The simplest case of a true symmetric top, a particle for which the geometrical and optical symmetries share the same cylindrical character, will serve to illustrate the principles. Later, the validity of this model will be considered. For the true symmetrical top, the signal strength is proportional to $N\beta^2$ where $\beta = \alpha_{\|} - \alpha_{\perp}$ is the difference in polarizabilities along the principal axes of the particle, and N is the number of particles detected. The modified electric field correlation function is [1]

$$g^{(1)}(\tau) = (1/15)\, N\beta^2 \exp[-(q^2 D + 6\Xi)\tau] \tag{6}$$

where Ξ is the rotational diffusion constant for tumbling (end-over-end) motion about one of the shorter axes of the symmetric top. Spinning motions about the cylindrical axis are not visible. Strictly speaking, this equation is for small anisotropic scatterers, and the situation for larger anisotropic particles is more complex, especially at large angles [10]. At zero angle, translational motion does not contribute to the decay of the correlation function (set $q = 0$ in Eqn. 6 above), allowing a potentially very simple and straightforward determination of the rotational diffusion coefficient from just one measurement. The first such attempts were on biopolymers, such as tobacco mosaic virus [11—13], collagen [14], and nucleic acids [15, 16]. For most biopolymers, the depolarized signal is relatively weak (small β), and all but one of the measurements were in the heterodyne mode, because of stray light from optical components sandwiched between the polarizers together with the cell or from the cell itself. In a heterodyne experiment, the small useful signal sits on top of a very large baseline [1, 2], so that the

baseline-subtracted signal is noisy. Han and Yu [17] reported the first zero-angle depolarized measurements on synthetic polymers, measuring the rotational diffusion of poly(hexyl isocyanate) and internal motion in isotactic polystyrene. Crosby et al. [18] reported zero-angle depolarized measurements on poly(*p*-phenylene benzobisthiazole) in chlorosulfonic acid [18]. Once again, a heterodyne signal was recorded, and the noise level was substantial. The only homodyne measurements appear to be those of Schurr and Schmitz [13] who used a very long pathlength to raise the scattered intensity of TMV solutions relative to the level of direct beam transmitted by the optics. The generally low signal quality has hindered application of zero-angle depolarized scattering, and it has largely been supplanted by finite-angle depolarized measurements, either as a function of q or at just one angle in conjunction with polarized measurements to obtain the diffusive term [19], or by a perturbing technique, transient electric birefringence [20], for applications where the depolarization is low.

In this paper, it will be emphasized that there are many strongly depolarizing particles which yield almost noise-free signals in a zero-angle Hv experiment. In these cases, the method is advantageous, because of its simplicity and non-perturbing nature. Additionally, it is particularly well suited to the study of polydisperse samples. In the zero-angle Hv experiment, the normalized electric-field correlation function is again Eqn. 4 but now the $A(\Gamma)$ are proportional to $N\beta^2$ (for true symmetric tops) and $\Gamma = 6\Xi$. Both β and Ξ depend implicitly on the dimensions of the molecule. In addition, β depends on its optical properties. The principal advantage over conventional finite-angle measurements for particle sizing is that Ξ is inversely proportional to the cube of the characteristic dimension. For spheres of radius R,

$$\Xi = kT/8\pi\eta_0 R^3 \tag{7}$$

Hence, two spherical particles differing in size by a factor of two have translational diffusion coefficients different by a factor of two, while their rotational diffusion coefficients differ by a factor of eight. As the maximum decay rate resolution of most Laplace inversion algorithms is near a factor of 2, this means that only particles with radii differing by more than about 100% can be resolved by conventional means, while, if there is a substantial depolarized signal, particles with radii separated by as little as 25% become separable in a zero-angle depolarized measurement. Additionally, many of the particles which qualify for zero-angle depolarized measurements (e.g., crystalline colloids) are large enough that form-factor corrections in conventional measurements would be very significant. No such correction is required at zero angle. Furthermore, to avoid multiple scattering, many of the larger particles would have to be measured in such dilute solution that many conventional finite-angle instruments would measure too small a volume, leading to slow number fluctuations [1] which will corrupt the signal and masquerade as excessive slow components upon Laplace inversion. In a zero-angle experiment, number fluctuations are not often a problem even in very

dilute solutions because the viewed volume, being essentially the beam cross-section times the length of the cell, is orders of magnitude larger than in a conventional measurement. Even compared to transient electric birefringence, zero-angle depolarized scattering may have some advantage where polydisperse samples are concerned, because the degree of alignment imposed by the transient electric field prior to relaxation by rotational diffusion may vary across the distribution in a way that is not known. It should also be mentioned that many candidates for zero-angle depolarized scattering are too large for molecular-exclusion chromatography.

The principal disadvantage of zero-angle depolarized measurements (aside from their inapplicability to particles with low optical anisotropy) is that when the Laplace transform is applied, one does not obtain a simple number or concentration distribution. Even in the simplest case of a true symmetric top, one obtains the distribution $N\beta^2$ vs. size (or molecular weight if a size/molecular weight relationship is known previously). When the relationship between β and size (or molecular weight) is known, as for thin rods ($\beta \approx L$), this presents no difficulty. In general, however, one may have to settle for the $N\beta^2$ distribution. Even in this case, however, the zero-angle method is a useful, discriminating and non-perturbing means of following changes in size and/or aggregation.

EXPERIMENTAL

Materials

Fluon latex particles [21] synthesized by ICI were the generous gift of Professor R. L. Rowell, University of Massachusetts. These came in the form of a semi-stable suspension containing about 70% particles by weight. Water from a Millipore R/Q purifier having >2.5 MΩ cm resistivity was additionally filtered through 0.45-μm or 0.1-μm Millipore MF filters into pre-rinsed plastic cuvettes and tested for absence of dust (by inserting the cuvettes into the light-scattering apparatus and observing the laser beam at 100× through the ocular) before being used to dilute the suspension. The diluted suspension was then passed through a well-rinsed Millipore RA 1.2-μm filter into square fluorimeter cells made of glass (1-cm pathlength) which had been washed exhaustively on an acetone percolation device. Each fluorimeter cell used was checked carefully for birefringence by placing it empty between the crossed polars and looking for leakage of laser light. It should be noted that simple test tubes also work well and some actually have less birefringence than the square cells, which are assembled by a process that can introduce strain. To avoid aggregation, measurements were made as quickly as possible after filtration. After measurement, aliquots were withdrawn for electron microscopy and for determination of concentration by vacuum drying to constant weight.

Electron microscopy

A drop of the latex suspension was pipetted onto a parlodian support film (Ted Pella; Lot KJHA) on a 50-mesh copper grid (Ted Pella) and air-dried for 1 h. A drop of aqueous 2% (w/v) tungstophosphoric acid (Fisher Scientific) was pipetted onto the grid. The excess was drawn off with filter paper, and the stained sample was then air-dried for 2 h. The sample was viewed on a Jeol 100-CX transmission electron microscope at an accelerating voltage of 80 kV and a magnification of 10 000.

Light scattering

The instrument, shown schematically in Fig. 1, has an optical train very similar to that of King et al. [12]. The goniometer is a custom-designed device manufactured and located at Louisiana State University, and is also used for finite-angle measurements with or without polarizers. Its principal features are highly reproducible selection of apertures and pinholes, together with an imaging system that permits the user to see exactly the same volume as the phototube at about 100× magnification. Two laser sources were used: a Lexel Model 95 argon ion laser, capable of producing about 2 W at 514.5 nm, and a Hughes 3227H-PC He—Ne laser producing about 4 mW at 632.8 nm. Because the long-term beam-pointing stability of argon lasers is usually mediocre, any light-scattering system using one should allow for rapid and simple realignment which should be tested daily, especially if room temperature fluctuations are severe, if laser power level is frequently varied, or if low-angle work is planned. Both lasers used in this work are aimed by stable three-point support systems. Installation and alignment of either laser is achieved without use of mirrors in less than 5 min. Samples are supported in a 3-in. copper block through which water is circulated. Temperature control and measurement to ±0.05°C is achieved by a platinum resistance thermometer placed in the water flow near the cell. The copper block is insulated by black teflon, and temperatures up to 150° C without misalignment are possible when the block is heated electrically by an Omega CN-2010 controller. (Stability above 95°C is ±0.5°C over several hours; higher temperatures are prevented only by softening of the lead solder joints used in sealing the water lines.) These studies involved either an EMI-9863 or Hamamatsu R928P phototube, with essentially equal results. A Precision Pacific Model 126 photometer amplified, discriminated and conditioned the photopulses before sending them to a Langley-Ford Model 1096 digital correlator equipped with

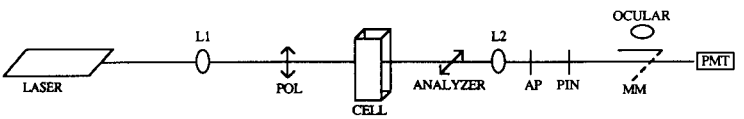

Fig. 1. Instrument for zero-angle depolarized scattering: POL, incident polarizer; L1, L2, lenses; AP, front aperture; PIN, rear pinhole; MM, movable mirror; PMT, photomultiplier tube.

272 channels. Data gathering and processing were performed by an IBM PC-AT computer, equipped with 80-bit numeric coprocessor (Intel 80287). Despite the large scattering volume and forward angle, most samples were sufficiently free of dust that automatic operation of the correlator was possible. About 15 short runs were made for each sample. A rapid cumulants analysis of each short run showed them to be consistent within error. The summed correlation function, having a baseline in excess of 10^8, was processed by a third cumulants routine, a nonlinear routine designed to fit 1—5 discrete exponentials (Marquardt algorithm [22], optimized to exponential functions), and finally to an exponential sampling algorithm (see data processing below).

Very high-quality polarizers are required for zero-angle depolarized experiments. Because the laser is approximately vertically polarized, a low-power Glan-Thomson polarizer (Karl Lambrecht MGT3E5; 1 W cm^{-2}) is sufficient to eliminate the small horizontal component. However, the analyzer must be able to dissipate the full power of the laser beam. A suitable analyzer is the Karl Lambrecht MGLQD8, employing double-escape window construction to permit the rejected beam to exit. The power rating of this device (500 W cm^{-2}) provides a comfortable safety margin in case the polarizer is accidentally exposed to the focused laser beam. The advertised mutual extinction of these polarizers, neither of which is anti-reflection coated, is 10^{-6}. Each polarizer was mounted in a Newport Research Model 470-B rotator, with angular resolution to 0.0012°. Other than the sample cell, no other optics should be placed between the polarizers, as has often been done in the past (see below).

Alignment of polarizers. The polarizers were aligned as described in the following five steps. First, a dilute polystyrene latex suspension was installed in the sample chamber and the analyzer was set to produce minimum intensity at a 90° scattering angle with the argon ion laser running near full power. This adjustment can be done visually using the 100× ocular or photometrically with identical results. Visually, the effect is to reduce a painfully bright scattering level to total invisibility (except for occasional dust particles). Secondly, the latex sample was removed, the laser power was reduced (or the HeNe laser installed) and the detector arm was rotated to 0°. The polarizer was installed and rotated to minimize transmitted light. (EXTREME CAUTION IS ADVISED AT THIS STEP. Both polarizer and analyzer should be firmly attached, and the initial adjustment should be done while the transmitted beam cast upon a piece of paper is observed.) The final alignment can be done photometrically, but direct visual observation is preferred because it is easier to identify the sources and polarization of any residual light. However, one should always approach the ocular very carefully, as extremely small misalignments can lead to disastrously high light levels. Although we have not done so, it should be possible to achieve visual alignment without any danger to the eye by using a video camera attached to the ocular together with a television monitor.

In the third step, the sample to be measured was inserted, and its bright-field image brought into proper focus. (CAUTION is needed; sometimes strain in the cell or a smudge on its surface can cause dangerously high light levels.) A visual check was needed for dust. Trying to identify dusty samples from intensity fluctuations monitored on a ratemeter was not always successful because the coherent signal from the slowly rotating particles of interest fluctuated dramatically on a time scale to which the ratemeter could respond. Hence, the ability to observe the sample through the ocular is judged essential to the successful completion of these experiments. The visual result at this point was the observation of a high-contrast, fluctuating circular speckle pattern against a background completely free of transmitted light. In order to test that this image was collected precisely in the forward direction, the polarizer could be temporarily rotated just slightly to reveal directly transmitted laser light precisely in the center of the pattern. With lens L2 (8-cm focal length at about 13.5-cm working distance from the cell), the pattern was then adjusted to coincide precisely with the pinhole (typically 100-μm diameter at a distance of 35 cm from the cell). Next, the front aperture was adjusted to limit the intensity and acceptance angle (a typical setting was 800 μm at about 22 cm from the cell). If the pinhole was then opened to a large value again (say 3000 μm), a fluctuating speckle pattern appeared in which the speckle size now greatly exceeded 100 μm. Thus, less than one coherence area was detected when the 100-μm pinhole was reinserted, at which point one will observe "on-off" twinkling in that tiny spot. (The ability to see the twinkling effect by eye should not be expected for rapidly rotating particles.)

In a fourth possible step, one final adjustment of the analyzer is sometimes helpful for chiral samples when long pathlengths are used, because the initially vertical beam is somewhat rotated [13]. This step was not necessary in the present experiments.

In the final step, the mirror was switched to pass the scattered light to the photomultiplier tube. If the light level was too high, then neutral-density filters were inserted. At this point, the alignment had to be repeated, because the neutral-density filters cause a slight lateral shifting of the beam.

RESULTS AND DISCUSSION

Electron microscopy

Figure 2 shows an electron microscope image of the Fluon particles from a preparation used for light scattering. The distribution of length, L, width, W, and axial ratio, $p = L/W$, of 266 particles is shown in Fig. 3. Electron microscope images of unfiltered samples are very similar but do reveal small numbers of very long, rod-shaped particles.

Light scattering

Raw data. Figure 4 shows a zero-angle depolarized correlation function. Notable is the very high signal quality, easily the equal of many finite-angle,

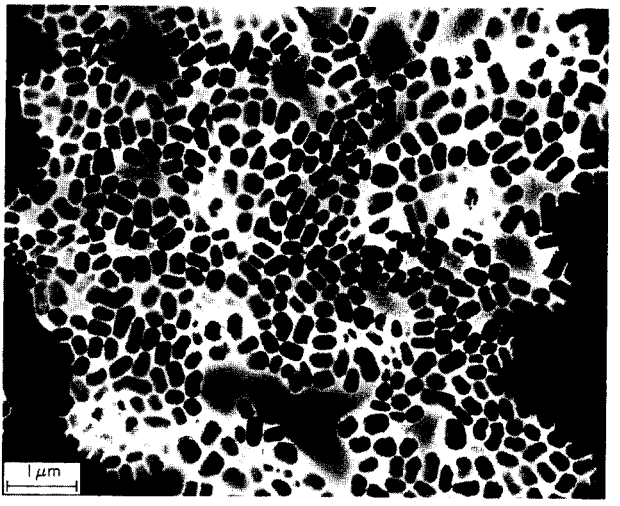

Fig. 2. Electron micrograph of Fluon latex. Bar marker, 1 μm.

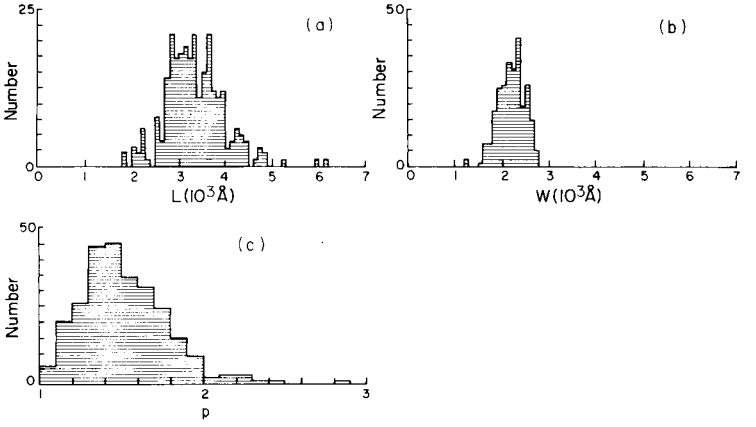

Fig. 3. Histograms from electron microscopy of 266 particles taken from a solution used for light scattering: (a) length; (b) width; (c) axial ratio.

non-polarized experiments. There is a very small degree of systematic noise evident after about seven decay times. The source of this is unknown; it is not evident at finite angles and is a somewhat intermittent problem. The correlation function is undeniably homodyne, as evidenced by the fact that the maximum coherent signal exceeds 70% of the baseline (i.e., the coherence factor f in Eqn. 2 is >0.7). This approximately matches the performance of the present apparatus in finite-angle experiments using the same settings of the pinhole/aperture and for similar ratios of scattered signal to dark count. The coherence factor was not dependent on concentration. By adjusting the polarizer as described below, it was possible to force heterodyning, with the expected result that noise-free correlation functions required much longer acquisition times and that the average decay rate was reduced by half.

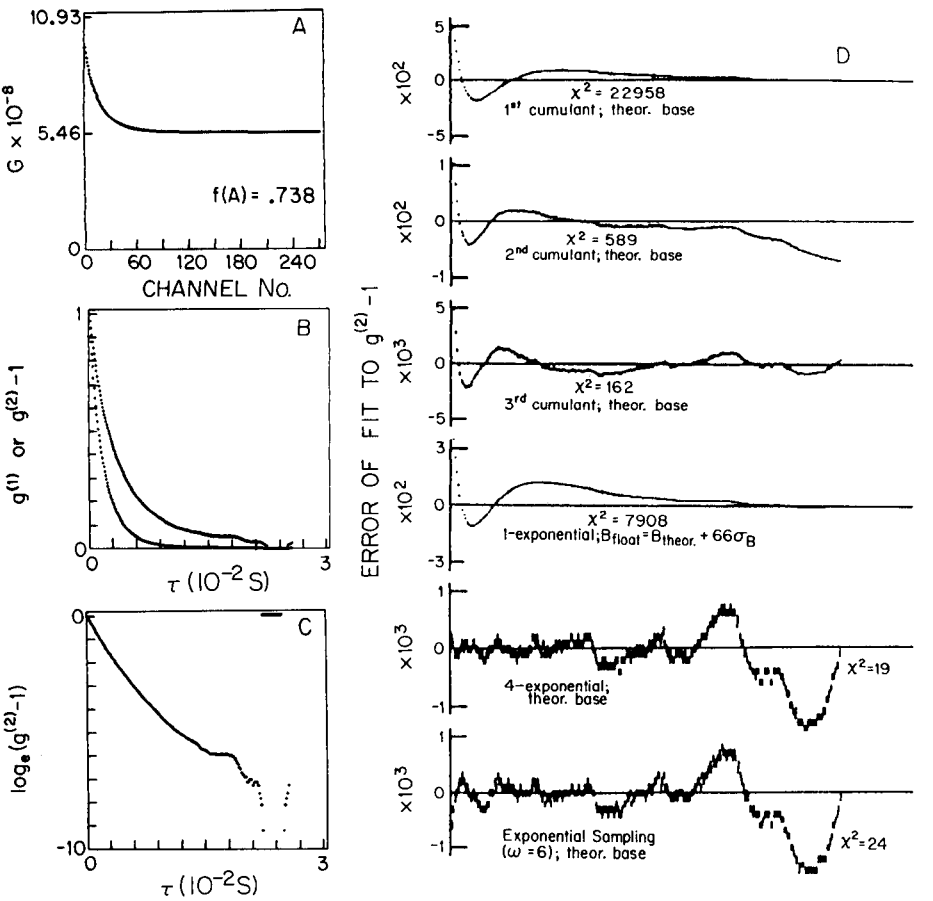

Fig. 4. Typical zero-angle depolarized correlation function, for c = 1.19 mg ml^{-1} solution. Conditions: λ_0 = 514.5 nm, 30°C, channel time 10^{-4} s, sum of 11 short runs with net acquisition time of 1 h. At $\tau > 0.02$ s, some noise is evident, causing apparent negative data in some channels. These points were converted to constants to prevent computational overflow. The correlation function appears in several useful representations: (A) $G^{(2)}(\tau)$, showing baseline and the large coherent signal above baseline; (B) normalized first- and second-order correlation functions, computed without any modification to the theoretical baseline from run time and intensity; (C) semilogarithmic plot of normalized second-order correlation function. (D) Error plots for various fits: abscissa, same as panel B; the height of the bars is the statistical error of measurement of the normalized second-order correlation function, while the center of the bars indicates the difference between the fit and the actual data; the scale is expanded as the fit improves; χ^2 = 1 when all error bars touch the horizontal line of zero error; $\chi^2 \approx 1$ for $\tau < 0.025$ s in 4-exponential and Exponential Sampling fits.

Performance was significantly degraded if the positions of the input lens, L1, and polarizer were interchanged, although this is permissible for a finite-angle Hv experiment. Visual observation of the sample in this configuration revealed a level of unscattered transmitted light sufficient to obscure the fluctuating speckle pattern, caused by birefringence of the lens. This light was horizontally polarized. Correlation functions measured in this configura-

tion showed substantially lowered coherence ($f \approx 0.1$), indicating partial heterodyning. It can be concluded that a minimum of optical components should be placed between the polarizing elements. Even with this optimal configuration, heterodyning may be unavoidable for very weakly depolarizing samples and short pathlengths, in which case it must be controlled. The strength of the local oscillator signal can be varied by offsetting the polarizer slightly, thus permitting horizontal components from the laser to pass. The Hh polarized component of scattered light will not contribute to the decay of the correlation function because $q = 0$.

A small amount of incident light is reflected at the exit window of the cell and can give rise to a depolarized scattering at 180° scattering angle. This back-scattered component is weakened substantially, because the reflectivity of the glass/air interface is only about 4%, and because it is subject to intramolecular interference (form factor reduction). Nonetheless, potential artifacts arising from this component are of some concern. This weakened component would decay more rapidly than the forward signal, because a q^2D term would be present (see Eqn. 6). This term would change with laser wavelength according to λ^{-2}. Arguing against the importance of the back-scattered component is the observation that correlation functions measured with three different laser lines (632.8, 514.5 and 488.0 nm) were virtually indistinguishable.

Simple evaluation. From the outset, it was clear that the correlation functions were distinctly non-exponential and would require more than the fitting of polynomials to the semi-logarithmic representation (i.e., cumulants analysis [23], although the formal significance of the cumulants is altered from their usual meanings in conventional experiments). Nonetheless, experience indicates that meaningful average decay rates are obtained from third-order polynomial analysis using a baseline derived from intensity and run

TABLE 1

Concentration dependence of initial decay rates, as obtained by fitting three cumulants with calculated baseline and a single exponential, allowing the baseline to float as a fitted parameter

c (mg ml^{-1})	Volume fraction[a], ϕ	$\bar{\Gamma}$ (Hz)	
		Three cumulants derived base[b]	One exponential float base
1.19	5.2×10^{-4}	314	225
1.19[c]	5.2×10^{-4}	287	245
0.119	5.2×10^{-5}	298	251
0.0119[d]	5.2×10^{-6}	255	230

[a]Calculated using particle density = 2.275 [21]. [b]Calculated as P (P—O)/N where P is the number of photopulses (typically 10^8), N the total acquisition time divided by sample time (typically 10^8), and O the number of shift register overflows (typically <50). [c]Repeat run. [d]Some particulate matter ("dust") was visible in this solution.

duration [3], and also by performing one-exponential nonlinear fits, allowing the baseline to float. Table 1 summarizes the results.

Notably absent is any systematic concentration dependence for the average rotational diffusion coefficient, which is 48 ± 3 s^{-1} over the 100-fold concentration range measured from the cumulant analysis (40 ± 1 from single exponential analysis). This corresponds to a spherical particle with radius of 1635 ± 35 Å (cumulants), in reasonable agreement with the average radius of spheres with equivalent volume calculated from electron microscopy assuming a right circular cylindrical shape (1450 Å; see Fig. 5c below). Observation of the samples over several days, together with Laplace inversion analysis, suggests that what minor and unsystematic variation is seen here can be traced to time-dependent aggregation, not concentration per se. More detailed studies to obtain size distributions were made on samples measured within 2 h after filtering. It should be noted that well-aged solutions of smaller, more uniform Fluon particles stabilized with 0.01 M potassium perfluorooctanoate show some concentration dependence of both translational and rotational motions [24].

Exponential sampling evaluation and conversion to size distribution. While the simple treatments above are useful for getting average parameters, neither adequately fits the data, as indicated by the high value of the weighted mean

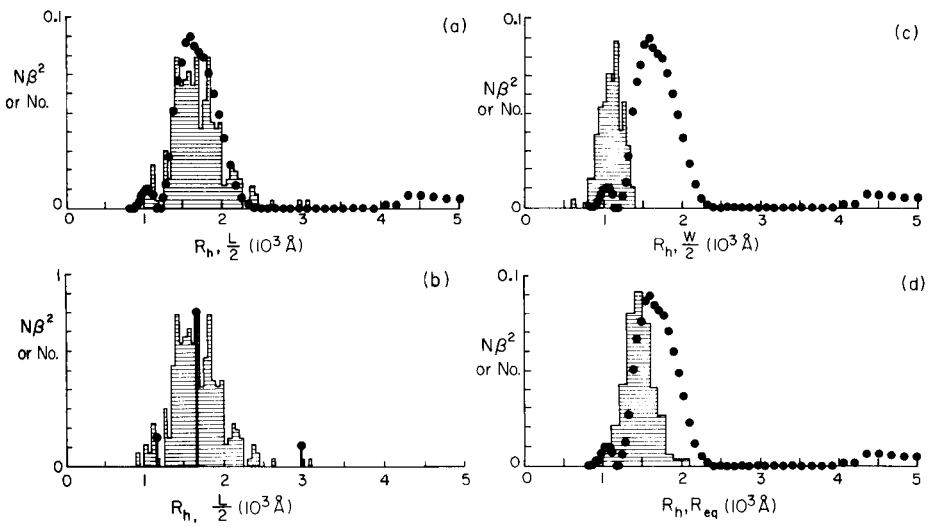

Fig. 5. Overlay plots comparing apparent hydrodynamic radius, R_h, from zero-angle depolarized scattering (black circles) to various size parameters from electron microscopy (shaded histograms): (a, b) length; (c) width; and (d) radius of a sphere with equivalent volume (see Eqn. 12). In (a, c and d) the light-scattering distribution comes from exponential sampling; in (b), it comes from a nonlinear fit to 4 discrete exponentials, two of which overlap (see text). The vertical scale is such that the sum of all points from light scattering is unity while the electron microscopy data are scaled vertically to provide a convenient comparison.

square residual error, χ^2 [22], and the channel-to-channel correlation of errors (see Fig. 1). A much better fit can be obtained by using a Laplace inversion algorithm to obtain the $A(\Gamma)$ in Eqn. 4. The adaptation of the exponential sampling method [25] chosen for this work lays a "comb" of exponentially decaying functions along a logarithmic decay rate space, with the "teeth" spaced at equal intervals according to the data quality, i.e., the decay rates of any two exponential functions obey

$$\Gamma_{i+1} = \Gamma_i \exp(\pi/\omega), \tag{8}$$

where the resolution parameter ω is limited by the noise in the correlation function. The lengths of the "teeth", i.e., the amplitudes of the decay functions, are determined by a rapid linear fit. The term minimized is

$$\chi^2_{\mathrm{mod}} = \sum_{v=1}^{N} w_v [y_v - \sum_{i=1}^{M} A_i \exp(-\Gamma_i \tau_v)]^2 + \epsilon_1 \sum_{i=1}^{M} [A_i \exp(-\Gamma_i \tau_v) - A_{i+1} \exp(-\Gamma_{i+1} \tau_v)]^2 \tag{9}$$

where χ^2_{mod} is a modified χ^2 to allow smoothing; y_v is the measured N-point function, which may be either $G^{(2)}(\tau)$ or $(G^{(2)}(\tau) - B)^{1/2} \approx g^{(1)}(\tau)$ in the present adaptation; w_v is a weighting factor for the vth data point in a set of N, taken as σ^{-2} where σ is the uncertainty in y, calculated by standard propagation of error formulae [22] assuming the uncertainty of the raw correlation function is $\sigma_G = G^{1/2}$ [3] and no baseline uncertainty. Each term, $\exp(-\Gamma_i \tau)$, represents one of M exponentially decaying functions with amplitude A_i. When ϵ_1 is nonzero, the second term has the effect of smoothing the solution, by preventing wild oscillations. To prevent physically unrealistic negative amplitudes, decay functions associated with negative amplitudes are discarded and the fit repeated until no negative amplitudes are found. Following Ostrowski et al. [25], the comb is then translated one-sixth of the distance between any two "teeth" and the process repeated five times. Next, the decay rate space over which solutions are sought is constricted and the whole process repeated. The algorithm was tested with simulated, noise-corrupted data and with real data from mixtures of polystyrene latex sphere standards and mixtures of standard polystyrenes in toluene. With data of reasonable quality (i.e., $B > 10^8$ and $f \geqslant 0.2$) the routine can cleanly and accurately separate functions with decay rates separated by a factor of two or more. This is similar to other Laplace inversion techniques [26]. In the present work, the final fit was to $(G^{(2)}(\tau) - B)^{1/2} \approx g^{(1)}(\tau)$, so the baseline B was required. The theoretical baseline from run duration and scattered intensity was modified by 0—10 statistical uncertainties ($\sigma_B = B^{1/2}$, typically $<0.05\%$ in these determinations). This represents relatively low systematic error caused by dust, correlated noise, laser intensity drift, etc. The decay-rate distributions obtained were very little affected by this degree of baseline adjustment, one of the advantages of a homodyne experiment, where f is relatively large.

In all cases attempted, χ^2 was reduced dramatically by exponential sampling; however, it usually remained substantially above unity. This is not alarming for three reasons: (1) χ^2 is near unity for the first 2/3 of the correlation function where systematic noise does not contribute, and, because the uncertainties are based on statistical noise, it is the systematic noise regime which raises χ^2; (2) the maximum error of the fits was typically $<0.1\%$, even in the systematic noise regime, and the errors were not highly correlated, as for the simpler fits; (3) because χ^2 is normalized by the uncertainties, a low χ^2 is always possible for poor data with high uncertainties and does not indicate the accuracy of the fit, merely its adequacy. Our routines inadequately fit the systematic noise, as desired. For comparison, results are provided (see Fig. 5) for a discrete nonlinear fitting algorithm, using four exponentials to fit $g^{(1)}(\tau)$. In fact, this analysis is routinely performed prior to the exponential sampling, as it rapidly gives some clue as to the range of decay rates over which solutions should be sought. It is somewhat sobering that this relatively simple, rapid (ca. 1 min), robust and non-biased analysis fits the data as well as, or better (see Fig. 4) than, the much slower (ca. 20 min) exponential sampling algorithm. Two of the four decay rates were identical to within 2 s^{-1} (0.6%); thus, the data are essentially fitted by three exponentials, as shown in Fig. 5.

Once the Laplace inversion of the correlation function is completed, it is possible to obtain a size distribution. As already noted, even in the simplest case, the $A(\Gamma)$ are proportional to $N\beta^2$ and β depends on details of the particle which are often unknown. Fluon particles do not strictly fit this simple model. Thus, it is necessary to consider the degree of approximation involved if the simple theory for a true symmetric top is invoked, as well as what more complex theories have to offer.

A particle of arbitrary shape and arbitrary polarizability is the most general case. The forward depolarized correlation function from a monodisperse collection of such particles can contain up to five exponentials with decay rates which are linear combinations of three rotational diffusion coefficients, Ξ_{XX}, Ξ_{YY}, and Ξ_{ZZ} about three orthogonal axes selected to diagonalize the rotational diffusion tensor in the particle frame of reference [1]. The amplitudes of these modes depend on the orientation of the polarizability tensor with respect to this frame of reference. The information to use this theory for Fluon particles is simply not available. However, by inspection of Fig. 3, it seems likely that the three rotational diffusion coefficients will not be very different, because the axial ratio is small. In this case, the decay rates of the five exponentials (Eqn. 7.5.25 [1]) will be similar to within the usual precision, i.e., an average would be obtained.

To make a more useful approximation which does not involve excessive risk, one can treat the Fluon particles as symmetric diffusors, using Perrin's equations for prolate ellipsoids of revolution [27] to estimate what effect geometric anisotropy has on the rotational motion. Defining a to be the longer axis of the ellipsoid, b the shorter axis, and $p = a/b > 1$ the axial ratio, then for rotation about the longer axis (spinning):

$$\Xi_a = kT/8\pi\eta_0 R_{eq}^3 F_a \tag{10a}$$

where $F_a = 4(1-p_p^2)/3(2-p_p^2 S)$ in which $p_p = 1/p = b/a < 1$, R_{eq} is the radius of a sphere with same volume as the ellipsoid, and

$$S = [2/(1-p_p^2)^{1/2}] \ln [1 + (1-p_p^2)^{1/2}/p_p]$$

Likewise, for rotation about the shorter axis (tumbling),

$$\Xi_b = kT/8\pi\eta_0 R_{eq}^3 F_b \tag{10b}$$

where $F_b = 4(1-p_p^4)/3p_p^2 [S(2-p_p^2) - 2]$

From these equations, one can quickly calculate that rotational motion about the long axis (spinning) is only about 40% faster than that about the short axis (end-over-end tumbling). Although the rotational diffusion is cylindrically symmetrical in this model, the polarizability tensor is still arbitrary. The appropriate correlation function at zero angle is (see Eqn. 7.5.19 [1])

$$g^{(1)}(\tau) = (N/10)\{A_0 \exp(-6\Xi_b\tau) + A_1 \exp[-(6\Xi_b + (\Xi_b - \Xi_a))\tau] +$$
$$+ A_2 \exp[-(6\Xi_b + 4(\Xi_b - \Xi_a))\tau]\}$$

where the A_i (given by Eqn. 7.4.1 [1]) once again depend on the symmetry relationship between the polarizability tensor and the rotational diffusion tensor. The above expression reduces to Eqn. 6 when the polarizability and rotational diffusion tensors share the same cylindrical symmetry (i.e., when they are both diagonalized in the same reference frame). If $\Xi_a \approx 1.4\,\Xi_b$, as suggested by the Perrin equations, then the decay rates of the three exponentials are $6\Xi_b$, $5.6\Xi_b$, and $4.4\Xi_b$. Because almost no level of data precision would resolve such closely-spaced exponential decays, it is justifiable to return to the simplest treatment, embodied in Eqn. 6. Thus, the multiexponential nature of the correlation functions is associated completely with size polydispersity. However, it should be recognized that β^2 is an apparent quantity, because there is no guarantee that the polarizability is, in fact, cylindrically symmetric with the same sense as the (assumed) cylindrically symmetric rotational diffusion tensor. This suggests that an appropriate and simple size parameter would be the apparent hydrodynamic radius, $R_{h,i}$, of the ith species, calculated from the equation for a simple sphere:

$$\Xi_i = kT/8\pi\eta_0 R_{h,i}^3 = \Gamma_i/6 \tag{11}$$

The size distribution obtained in this way is superimposed on the length and width distributions from electron microscopy in Fig. 5. Also shown is a comparison to the equivalent sphere radii calculated from the electron microscope by assuming a cylindrical shape for the particles:

$$R_{eq,i} = (3\,L_i W_i^2/16)^{1/3} \tag{12}$$

It is not always emphasized enough that any Laplace inversion algorithm has an inherent width because the high-frequency information cannot be extracted without corruption by noise. This means that the true distribution of

frequencies will generally be narrower than the distribution from Laplace inversion. However, it is very gratifying that the distribution from Laplace inversion is, in this case, very similar in width to that from electron microscopy. This close agreement is a direct consequence of the cube-law dependence of rotational diffusion, which expands the decay-rate distribution, permitting a more detailed size analysis. It should be noted that the abscissa scales in Fig. 5 are linear, not the usual logarithmic scale. While the agreement with the electron microscope data (particularly the length distribution) is most encouraging, the limitations involved should be remembered: first, $N\beta^2$ (light scattering) is being compared to particle number (electron microscopy), where β^2 is an apparent value because the orientation of the polarizability tensor to the rotational diffusion tensor is unknown; and secondly, the apparent size is that of a hydrodynamically equivalent sphere.

These limitations could not be removed in the present case. However, it was possible to estimate their effects on the distributions obtained. For example, in order to gauge the first effect, it was assumed that $N\beta^2 \approx NM^2$ with M the molecular weight, proportional to R_h^3. While the number distribution obtained in this way strongly amplifies the small peak centered at about 1000 Å in Fig. 5, the overall shift in the distribution is only about −15%. Hence, the first limitation is not very severe.

To explore the error introduced into the size distribution by treating the particle as a hydrodynamic sphere, an attempt was made to obtain length and width distributions from light scattering by alternately imagining that the rotation detected was Ξ_b (tumbling) or Ξ_a (spinning), even though the spinning motion can never be observed separately. In these calculations, the average axial ratio ($P_{avg} = 1.516$) was used. For example, to approximate the length distribution, it was assumed that only Ξ_b was detected and the equation

$$\Xi_{b,i} = kT/8\pi\eta_0 R_{eq,i}^3 F_b = \Gamma_i/6 \tag{13}$$

was solved for $R_{eq,i}$, using the Γ_i supplied from exponential sampling, and $F_b = 1.202$ for $p_{avg} = 1.516$ ($p_p = 0.660$ in Eqn. 10). Next, the $R_{eq,i}$ were converted to length using Eqn. 12 where $W = L/p_{avg}$. The comparison of this length with that from electron microscopy is shown in Fig. 6, together with the equivalent calculation using the expression for Ξ_a to obtain W. The size

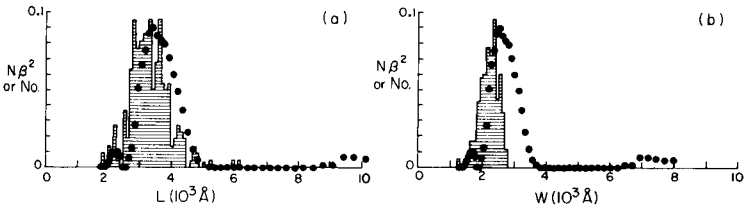

Fig. 6. Overlay plots showing length (a) and width (b) estimates from zero-angle depolarized scattering together with the electron microscope results. See text. Vertical scaling as in Fig. 5.

distributions from light scattering agree reasonably well with those from electron microscopy in both instances, showing the relative unimportance of shape anisotropy. However, the length calculation is in somewhat better agreement, probably because the decay terms really do approximate $6\Xi_b$ more closely, as already discussed.

CONCLUSION

The main conclusion from this work is that non-perturbing zero-angle depolarized measurements on optically anisotropic particles can be simple and provide very high quality correlation functions, with the enhanced resolution that attends sizing based on rotational diffusion. Moreover, changes in the state of particles in solution, such as degree of aggregation, could be followed provided that the process is much slower than the acquisition time required for the desired resolution. The technique is emphatically not a replacement for traditional submicron methods such as molecular-exclusion chromatography, conventional finite-angle dynamic light scattering, and ultracentrifugation. Rather, it is one which should be attempted for polymers and colloids which are likely to display a reasonable optical anisotropy and which are difficult to study by other methods. Examples of systems which may be well suited to zero-angle depolarized analysis are: ferrofluids, including polymeric suspensions of magnetic recording particles where the polymer matrix is only weakly optically anisotropic, asbestos fibers and other mineral suspensions, and soot in flames (using Fabry–Perot interferometry and Fourier inversion). It should be noted that the ambiguities associated with a particle such as Fluon (see above) which prevent absolute number vs. size distributions from being obtained should not hinder studies of the colloidal stability of such solutions, and that the method retains a number of advantages in this application.

This work was supported by an equipment grant from the NSF (Division of Materials Research No. 8413055) and by the Petroleum Research Fund, administered by the American Chemical Society. L. M. D. was supported by the Louisiana Center for Energy Studies. P. R. is grateful for financial support from the NSF (Division of Materials Research No. 8520027) during the preparation of this manuscript. Finally, we are indebted to Mr. Levi K. Stephens who measured the electron microscopy histograms.

REFERENCES

1 B. Berne and R. Pecora, Dynamic Light Scattering, Wiley, New York, 1976.
2 B. Chu, Laser Light Scattering, Academic Press, New York, 1974.
3 N. C. Ford, in B. E. Dahneke (Ed.), Measurement of Suspended Particles by Quasi-elastic Light Scattering, Wiley, New York, 1983.
4 C. Tanford, Physical Chemistry of Macromolecules, Wiley, New York, 1961.
5 C. M. Kok and A. Rudin, Makromol. Chem., Rapid Commun., 2 (1981) 655.

6 P. Klarner, in J. Brandrup and E. H. Immergut (Eds.), Polymer Handbook, 2nd edn., Wiley, New York, 1975.
7 P. Kratochvil, in M. B. Huglin (Ed.), Light Scattering from Polymer Solutions, Academic Press, New York, 1972.
8 J. W. Pope and B. Chu, Macromolecules, 17 (1984) 2633.
9 B. Chu, C. Wu and J. R. Ford, J. Coll. Interface Sci., 105 (1985) 473.
10 S. R. Aragon and R. Pecora, J. Chem. Phys., 66 (1977) 2506.
11 A. Wada, N. Suda, T. Tsuda and K. Soda, J. Chem. Phys., 50 (1969) 31.
12 T. A. King, A. Knox and J. D. G. McAdam, Biopolymers, 12 (1973) 1917.
13 J. M. Schurr and K. S. Schmitz, Biopolymers, 12 (1973) 1021.
14 J. C. Thomas and G. C. Fletcher, Biopolymers, 18 (1979) 1333.
15 J. M. Schurr and K. S. Schmitz, Biopolymers, 12 (1973) 1543.
16 K. H. Langley, M. R. Patel and M. J. Fournier, in D. B. Satelle, W. I. Lee and B. R. Ware (Eds.), Biomedical Applications of Laser Light Scattering, Elsevier, New York, 1982.
17 C. C. Han and H. Yu, J. Chem. Phys., 61 (1974) 2650.
18 C. R. Crosby III, N. C. Ford Jr, F. E. Karasz and K. H. Langley, J. Chem. Phys., 75 (1981) 4298.
19 S. Michielson and R. Pecora, Biochemistry, 20 (1981) 6994.
20 D. Eden and J. G. Elias, in B. E. Dahneke (Ed.), Measurement of Suspended Particles by Quasi-elastic Light Scattering, Wiley, New York, 1983.
21 R. H. Ottewill and D. G. Rance, Croat. Chem. Acta, 50 (1977), 65.
22 P. R. Bevington, Data Reduction and Error Analysis for the Physical Sciences, McGraw-Hill, New York, 1969.
23 D. E. Koppel, J. Chem. Phys., 57 (1972) 4814.
24 S. Kuehl, Ph.D. Thesis, University of Massachusetts, 1986.
25 N. Ostrowski, D. Sornette, P. Parker and E. R. Pike, Optica Acta, 28(8) (1981) 1059.
26 See, e.g., B. E. Dahneke (Ed.), Measurement of Suspended Particles by Quasielastic Light Scattering, Wiley, New York, 1983.
27 See, e.g., C. R. Cantor and P. R. Schimmel, Biophysical Chemistry, W. H. Freeman, San Francisco, CA, 1980.

Analytica Chimica Acta, 189 (1986) 89—99
Elsevier Science Publishers B.V., Amsterdam — Printed in The Netherlands

FLUORESCENCE QUENCHING STUDIES ON POLY(METHYL METHACRYLATE) PARTICLES
Matching of the Refraction Index of the Stabilizer Phase to that of the Solvent with Added Carbon Disulphide

MITCHELL A. WINNIK* and LUKE S. EGAN

Lash Miller Laboratories, Department of Chemistry and Erindale College, University of Toronto, Toronto, Ontario M5S 1A1 (Canada)

SYLVIA M. OWENS and RONALD H. OTTEWILL

School of Chemistry, University of Bristol, Bristol BS8 1TS (Great Britain)

(Received 29th January 1986)

SUMMARY

Detailed information about the interior morphology of sterically stabilized colloid particles ought to be accessible from light-scattering measurements when the index of refraction of the stabilizer layer is matched to that of the diluent. When carbon disulphide is added to dispersions of poly(methyl methacrylate) (PMMA) latex particles stabilized with poly(12-hydroxystearic acid) (PHSA) in dodecane, the scattered light intensity varies continuously with time; a permanent match of indices of refraction in this system is not achieved. Fluorescence quenching experiments with CS_2 as quencher were performed on similar particles containing 0.02 mol% anthracene groups covalently bound to the PMMA chains in order to obtain information about CS_2 swelling of these particles. Time-dependent quenching experiments indicate rapid penetration of CS_2 (<10 min) into the 150-nm diameter particles. Stern-Volmer analysis of steady-state CS_2 quenching data yielded results typical for polymeric systems containing fluorophores in a distribution of environments; the particle-bound anthracenes are not all equally accessible to quencher. Nevertheless, all the anthracene labels are quenched to some extent. It is concluded that within 10 min after exposure, CS_2 penetrates throughout the entire volume of the particles.

Scattering techniques can often aid the characterization of polymer conformation, dynamics, and morphology of complex polymeric materials [1]. Three major classes of scattering experiments can be performed in this respect: light, x-ray, and small angle neutron scattering (SANS). The aspect which dictates the choice of technique to use for a particular experiment is the wave vector (q) range ($q = (4\pi/\lambda)\sin(\theta/2)$). In essence, the parameter, q, sets the overall resolution of the experiment. In light-scattering studies, the wavelength, λ, of the radiation source is generally on the order of 500 nm, yielding a typical resolution (q^{-1}) of 100–500 nm. The SANS technique, however, utilizes an incident neutron beam of low wavelength (0.5 nm) and can provide molecular-level information because the accessible q^{-1} range can vary from 0.8 to 50 nm.

0003-2670/86/$03.50

In SANS studies, one introduces isotopically-labelled (deuterated) probe molecules into a hydrogenated matrix (polymer or solvent). Because of the differences in the coherent scattering length of deuterium and hydrogen, contrast is established so that either the deuterated or hydrogenated phase can be selectively investigated. In this way, the SANS technique applied to polymer blends can yield information about both chain conformation of a particular phase and phase-domain size.

Recent experiments on polymer colloids were conducted by Wai et al. [2] who used the "contrast matching" technique, where the ratio of deuterated to hydrogenated solvent is varied in order to achieve conditions for which the total scattering cross-section is related to only one of the components. They examined latex systems composed of a 50/50 styrene/methyl methacrylate (MMA) core surrounded by a shell of partially deuterated MMA, and showed that well-defined core and shell phases exist. For non-aqueous dispersions of poly(d-MMA) particles sterically stabilized with poly(12-hydroxystearic acid) (PHSA), Ottewill [3] pointed out that either phase can be contrast-matched (core or shell). If one disperses the particles in a deuterated hydrocarbon, the solvent medium matches the core and so the stabilizer layer can be probed. In a hydrogenated medium, the stabilizer phase is matched so that the core phase can be investigated. Using the former method, Ottewill [3] found the shell to be 6 nm thick, in agreement with results obtained by other techniques.

There exists a contrast-matching technique in light scattering as well. Rather than match the coherent scattering length of the solvent with that of a particular polymeric phase (as in SANS), in light scattering one matches the indices of refraction of the desired phases. In principle, by adding carbon disulphide to a dispersion of PHSA-stabilized PMMA particles (PHSA/PMMA) in dodecane, the index of refraction of the stabilizer phase can be matched to that of the diluent. With this technique, detailed information about the internal morphology of the particle core, on a distance scale of 100—500 nm, should be attainable [4]. Experimentally, however, it is observed that the above system moves "off-match" as a function of time [4]. It was thought that this occurs because CS_2 penetrates (swells) the particles, therefore, rendering any attempt at a match of indices impossible, except at equilibrium swelling.

Fluorescence quenching techniques provide a convenient means of measuring the penetration of small molecules into polymers. For example, CS_2 is a powerful quencher of anthracene fluorescence. Exposure to CS_2 of latex particles labelled in the core with anthracene groups would, therefore, result in fluorescence quenching if the CS_2 diffused into the core. In addition, the time dependence of this quenching would provide a measure of the sorption rate.

In order to test this hypothesis, fluorescence quenching studies were conducted, with CS_2 as quencher, on PHSA-stabilized PMMA particles covalently labelled in the core phase with anthrylmethyl methacrylate (1) groups.

These were compared to a model system consisting of anthrylmethyl pivalate (2) plus CS_2 in dodecane.

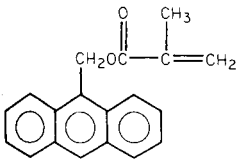

(1)

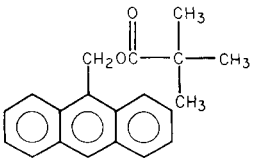

(2)

The results indicate that CS_2 penetrates readily into the particles and that all the fluorophores are accessible to quencher. The kinetics of quencher sorption was also investigated. These experiments showed that penetration is very rapid; anthracene fluorescence decreases to reach its limiting value in approximately 10 min. This paper presents the results from these CS_2-quenching experiments on anthracene-labelled PHSA/PMMA particles.

EXPERIMENTAL

Synthesis and characterization of the particles

The anthracene-labelled poly(12-hydroxystearic acid)-stabilized poly(methyl methacrylate) particles (PHSA/PMMA/A) were prepared in Bristol using the four-step dispersion polymerization method [5, 6]. The only modifications were the addition of 0.02 mol% anthracene methyl methacrylate (AMMA) to the MMA feed, and the omission of the thiol-chain transfer agent.

Only a brief description of the synthesis method and the characteristics of the materials used are presented here. The comb stabilizer used (m.w. ≈ 10 000) was prepared by polymerizing a glycidyl methacrylate (GMA)-terminated poly(12-hydroxystearic acid) macromonomer (m.w. ≈ 1500) with methyl methacrylate (MMA) and GMA in the ratio 50:45:5, respectively. The particles were prepared in dodecane (BDH) by copolymerizing MMA and AMMA in the presence of the comb stabilizer. They were washed several times by centrifugation with filtered solvent, yielding a particle volume fraction (V_p) of 0.17, as measured by dry weight. The average particle diameter and size dispersity, determined from electron microscopy, were found to be 148 nm and 100—210 nm, respectively. These particles are smaller than those prepared (380 nm) by this recipe in the absence of AMMA and in the presence of the thiol-chain transfer agent.

The reactivity ratios for copolymerization of MMA and naphthylmethyl methacrylate (conversion <7%) in benzene at 80°C are r_1, $r_2 \approx 0.85$ [7]. The magnitudes of r_1 and r_2 ought to be similar for the MMA/AMMA pair. For this reason, and because AMMA is added in such low proportion in the preparation of particles, a random distribution of anthracene units and very few adjacent chromophore pairs are expected.

Quenching experiments

Dodecane was purified by fractional distillation (b.p. 47°C) under vacuum (0.75 mm Hg). The middle fraction collected was found to be transparent down to 235 nm by ultraviolet (u.v.) spectroscopy. Carbon disulphide, used as the fluorescence quencher, was distilled (b.p. 45°C) over calcium chloride in air. The fluorescent monomer anthryl methylmethacrylate (AMMA) used in the synthesis of the labelled particles and the model compound anthryl methylpivalate (AMP) were prepared and purified by the method of Ng and Guillet [8].

A stock dispersion (V_p = 0.005) for fluorescence studies was prepared by diluting an aliquot of the original concentrated colloidal sample (V_p = 0.17) with purified dodecane and 3 ml of the stock dispersion was introduced into square (1 cm^2) quartz sample tubes fitted with rubber septum caps. These were then deoxygenated by purging with argon for 45 s. Deoxygenated CS_2 (final [CS_2] = 1.72 M) was added to each sample through the septum cap from a 100-μl syringe. Samples were then allowed to equilibrate for 30—40 min. A similar procedure was used in the model (AMP/dodecane) CS_2 quenching studies.

Steady-state fluorescence spectra were obtained with a Perkin-Elmer MPF-44B spectrometer. Samples were excited at 387 nm where the light absorption by CS_2 is negligible. Transient fluorescence decay curves, $I(t)$, were generated by using the time-correlated single-photon counting technique [9]. The excitation wavelength (λ_{ex}) was 365 nm and the fluorescence emission was isolated with a Corion Corporation SS4416-1 interference filter (λ_{em} = 442 nm). These data were processed by the method of non-linear least squares iterative reconvolution [10].

The time dependence of CS_2 quenching of anthracene fluorescence (I_A) was measured by steady-state fluorescence spectroscopy by monitoring I_A (λ_{ex} = 365 nm and λ_{em} = 415 nm) as a function of time after rapid mixing of deoxygenated CS_2 and the stock dispersion. Sorption profiles were obtained for quencher concentrations of 0.5 and 1.0 M.

RESULTS AND DISCUSSION

Fluorescence quenching in isotropic solutions

When samples containing excited fluorescent sensor groups are exposed to an added quencher, the fluorescence decay time and emission intensity usually decrease. For small molecules in fluid solution, the kinetics of fluorescence quenching can be evaluated using the Stern-Volmer equation [11, 12]:

$$I^0/I = \tau^0/\tau = 1 + k_q \tau^0 [Q] \quad (1)$$

where τ^0, τ, I^0 and I are the fluorescence decay times and intensities in the absence and presence of quencher (Q), respectively, and k_q is the bimolecular quenching rate constant. Equation 1 requires that the ensemble of fluorophores in the sample exhibit exponential decay behavior (i.e., they

must have a unique decay time) and that quenching be characterized by a single rate constant, k_q.

From a plot of I^0/I or τ^0/τ versus [Q], k_q can be calculated. Once its value is known, k_q can be related to the sum of the diffusion coefficients of the interacting species using the time-independent Smoluchowski equation [11, 12]

$$k_q = p\, k_{diff} = 4\pi N_A DpR/1000 \ (M^{-1}\ s^{-1}) \qquad (2)$$

In Eqn. 2, $D = D_F + D_Q$ is the sum of the diffusion coefficients of the fluorophore and quencher, respectively, $R = R_F + R_Q$ represents the sum of their interaction radii, N_A is Avogadro's number, and p is a factor describing the reaction probability per collision. When $k_q = k_{diff}$ (i.e., $p = 1$ and every bimolecular collision between F and Q results in a quenching event), the quenching process is said to be diffusion-controlled and must, therefore, depend on the medium viscosity.

One must take certain considerations into account in the interpretation of results from fluorescence-quenching studies on samples of polymer-bound dyes in solution, and on heterogeneous samples containing fluorophores in condensed polymeric phases. Our core-labelled PHSA/PMMA particles are an example of the latter class of sample. It may happen that the quencher concentrations inside and outside a polymer coil or on the interior and exterior of condensed phases may be dissimilar as a result of a partition coefficient different from unity. In addition, if polymer density or composition gradients exist in such systems, the diffusion coefficient of quencher throughout the sample may not be uniform. These kinds of effects have recently been observed in oxygen-quenching studies on sterically stabilized nonaqueous dispersions of poly(vinyl acetate) particles [13]. Time-dependent swelling effects must also be considered [14].

For the anthracene/CS_2 pair, it is assumed that quenching involves electron transfer from excited anthracene to CS_2. Electron-transfer reactions are known to occur over distances of 0.4—2.5 nm [15, 16]. Thus, even in the presence of particle swelling, the present fluorescence-quenching measurements ought to be able to distinguish between those anthracenes that are within the range for efficient electron transfer and those that are far from quencher.

The fluorescence spectra (λ_{ex} = 387 nm) of solutions of AMP in dodecane at various CS_2 quencher concentrations are shown in Fig. 1. These spectra are very similar to those obtained from samples of PHSA/PMMA/A dispersed in dodecane. The structured emission between 380 and 500 nm corresponds to the $S_0 \rightarrow S_1$ transition of anthracene. As the CS_2 concentration is increased, the intensity of fluorescence decreases, in accord with the predictions of the Stern-Volmer law (Eqn. 1). Shown in Fig. 2 are the fluorescence intensity data plotted as I^0/I vs. [CS_2].

The time-correlated single-photon counting technique was used to measure fluorescence decay times (τ) of 2.9, 1.3, and 0.8 ns for dodecane solutions of

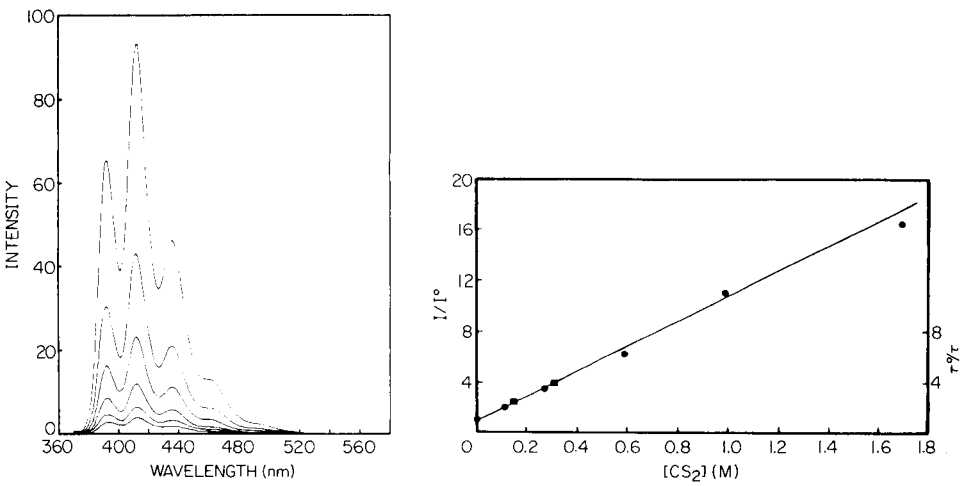

Fig. 1. Fluorescence spectra of dodecane solutions of anthrylmethyl pivalate (AMP) (7.7×10^{-5} M) at 23°C in the presence and absence of CS_2 quencher (λ_{ex} = 387 nm). CS_2 concentration for lowest to highest curves: 1.69, 0.99, 0.59, 0.27, 0.11, 0.00 M.

Fig. 2. Plots of τ^0/τ (■) and I^0/I (●) vs. $[CS_2]$ for samples of anthrylmethyl pivalate in dodecane at 23°C.

AMP containing CS_2 at levels of 0, 0.11, and 0.27 M, respectively. In these experiments, the fluorescence decay times were calculated by fitting the time dependence of the fluorescence intensity, $I(t)$, to a single exponential decay function of the form $I(t) = A \exp(-t/\tau)$. Data at higher CS_2 concentrations were not collected because the decay times would have been below the resolution of the instrument (<0.5 ns). Nevertheless, the data, when plotted as τ^0/τ versus $[CS_2]$, fall on the line defined by the I^0/I data in Fig. 2. This result indicates that quenching is simple and well behaved, that CS_2 must diffuse to excited anthracene to quench it, and that static interactions between anthracene and CS_2 prior to excitation are unimportant. From the slope of the line in Fig. 2 and using Eqn. 1, where τ^0(AMP) = 2.9 ns, the rate constant (k_q) for quenching of AMP fluorescence by CS_2 in dodecane was calculated to be 3.2×10^9 M^{-1} s^{-1}, a value typical of a diffusion-controlled process.

Kinetics of CS_2 sorption into PHSA/PMMA/A particles

Shown in Fig. 3 are the time-dependent quencher sorption curves obtained on PHSA/PMMA/A in dodecane at CS_2 concentrations of 0, 0.5, and 1.0 M. The fluorescence intensity of the control profile without CS_2 (curve a) is time-invariant. This result indicates the stability of the excitation source and emission photomultiplier tube response over the relatively short time intervals which are of interest. Curve (b) shows that most (82%) of the fluorescence quenching occurs within 10 s of mixing the CS_2 and the colloidal

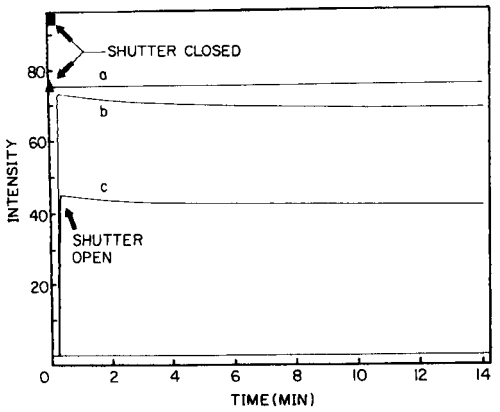

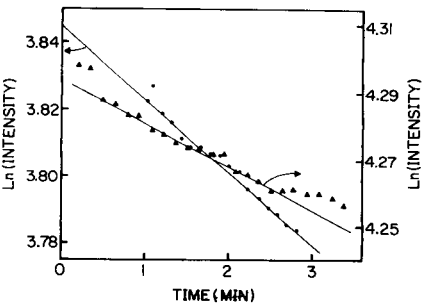

Fig. 3. Quencher (CS_2) sorption curves presented as the intensity of anthracene fluorescence in PHSA/PMMA/A particles as a function of time at 23°C (λ_{ex} = 365 nm, λ_{em} = 415 nm). CS_2 concentration: (a) 0; (b) 0.5 M; (c) 1.0 M. Points ▪ and ▲ on the vertical axis indicate the dispersion fluorescence intensities prior to the addition of CS_2 in the 0.5 and 1.0 M CS_2 experiments, respectively.

Fig. 4. Plots of the natural logarithm of the fluorescence intensity vs. time for the data shown in Fig. 3: (▲) 0.5 M CS_2; (●) 1.0 M CS_2.

dispersion. It was impossible to obtain data during this time interval. Subsequently, the fluorescence signal decreases more slowly, reaching its steady-state value after ca. 10 min. For the sample containing 1.0 M CS_2, the limiting fluorescence intensity is reached after only 3—4 min.

It is tempting to assign the initial rapid decrease in I_A ($t < 10$ s) to CS_2 diffusion into regions of PMMA within the particle cores swollen with solvent and the subsequent slow decrease in I_A to CS_2 penetration deep into the glassy PMMA phase within the particles (see final paragraph of this section). The data in Fig. 3 are not very precise and only suggestive of a two-stage penetration process. Nevertheless, there are indications in another system [poly(vinyl acetate) particles stabilized by poly(2-ethylhexyl methacrylate)] that the stabilizer chains exist in the particle interior, mixed with poly(vinyl acetate), and form a solvent-swollen interphase [17].

One can make a simple estimate for the effective diffusion coefficient, D, for CS_2, at 0.5 M in the continuous phase, to penetrate fully into the particles. If the diffusion distance d is the particle radius (ca. 100 nm) and diffusion occurs over approximately 10 min, then from the Einstein equation, $d = (2Dt)^{1/2}$, it can be calculated that $D = 8 \times 10^{-14}$ cm^2 s^{-1}. This value is not unreasonable for a molecule the size of CS_2 in PMMA at room temperature.

Curves (b) and (c) in Fig. 3 were digitized and fitted to single exponential decay functions, i.e., ln $I(t)$ values were plotted as a function of time according to the equation $I(t) = C \exp(-k_s t)$, where C is a constant. The plots shown in Fig. 4 exhibit linear behavior within the experimental error for data after the initial fast decrease in $I(t)$. From the slope of the linear portions of

the curves, quencher sorption rates (k_s) were calculated; k_s values for the 0.5 M and 1.0 M CS_2 concentrations were found to be 2.2×10^{-4} s^{-1} and 3.65×10^{-4} s^{-1}, respectively. A larger sorption rate, as one might expect, was obtained for the sample with the higher CS_2 concentration.

The data presented in the following section suggest that the PMMA phase within the particles is glassy. However, the observation of room-temperature phosphorescence in naphthalene-labelled PMMA particles stabilized by poly-(isobutylene) [18] is strong evidence for the glassy nature of the core of PMMA particles (cf. [14]).

Factors affecting the fluorescent label

The fluorescence decay profiles of excited anthracene in the labelled particles do not have a simple exponential form. Furthermore, the fluorescence decay rates are much slower than for the same chromophore in fluid solution where the (exponential) lifetimes are on the order of 2 ns. There is some indication from other studies [19] that the fluorescence decay rate of anthracene depends on (local) solvent viscosity and/or free volume [20], factors which normally restrict motion lead to longer lifetimes.

Figure 5 compares the fluorescence decay profiles from a sample containing a trace of AMP in PMMA (curve a) and a sample of PHSA/PMMA/A particles in dodecane without CS_2 (curve b). It is interesting to note that the shapes of these two decay curves are practically superimposable. This is taken to mean that the nature of the environments containing AMP probes in solid PMMA, and anthracene labels in PHSA/PMMA/A particles are similar. Furthermore, the magnitude of the average lifetime for PHSA/PMMA/A (see Table 2, entry 1) is identical to the value for AMP in pure PMMA.

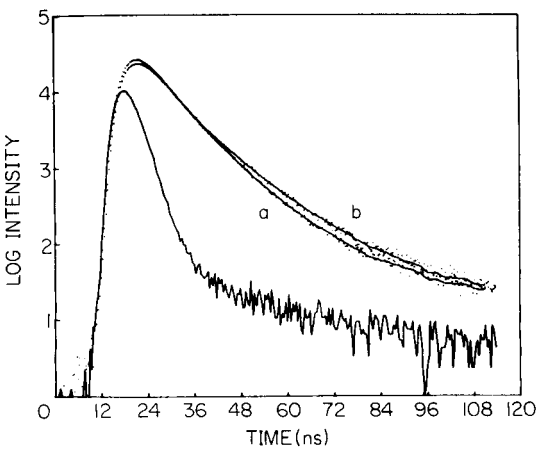

Fig. 5. Transient fluorescence decay profiles at 23°C comparing the behavior of anthracene in PHSA/PMMA/A particles (curve a) and in MMA (1) (curve b). (λ_{ex} = 365 nm, λ_{em} = 442 nm.)

Quenching studies on PHSA/PMMA/A particles

The fluorescence decay profiles, $I_A(t)$, from deoxygenated samples of PHSA/PMMA/A in dodecane at 23°C were fitted to a sum of two exponential terms

$$I_A(t) = a_l \exp(-t/\tau_l) + a_{sh} \exp(-t/\tau_{sh}) \quad (3)$$

where the subscripts l and sh refer to the long and short components of the fit, respectively. The decay parameters obtained are listed in Table 1. The absolute magnitudes of the individual parameters are not significant; it is more useful to calculate, using these parameters, the mean decay times [21], $\langle\tau\rangle$, for the samples:

$$\langle\tau\rangle = (a_1\tau_1^2 + a_2\tau_2^2)/(a_1\tau_1 + a_2\tau_2) \quad (4)$$

Values of $\langle\tau\rangle$, also expressed as $\langle\tau^0\rangle/\langle\tau\rangle$ for each concentration of CS_2 quencher, are presented in Table 2. Here, $\langle\tau^0\rangle$ refers to the sample with $[CS_2]$ = 0 M. For anthracene fluorescence in PHSA/PMMA/A particles, $\langle\tau\rangle$ becomes shorter with increasing $[CS_2]$. Addition of CS_2 to the latex samples also decreases the steady-state fluorescence intensities. These values, reported as I^0/I, are also listed in Table 2.

Results of steady-state and transient fluorescence quenching experiments on PHSA/PMMA/A are presented in Fig. 6, plotted according to Eqn. 1. Both curves in Fig. 6 exhibit downward curvature. Steady-state data of this kind are usually evaluated in terms of a model which assumes the existence of distinct populations of buried and accessible fluorophores [22]. If there are two discrete populations of fluorescence groups, only one of which can be quenched, a plot of $I^0/(I^0 - I)$ vs. $[\text{quencher}]^{-1}$ will yield a linear plot with $1/f_a$ as the y-intercept, where f_a is the fraction of accessible fluorophores. When the steady-state data in Fig. 6 are plotted in this way, a curved plot is still obtained, as shown in Fig. 7. This indicates that the assumption of two distinct populations of anthracene moieties in the particles is clearly an oversimplification; instead, it seems likely that the anthracene groups are

TABLE 1

Fluorescence decay parameters from samples of PHSA/PMMA/A colloid containing varying concentrations of CS_2. Deoxygenated dispersions in dodecane were investigated (λ_{ex} = 365 nm)

$[CS_2]$ (M)	τ_{sh} (ns)	τ_l (ns)	a_{sh}	a_l	χ^2	$\%\tau_l$
0	5.25	9.28	0.020	0.010	1.48	33
0.055	4.86	9.28	0.028	0.013	1.99	32
0.110	4.25	8.45	0.021	0.015	1.12	41
0.245	4.75	9.18	0.025	0.010	1.74	29
0.483	4.05	8.25	0.023	0.016	0.94	41
0.890	3.02	7.37	0.024	0.020	1.63	45
1.727	2.28	6.84	0.048	0.037	1.88	43

TABLE 2

Steady-state (I^0/I) and transient decay ($\langle\tau\rangle$) data for CS_2 quenching of anthracene fluorescence in PHSA/PMMA/A particles in dodecane at 23°C. $\langle\tau\rangle$ values calculated from Eqn. 4

$[CS_2]$ (M)	I^0/I	$\langle\tau\rangle$ (ns)	$\langle\tau^0\rangle/\langle\tau\rangle$	$[CS_2]$ (M)	I^0/I	$\langle\tau\rangle$ (ns)	$\langle\tau^0\rangle/\langle\tau\rangle$
0	1	7.13	1	0.43	1.289	—	—
0.06	—	6.91	1.030	0.48	—	6.49	1.097
0.08	1.094	—	—	0.84	1.500	—	—
0.11	—	6.70	1.063	0.89	—	5.95	1.197
0.19	1.177	—	—	1.51	1.819	—	—
0.25	—	6.65	1.071	1.73	—	5.45	1.306

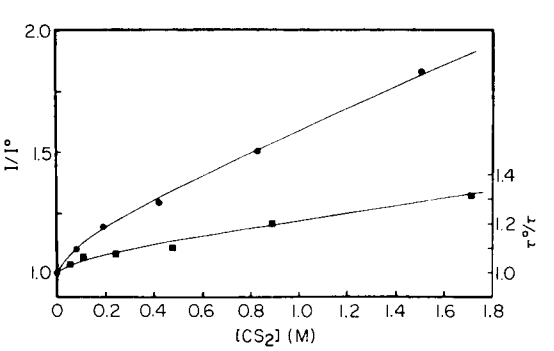

Fig. 6. Stern-Volmer plots of steady-state (•) and transient decay (▪) data from CS_2-quenching studies on PHSA/PMMA/A in dodecane at 23°C.

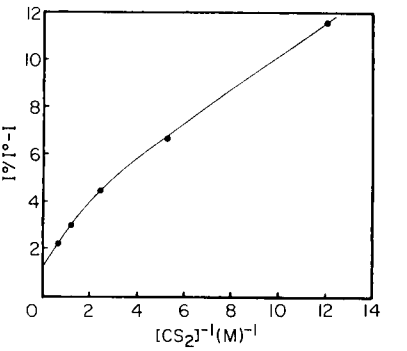

Fig. 7. Plot of $I^0/(I^0 - I)$ vs. $[CS_2]^{-1}$ for the steady-state quenching data on PHSA/PMMA/A particles.

located in a host of different environments characterized by varying degrees of quencher penetration.

The curvature in the plot in Fig. 7 prevents an accurate determination of the y-intercept, but the intercept is obviously near unity. Coupled with the transient decay data in Table 1 which show decreasing values of τ_{sh} and τ_l for increasing concentrations of CS_2, this result indicates that all anthracene groups are quenched by CS_2 to some extent.

From Eqn. 1 with the first few points composing the upper curve in Fig. 6, the 'initial' rate constant (k_q^i) for CS_2 quenching of anthracene in PHSA/PMMA/A was estimated to be 1.34×10^8 M^{-1} s^{-1}. This value is 24-fold less than that obtained for CS_2 quenching of AMP in dodecane. If it is assumed that p and R in Eqn. 2 are equivalent for CS_2 quenching of anthracenes in dodecane and in the particles, then this indicates that the magnitude of the diffusion coefficient for CS_2 in the particles is at least 24 times less than in fluid dodecane solution.

It should be noted, however, that these experiments are fundamentally different from the fluorescence-quenching measurements of the sorption rate using the fluorescence spectrometer. Those measurements followed the fluorescence decrease over a period of minutes, corresponding to CS_2 diffusion over a distance of 100 nm. The fluorescence decay experiments examine concentration fluctuations of quencher on a time scale of 5 ns, corresponding to CS_2 diffusion over a few tenths of a nanometer.

REFERENCES

1 L. H. Sperling, Polym. Eng. Sci., 24 (1984) 1.
2 M. P. Wai, R. A. Gelman, M. G. Fatica and G. D. Wignall, Bull. Am. Phys. Soc., 28 (1983) 517.
3 R. H. Ottewill, in J. W. Goodwin (Ed.), Colloidal Dispersions, Special Publication No. 43, Royal Society of Chemistry, London, 1982.
4 R. H. Ottewill, private communications.
5 K. E. J. Barrett (Ed.), Dispersion Polymerization in Organic Media, Wiley-Interscience, New York, 1975.
6 R. J. R. Cairns, R. H. Ottewill, D. W. J. Osmond and I. Wagstaff, J. Colloid Interface Sci., 54 (1976) 45.
7 L. Chen and M. A. Winnik, unpublished data.
8 D. Ng and J. E. Guillet, Macromolecules, 15 (1982) 724.
9 W. R. Ware, in A. A. Lamola (Ed.), Creation and Detection of the Excited State, Vol. 1, Part A, M. Dekker, New York, 1971, Chap. 5.
10 J. N. Demas, Excited-State Lifetime Measurements, Academic Press, New York, 1983, Chaps. 8 and 9.
11 J. B. Birks, Photophysics of Aromatic Molecules, Wiley-Interscience, New York, 1971, pp. 441–451 and 508–513.
12 J. R. Lackowitz, Principles of Fluorescence Spectroscopy, Plenum, New York, 1983, pp. 260–275.
13 L. S. Egan, M. A. Winnik and M. D. Croucher, Macromolecules, (1986) in press.
14 M. A. Winnik, M. H. Hua, B. Hougham, B. Williamson and M. D. Croucher, Macromolecules, 17 (1984) 262.
15 J. R. Miller, L. T. Calcaterra and G. L. Closs, J. Am. Chem. Soc., 106 (1984) 3047.
16 J. R. Miller, J. A. Peeples, M. J. Schmitt and G. L. Closs, J. Am. Chem. Soc., 104 (1982) 6488.
17 L. S. Egan, M. A. Winnik and M. D. Croucher, Polym. Eng. Sci., 26 (1986) 15.
18 M. A. Winnik, O. Pekcan and M. D. Croucher, Can. J. Chem., 63 (1985) 129.
19 G. Chiu, M. A. Winnick and M. D. Croucher, Colloid Polym. Sci., 264 (1986) 25.
20 R. O. Loutfy and B. A. Arnold, J. Phys. Chem., 86 (1982) 4205.
21 R. K. Bauer, P. de Mayo, K. Odaka, W. R. Ware and K. C. Wu, J. Phys. Chem., 87 (1983) 460.
22 S. S. Lehrer, Biochemistry, 10 (1971) 3254.

Analytica Chimica Acta, 189 (1986) 101—116
Elsevier Science Publishers B.V., Amsterdam — Printed in The Netherlands

STRUCTURAL STUDIES OF VINYLIDENE FLUORIDE-TETRAFLUOROETHYLENE COPOLYMERS BY NUCLEAR MAGNETIC RESONANCE SPECTROSCOPY

RUDOLF E. CAIS* and JANET M. KOMETANI
AT and T Bell Laboratories, Murray Hill, New Jersey 07974 (U.S.A.)
(Received 20th March 1986)

SUMMARY

The application of high-resolution nuclear magnetic resonance (n.m.r.) spectroscopy to structural studies of copolymers is illustrated by an investigation of the vinylidene fluoride (VF_2)-tetrafluoroethylene (F_4E) system. Copolymers of VF_2 with F_4E are of topical interest owing to their ferroelectric behavior, and n.m.r. provides the only method for accurate determination of their composition and chemical microstructure. Many copolymer properties are highly sensitive to these structural variables, which must be characterized prior to the evaluation of physical behavior. A series of copolymers with compositions ranging from 100 to 50 mol% VF_2 is studied by proton, carbon-13, and fluorine-19 n.m.r. Proton and carbon-13 n.m.r. experiments distinguish monomer sequence triads. Fluorine-19 n.m.r. is the method of choice for the most detailed study because this probe resolves all monomer sequence pentads, as well as some longer-range sequences. Assignment of microstructure at this detailed level is aided by an extrapolation of known assignments for PVF_2 homopolymer, and computer simulation of peak probabilities based on a terpolymerization scheme involving both forward and reverse VF_2 addition, as well as F_4E addition. Necessary statistical relationships between observed carbon sequences and monomer sequences are derived to facilitate the study. The VF_2-F_4E system provides a particularly good example of the potential of high-resolution n.m.r. as an analytical tool for copolymer studies.

Fluoropolymers are important speciality materials with many unique properties, including excellent thermal and chemical resistance [1]. There has been a resurgence of interest in one particular polyfluoroethylene, namely polyvinylidene fluoride (PVF_2), since it was discovered to have extraordinary piezoelectric and pyroelectric properties. These properties are manifest only by the β-phase of PVF_2, which has its molecular chains extended in the all-trans conformation. However, this phase is thermodynamically less stable than the more common α-polymorph, and must be obtained by mechanical deformation of melt-crystallized films [2].

Alternatively VF_2 can be copolymerized with tetrafluoroethylene (F_4E) to achieve the useful β-form, provided that the composition is adjusted to be in the appropriate regime [3]. Accordingly, detailed compositional resolution is an absolute prerequisite for evaluation of any given VF_2-F_4E copolymer sample.

0003-2670/86/$03.50

Traditional elemental analysis is not particularly sensitive to small changes in composition in these highly fluorinated materials. High-resolution n.m.r. spectroscopy is the preferred method for quantifying not only the composition of copolymers but also the statistical distribution of monomer units along their chains [4, 5]. The latter measure is in fact more revealing because two copolymers with identical monomer ratios may have entirely different distributions of monomer types.

Here, the potential of proton, carbon-13, and fluorine-19 n.m.r. is evaluated for examining the composition and sequence distribution of VF_2-F_4E copolymers. The study demonstrates the applicability of n.m.r. to copolymer structural problems, and highlights the unique sensitivity of this probe. In fact, fluorine-19 n.m.r. is so sensitive to minor structural perturbations that spectral evaluation is by no means straightforward.

The main goal in this paper is to establish the basic carbon-sequence triad and pentad assignments and show how these lead to an expression for copolymer composition. All heptad fine structure can be assigned, which illustrates how the technique can be extrapolated to longer-range sequences. Particular attention is given to the task of relating sequences observed by n.m.r., which are defined by an odd number of carbons, to sequences generated by addition of monomers, which are defined by an even number of carbons. This relationship is central to the derivation of a copolymerization model [6] that enables the probability of any sequence to be estimated from the basic assignments.

EXPERIMENTAL

Monomers and copolymerizations

Vinylidene fluoride (VF_2) was purchased from PCR Speciality Chemicals and passed through columns containing silica gel and molecular sieves to remove the inhibitor and water. The gas was then condensed at liquid-nitrogen temperature and fractionally distilled under high vacuum. Tetrafluoroethylene (F_4E) was prepared as needed by the depolymerization of pure polytetrafluoroethylene at 600°C in a quartz tube maintained under vacuum [7]. The gaseous monomer was condensed and subjected to several freeze/pump/thaw cycles on a vacuum system to remove traces of air and then fractionally distilled.

The VF_2-F_4E copolymers were prepared by an emulsion technique at 60°C using a standard procedure [8]. The reaction was done in a stainless steel autoclave fitted with a mechanical stirrer and regulated at constant temperature. The reactor was charged under nitrogen with 200 ml of oxygen-free distilled water which contained sodium sulfite (0.5 g) and sodium phosphate (0.11 g) buffer, ammonium peroxodisulfate initiator (1.22 g) and an ammonium perfluorooctanoate emulsifier (2.97 g; 3 M product FC-143). Ammonia solution was added to bring the pH into the range 8.8—9.0. The reactor contents were then frozen and the nitrogen was pumped out under high vacuum.

The respective monomers were measured according to their gas pressure in a calibrated volume and distilled into the reactor which was then sealed and warmed to 60°C with rapid stirring. The initial monomer feed ratios did not change appreciably with conversion because the resultant copolymers contained almost the same ratio so that neither monomer was depleted preferentially. The copolymerization was stopped after 45 min and the excess of pressure vented, after which the copolymer was recovered by coagulation in a water/methanol mixture containing some aluminum sulfate. Conversions were in the range 30—50% by weight. The copolymer was then purified after preliminary drying by being dissolved in dimethylformamide and reprecipitated in fresh methanol.

N.m.r. spectroscopy

A JEOL GX500 spectrometer having a magnetic field strength of 11.7 T was utilized to observe protons and fluorine-19 at resonance frequencies of 500 and 470.7 MHz, respectively. Copolymer samples were dissolved in either dioxane-d_8 or dimethylformamide-d_7 to give ca. 7% solutions (by weight) which were sealed in 5-mm sample tubes.

Proton n.m.r. spectra were obtained at 30°C with dioxane-d_8 as the solvent. A total of 32 transients was accumulated using 32K computer locations to cover a window of 12 kHz. A 90° flip angle resulted from a 9.0-μs pulse width and a 6.0-s delay was used between successive pulses.

Fluorine-19 n.m.r. spectra were recorded from dimethylformamide-d_7 solutions maintained at 90°C. Broad-band proton decoupling was utilized, with a sweep width of 30 kHz and 132K memory for the accumulation of up to 2000 transients using a 90° (10-μs) pulse. The pulse spacing was 15 s to allow complete relaxation of the nuclei to equilibrium between pulses. Hexafluorobenzene was used as the internal chemical shift reference ($\Phi^* = -163$ ppm). The chemical shifts of several peaks were very sensitive to the observation temperature and solvent, so their relative positions changed with these variables.

Dynamic fluorine-19 n.m.r. experiments were done at a lower frequency of 188.2 MHz on a Varian XL-200 spectrometer. The purpose of these measurements was to record spin-lattice relaxation times (T_1) and nuclear Overhauser enhancements to establish experimental conditions for the quantitative observation of peak intensities [9]. The respective T_1 and nuclear Overhauser enhancement values were 0.9 s and 1.1 at 90°C for a copolymer containing 70 mol% VF_2, and did not vary with sequence type within a given sample.

Carbon-13 n.m.r. spectra were also obtained on the XL-200, at a frequency of 50.31 MHz. Copolymers were dissolved in acetone-d_6 at 20% concentration (by weight), and the solution was observed at 50°C in a 10-mm sample tube. A total of 20 000 scans was accumulated with a sweep width of 10 kHz and 20K computer locations. The 90° pulse width was 19.0 μs, and a 3.0-s pulse delay was chosen.

RESULTS AND DISCUSSION

Samples

Table 1 gives the compositions of the initial monomer mixtures and the copolymers resulting therefrom, along with the crystalline melting temperatures which vary strongly with composition, and pass through a minimum of ca. 120°C around 80 mol% VF_2. These copolymer compositions were determined from n.m.r. data as described below. Compositions containing less than 50 mol% VF_2 were not soluble and could not be studied by high-resolution n.m.r., so the present study is limited to the range 100—50 mol% VF_2. The decrease in solubility is not surprising as the copolymer becomes richer in F_4E and behaves more like the homopolymer PF_4E which dissolves only near its melting temperature in perfluorokerosene.

Notation

The present study was greatly aided by a binary notation to represent carbon types. There are just two carbon types in the copolymers (neglecting end groups, branch points, and other irregular structures); these are the methylene carbon $-CH_2-$ and the difluorocarbon $-CF_2-$, which we designate types 0 and 2, respectively, to represent the number of fluorines attached to a particular carbon. Copolymers of VF_2 with F_4E result from the linear addition of these monomers to create $-CH_2-CF_2-$ and $-CF_2-CF_2-$ units, respectively. Thus, in terms of the above notation, carbon-type sequences may be visualized as the concatenation of 02 and 22 blocks or segments.

The set of carbon sequences of length n is designated S_n, where only sequences with odd n are observed directly by n.m.r. The aim of the present study is to derive the unconditional probabilities of these sequences, denoted by $p(S_n)$, from the n.m.r. spectra. Sequences of length $n + 1$ must have either a 0- or a 2-type carbon immediately preceding or succeeding S_n, and these are written as $0S_n$, $2S_n$, S_n0 and S_n2.

There is one particular complication not usually encountered in copolymer studies in that VF_2 can add in two ways [10], either with the forward directional sense 02, or the reverse sense 20. Forward and reverse are some-

TABLE 1

Compositions and crystalline melting points of VF_2/F_4E copolymers prepared by emulsion polymerization at 60°C using the monomer feed compositions indicated

Mol% VF_2		T_m (°C)	Mol% VF_2		T_m (°C)
Monomer	Copolymer		Monomer	Copolymer	
100	100	178	70	70	143
90	88	140	60	63	155
80	78	125	50	53	186

what arbitrary directions, and here the forward sense is considered to be the more likely addition mode [11] to a VF_2 sequence growing from left to right. Therefore, if VF_2 adds in the forward sense to a $-CF_2$ chain end, the usual head-to-tail linkage 2—0 results. Conversely, addition in the reverse sense creates the less probable head-to-head linkage 2—2. Copolymers of VF_2 with F_4E also contain 22 sequences from the latter monomer, so that copolymerization can be viewed as a means for introducing additional head-to-head linkages, which can favorably modify properties [12].

The three different atoms in VF_2-F_4E copolymers all have spin-1/2 nuclei that are routinely observed by contemporary n.m.r. experiments, namely ^1H, ^{13}C, and ^{19}F. However, as will be seen, only fluorine-19 n.m.r. provides sufficient detail to resolve long-range differences in structural sequences, so emphasis will be placed on the observation of this nucleus.

Proton n.m.r.

Figure 1 shows the 500-MHz proton n.m.r. spectra of PVF_2 that has twice the usual head-to-head and tail-to-tail content so that these defects can be observed more readily [13], and two VF_2/F_4E copolymers with 88/12 and 78/22 molar compositions. Five peaks can be distinguished with relative intensities that depend on composition. These peaks monitor the probabilities of the different carbon-sequence pentads belonging to the set S_5. Because these sequences must be centered on the protonated carbon type 0 they are

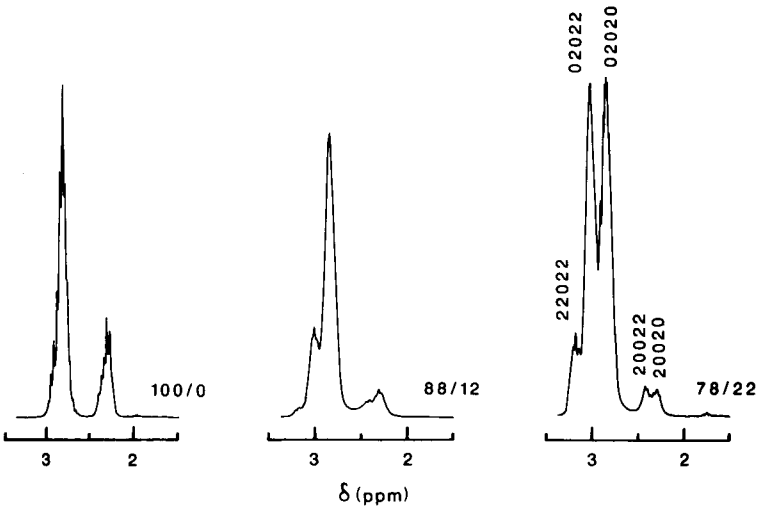

Fig. 1. Proton n.m.r. spectra (500 MHz) of copolymers containing VF_2/F_4E molar ratios of 100/0, 88/12, and 78/22. These spectra were recorded at 30°C using 5% solutions in dioxane-d_8, with tetramethylsilane as the internal chemical shift reference. The sample of PVF_2 (100/0 ratio) has an enhanced level of head-to-head and tail-to-tail additions (11.4%), and was specially prepared in this laboratory [13]. The carbon-sequence pentad assignments are indicated in the righthand spectrum where 0 = $-CH_2-$ and 2 = $-CF_2-$.

02020, 02022, 22022, 20022, and 20020. The sequence 22022 cannot be present in PVF_2.

The methylene protons are equivalent, so the large geminal ^2J-(^1H—^1H) coupling of ca. 10 Hz is not manifest. Vicinal proton and fluorine couplings cause the fine structure apparent on the peaks, and prevent the distinction of S_5 sequences at lower observing frequencies.

The methylene protons belonging to the 202-centered group give the main set of peaks around 3.0 ppm, and those belonging to the 002-centered group give the weaker set around 2.4 ppm. These assignments are straightforward because it is known from studies on PVF_2 that the tail-to-tail or 0–0 linkage is less likely than the head-to-tail linkage 2—0 [14]. Therefore, all sequences containing the 00 segment must be rare. For this reason, we chose to observe the special PVF_2 sample with enhanced levels of 0—0 links [13] so the 002-centered peaks were more visible.

The relative intensities of the five peaks as a function of copolymer composition provide the pentad assignments. The δ values are, in order of increasing field strength: 22022, 3.16; 02022 + 22020, 3.01; 02020, 2.81; 20022 + 22002, 2.44; and 02002 + 20020, 2.30 ppm. An unsymmetrical carbon sequence is observationally equivalent to its reverse sequence, and both contribute to the total peak intensity.

The full set of S_5 peaks cannot be detected by proton n.m.r. because the 2-centered sequences have no protons on the central carbon. Moreover the strong overlap between peaks precludes the accurate measurement of individual pentad intensities. Proton n.m.r. can provide the ratio of S_3 triads 020/022 as these groups are well resolved, but fluorine-19 n.m.r. provides more detailed information (vide infra).

Carbon-13 n.m.r.

Carbon-13 n.m.r. is somewhat more revealing than proton n.m.r., as both 0- and 2-centered sequences are detected. Carbons type 0 are sensitive to pentad sequences S_5. These are shown in Fig. 2 as the high-field set of peaks from 45 to 23 ppm. The low-field set of peaks from 125 to 105 ppm results from the type-2 carbons, which are strongly deshielded by their electronegative fluorine substituents. However, the latter carbon types experience a large $^1J(^{19}F—^{13}C)$ scalar coupling of 248 Hz, which imposes a triplet splitting from the two equivalent fluorines (A_2X spin system). This splitting, plus a smaller $^2J(^{19}F—^{13}C)$ coupling of ca. 24 Hz, obscures much of the carbon sequence detail, so the 2-carbon resonances resolve just the triads 020, 022, and 222, as indicated in Fig. 2.

The 0-centered pentad assignments for the high-field resonances were made on the basis of relative peak intensities, and the known assignments for PVF_2 [15], which establish the principal 02020 resonance, as well as the 02022, 02002, and 22002 peaks associated with head-to-head (2—2) and tail-to-tail (0—0) links. The weakest peaks must contain the dilute 00 segment, and those which increase as the F_4E content increases must contain the 22 segment.

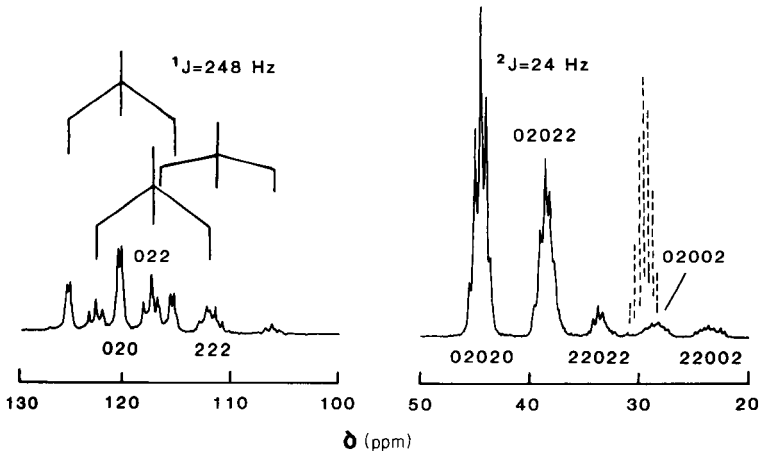

Fig. 2. Proton-decoupled carbon-13 n.m.r. spectrum (50.31 MHz) of the 78/22 VF_2/F_4E copolymer dissolved in acetone-d_6 (20% by weight) at 50°C. The septuplet pattern (dashed lines) centered around 29 ppm results from the solvent. The type-2 carbons ($-CF_2-$) are triplets from the large one-bond coupling of 248 Hz with fluorine. The type-1 carbons ($-CH_2-$) experience a smaller two-bond coupling of 24 Hz, which causes the pentuplet fine structure on the 202-centered sequences.

These carbon-13 n.m.r. spectra are more informative than the proton spectra described above, and in principle they could be used to derive copolymer composition, as the full set of S_3 peaks is resolved. In practice, the difluoro carbons 2 have reduced peak intensities owing to the removal of their nuclear Overhauser enhancements by the strong dipolar interaction with the directly bonded fluorines, so peak intensities do not bear a true 1:1 correspondence to sequence populations. Moreover, carbon-13 n.m.r. is more demanding of instrument time than either proton or fluorine-19 n.m.r., owing to the significantly lower sensitivity arising from lower natural abundance and magnetic moment. For these reasons, and given the compelling advantages of fluorine-19 n.m.r. (vide infra), carbon-13 n.m.r. is not the ideal choice for study of VF_2-F_4E copolymers.

Principal features of fluorine-19 n.m.r. spectra

The principal features of the 470.7-MHz fluorine-19 n.m.r. spectrum of a VF_2-F_4E copolymer are illustrated in Fig. 3. Three groups of resonances may be distinguished from low to high field, corresponding to the central fluorines in 020, 022, and 222 carbon-type sequences, respectively. A fluorine-19 resonance is shielded by about 8 ppm when the substituent γ to the observed fluorine is fluorine instead of hydrogen. Accordingly, the 222 geminal pair of fluorines (4 γ-F substituents) appear ca. 15 ppm upfield from the 022 fluorines (2 γ-F substituents), which in turn are ca. 18 ppm upfield from the 020 fluorines (no γ-F substituents).

Each of these regions shows considerable fine detail on closer examina-

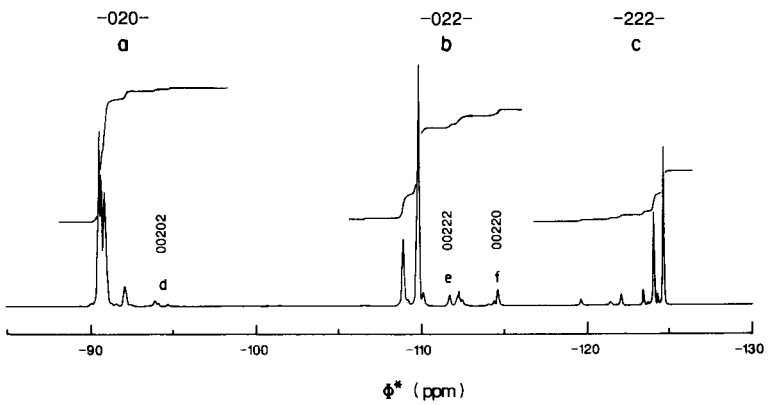

Fig. 3. Proton-decoupled fluorine-19 n.m.r. spectrum (470.7 MHz) with the integral traces for the 78/22 VF_2/F_4E copolymer dissolved in dimethylformamide-d_7 (7% by weight) at 90°C. The chemical shift reference is internal hexafluorobenzene ($\Phi^* = -163$ ppm). The integrated areas of the three S_3 groups 020, 022 + 220, and 222 from low to high field are designated by *a*, *b*, and *c*, respectively. These areas, as well as those from the S_5 sequences 00202, 00222, and 00220 (*d*, *e*, and *f*, respectively), are required to calculate composition (see text).

tion, corresponding to higher-order sequence structure. In order to understand this, it is necessary to consider the number of structurally unique sequences possible by the permutation of 02, 20, and 22 units at a given level of *n*-ad resolution. There are 3, 9, 26, and 81 different sequences for $n = 3$, 5, 7, and 9, respectively. The three main groups complete the set S_3, but the fine structure within each group exhibits a hierarchy of splittings from all 26 S_7 peaks, each of which has S_9 fine structure, which in turn is split by S_{11} and even some S_{13} sequence effects.

Murasheva et al. [16] have given prior consideration to this fine structure. However, their spectra had limited resolution owing to the reduced fluorine-19 observation frequency of 84.68 MHz, so that only 15 peaks out of the full set of 26 S_7 resonances were recognized. Also they worked with just one copolymer composition and could not exploit the added information provided by the change in peak intensities with composition (vide infra). Their assignments were based on an empirical additivity scheme to predict chemical shifts.

The procedure used here does not rely on predicting chemical shifts, beyond the distinction made above between 020, 022, and 222 on the basis of a γ-shielding effect by fluorine substituents [17]. Instead use is made of the relative intensities of peaks as a function of the VF_2/F_4E monomer ratio taken to prepare the various copolymers.

Assignment of carbon-sequence pentads

All nine S_5 regions within the S_3 main groups above can be readily delineated. Four of these S_5 regions are known from PVF_2 studies; they are

20202, 20200, 20220, and 00220 [18]. The remaining five are unique to the copolymers, and comprise 20222 plus 00222 within the middle 022 group, and 22222, 22220, plus 02220 within the upfield 222 group. These are readily identified by their relative intensities. The 00222 sequence is least likely as it contains the tail-to-tail linkage 0—0, leaving 20222 as the final unassigned region within the 022 group. Within the 222 group, the intensity must increase for the 22222 region at the expense of the 02220 region as the F_4E content increases, so that these regions become evident upon comparing spectra from copolymers that are rich and poor in F_4E. The 22220 region then follows as the last assignment by default.

Sequence probabilities and composition analysis

The integrated intensities were recorded for all 2-centered carbon-sequence pentads assigned above and converted to the appropriate unconditional probabilities [19] of these sequences. The normalization area, which is the sum of both 2- and 0-centered sequences, must be evaluated prior to this step. The derivation is given below after certain probability relationships are introduced.

There are various conservative equations which the unconditional carbon-sequence probabilities must obey. The relevant principles are as follows. First, any carbon selected at random must be type 0 or 2, so that $p(0) + p(2) = 1$. Likewise the full set of n-ad probabilities for each $n > 1$ must sum to unity; the equation for $n = 3$ is

$$p(020) + p(022) + p(220) + p(222) + p(202) + p(200) + p(002) = 1$$

Unsymmetrical dyad and triad sequences are equally probable on reversal: $p(02) = p(20)$, $p(002) = p(200)$, $p(022) = p(220)$. It is important to stress that any sequence is observationally indistinguishable from its reverse by n.m.r.; for example, the peak designated 022 is the sum of 022 and 220 sequences. Both sequences will be written explicitly in the equations, but just one will be given for brevity in the assignment table and discussion. Finally, any sequence must be preceded or succeeded by either 0 or 2, so that

$$p(S_n) = p(0S_n) + p(2S_n) = p(S_n0) + p(S_n2)$$

This equation relates S_n to S_{n+1}; for example, $p(02) = p(002) + p(202) = p(020) + p(022)$, etc.

The simplest measure of copolymer structure is the macroscopic composition, expressed as the mole percent of monomer. It is easily shown that

$$1/2\ [\text{mol\%}(VF_2)] = 100[p(0)]$$

The above equations allow $p(0)$ to be related to the observable triad and pentad sequences, according to

$$p(0) = p(00) + p(02) = p(000) + p(002) + p(020) + p(022)$$

It should be noted that the sequences having three or more adjacent 0

carbons are not possible, nor are sequences of the type 00200 etc. which cannot be constructed from 02, 20, and 22 blocks, so that finally

$$p(0) = p(00202) + p(00220) + p(00222) + p(020) + p(022)$$

These pentads and triads have all been assigned in the spectra (they are explicitly designated in Fig. 3), and their integrated intensities allow the copolymer composition to be computed as indicated above.

As noted earlier, the normalization area is needed to convert peak areas to unconditional probabilities. The correct normalization area is the sum

$$\Sigma = A(020) + A(022) + A(220) + A(222) + A(202) + A(200) + A(002)$$

The integrated area, A, for the 0-centered triads is not directly observed in the spectra, but can be evaluated from the observed 2-centered sequences according to

$$A(202) + A(200) + A(002) = A(020) + A(220) + A(00202) + A(00220) + A(00222)$$

This equation follows from the probability relationships established above.

Those groups of peaks necessary to derive composition are represented by the letters a–f (Fig. 3), where a = 020, b = 022 + 220, c = 222, d = 00202 + 20200, e = 00222 + 22200 and f = 00220 + 02200. The integrated areas of regions a–f are used to derive the composition from

$$\text{mol\%}(VF_2) = 200 \times (2a + b + d + e + f)/(4a + 3b + 2c + d + e + f)$$

The results from this study of copolymer composition are given in Table 1. The composition values were reproducible to within 0.5% for each copolymer batch when the experiments were repeated with fresh samples.

Monomer sequence

It has been shown above how the fluorine-19 n.m.r. spectra can be interpreted in terms of carbon sequence pentads and used to determine composition. Here the relationship between carbon sequences and monomer sequences is considered in order to predict the intensities of longer-range sequence structure. There are two chemically distinct monomers, VF_2 and F_4E, but as has been seen, the former can be incorporated into sequences with the forward sense 02, or the reverse sense 20. These two orientations are distinguished by F and R, respectively, and the F_4E unit is denoted by T. Therefore, all monomer sequences will consist of some permutation of F, R, and T units. Sequences with n such units belong to the set $\mathbf{M}_n$, which also defines the set $\mathbf{S}_{2n}$ of carbon sequences. The problem here is to establish the $\mathbf{M}_n$–$\mathbf{S}_{2n-1}$ relationships.

The concept of "window" probabilities w allows the connection between monomer sequences and carbon sequences to be visualized [18]. For example, the $\mathbf{S}_3$ sequence 022 exists within the $\mathbf{M}_2$ sequences FT (02,22), FR (02,20), and RT (20,22). There is an equal chance that the sequence 022,

when viewed through a three-carbon window, was formed by an 02,2X or an X0,22 pair of monomers (X = 0 or 2), so that [18]

$$p(022) = 1/2w(02,20) + 1/2w(02,22) + 1/2w(00,22) + 1/2w(20,22)$$

The 00 monomer unit (ethylene) is not present, thus

$$p(022) = 1/2p(FR) + 1/2p(FT) + 1/2p(RT)$$

In this manner, the unconditional probabilities of S_{2n-1} can be related to M_n for all $n > 2$.

The relationships for all members of these sets for n = 2 are

$$p(020) = 1/2[p(FF) + p(RR)]$$

$$p(022) = 1/2[p(FR) + p(FT) + p(RT)]$$

$$p(220) = 1/2[p(FR) + p(TF) + p(TR)]$$

$$p(222) = 1/2[p(TR) + p(FT) + 2p(TT)]$$

$$p(202) = 1/2[p(RR) + p(RT) + p(FF) + p(TF)]$$

$$p(200) = 1/2p(RF)$$

$$p(002) = 1/2p(RF)$$

The M_2 probabilities can be used to predict higher-order M_n probabilities for any n, provided that the copolymerization obeys first-order Markov statistics [20]. The first-order Markov model can be fitted knowing the M_2 probabilities, but it can be tested only with M_3 or higher probabilities. The S_5 probabilities obtained in the previous section are adequately described by the first-order Markov model, which then can be used to predict the S_7 peak intensities as shown below.

The prediction is made by using conditional monomer addition probabilities of the form, $P(A|B)$, which is the probability that monomer B adds to the growing copolymer chain on the condition that the terminal unit was formed by monomer A. The appropriate relationships for n = 2 are

$$p(FF) = p(F) \times P(F|F); p(FR) = p(F) \times P(F|R); p(RF) = p(R) \times P(R|F)$$

$$p(RR) = p(R) \times P(R|R); p(FT) = p(F) \times P(F|T); p(TF) = p(T) \times P(T|F)$$

$$p(RT) = p(R) \times P(R|T); p(TR) = p(T) \times P(T|R); p(TT) = p(T) \times P(T|T)$$

Some additional useful relationships are

$$100 \times [p(F) + p(R)] = \text{mol\% } VF_2$$

$$p(F) + p(R) + p(T) = 1$$

$$P(F|F) + P(F|R) + P(F|T) = 1$$

$$P(R|F) + P(R|R) + P(R|T) = 1$$

$$P(T|F) + P(T|R) + P(T|T) = 1$$

$$p(\mathrm{FF}) + p(\mathrm{FR}) + p(\mathrm{FT}) + p(\mathrm{RF}) + p(\mathrm{RR}) + p(\mathrm{RT}) + p(\mathrm{TF}) + p(\mathrm{TR}) + \\ + p(\mathrm{TT}) = 1$$

Heptad carbon sequence

The S_7 sequence assignments are not as obvious in the fluorine-19 spectra as the S_5 assignments. For this reason, the above analysis is used to predict the relative intensities for the observed 2-centered S_7 sequences according to first-order Markov statistics. Many ambiguous assignments can then be resolved from the observed intensities.

It would be tedious to show explicitly the derivations for all 26 observationally distinct heptads, so just the 2202202 peak is chosen for illustration. This sequence is asymmetrical, so the observed area after normalization will be

$$A(2202202) = p(2202202) + p(2022022)$$
$$= 1/2\,[w(22,02,20,20) + w(22,02,20,22) + w(02,20,22,02) + \\ + w(22,20,22,02) + w(20,22,02,20) + w(20,22,02,22) + \\ + w(02,02,20,22) + w(22,02,20,22)]$$
$$= 1/2\,[p(\mathrm{TFRR}) + 2p(\mathrm{TFRT}) + p(\mathrm{FRTF}) + p(\mathrm{TRTF}) + \\ + p(\mathrm{RTFR}) + p(\mathrm{RTFT}) + p(\mathrm{FFRT})]$$

This is a good illustration that not all resonances correspond to a unique monomer sequence; here it is seen that seven different monomer combinations are observationally indistinguishable at the heptad carbon sequence level.

The S_3 probabilities are then used to derive the conditional addition probabilities as shown above to compute these M_4 probabilities. For example,

$$p(\mathrm{FRTF}) = p(\mathrm{F}) \times P(\mathrm{F|R}) \times P(\mathrm{R|T}) \times P(\mathrm{T|F})$$

The other monomer sequence tetrad probabilities are calculated in like manner. A FORTRAN program was written for this purpose using the areas of peaks *a*—*f* as input and providing copolymer composition and the M_4 sequence probability table as output.

As a first approximation, the reversal of VF_2 units was ignored to identify just those twelve S_7 peaks which do not involve the dilute 00 segment. Then the percent of VF_2 units adding as R was assumed constant and equal to the value for PVF_2 (ca. 5%) [18], so that

$$p(\mathrm{F}) = 0.95 \times [\mathrm{mol\%\ VF_2}/100.0]$$

The intensities of the remaining fourteen S_7 peaks which incorporate R units were calculated accordingly. The predicted S_7 intensities are given in Tables 2—4 and were compared with observed intensities for different copolymer compositions to establish the assignments. In many cases, several

TABLE 2

The five observationally distinct 020-centered carbon-sequence heptads with estimated probabilities for 88/12 and 63/37 VF_2/F_4E copolymer compositions

No.[a]	S_7	Probability	
		$p(T) = 0.12$	$p(T) = 0.37$
1	0202020	0.262	0.028
2	0202022	0.092	0.069
3	2202022	0.008	0.043
4	2202002	0.003	0.002
5	0202002	0.011	0.000

[a]See assignments in Fig. 4.

TABLE 3

The twelve observationally distinct 022-centered carbon-sequence heptads with estimated probabilities for 88/12 and 63/37 VF_2/F_4E copolymer compositions

No.[a]	S_7	Probability		No.[a]	S_7	Probability	
		$p(T) = 0.12$	$p(T) = 0.37$			$p(T) = 0.12$	$p(T) = 0.37$
6	2202220	0.021	0.184	12	0202202	0.003	0.003
7	2202222	0.000	0.010	13	0202200	0.012	0.001
8	0202222	0.000	0.008	14	2202202	0.007	0.017
9	0202220	0.168	0.147	15	2202200	0.002	0.002
10	2002220	0.003	0.003	16	2002202	0.014	0.003
11	2002222	0.003	0.004	17	2002200	0.001	0.000

[a]See assignments in Fig. 5.

TABLE 4

The nine observationally distinct 222-centered carbon-sequence heptads with estimated probabilities for 88/12 and 63/37 VF_2/F_4E copolymer compositions

No.[a]	S_7	Probability		No.[a]	S_7	Probability	
		$p(T) = 0.12$	$p(T) = 0.37$			$p(T) = 0.12$	$p(T) = 0.37$
18	2222222	0.000	0.001	23	0222202	0.004	0.013
19	0222222	0.000	0.001	24	0222200	0.003	0.003
20	0222220	0.000	0.009	25	2222200	0.000	0.000
21	2222202	0.000	0.019	26	0022202	0.003	0.004
22	2022202	0.068	0.166				

[a]See assignments in Fig. 6.

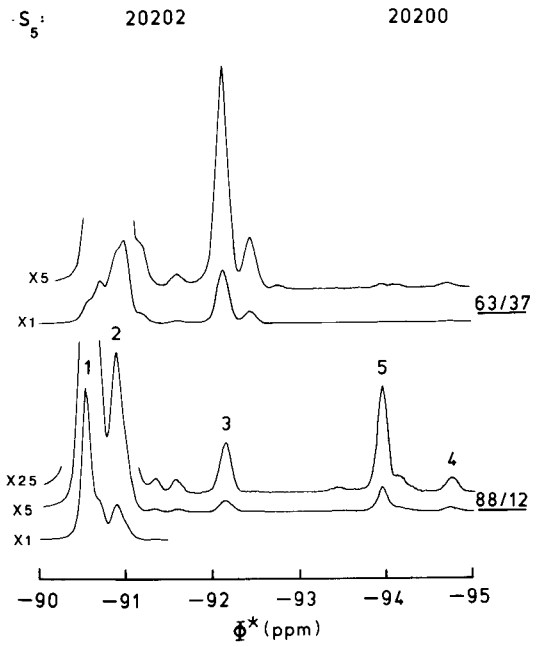

Fig. 4. Expansion of the 470.7-MHz fluorine-19 resonances from all 020-centered carbon sequences in two VF_2/F_4E copolymers containing 88/12 and 63/37 monomer ratios. The S_7 assignments (numbered 1—5) are given in Table 2.

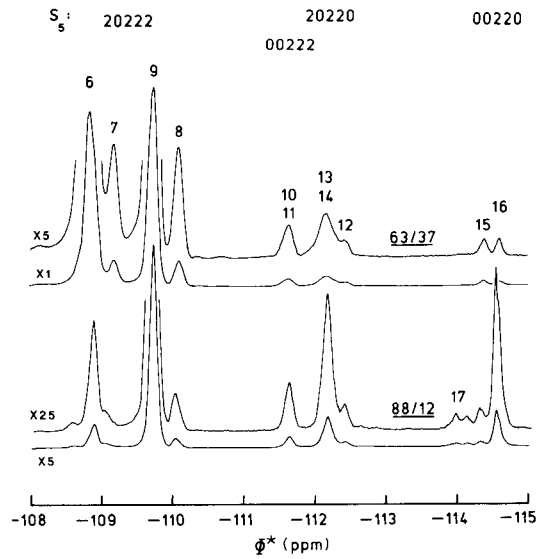

Fig. 5. Expansion of the 470.7-MHz fluorine-19 resonances from all (022 + 220)-centered carbon sequences in two VF_2/F_4E copolymers containing 88/12 and 63/37 monomer ratios. The S_7 assignments (numbered 6—17) are given in Table 3.

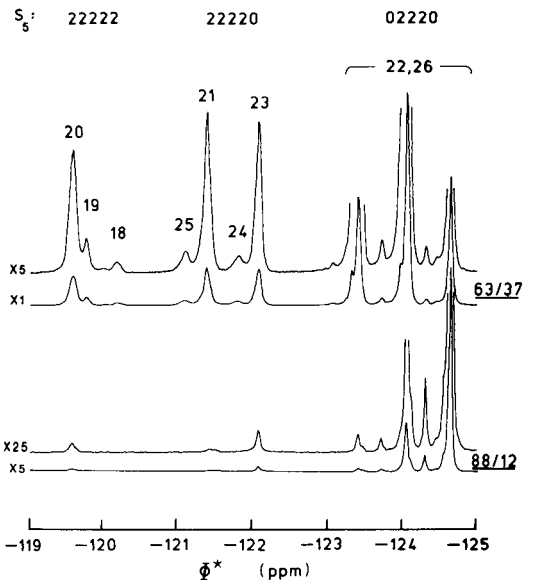

Fig. 6. Expansion of the 470.7-MHz fluorine-19 resonances from all 222-centered carbon sequences in two VF_2/F_4E copolymers containing 88/12 and 63/37 monomer ratios. The S_7 assignments (numbered 18—26) are given in Table 4.

individual peaks have to be combined to correspond to the predicted S_7 intensity owing to splitting beyond the heptad level. The heptad assignments are indicated by the numbers 1 to 26 on Figs. 4—6 which show detailed expansions of the fluorine-19 resonances from 020-, 022-, and 222-centered sequences.

It is clear from the detail in Figs. 4—6 that even a heptad carbon-sequence analysis is inadequate. There are splittings which indicate that S_{11} and S_{13} sequences have an effect on fluorine chemical shift. This is particularly noticeable in the 02220-centered sequences (Fig. 6). Such a long-range sensitivity is not surprising in view of the resolution of carbon-sequence 11-ads for PVF_2 [21, 22] by high-field fluorine-19 n.m.r. It is beyond the scope of the present paper to explore this fine structure in detail and examine nuances in the copolymerization model. More detailed considerations will be presented in a separate publication where additional experimental evidence involving two-dimensional n.m.r. techniques and deuterium-labelled samples will be used.

We are grateful to Mr. J. W. Simmons of 3M Commercial Chemicals Division for donation of the sample of Fluorad FC-143 surfactant used for the emulsion copolymerizations.

REFERENCES

1 L. A. Wall (Ed.), Fluoropolymers, Wiley-Interscience, New York, 1972.
2 A. J. Lovinger, in D. C. Bassett (Ed.), Developments in Crystalline Polymers-1, Applied Science, London, 1982, Ch. 5.
3 J. B. Lando and W. W. Doll, J. Macromol. Sci. Phys., 2 (1968) 205.
4 F. A. Bovey, High Resolution NMR of Macromolecules, Academic Press, New York, 1972.
5 J. C. Randall, Polymer Sequence Determination Carbon-13 NMR Method, Academic Press, New York, 1977.
6 J. L. Koenig, Chemical Microstructure of Polymer Chains, Wiley-Interscience, New York, 1980, Ch. 5.
7 E. E. Lewis and M. A. Naylor, J. Am. Chem. Soc., 69 (1947) 1968.
8 J. E. Fearn, in L. A. Wall (Ed.), Fluoropolymers, Wiley-Interscience, New York, 1972, p. 8.
9 C. H. Sotak, C. L. Dumoulin and G. C. Levy, in G. C. Levy (Ed.), Topics in Carbon-13 NMR Spectroscopy, Vol. 4, Wiley-Interscience, New York, 1984, Ch. 4.
10 V. L. Maksimov and E. G. Zotikov, Vysokomol. Soedin. Ser., B, 11 (1969) 818.
11 R. E. Cais and J. M. Kometani, Macromolecules, 17 (1984) 1887.
12 G. Moggi and P. Bonardelli, J. Polym. Sci. Polym. Phys. Ed., 22 (1984) 357.
13 R. E. Cais and J. M. Kometani, Macromolecules, 18 (1985) 1354.
14 R. C. Ferguson and E. G. Brame, Jr., J. Phys. Chem., 83 (1979) 1397.
15 F. A. Bovey, F. C. Schilling, T. K. Kwei and H. L. Frisch, Macromolecules, 10 (1977) 559.
16 Ye. M. Murasheva, A. S. Shashkov and A. A. Dontsov, Polym. Sci. USSR, Engl. Trans., 3 (1981) 711.
17 A. E. Tonelli, F. C. Schilling and R. E. Cais, Macromolecules, 15 (1982) 849.
18 R. E. Cais and N. J. A. Sloane, Polymer, 24 (1983) 179.
19 B. D. Coleman and T. G. Fox, J. Polym. Sci. Part A, 1 (1963) 3183.
20 F. P. Price, in G. G. Lowry (Ed.), Markov Chains and Monte Carlo Calculations in Polymer Science, Marcel Dekker, New York, 1970, Ch. 7.
21 R. C. Ferguson and D. W. Ovenall, Polym. Prepr., Am. Chem. Soc., Div. Polym. Chem., 25 (1984) 340.
22 V. A. Lovchikov, A. M. Shylakov and I. M. Doglopolskii, Issled. Str. Makromol. Metodom YAMR Vysok. Razresh., M., (1983) 51.

Analytica Chimica Acta, 189 (1986) 117—133
Elsevier Science Publishers B.V., Amsterdam — Printed in The Netherlands

CHARACTERIZATION OF THE CHEMICAL STRUCTURE OF THERMOSETTING RESINS BY HIGH-RESOLUTION SOLID- STATE CARBON-13 NUCLEAR MAGNETIC RESONANCE SPECTROMETRY

FRANÇOISE LAUPRETRE* and LUCIEN MONNERIE

Laboratoire de Physico-chimie Structurale et Macromolêculaire associê au C.N.R.S., 10 rue Vauquelin, 75231 Paris Cêdex 05 (France)

BERTRAND BLOCH

Division des Matêriaux, O.N.E.R.A., 29 avenue de la Division Leclerc, 92320 Châtillon (France)

(Received 20th March 1986)

SUMMARY

The combination of proton-dipolar decoupling, magic-angle spinning and cross-polarization techniques results in high-resolution ^{13}C-nuclear magnetic resonance (n.m.r.) spectra of solid-state compounds. In homogeneous materials, using a relatively low external field and in the absence of motional line broadenings, the chemical structure of totally insoluble cured polymer resins can be estimated quantitatively, and the chemical mechanisms leading to their formation can be elucidated. The capability of high-resolution solid-state ^{13}C-n.m.r. for solving such problems is illustrated by the example of the polystyrylpyridine system obtained by reaction of terephthalic aldehyde with pyridine. The decreasing amounts of aldehyde and methyl groups and the appearance of network cross-linkages were studied as a function of both the temperature and the duration of the curing treatment. The results are interpreted quantitatively in terms of two chemical mechanisms: first, the addition of a methyl group from the collidine molecule to the aldehyde function of terephthalic aldehyde followed by elimination of water; secondly, a cross-linking reaction consisting of the addition of a collidine methyl group to the double bonds formed in the first process. The high resolution of the ^{13}C-n.m.r. spectra also makes it possible to observe the different reactivities of the *o*- and *p*-methyl substituents of the collidine molecule. *p*-Methyl reactions occur only when most of the *o*-methyl functions have disappeared. Thus, high-resolution solid-state ^{13}C-n.m.r. provides a precise characterization of the polystyrylpyridine resins in terms of both their quantitative chemical composition and their reaction mechanisms.

For many years, high-resolution carbon-13 nuclear magnetic resonance (n.m.r.) in solution, which provides a one-to-one correspondence between the carbon atoms of a molecule and its n.m.r. spectrum peaks, has become established as one of the most powerful analytical techniques in organic chemistry. However, until some recent developments [1—3], n.m.r. could be applied only to samples in solution, and its use in the field of polymer resins was restricted to the early stages of formation where the products remained soluble. In solution, the tensile interactions such as the chemical shift anisotropy, the homonuclear and heteronuclear dipolar couplings, and the

0003-2670/86/$03.50

quadrupolar couplings in the case of spins higher than 1/2, are averaged to zero by the rapid Brownian motions of the molecules and the resulting linewidths are very narrow (<1 Hz). In a solid, such as a polymer below its glass transition temperature or a cured resin, rapid isotropic motions do not usually occur and the anisotropic interactions are not or are only partly averaged. The observed linewidths for a solid compound under the experimental conditions of high-resolution ^{13}C-n.m.r. in solution are of the order of several kilohertz and the spectrum does not show any resolution.

Recently, developments of proton-dipolar decoupling, magic-angle spinning and cross-polarization methods [1–3] have allowed the suppression of the main solid-state line-broadening mechanisms and the recovery of the high resolution and sensitivity of the technique when applied to solid-state samples. The advantage of a direct solid-state investigation must be emphasized; this approach eliminates structural uncertainties associated with the dissolution process and provides the opportunity to study insoluble compounds under non-destructive conditions. It has proved particularly useful in the case of cured polymer resins which are totally intractable materials and for which the reactions occurring during the curing process may differ from the behavior observed in the early stages of resin formation [4]. Magic-angle spinning, proton-dipolar decoupling, cross-polarization ^{13}C-n.m.r. has been successfully applied to different cured polymer systems such as phenolic [5–9], urea-formaldehyde [10], furfuryl alcohol [4, 11], resol-type phenol-formaldehyde [12], epoxy [13–21] and polyimide [22, 23] matrices. The same techniques have allowed the observation of ^{15}N in urea-formaldehyde resins [24].

In the present paper, the principles on which high-resolution solid-state ^{13}C n.m.r. is based will first be reviewed briefly. Then it will be shown how this technique, applied to the particular example of the cured polystyryl-pyridine system, allows the determination of chemical structure and the characterization of the chemical reactions involved in the case of totally insoluble compounds.

HIGH-RESOLUTION SOLID-STATE ^{13}C-N.M.R.

High-power proton dipolar decoupling

The major cause of line broadening in ^{13}C-n.m.r. spectra of solid compounds is the dipolar coupling of the carbon nuclei with neighbouring protons. Each proton, and in a more general way, each spin placed in an external magnetic field, H_0, creates its own induced field which adds to or subtracts from the external field according to the proton spin state. For a ^{13}C proton pair in a given orientation, the resulting ^{13}C-n.m.r. spectrum is a doublet centered at the Larmor spin frequency. The observed splitting is

$$(\gamma_C \gamma_H \hbar/2\pi)(1 - 3\cos^2\theta_{CH})/r_{CH}^3 \qquad (1)$$

where r_{CH} is the internuclear C–H distance and θ_{CH} the angle made by the C–H vector with the external magnetic field, H_0.

Dipolar couplings for $^{13}C-^{1}H$ are large. They can be as much as 40 kHz in the case of a C—H vector parallel to the H_0 magnetic field. In a polycrystalline powder where all the orientations of the C– H vector exist, and where a given carbon is coupled to many different protons, the proton-coupled carbon line is broad and structureless.

The way to remove the heteronuclear dipolar broadening is to irradiate protons with a strong radiofrequency field in the neighbourhood of their Larmor frequency [25]. This irradiation is similar to the selective decoupling of the scalar interactions in solution ^{13}C-n.m.r. However, the required intensity of the radiofrequency field is much larger. The intensity must not only be larger than the $^{13}C-^{1}H$ dipolar coupling strength, but also greater than the natural proton dipolar linewidth [26].

It should be noted that, because of the natural dilution of carbon-13 atoms, homonuclear dipolar coupling between two carbon-13 nuclei can be neglected.

Magic-angle spinning [2]

Even when the proton-carbon dipolar coupling is suppressed by appropriate irradiation, the carbon linewidths of a solid compound remain broad because the chemical shift of a given nucleus depends on the orientation of its attached chemical shift tensor with respect to the external magnetic field. In a polycrystalline powder in which all orientations are equally probable, the resulting spectrum is a superposition of all the elementary chemical shifts corresponding to each orientation. The chemical shift anisotropy of a given carbon nucleus can be as large as 200 ppm.

For a given orientation, the observed chemical shift corresponds to the σ_{zz} component of the chemical shift tensor along the H_0 external field:

$$\sigma_{zz} = \sum_{i=1}^{3} \sigma_i \cos^2 \theta_i \tag{2}$$

where σ_i are the principal tensor components and θ_i the angle of the i-component with H_0.

When the sample is spun rapidly at an angular frequency, ω_r, about an axis making an angle, ϕ, with the external field, the θ_i angles become time-dependent:

$$\cos \theta_i = \cos \phi \cos R_i + \sin \phi \sin R_i \cos (\omega_r t + \psi_i) \tag{3}$$

and the time average of σ_{zz} is written as:

$$\overline{\sigma_{zz}} = 3/2\, \sigma \sin^2 \phi + 1/2\, (3 \cos^2 \phi - 1) \sum_i \sigma_i \cos^2 R_i \tag{4}$$

where σ is the tensor trace, $\sigma = 1/3\ \Sigma_{i=1}^{3}\ \sigma_i$, and R_i are the angles between the rotation axis and the principal components of the σ tensor.

At the magic angle, $\phi = 54.7^\circ$ and $\bar{\sigma}_{zz} = \sigma$, with subsidiary terms periodic in ω_r which create spinning side-bands. The resulting ^{13}C-n.m.r. spectrum

depends on the extent of chemical shift anisotropy modulation by magic-angle spinning. If $\omega_r/2\pi$ is large relative to the chemical shift anisotropy expressed in hertz, the spectrum consists of one peak per magnetically inequivalent carbon, the location of which is given by the trace of the tensor. Conversely, if $\omega_r/2\pi$ is smaller than the chemical shift anisotropy, there appear, together with the main resonance, spinning side-bands at a distance $\omega_r/2\pi$ from each other. The envelope of the spinning side-bands is related to the shape of the chemical shift tensor [27].

The existence of the spinning side-bands leads to consideration of using a more or less intense external magnetic field. The signal-to-noise ratio is an increasing function of the external magnetic field intensity. However, consider the classical case of an unsaturated carbon characterized by a chemical shift anisotropy of about 100 ppm. At a carbon resonance frequency of 25 MHz, the rotor has to spin at a speed greater than 2500 Hz for efficient modulation of the chemical shift anisotropy. Such spinning speeds are easily achieved and the resulting ^{13}C-n.m.r. spectra are readily interpreted. At a carbon resonance frequency of 75 MHz, the minimum rotor spinning speed for efficient modulation is 7500 Hz. Spinners currently available do not reach such spinning speeds, so the spectra obtained at such a field are obscured by spinning side-bands and the signal intensity is split between the main resonance peak and its harmonics.

By use of appropriate pulse sequences such as the TOSS sequence designed by Dixon [28], it is possible to suppress the spinning side-bands artificially and to recover easily tractable spectra. However, in the case of the TOSS sequence, two situations must be distinguished. Calculations [29] have shown that when the TOSS sequence is used to suppress small spinning side-bands, the intensity of the TOSS center band is only slightly less than the full spectral intensity obtained by integration of the entire ordinary magic-angle spinning spectrum. In this regime of small rotational side-bands, and neglecting the relaxation processes occurring before the acquisition of the signal, the sort of quantitative error involved in using the TOSS sequence is only a few per cent, which is less than what is demanded of most n.m.r. applications. In the opposite limit of large spinning side-bands, the percentage of the total intensity in the TOSS sequence decreases and the use of the TOSS sequence cannot provide any quantitative estimate of the chemical structure of an unknown compound. Therefore, if, from a practical point of view, the problem consists of estimating such a structure, the n.m.r. experiments must be done at a low external magnetic field and with a high enough rotor-spinning speed to ensure efficient modulation. Moreover, experiments done on polymer resins at different external field strengths have shown that there is usually no gain in resolution with increasing field strength [6]. Besides, sensitivity increases with increasing field strength are often lost in bigger side-bands and longer spin-lattice relaxation times. The only inconvenience in using a low external field is the complex patterns observed in the case of residual ^{13}C—^{14}N dipolar couplings which simplify at high field [30–32].

It is also noticeable that although magic-angle spinning with a low external magnetic field is efficient enough to suppress the effects of chemical shift anisotropy, the rotor spinning speed will always be too low for efficient modulation of the carbon—proton dipolar couplings in a solid polymer below its glass-transition temperature. Moreover, the proton-proton dipolar interactions produce a substantial "homogeneous" character in the sense used by Maricq and Waugh [33]; if the rotation rate is less than the proton dipolar linewidth, the averaging effects of magic-angle rotation on carbon—proton dipolar couplings are nullified by the energy-conserving flip-flop transitions of the proton spins.

Cross-polarization [1]

A further problem encountered in the n.m.r. study of rare spins such as carbon-13 nuclei is the attainable sensitivity. The resonance signal is proportional to the magnetization of the I spin system placed in an external magnetic field, H_0, which, for a spin 1/2 system, can be written as

$$M_I = N_I \gamma_I^2 \hbar^2 H_0 / 4 k T_L \tag{5}$$

where N_I is the number of I spins in the sample, γ_I is the gyromagnetic ratio of the I spins, and T_L is the absolute temperature of the lattice.

Because protons have high gyromagnetic ratios and natural abundance, their magnetization, M_H, is of course much higher than that of the carbon-13 nuclei, M_C. A way of increasing M_C consists of transferring a small fraction of the proton magnetization to the carbon spin system. This can be achieved by spin-locking the protons with a radiofrequency field, H_{1H}, parallel to the proton rotating frame magnetization [1]. The proton spin system then passes suddenly from a high field (H_0) in the laboratory frame to a low one (H_{1H}) in the rotating frame. The M_H magnetization is maintained and therefore the spin temperature is lowered. Thus, M_H can be written as

$$M_H = N_H \gamma_H^2 \hbar^2 H_0 / 4 k T_L = N_H \gamma_H^2 \hbar^2 H_{1H} / 4 k T_0 \tag{6}$$

where T_0 is the proton spin-temperature in the spin-lock experiment: $T_0 = T_L H_{1H}/H_0$. The important result is that T_0 is much lower than T_L because H_{1H} is much weaker than H_0. Then the proton magnetization follows a $T_{1\rho}(^1H)$ decrease during the spin-lock sequence.

During the proton spin-lock time, a second radiofrequency field is applied at the carbon resonance frequency under the Hartmann-Hahn condition [34]: $\gamma_H H_{1H} = \gamma_C H_{1C}$. This condition establishes the "thermal contact". The differences between the energy levels of the protons and the carbons are now equal in the doubly rotating frame. A fraction of the proton magnetization can thus be transferred to the carbon system by the flip-flop mechanism responsible for spin diffusion; protons get warmer while carbon-13 atoms are cooled. At equilibrium, the carbon magnetization can be written as

$$M_C \approx (\gamma_H/\gamma_C)(\gamma_C^2 \hbar^2 H_0 / 4 k T_L) \tag{7}$$

Thus the carbon magnetization is multiplied by a factor of about 4. Moreover, before repeating the pulse sequence, one has only to wait for near-equilibrium recovery of the proton magnetization. This is characterized by a spin-lattice relaxation time, $T_1(^1H)$, which is generally much shorter than $T_1(^{13}C)$ because of the efficiency of the spin diffusion mechanism between strongly coupled protons. The gain in sensitivity is thus accompanied by a gain in time.

Quantitative studies

During the thermal contact, the carbon-13 magnetization increases rapidly in an exponential growth characterized by the cross-polarization time T_{CH}, which is governed by the strength of the $^1H—^{13}C$ dipolar coupling. Simultaneously, the proton magnetization decreases according to a $T_{1\rho}(^1H)$ decay. In the absence of magnetization transfer, M_C, once established, would obey a $T_{1\rho}(^{13}C)$ decay.

The dependence of the carbon-13 magnetization as a function of the contact time t may be written [26] as

$$M_C = M_{OC}\,[1 - \exp(-\lambda t/T_{CH})]\exp[-t/T_{1\rho}(^1H)] \tag{8}$$

with $\lambda = 1 + (T_{CH}/T_{1\rho}(^{13}C)) - (T_{CH}/T_{1\rho}(^1H))$

Very often, in polymeric materials, $T_{CH} \ll T_{1\rho}(^1H)$ and $T_{1\rho}(^{13}C)$, and Eqn. 8 can be simplified to

$$M_C = M_{OC}\,[1 - \exp(-t/T_{CH})]\,\exp[-t/T_{1\rho}(^1H)] \tag{9}$$

Therefore, determination of the behaviour of the carbon-13 magnetization as a function of the contact time t allows the evaluation of the quantity M_{OC} which is proportional to the number of resonant ^{13}C spins, and thus facilitates quantitative measurements. The quantitative character of such determinations has been checked by several authors [35—38]. Difficulties arise for heterogeneous materials where the spin-lattice relaxation in the rotating frame is not simply described by a single relaxation time [39]. In the same way, overlap of carbon lines with very different T_{CH} renders the individual M_{OC} determinations difficult. Line-broadening mechanisms arising from molecular motions [40, 41] may also be a cause of poor quantitative reproducibility of the measurements. All these aspects have been discussed by Havens and Koenig [42].

Line-broadening mechanisms

Line-broadening mechanisms in glassy materials have been reviewed recently [43]. They may be of static or dynamic origin. In linear polymers, the static mechanisms, which arise from the bulk susceptibility of the sample, or from chemical-shift dispersions caused by packing effects, bond distortion and conformational inequivalence, induce only small effects [43]. In Fig. 1, the ^{13}C-n.m.r. spectrum of a linear polymer is compared with that of a cross-linked one. In the case of the cross-linked organic matrix, the chemical shift

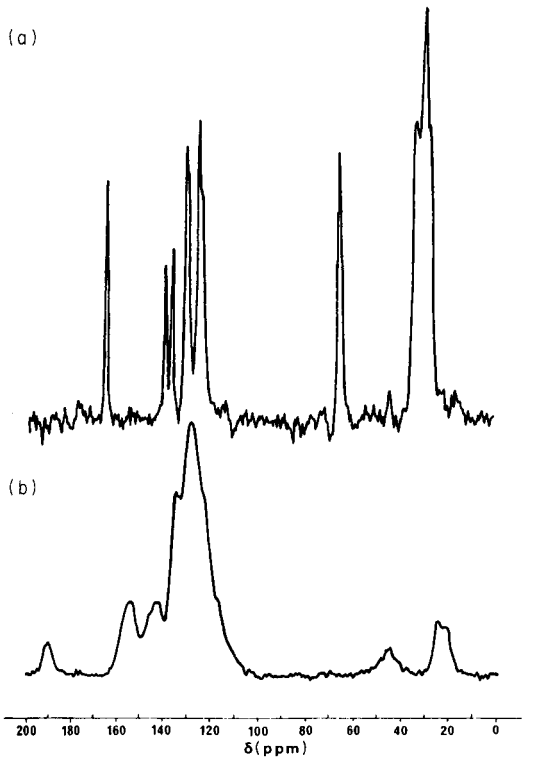

Fig. 1. Magic-angle spinning cross-polarization proton-dipolar decoupled ^{13}C-n.m.r. spectra (25 MHz): (a) a linear aryl-aliphatic polyester in bulk below its glass-transition temperature; (b) a cured PSP sample.

dispersions are much more important, of the order of 10 ppm: they reflect the variety of environments of a given functionality in a complex cross-linked compound and therefore they limit the resolution of the spectrum. In such cases, the use of model compounds greatly facilitates the interpretation of the spectra.

The dynamic line-broadening mechanisms result from molecular motions either with frequencies of the order of the rotor-spinning frequency or of the order of the high-power proton decoupling [40, 41]. In the first case, the broadening is due to the motional modulation of the shielding anisotropy. This is particularly important for carbons presenting a large shielding anisotropy and depends on the strength of the applied external magnetic field [40]. In the second case, the broadening arises from the motional modulation of the carbon-proton dipolar coupling and affects the strongly coupled protonated carbons [41].

Selective pulse sequences in high-resolution solid-state ^{13}C-n.m.r.

The selective pulse sequences in high-resolution solid-state ^{13}C-n.m.r. are based either on the difference in strength of the dipolar carbon—proton

couplings or on the difference in relaxation times, i.e., $T_1(^{13}C)$, $T_{1\rho}(^1H)$ [44, 45]. For example, the way to achieve selective observation of the protonated carbons (CH and CH_2) which, in the absence of molecular motions, are strongly coupled to protons, is to use a cross-polarization sequence with a very short contact time (10—20 μs). Under these conditions, only the strongly coupled carbons have enough time to cross-polarize.

Conversely, selective observation of the quaternary or methyl carbons, which have very weak coupling to protons, is possible by using the pulse sequence described by Opella and Frey [44]; this consists of a normal cross-polarization sequence with a short delay (50—100 μs) inserted between the ^1H—^{13}C contact and the data acquisition during which both carbon and proton radio-frequency fields are turned off. In the absence of irradiation, the CH and CH_2 carbon magnetizations are rapidly dephased because of the large proton—carbon dipolar interactions, while the magnetization of the quaternary and methyl carbons decays more slowly. Therefore the net result is selective observation of the latter carbons.

Carbon-13 n.m.r. study of polystyrylpyridine matrices

Polystyrylpyridine resins (PSP) are thermosetting matrices used in composite materials, which are stable at high temperature. They are obtained by reaction of terephthalic aldehyde with methyl derivatives of pyridine, usually collidine (2,4,6-trimethylpyridine) [46].

A fundamental study of the chemical reactions involved in the synthesis of these compounds has been done by Clavreul et al. [47] on model compounds. Two chemical reactions have been shown to occur during the first steps. First, the addition of a methyl group from the collidine molecule to the aldehyde function of terephthalic aldehyde is followed by the elimination of water:

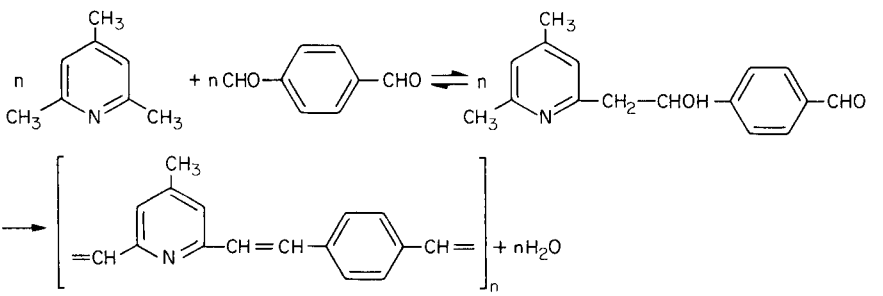

In a secondary cross-linking reaction, a collidine methyl group is added to the double bonds formed in the first process:

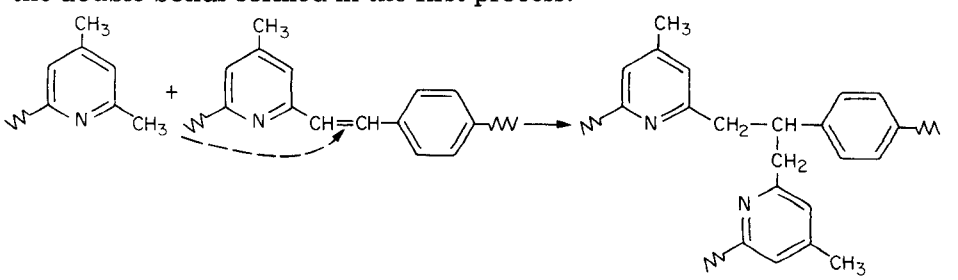

Though this addition mechanism is not the only reaction liable to occur, it appears to be the most favoured one [47]. The problem then consists of establishing to what extent these two mechanisms, which were deduced from model compounds, account for the reactions occurring during the curing of the PSP resins.

After the initial reaction stages, PSP resins are totally insoluble materials. The only available techniques allowing access to their chemical structure are Fourier-transform infrared spectroscopy and high-resolution solid-state ^{13}C-n.m.r. Results presented in this paper are concerned with the latter technique. However, as a preliminary to the solid-state investigation, the chemical shifts of the elementary units of the PSP networks were studied by ^{13}C-n.m.r. in solution on soluble model compounds and prepolymers.

EXPERIMENTAL

High-resolution ^{13}C-n.m.r. experiments in $CDCl_3$ or DMSO-d6 solution were conducted at 20 MHz and 62.9 MHz with a Varian CFT-20 spectrometer and a Bruker WP-250 spectrometer, respectively. Carbon-13 cross-polarization, proton dipolar decoupling and magic-angle spinning n.m.r. experiments were done at 25 MHz on a Bruker CXP-100 spectrometer, with quadrature detection and a single r.f. coil, which was double-tuned for both ^{13}C and ^{1}H. The matched spin-lock cross-polarization transfers used ^{13}C and ^{1}H magnetic field strengths of 50 kHz.

In the quantitative work, the PSP sample chemical composition was evaluated from a plot of the relative magnitude of the carbon magnetization as a function of the carbon—proton contact time. In all the spectra, spin-temperature inversion techniques were used to minimize baseline noise and roll [48]. Flip-back [49] was also used to shorten the delay time between two successive pulse sequences. Spinning experiments were done with boron nitride rotors at spinning speeds of 3.5 kHz. Depending on the sample, 2000—10 000 scans were needed to obtain a good signal-to-noise ratio.

Samples of PSP were prepared in bulk from terephthalic aldehyde and pure collidine in equimolar proportions, with *p*-toluene sulfonic acid as catalyst. The soluble prepolymer thus obtained is referred to as B251. The curing treatments undergone by the B251 prepolymer and the abbreviated names of the resulting PSP samples are described in Table 1.

RESULTS AND DISCUSSION

Study of PSP model compounds and prepolymers in solution by ^{13}C-n.m.r.

The formulae, abbreviations and chemical shifts of the model molecules representing the constituent units of the PSP resins obtained from the polycondensation and the cross-linking reactions are listed in Table 2.

TABLE 1

Curing treatments undergone by the PSP B251 prepolymer and leading to PSP samples under study

Sample	Curing treatment
PSP 1	3 h at 200°C
PSP 2	3 h at 200°C + 2 h at 250°C
PSP 3	3 h at 200°C + 16 h at 250°C
PSP 4	8 h at 200°C
PSP 5	8 h at 200°C + 2 h at 250°C
PSP 6	8 h at 200°C + 16 h at 250°C
PSP 7	8 h at 200°C + 48 h at 250°C

TABLE 2

Formulae, abbreviated names and ^{13}C chemical shifts of model compounds of PSP resins

Formula	Abbreviation	^{13}C chemical shifts (ppm/TMS)
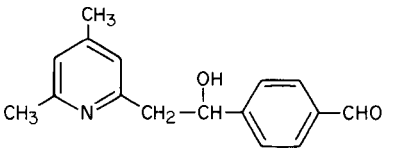	CT · H_2O	(CHOH): 73.0 (CH_2): 44.6
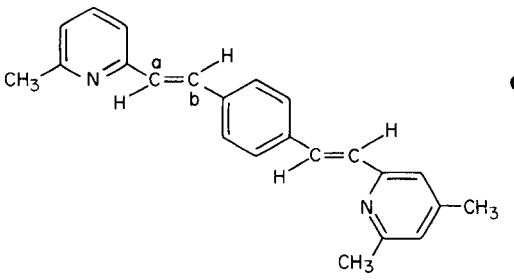	CTC	(CH_a): 128.6 (CH_b): 131.7
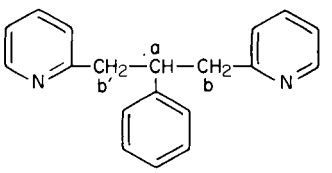	BP_2	(CH_a): 46.4 ($CH_{2b;b'}$): 44.9

The ^{13}C-n.m.r. spectrum of prepolymer B251, obtained at 62.9 MHz with proton decoupling (Fig. 2a) presents two interesting peaks, one at 72.8 ppm and the other at 44.8 ppm. The proton-coupled spectrum (Fig. 2b) recorded under quantitative conditions shows that the 72.8-ppm line is a doublet, corresponding to a CH carbon. The 44.8-ppm line appears as a triplet; it

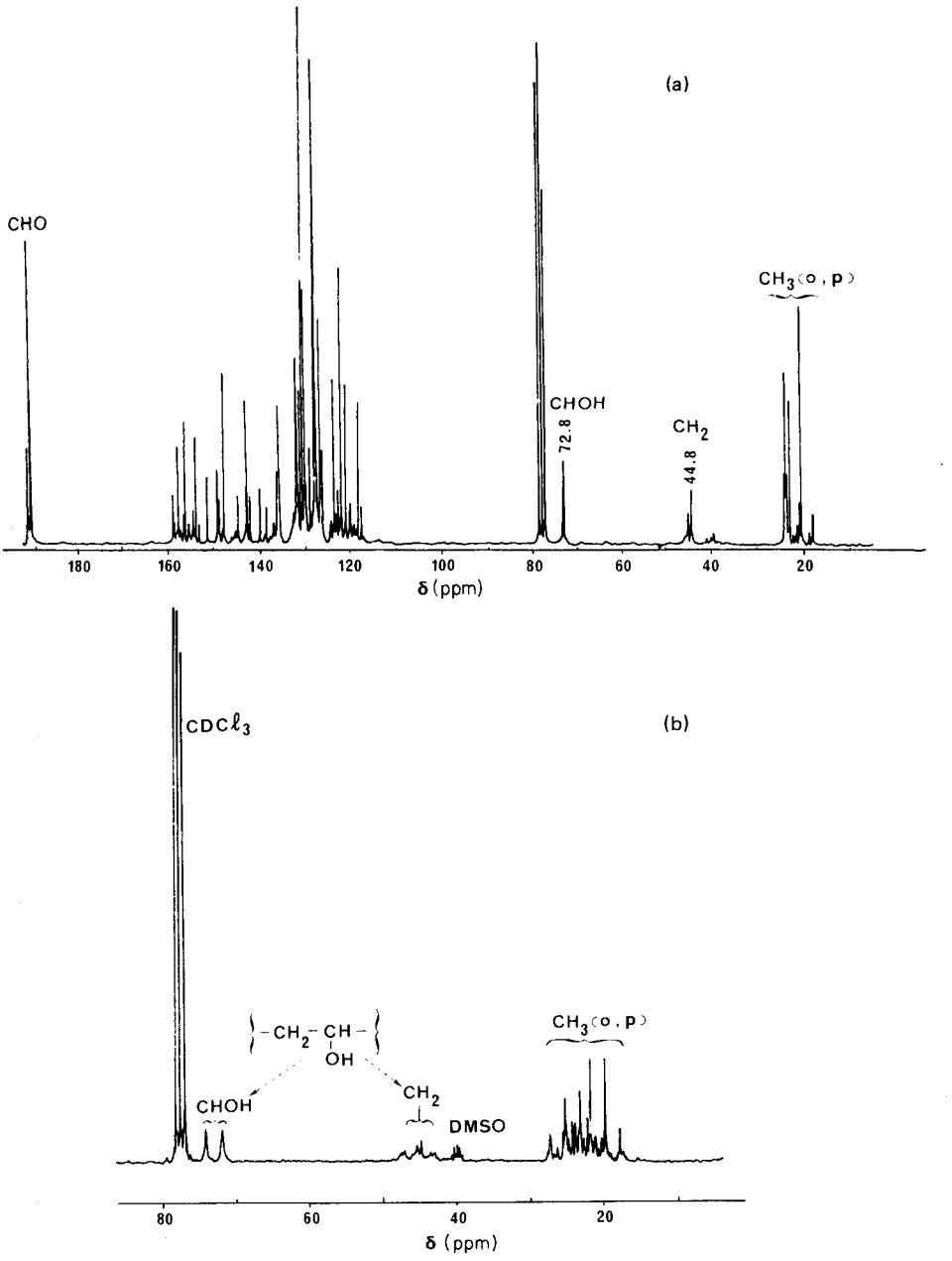

Fig. 2. ^{13}C-n.m.r. spectra (62.9 MHz) of B251 prepolymer in $CDCl_3$ solution (against TMS): (a) with proton scalar decoupling; (b) without proton scalar decoupling.

corresponds to a CH_2 carbon. Integration shows that the areas of the two lines (doublet and triplet) are equal. Therefore the two carbons belong to a $-CH_2-CHOH-$ sequence similar to that of the $CT \cdot H_2O$ molecule. This result indicates that the first stage of the polycondensation reaction has begun. Moreover, the absence of any doublet on the spectrum in the neighbourhood of 45 ppm indicates that the prepolymer does not undergo any aliphatic cross-linking.

Quantitative study of cured PSP resins by high-resolution solid-state ^{13}C-n.m.r.

A 25-MHz magic-angle spinning cross-polarization ^{13}C-n.m.r. spectrum of a typical PSP sample is shown in Fig. 3 together with stick spectra of the model molecules BP_2 and CTC. It should be noted that, at a resonance frequency of 25 MHz, a spinning speed of 3500 Hz is high enough to avoid the presence of noticeable spinning side-bands in the spectrum. The solid-state spectrum consists of several lines which were identified by comparison with the solution-state spectra of the model compounds and prepolymers and assigned from right to left, in order of decreasing magnetic field, as a composite line produced by the *p*- and *o*-collidine methyl carbons, a composite line corresponding to the CH and CH_2 of the cross-linking points, a broad line from the aromatic and ethylene carbons, and a line from the aldehyde carbons. The two aromatic

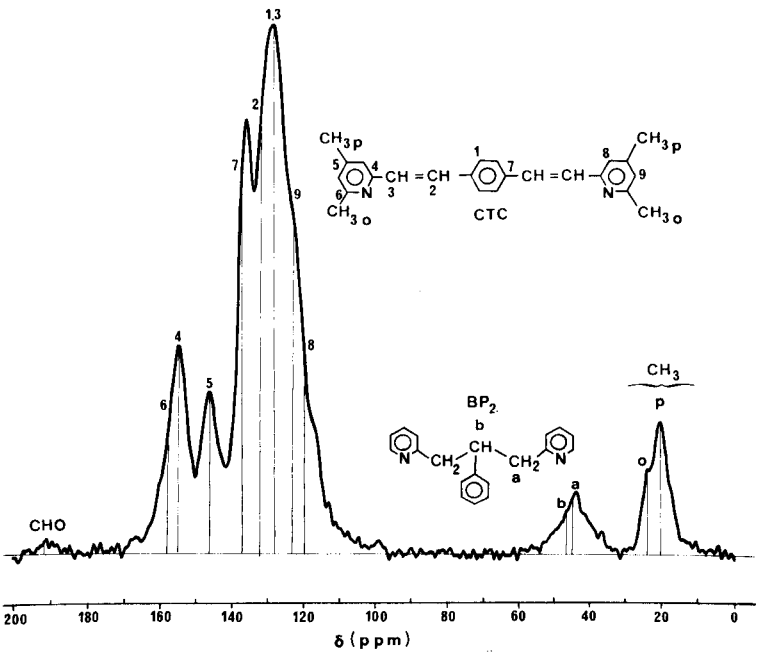

Fig. 3. Magic-angle spinning cross-polarization proton-dipolar decoupled ^{13}C-n.m.r. spectrum (25 MHz) and peak assignments of a cured PSP sample. Stick spectra are drawn from ^{13}C-n.m.r. spectra of the model compounds CTC and BP_2 in solution [47].

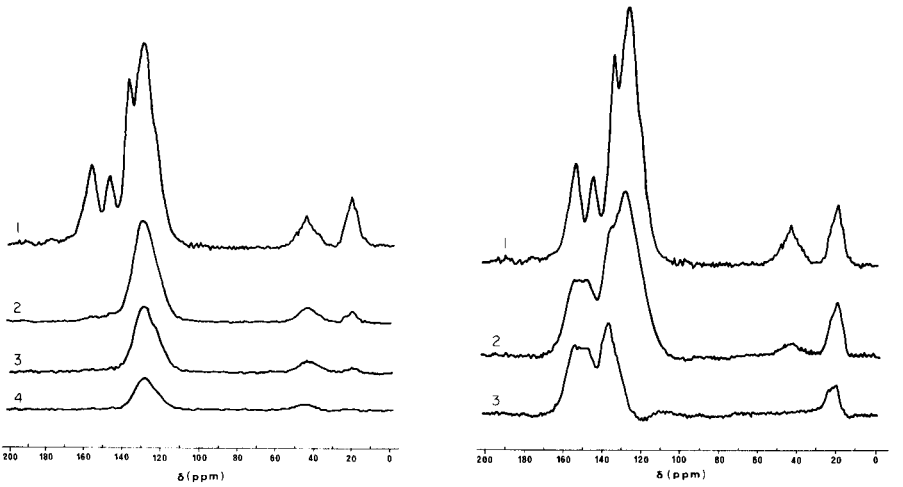

Fig. 4. Selective observation of the CH and CH_2 carbons in a cured PSP sample using cross-polarization with very short contact times: (1) 1 ms; (2) 40 μs; (3) 20 μs; (4) 10 μs.

Fig. 5. Selective observation of the quaternary and methyl carbons in a cured PSP sample using the sequence of Opella and Frey [44] and various delay times: (1) 0 μs; (2) 20 μs; (3) 50 μs.

peaks furthest left correspond to the three quaternary carbons of the pyridine ring. The spectral resolution is good enough to distinguish the separate contributions of the *o*- and *p*-methyl collidine carbons.

These assignments are supported by the selective observations of the CH and CH_2 carbons on the one hand and of the quaternary and methyl carbons on the other; cross-polarization spectra with very short contact times are shown in Fig. 4. On the 10-μs spectrum, only the CH and CH_2 lines are observed. Spectra on Fig. 5 were obtained by using the pulse sequence of Opella and Frey [44]. The 50-μs spectrum shows only the methyl and quaternary carbon peaks. It should be noted that all the observed signals belong to elementary units contained in the above model molecules and can be interpreted either in terms of poly-addition followed by water elimination or in terms of formation of cross-linkages as in the two reaction mechanisms outlined above.

In Fig. 6, the magic-angle spinning cross-polarization spectra (obtained with the optimum contact time of 1 ms) of PSP samples are plotted as a function of the curing parameters. They show qualitatively the decreasing amounts of aldehyde and methyl carbons and the increasing number of cross-linkages. The aldehyde carbons are still observed in the spectrum of PSP cured for 48 h. Moreover the *o*- and *p*-methyl groups in collidine show different reactivities; the *o*-methyl groups react first, whereas the reaction of the *p*-methyl groups becomes noticeable only when most of the *o*-methyl groups have disappeared.

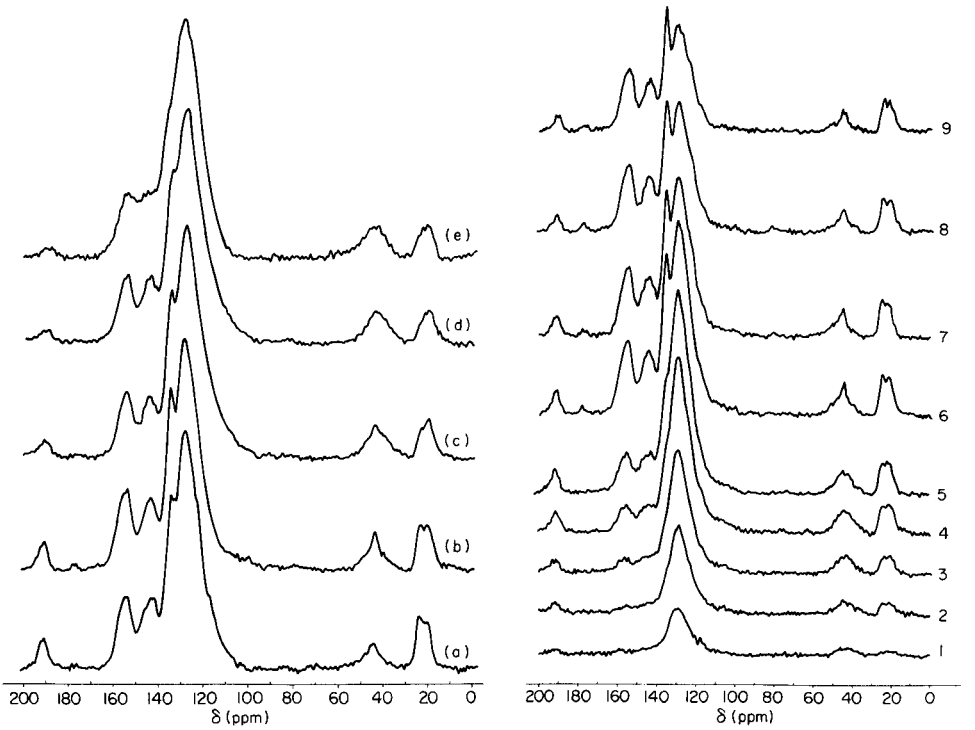

Fig. 6. Magic-angle spinning cross-polarization proton-dipolar decoupled ^{13}C-n.m.r. spectra (25 MHz) of PSP samples as a function of the curing parameters (contact time, 1 ms): (a) PSP 1; (b) PSP 4; (c) PSP 5; (d) PSP 6; (e) PSP 7.

Fig. 7. Evolution of ^{13}C-n.m.r. spectra for a cured PSP as a function of contact time, t (in ms): (1) 0.1; (2) 0.3; (3) 0.5; (4) 0.8; (5) 1; (6) 3; (7) 5; (8) 7; (9) 9 ms.

The chemical composition of the PSP resins was studied quantitatively, as described in the relevant section above. The evolution of a PSP spectrum as a function of the contact time (t) is shown in Fig. 7. The evolution of the individual carbon magnetizations as a function of contact time is plotted in Fig. 8. It can be seen that the long-time magnetization decays measured for each carbon are mono-exponential and described by the same $T_{1\rho}(^1H)$, indicating a homogeneous material on the scale of the experiment. Experimental curves were fitted to an expression of the type given in Eqn. 9 and M_{OC} was calculated for each carbon. The number of pyridine rings, which is not modified by the chemical reactions involved, can be considered as an internal reference and estimated from the two peaks furthest left among the aromatic lines. Here, x_{CH_3}, x_{CHO} and x_{cl} are defined as the number of methyl (*o*- and *p*-groups), aldehyde and aliphatic cross-linking elements respectively per 100 pyridine rings and D_{CH_3}, D_{CHO} and D_{cl} as their variations from one curing stage to the next. Results of the quantitative n.m.r. experiments are listed in

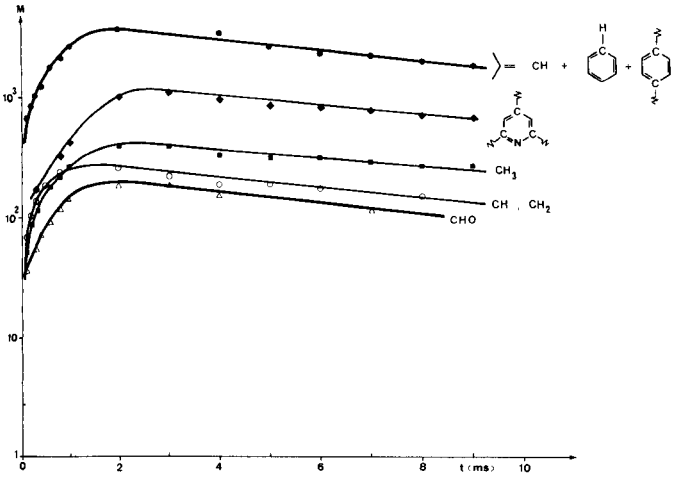

Fig. 8. Evolution of carbon magnetizations in a cured PSP sample as a function of the contact time t.

TABLE 3

Number of methyl, aldehyde and cross-linking groups per 100 pyridine cycles in PSP samples studied

PSP sample	x_{CHO}	D_{CHO}	x_{CH_3}	D_{CH_3}	x_{cl}	D_{cl}
PSP B251	145		230		0	
PSP 1	61	84	109	121	24	24
PSP 2	28	33	62	47	25	1
PSP 3	20	8	55	7	28	3
PSP 4	40	105	93	137	26	26
PSP 5	29	11	83	10	32	6
PSP 6	27	2	77	6	34	2
PSP 7	25	2	67	10	41	7

Table 3. Within experimental error, from one curing step to the next, the variations of the relative numbers of the various functionalities obey the relationship $-D_{CH_3} = -D_{CHO} + D_{cl}$, which indicates that the loss of methyl groups is mainly obtained via the two mechanisms, polycondensation and cross-linking, observed for the initial stages of the synthesis [47].

The different reactivities of the *o*- and *p*-collidine methyl groups were studied quantitatively by decomposing the composite methyl carbon line into two separate peaks at 20 ppm and 24 ppm, accounting for the *p*- and *o*-methyl carbons, respectively. Results are shown in Table 4. They are similar to those obtained on small monofunctional model molecules for which *o*-methyl groups were found to be much more reactive than *p*-methyl groups [47].

TABLE 4

Number of ortho- and para-methyl groups per 100 pyridine cycles in PSP samples

PSP sample	PSP 4	PSP 5	PSP 6	PSP 7
No. of o-CH_3 groups	35	22	18	19
No. of p-CH_3 groups	58	61	59	48

Conclusion

The chemical evolution of the polystyrylpyridine resins as a function of the duration and temperature of the curing treatment can be followed qualitatively using dipolar-decoupling, magic-angle spinning and cross-polarization ^{13}C-n.m.r. at 25 MHz. From the variations of the carbon magnetizations as a function of the contact time in the cross-polarization sequence, it is possible to obtain quantitative data on the chemical composition of these insoluble materials. Results thus obtained are interpreted in terms of two chemical reactions involving first the addition of a methyl group of the collidine molecule to the aldehyde function of terephthalic aldehyde followed by the elimination of water, and secondly a cross-linking reaction consisting of the addition of a collidine methyl group to the double bonds formed in the first process. The high resolution of the n.m.r. spectra enables the different reactivities of the o- and p-methyl substituents of the collidine molecule to be observed. p-Methyl reactions occur mainly when most of the o-methyl groups have disappeared. Thus, high-resolution solid-state ^{13}C-n.m.r. provides precise characterization of the polystyrylpyridine resins in terms of both their quantitative chemical composition and their formative reactions.

REFERENCES

1 A. Pines, M. G. Gibby and J. S. Waugh, J. Chem. Phys., 59 (1973) 569.
2 E. R. Andrew, Prog. Nucl. Magn. Reson. Spectrosc., 8 (1971) 1.
3 J. Schaefer, E. D. Stejskal and R. Buchdahl, Macromolecules, 10 (1977) 384.
4 G. E. Maciel, I.-S. Chuang and G. E. Myers, Macromolecules, 15 (1982) 1218.
5 C. A. Fyfe, A. Rudin and W. J. Tchir, Macromolecules, 13 (1980) 1320.
6 R. L. Bryson, G. R. Hatfield, T. A. Early, A. R. Palmer and G. E. Maciel, Macromolecules, 16 (1983) 1669.
7 C. A. Fyfe, M. S. McKinnon, A. Rudin and W. J. Tchir, Macromolecules, 16 (1983) 1216.
8 C. A. Fyfe, M. S. McKinnon, A. Rudin and W. J. Tchir, J. Polym. Sci., Polym. Lett. Ed., 21 (1983) 249.
9 S. So and A. Rudin, J. Polym. Sci., Polym. Lett. Ed., 23 (1985) 403.
10 G. E. Maciel, N. M. Szeverenyi, T. A. Early and G. E. Myers, Macromolecules, 16 (1983) 598.
11 I.-S. Chuang, G. E. Maciel and G. E. Myers, Macromolecules, 17 (1984) 1087.
12 G. E. Maciel, I.-S. Chuang and L. Gollob, Macromolecules, 17 (1984) 1081.
13 A. N. Garroway, W. B. Moniz and H. A. Resing, ACS Symp. Ser., 103 (1979) 67.
14 A. N. Garroway, W. B. Moniz and H. A. Resing, Faraday Symp. Chem. Soc., 13 (1979) 63.

15 A. N. Garroway, W. B. Moniz and H. A. Resing, Am. Chem. Soc., Div. Org. Coat. Plast., Chem. Prepr., 36 (1976) 133.
16 A. N. Garroway, W. M. Ritchey and W. B. Moniz, Macromolecules, 15 (1982) 1051.
17 R. K. Harris, K. J. Packer and B. J. Say, Makromol. Chem., Suppl., 4 (1981) 117.
18 A. N. Garroway, D. L. VanderHart and W. L. Earl, Philos. Trans. R. Soc. London, Ser. A, 299 (1981) 609.
19 R. K. Harris, K. J. Packer, A. G. Oliver and B. J. Say, in F. Conti (Ed.), Proc. Eur. Conf. NMR Macromol., Lerici, Rome, 1978, p. 29.
20 A. Cholli, W. M. Ritchey and J. Koenig, Am. Chem. Soc. Org. Coat. Appl. Polym. Sci. Proc., 48 (1983) 450.
21 M. F. Grenier-Loustalot, F. Cazaux, J. Berecoechea and P. Grenier, Eur. Polym. J., 20 (1984) 1137.
22 M. D. Sefcik, E. O. Stejskal, R. A. McKay and J. Schaefer, Macromolecules, 12 (1979) 423.
23 A. C. Wong, A. N. Garroway and W. M. Ritchey, Macromolecules, 14 (1981) 832.
24 I.-S. Chuang, B. L. Hawkins, G. E. Maciel and G. E. Myers, Macromolecules, 18 (1985) 1482.
25 F. Bloch, Phys. Rev., 111 (1958) 841.
26 M. Mehring, NMR Basic Principles and Progress, Vol. 11, Springer Verlag, Berlin, 1976.
27 J. Herzfeld and A. Berger, J. Chem. Phys., 73 (1980) 6021.
28 W. T. Dixon, J. Chem. Phys., 77 (1982) 1800.
29 E. T. Olejniczak, S. Vega and R. G. Griffin, J. Chem. Phys., 81 (1984) 4804.
30 N. Zumbulyadis, P. M. Henrichs and R. H. Young, J. Chem. Phys., 75 (1982) 1603.
31 A. Naito, S. Ganapathy and C. A. McDowell, J. Chem. Phys., 74 (1981) 5393.
32 J. C. Hexem, M. H. Frey and S. J. Opella, J. Am. Chem. Soc., 103 (1981) 224.
33 M. M. Maricq and J. S. Waugh, J. Chem. Phys., 70 (1979) 3300.
34 S. R. Hartmann and E. L. Hahn, Phys. Rev., 128 (1962) 2042.
35 C. A. Fyfe, J. R. Lyerla, W. Volksen and C. S. Yannoni, Macromolecules, 12 (1979) 757.
36 H. A. Resing, A. N. Garroway and R. N. Hazlett, Fuel, 57 (1978) 450.
37 G. E. Maciel, V. J. Bartuska and F. P. Miknis, Fuel, 58 (1979) 391.
38 H. L. Retcofsky and D. L. VanderHart, Fuel, 57 (1978) 421.
39 W. L. Earl and D. L. VanderHart, Macromolecules, 12 (1979) 762.
40 D. Suwelack, W. P. Rothwell and J. S. Waugh, J. Chem. Phys., 73 (1980) 2559.
41 W. P. Rothwell and J. S. Waugh, J. Chem. Phys., 74 (1981) 2721.
42 J. R. Havens and J. L. Koenig, Appl. Spectrosc., 37 (1983) 226.
43 D. L. VanderHart, W. L. Earl and A. N. Garroway, J. Magn. Reson., 44 (1981) 361.
44 S. J. Opella and M. H. Frey, J. Am. Chem. Soc., 101 (1979) 5854.
45 R. S. Aujla, R. K. Harris, K. J. Packer, M. Parameswaran, B. J. Say, A. Bunn and M. E. A. Cudby, Polym. Bull., 8 (1982) 2353.
46 M. Ropars and B. Bloch, French Patents no. 2261296 and 2261297 (1974).
47 R. Clavreul, B. Bloch, M. Brigodiot and E. Maréchal, Makromol. Chem., 187 (1986) in press.
48 E. D. Stejskal and J. Schaefer, J. Magn. Reson., 18 (1975) 560.
49 J. Tegenfeldt, U. Haeberlen and J. S. Waugh, J. Magn. Reson., 36 (1979) 453.

Analytica Chimica Acta, 189 (1986) 135—143
Elsevier Science Publishers B.V., Amsterdam — Printed in The Netherlands

MACROMOLECULAR DYNAMICS AND FREE VOLUME IN POLYMER MELTS

A. D. ENGLISH*

Central Research and Development Department, E. I. du Pont de Nemours and Company, Experimental Station, Wilmington, DE 19898 (U.S.A.)

P. ZOLLER

Department of Mechanical Engineering, University of Colorado, Boulder, CO 80309 (U.S.A.)

(Received 14th April 1986)

SUMMARY

The temperature dependence of the excess free volume, derived from the quasi-lattice theory of Simha and Somcynsky, above the glass-transition temperature for the noncrystalline component of four semicrystalline polymers [polyoxymethylene, poly(ethyleneterephthalate), polyethylene, and nylon-66] is used to facilitate the interpretation of ^{1}H-n.m.r. data. This method gives values for the crystalline content that agree well with values obtained by other methods. The correlation between the excess free volume of the quasi-lattice and the segmental mobility of the noncrystalline component above the glass-transition temperature is discussed.

Macromolecules have been investigated with nuclear magnetic resonance techniques virtually since the discovery of nuclear magnetic resonance (n.m.r.) [1]. These initial investigations were concerned with the origin of the temperature dependence of the widths of n.m.r. lineshapes. The presence of both broad and narrow components in the lineshapes of semicrystalline polymers has been attributed to the relatively rigid crystalline component and the relatively mobile noncrystalline component, respectively. The relatively mobile fraction is differentiated from the less mobile fraction by the presence of either faster or larger amplitude motions that more effectively average some nuclear spin interaction (dipolar, chemical shift). Nearly all conventional n.m.r. studies [2—4], as well as dielectric and anelastic studies, have focused on local modes of motion that are characterized by a relatively slow rate (the temperature dependence of which is measured) and an amplitude with a temperature dependence that is assumed to be unimportant. Motions that can be characterized as being rapid on the n.m.r. time scale above 100 K and that have an increasing amplitude with increasing temperature have been recognized as a possibility for some time [2] and identified as being important more recently [5—8] for the averaging of nuclear spin interactions. Both types of motions have been observed with modern n.m.r.

0003-2670/86/$03.50

methods in a variety of semicrystalline polymers: polytetrafluoroethylene [6], polyethylene [7], poly(ethyleneterephthalate) [9], etc. The latter types of motion are identified as the dominant factor in determining the temperature dependence of the n.m.r. lineshapes, especially above the glass-transition temperature, via the concomitant observation of a narrowing of the dipolar lineshape and the monotonic decrease of spin-lattice relaxation times (T_1, $T_{1\rho}$) [9]. These motions are thought to be responsible for a substantial portion of the observed temperature dependence of not only the n.m.r. spin interactions, but also the nonspecific manner in which the modulus decreases with temperature (see below).

Results presented here demonstrate that the types of motion characterized by a growth in amplitude with temperature are substantially responsible for the mobility, as observed by n.m.r., of the noncrystalline component for many semicrystalline polymers. Further, it is shown that the temperature dependence of the excess free volume of a polymer melt obtained from the Simha-Somcynsky [10, 11] equation of state can be used to interpret the temperature dependence of the ^{1}H-n.m.r. lineshapes and ultimately to identify the amount of noncrystalline component present. Additionally, the identification of a relationship between the equilibrium properties and segmental dynamics of a polymer melt reveals the possibility of yet another method for estimating the glass-transition temperature in semicrystalline polymers.

EXPERIMENTAL

The ^{1}H-n.m.r. data were acquired at 200 MHz with a MSL 200 n.m.r. spectrometer (Bruker Instruments) with a $\pi/2$ radiofrequency pulse length of 2 μs, a 4-μs blanking time before data acquisition, and repetition times larger than three times the spin-lattice relaxation times at all temperatures. Data on pressure, volume and temperature were acquired either with an apparatus previously described [12] or a newer commercial version of the apparatus (Gnomix Research, Boulder, CO). The polymers were as-polymerized polyoxymethylene ($M_n \approx 4 \times 10^4$) melt-crystallized poly(ethylene terephthalate) ($M_n \approx 3 \times 10^4$), as-polymerized polyethylene ($M_w \approx 3 \times 10^6$), and melt-recrystallized nylon-66 ($M_n \approx 1.7 \times 10^4$). All polymers were dried for 40—60 h in a vacuum oven with a nitrogen bleed at 100°C; residual water content was less than 0.2% by weight as determined by thermogravimetry. Differential scanning calorimetry (d.s.c.) was done with 5 mg of sample at a heating rate of 20°C min^{-1} on a Mettler TA-3000 instrument.

RESULTS

Definition of the fraction of a semicrystalline polymer that is "mobile" in a conventional n.m.r. experiment depends substantially on temperature. As is illustrated in Fig. 1, the ^{1}H-n.m.r. spectra of as-polymerized polyoxymethylene vary not only in the fraction of narrow component in the line-

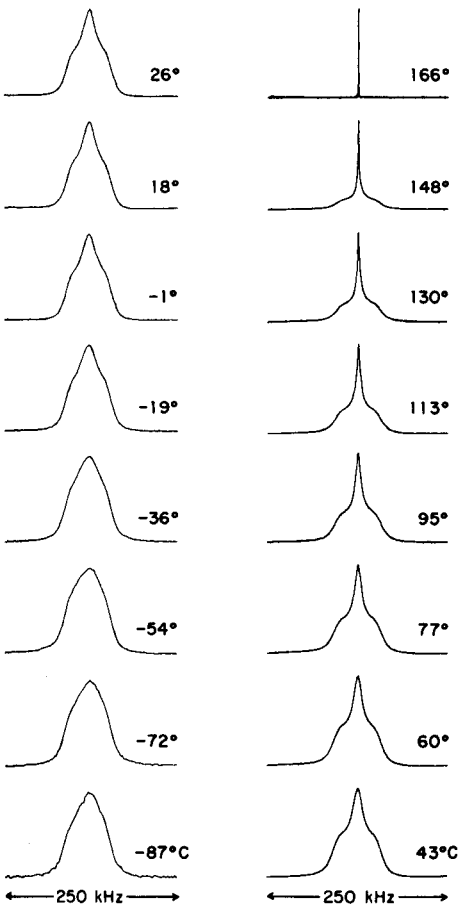

Fig. 1. ^{1}H-n.m.r. spectra (200 MHz) of as-polymerized polyoxymethylene as a function of temperature (°C).

shape ("mobile spins") but also in the ease with which a narrow lineshape can be differentiated from the broad lineshape. The less mobile spins have a near Gaussian lineshape and the more mobile spins have a near Lorentzian lineshape above about 60°C. The relative amounts and the temporal character of the two components in the lineshape can be measured in the time domain and thus the relative amount of mobile material (δ) can be determined [13]. The temperature dependence of the relative amount of mobile material is given in Table 1, which shows a monotonic increase with temperature; the highest temperature for which δ is measured is fixed by the temperature at which the smallest crystallites begin to melt (T_{max}) as observed by differential scanning calorimetry.

TABLE 1

Temperature dependence of the mobile fraction (δ) as observed by ^{1}H-n.m.r. in polyoxymethylene

Temp. (°C)	60	77	95	113	130	148
δ	0.20	0.23	0.26	0.28	0.30	0.33

Table 2 shows that the fraction of immobile material ($1-\delta$) in polyoxymethylene (POM) as determined from ^{1}H-n.m.r. agrees with other methods if T_{max} is chosen as the reference temperature. This agreement indicates that all of the noncrystalline component can undergo sufficiently large amplitude motions to be distinguished from the crystalline component before any of the crystallites melt. Data in Table 2 show similarly good agreement between ($1-\delta$) at T_{max} and other measures of crystallinity for polyethylene (PE). The fortuitous nature of this agreement between ($1-\delta$) at T_{max} and the crystalline content as observed by other methods for POM and PE is illustrated by the data for poly(ethylene terephthalate) (PET) and nylon-66. In these cases, the ($1-\delta$) values at T_{max} give values of crystallinity that sharply disagree with values of crystallinity measured by other methods: PET [($1-\delta$) = 82%, 55% crystalline] and nylon-66 [($1-\delta$) = 67%, 45% crystalline]. This disagreement is not uncommon and is the motivation for examining other methods of examining the temperature dependence of δ to extract a meaningful value for the crystalline content of the polymer.

DISCUSSION

In a high-molecular-weight macromolecule, essentially all degrees of freedom can be identified with vibrations. In the solid state, a large number of

TABLE 2

Crystallinity values obtained by various methods

Polymer	$(1-\delta)^a$ (%)	T_{max}	$(1-\delta_0)$ (%)	T_o (K)	$T_g{}^b$ (K)	Crystallinity (%)
POM	67	148	62	277	198	56—67[c] 69[d]
PET	82	238	55	421	343	53[e] 58[f]
PE	75	103	68	253	?	76[g]
Nylon-66	67	220	49	368	323	45[h]

[a]At T_{max}. [b]Values for T_g from [14]. [c]D.s.c. (ΔH_f = 78 cal g^{-1} [15] or 93 cal g^{-1} [16] for 100% crystallinity). [d]^{13}C-n.m.r. (unpublished results). [e]Wide-angled x-ray scattering. [f]D.s.c. (ΔH_f = 32.5 cal g^{-1} for 100% crystallinity [17]). [g]D.s.c. (ΔH_f = 70 cal g^{-1} for 100% crystallinity [18]). [h]D.s.c. (ΔH_f = 45.5 cal g^{-1} for 100% crystallinity [19]).

the vibrations can be identified with simple modes of motion (single bond stretching, simple bending modes, torsions), but a significant fraction is identified with relatively large-amplitude vibrations which usually have a large reduced mass, a small force constant, and consequently a low frequency. Some large-amplitude vibrations mainly involve motion of only a few atoms (e.g., methylene, phenyl or carbonyl groups) and it is these modes of motion that can be characterized by solid-state n.m.r. methods. The presence of these motions enables n.m.r. to characterize semicrystalline polymers in terms of the relative amounts of mobile and immobile material [2]. The difficulty of identifying each component of the lineshape with some combination of crystalline and noncrystalline material is illustrated by the present results. Even in the most simplistic case of a two-phase model, with no allowance for other subtleties (interfacial material, taut loops, etc.), the amount of noncrystalline material observed in each component of the lineshape at some arbitrary temperature is not obvious.

At temperatures well below the glass-transition temperature, essentially all the modes of motion are either sufficiently slow or are of sufficiently small amplitude so as not to average the nuclear dipole—dipole interactions for most macromolecules. As the temperature is increased, specific modes of motion (methylene trans—gauche isomerization, phenyl ring flipping, etc.) begin to have frequency components similar to the strength of the dipolar interactions and average some of these interactions and thus line-narrowing is observed. These specific modes of motion can be related to changes observed in mechanical properties [14]. In some cases, such as polytetrafluoroethylene, the specific relaxations have been definitively identified [6] and correspond to large changes in the modulus of the material [14]. However, in most cases the activation of specific modes of motion has a minute effect on the mechanical properties; for example, specific modes of motion have been identified in PET [9] but their effect upon the modulus [14] is very small. Thus, in most cases there must exist some other class of motions that relate to the mechanical properties. The present results indicate that these modes of motion are large-amplitude vibrations and are responsible for the weak temperature dependence of the modulus.

At temperatures well above the glass-transition temperature, the n.m.r. lineshape of a semicrystalline polymer will have contributions from narrow and broad components. As the temperature increases, the broad component becomes less intense and the narrow component becomes more intense. At temperatures well below the melting point, the narrow component will contain contributions nearly exclusively from the noncrystalline component (disregarding oligomers and impurities) and the broad component will contain contributions from the crystalline component and that portion of the noncrystalline component that can not execute sufficiently fast or large enough amplitude motions to average the dipolar interactions significantly. (Observation of a narrow component in the n.m.r. spectrum of an abundant spin system requires that the nuclear spin interaction in some component be

averaged by a motional process to a smaller value than that observed in the static case; additionally, the residual static dipolar interaction must be sufficiently small to suppress spin diffusion or only one component, reflecting the averaged lineshape, will be observed.) The relative intensities of the two components should agree semiquantitatively with other measures of crystallinity if a temperature exists that is both below the melting point of the smallest crystallites (T_{max}) and is sufficiently high that all of the noncrystalline component can undergo sufficient motion to yield a narrow lineshape. As the data in Table 2 show, T_{max} is sufficiently high for POM and polyethylene to give a reasonable value for the crystallinity from the n.m.r. data, but T_{max} is not high enough for PET or nylon-66 to allow all noncrystalline material to contribute to the narrow lineshape. It is this difficulty that motivates the present use of information available from other physical methods to interpret the n.m.r. data.

Previous efforts [20] to use thermophysical data to aid in the interpretation of conventional n.m.r. spectra have centered on the idea that above some temperature (T_0) there exists sufficient free volume in the lattice to permit some fraction of the material (δ) to become more mobile; at sufficiently high temperatures, all noncrystalline material (δ_0) becomes sufficiently mobile to be differentiated from the crystalline material and the form by which δ approaches δ_0 is governed by the thermal expansion coefficient: and is

$$\delta = \delta_0 \exp \{-[\gamma V_{fkr}/(\alpha V_m(T - T_0))]\} \quad (1)$$

The ratio V_{fkr}/V_m is the excess free volume at T_0, α is the thermal expansion coefficient, and γ is a fitting parameter. This approach has had limited success [9]. An alternative formulation is presented here and is evaluated with more precise data on the temperature dependence of the excess free volume [$(1 - y) \equiv \psi$] as obtained from the Simha-Somcynsky equation of state analysis of pressure, volume and temperature (PVT) data [21]. Analyses of PVT data for PET [22], POM, polyethylene [23] and nylon-66 yielded values of the reducing parameters (T^*, V^* as K, $cm^3\ g^{-1}$) of (11710, 0.7408), (11024, 0.7686), (9772, 1.1417), and (11470, 0.8935), respectively; the reducing parameters were then used to calculate the excess free volume (ψ) as a function of temperature at zero pressure [10, 11]. Values of ψ as a function of temperature are given in Table 3. The excess free volume increases monotonically with temperature, whereas the temperature dependence of δ must be sigmoidal. It is proposed that there exists some value of ψ [e.g., $\psi(T_0)$] below which δ is zero and above which δ will increase to a plateau value of δ_0; such a relationship may be expressed as

$$\delta(T) = \delta_0\langle 1 - \exp \{-[[\psi(T) - \psi(T_0)]/\psi(T_0)]\}\rangle \quad (2)$$

Figure 2A illustrates the relative insensitivity of δ_0 to the value of T_0 used in fitting the data for polyoxymethylene; however, the value of T_0 is uniquely determined by the data. Figures 2B and C show the results of fitting the n.m.r.

TABLE 3

Simha-Somcynsky excess free volume at $P = 0$

Temperature (K)	Excess free volume			
	PET	POM	Nylon-66	PE
160				0.0025
200		0.0069		0.0158
240	0.0159	0.0218		0.0357
280	0.0323	0.0401	0.0348	0.0577
320	0.0505	0.0597	0.0536	0.0808
360	0.0693	0.0802	0.0730	0.1046
400	0.0889	0.1013	0.0931	0.1289
440	0.1089	0.1228	0.1136	
480	0.1292		0.1344	
520	0.1499		0.1555	

data for PET and nylon-66 to Eqn. 2 with the values of $\psi(T)$ given in Table 3; the values of T_0 and δ_0 found are given in Table 2.

The results given in Table 2 for the determination of $(1 - \delta_0)$ illustrate that the crystallinity values derived from the n.m.r. data by this method are in reasonable agreement with other methods for all four polymers. This agreement indicates that above the glass-transition temperature a correlation exists between the temperature dependence of the fraction of material that is characterized by n.m.r. as being mobile and the temperature dependence of the excess free volume in a polymer melt.

Values of T_0 found for the four polymers from fitting Eqn. 2 are all substantially above T_g. The large difference between T_0 and the glass-transition temperature (T_g) is expected because T_0 is the temperature at which some local molecular segment is able to execute a motion that is of sufficiently large amplitude ($\approx 20°$) to average the dipolar interaction enough ($\approx 10\%$) so that the mobile spins are differentiated from the immobile spins. Lastly, the adventurous might suggest that the values of $(T_g - T_0)$ given for POM, PET, and nylon-66 would indicate that the glass-transition temperature of polyethylene lies in the range of 190 ± 20 K. This relationship is similar to a method of estimating an upper bound for the glass-transition temperature from scalar decoupled ^{13}C-n.m.r. spectra [24, 25].

Conclusions

The temperature dependence of the excess free volume above the glass-transition temperature for the noncrystalline component of four semicrystalline polymers (POM, PET, PE, nylon-66) was used to facilitate the interpretation of ^{1}H-n.m.r. data. This gave a value for the crystalline content that is in good agreement with values obtained by other methods. The method also provides a value of T_0, which suggests a method for estimating the glass-

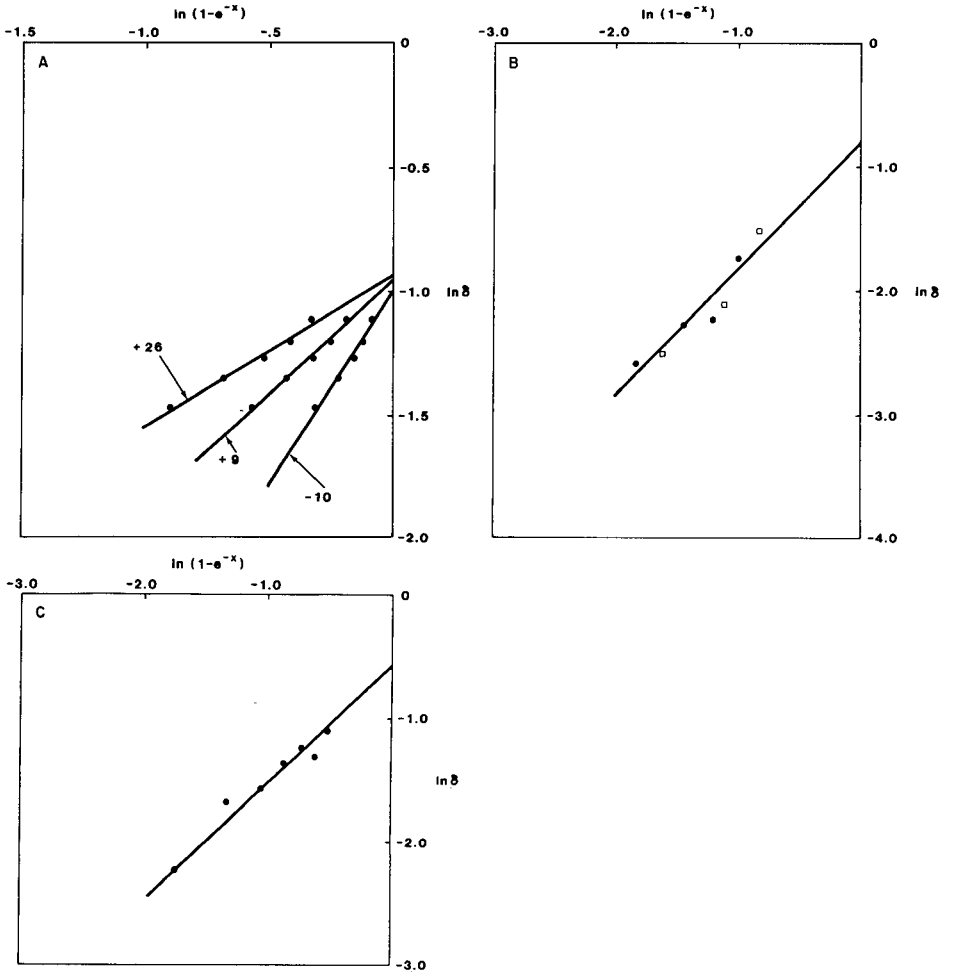

Fig. 2. Graphical representations of ln δ vs. ln $(1 - e^{-x})$ where $x = \psi(T) - \psi(T_0)/\psi(T_0)$ for different polymers: (A) as-polymerized polyoxymethylene at T_0 values of 26°C, 9°C and −10°C; (B) melt-recrystallized PET with T_0 = 421 K (closed circles are data from this work and open squares are data from previous work [9]); (C) melt-recrystallized nylon-66 with T_0 = 368 K.

transition temperature. Lastly, the success of the method reflects a correlation between the segmental mobility and the excess free volume of the quasi-lattice of the noncrystalline component above the glass-transition temperature. This correlation is consistent with large amplitude motions, that have a weak temperature dependence to their amplitude, giving rise to the weak dependence of modulus upon temperature for many polymers.

REFERENCES

1 N. L. Alpert, Phys. Rev., 72(1) (1947) 637.
2 D. W. McCall and E. W. Anderson, J. Polym. Sci., Part A, 1 (1963) 1175.
3 W. P. Slichter and D. D. Davis, J. Appl. Phys., 34 (1963) 98.
4 V. J. McBrierty and D. C. Douglas, J. Poly. Sci., Part D, 16 (1981) 295.
5 J. P. Cohen-Addad, J. Chem. Phys., 60 (1974) 2440.
6 A. J. Vega and A. D. English, Macromolecules, 13 (1980) 1635.
7 H. W. Spiess, Advances in Polymer Science, 66, Springer-Verlag, Berlin, 1985, pp. 23ff.
8 A. D. English, Macromolecules, 18 (1985) 178.
9 A. D. English, Macromolecules, 17 (1984) 2182.
10 R. Simha and T. Somcynsky, Macromolecules, 2 (1969) 342.
11 R. Simha, Macromolecules, 10 (1977) 1025.
12 P. Zoller, P. Bolli, V. Pahud and H. Ackermann, Rev. Sci. Instrum., 47 (1976) 948.
13 L. B. Schreiber and R. W. Vaughan, J. Catal., 40 (1975) 226.
14 N. G. McCrum, B. E. Read and G. Williams, Inelastic and Dielectric Effects in Polymeric Solids, Wiley, New York, 1967.
15 J. Bandrup and E. H. Immergut (Eds.), Polymer Handbook, 2nd edn., Wiley, New York, 1975, p. V-66.
16 H. W. Starkweather, P. Zoller and G. A. Jones, J. Polym. Sci. Polym. Phys. Ed., (1987) in press.
17 H. W. Starkweather, P. Zoller and G. A. Jones, J. Polym. Sci. Polym. Phys. Ed., 21 (1983) 295.
18 B. Wunderlich, Macromolecular Physics, Vol. 3, Academic Press, New York, 1980, p. 48.
19 H. W. Starkweather, P. Zoller and G. A. Jones, J. Polym. Sci. Polym. Phys. Ed., 22 (1984) 1615.
20 U. Eichhoff and H. G. Zachmann, Ber. Bunsenges. Phys. Chem., 74 (1970) 919.
21 P. Zoller, PVT Relationships and Equations of State of Polymers, Polymer Handbook, 3rd edn., Wiley, New York, in press.
22 P. Zoller and P. Bolli, J. Macromol. Sci. Phys., 18(3) (1980) 555.
23 O. Olabisi and R. Simha, Macromolecules, 8 (1975) 211.
24 D. E. Axelson and L. Mandelkern, J. Polym. Sci. Polym. Phys. Ed., 16 (1978) 1135.
25 L. Mandelkern, Pure Appl. Chem., 54(3) (1982) 611.

Analytica Chimica Acta, 189 (1986) 145—166
Elsevier Science Publishers B.V., Amsterdam – Printed in The Netherlands

THE INFLUENCE OF POLYMER SIZE AND SHAPE ON SELF-DIFFUSION OF POLYSACCHARIDES AND SOLVENTS

PAUL T. CALLAGHAN*

Department of Physics and Biophysics, Massey University, Palmerston North (New Zealand)

JOHN LELIEVRE

Department of Food Technology, Massey University, Palmerston North (New Zealand)

(Received 20th March 1986)

SUMMARY

Self-diffusion data obtained using pulsed-field-gradient nuclear magnetic resonance spectroscopy are presented for the poly-D-glucose molecules, dextran, amylopectin and glycogen in water and dimethyl sulphoxide. A model is developed for the influence of macroparticle shape on the concentration-dependence of polymer self-diffusion. The concentration-dependence of solvent and polymer self-diffusion indicates that amylopectin is planar with an axial ratio in excess of 6. In contrast, the dextran and glycogen data are consistent with random coil and spherical particle models, respectively. Both amylopectin and glycogen exhibit significantly different dimensions in the two solvents used.

One method of probing the sizes and shapes of polymers in solution is to use the self-diffusion coefficients of the polymer and the solvent. Both these coefficients can be measured by pulsed-field gradient nuclear magnetic resonance (PFG/n.m.r.) [1—3]. Separability is achieved in the case of the solvent by utilizing its overwhelmingly superior signal strength. When the solute signal is monitored, a perdeuterated solvent is used, for which the nuclear Larmor frequency differs markedly from that of the proton label. The present paper describes a PFG/n.m.r. study of the branched poly-D-glucoses amylopectin, glycogen and dextran that demonstrates some of the potential of the technique in the analysis of polymers. There are various solvents for these polysaccharides; the current study uses both water and dimethyl sulphoxide (DMSO).

The basic chemical structure of amylopectin is that of an $\alpha(1\rightarrow4)$-linked D-glucose polymer with some 4—5% $\alpha(1\rightarrow6)$ branch points (structure I). A feature of this polymer is that the ratio M_w/M_n is reported to be 300 [4] and there is some theoretical justification for this high ratio [5]. Previous work [6, 7] has indicated that the conformation of amylopectin is that of an oblate ellipsoid in DMSO. In water, the molecule aggregates to give a more spherical shape. The present study continues these investigations by further characterizing the molar mass, shape and dimensions of amylopectin.

0003-2670/86/$03.50

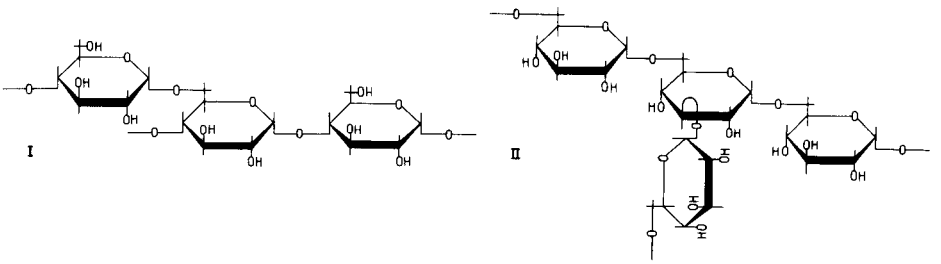

The structure and properties of glycogen have been reviewed in detail recently [8]. Electron microscopy studies show glycogen to consist of single spherical particles and of aggregates which are termed β- and α-particles respectively [9]. The β-particles have average diameters of about 25 nm and a molecular weight of about 10^7 daltons. The "fundamental unit" of α-particles appears to be two or three β-particles on a single protein backbone, and these fundamental units then associate into α-particles by the formation of disulphide bonds. The basic chemical structure of the β-particles of glycogen is that of an $\alpha(1\rightarrow4)$ linked D-glucose polymer with some 10% $\alpha(1\rightarrow6)$ branch points (structure I). The work presented here concerns an investigation of glycogen treated with proteolytic enzyme. Of the various glycogen forms that exist, such a polymer would be expected to be most similar to amylopectin. Both DMSO and water were used to see if effects, analogous to those taking place with amylopectin in these solvents, occur with glycogen.

Dextrans consist of glucose molecules bonded together by $\alpha(1\rightarrow6)$ linkages with about 5% $\alpha(1\rightarrow3)$ linkages serving as branch points (structure II). The branches are short and are mainly one or two glucose monomers in length [10]. The behaviour of dextran in aqueous solution has been the subject of several investigations [11—15], which have demonstrated that the polymer behaves as a random coil. Here, the study of dextran diffusion is extended to DMSO solutions, and the solvent diffusion in dilute solutions of the polymer is examined in both water and DMSO. The results obtained with this well-characterized macromolecule were used to provide a check of the PFG/n.m.r. findings on amylopectin and glycogen.

THEORY

The Brownian movement of a particle in solution is sensitive to interactions with surrounding particles which, in turn, depend on particle geometry. This paper is concerned with movement of macroparticles in a solvent, and with the Brownian movement of the solvent molecules themselves. These movements are used to characterize macroparticle size and shape. Models of polymer shape are required to interpret self-diffusion coefficients. Two basic structures are applicable in this study. These are the linear random coil and the highly branched polysaccharide. The conformation of random coils is well understood [16, 17]. In solution, an isolated random coil polymer

molecule can be considered to be a "ball" of mean size equivalent to the radius of gyration [16], R_G, where $R_G = aN^{\nu}$ and ν ranges between 0.6 and 0.5 in good and theta solvent conditions, respectively [17]. The branched polymers may be approximated by prolate or oblate ellipsoids of revolution. The ellipsoid shape is therefore determined by specifying the ratio of the semi-major to semi-minor axes (a/b).

Macroparticle self-diffusion

Infinite dilution. At infinite dilution, the macroparticle self-diffusion coefficient is given by the Stokes-Einstein expression

$$D_0 = k_B T/6\pi\eta R_H$$

where η is the solvent viscosity and R_H the hydrodynamic radius of the macromolecule. The hydrodynamic radius is a basic parameter describing the macromolecular conformation.

An estimate of the friction coefficient, $f_0 = (6\pi\eta R_H)^{-1}$, can be obtained by appropriate summation over the monomers each with friction ζ. This summation must account for the disturbance of solvent flow by the motion of each monomeric segment. Suppose one considers mean-square displacements along the laboratory z-axis. In the Kirkwood-Riseman theory [18]

$$D_0 = (1/N^2) \sum_{j,k=1}^{N} \langle k_B T [\zeta^{-1} + (1 - \zeta_{jk}) T_{jk}] \rangle = (D_m/N)\left[1 + (\zeta/N) \sum_{j,k=1}^{N} \langle T_{jk} \rangle\right] \quad (1)$$

where T_{jk} is the zz component of the Oseen tensor [19].

The chain friction is clearly much less than the monomer friction sum $N\zeta$ corresponding to simple free-draining. The implication of Eqn. 1 is that the hydrodynamic radius is a simple fraction of the random coil size. Thus $R_H \approx N^{1/2}$ for a theta solvent. For a good solvent where excluded volume interactions occur [20], $R_H \approx N^{\nu}$. The apparent restricted-draining behaviour of the open random coil structure, will have even greater applicability for branched polymers in which the average monomer proximity is greatly enhanced. Here it might be expected that the structure could be approximated by a solid particle of equivalent external dimensions. The effect of hydrodynamic "screening" is that the interior of the polymer does not contribute to the overall friction coefficient. In such circumstances, a simple relationship between size, shape and friction factor is suggested. The result for an ellipsoid of revolution is well known [21] and may be expressed in terms of the axial ratio, $\rho = a/b$, as $R_H = R_0 f_s$, with $f_s = (\rho^2 - 1)\,[\rho^{2/3} \tan^{-1} (\rho^2 - 1)^{1/2}]^{-1}$ and $R_0 = (a^2 b)^{1/3}$ (oblate ellipsoid), R_0 being the radius of the equivalent sphere. It is shown later, on the basis of the solvent-diffusion experiments, that the data presented herein are inconsistent with a prolate ellipsoidal shape. Hence these equations for R_H, f_s and R_0 are restricted to the oblate case.

Finite concentrations. At finite concentrations, the influence of neighbouring macromolecules on the self-diffusion of the labelled species is clearly affected by the polymer shape. In the random coil approach of Yamakawa [22], the polymer friction coefficient can be expanded in a power series of concentration as $f = f_0\ (1 + k_s c + \ldots)$. It is the first order behaviour applicable at high dilution which is of interest here.

It is important to note that the well known theories of Yamakawa and of Pyun and Fixman [23], relating to random coil macromolecules, predict k_s values pertaining to sedimentation. More recently, Akcasu [24] has formulated an approach to the concentration dependence of random coil friction which makes a clear distinction between the self- and sedimentation-frictional terms k_{DS} and k_s, respectively. For self-diffusion, the concentration effect arises from the dependence of the radius of gyration on the separation, R, of polymer pairs so that the configurational average is given by

$$k_{DS} = -4\pi n_p \int_0^R dR\, R^2\, \{[D^0_{ps}(R)/D] - 1\} \exp[-\beta V(R)] \qquad (2)$$

where $V(R)$ is the intermolecular potential, n_p is the number of polymers per unit volume and $D^0_{ps}(R)/D = R_G/R_G(R)$. When $V(R) = 0$, which occurs at the theta temperature, Akcasu found $k_{DS} = 1.063$ (where the concentration is expressed in volume fraction units). Using a Flory-Krigbaum potential and a uniform-density sphere model, it was shown that k_{DS} drops to 0.187 at the good solvent limit.

The treatment of the branched polymer case is very different. In contrast with the random coil, the conformation of branched polymers is expected to be much less sensitive to interpolymer separation. However, the hydrodynamic perturbations between branched polymers may well be more severe. In the non free-draining approximation in which the branched polymer is treated as an impenetrable semi-rigid ellipsoid, an alternative approach to the self-diffusion concentration dependence is necessary.

The Brownian movement of rigid spherical macroparticles interacting both through direct potential and through hydrodynamic effects has been treated by several authors [25—29]. In most of these models, k_{DS} lies in the vicinity of 1.8. In none of these treatments is the effect of non-spherical shape taken into account. It is apparent in the present work that k_{DS} varies greatly between different branched polysaccharides with identical monomer chemical units, and a significant influence of shape on the hydrodynamic interaction is suggested. It is obvious that the distribution of inter-segment spacings in highly ellipsoidal molecules and spheres at the same concentration will be quite different. In this section some shape dependence is incorporated in the interparticle hydrodynamic effects. To this end the model of Anderson and Reed [29] is used. In their approach the hydrodynamic interaction is incorporated by writing a one-dimensional Langevin equation for a particle of mass M and velocity U_1 as

$$M\, dU_1/dt = -fU_1 + B(t) \qquad (3)$$

where $B(t)$ is the fluctuating force on the "test" particle which is taken to be uncorrelated with the phase coordinates of all other particles. Anderson and Reed express the mean friction in terms of the number density, c_n, by

$$\langle U_1 \rangle = U_{10} - c_n \int_V g(r) \, (U_{10} - U_{12}) \, dV \tag{4}$$

where $\langle f^{-1} \rangle = \langle U_1/F_1 \rangle$ and F_1 is the force on sphere 1; U_{10} is the velocity which the labelled particle would have in the absence of neighbours, U_{12} is the resultant velocity of the labelled sphere where sphere 2 is located at displacement r with $F_2 = 0$, and $g(r)$ is the equilibrium radial distribution function and is isotropic.

For the case of spherical particles of radius a, Eqn. 4 reduces to

$$\langle U_1/U_{10} \rangle = 1 - 8 \phi \int_0^\infty g(x) \, 3 \, [1 - 2/3 \, (U_1/U_{10})_\perp - 1/3 \, (U_1/U_{10})_\parallel] \, dx \tag{5}$$

where the volume fraction ϕ is given by $4/3 \, \pi a^3 c$ and x is the dimensionless separation $[(r/2a) - 1]$. Equation 5 is sensitive to the macroparticle size only through ϕ. $(U_1)_\perp$ and $(U_1)_\parallel$ are the resultant velocities of the test sphere when a second sphere is placed perpendicular or parallel to the line of F_1 at distance r. The dependence of $(U_1/U_{10})_\perp$ and $(U_1/U_{10})_\parallel$ on r is standard hydrodynamic data [30, 31].

A simple method of dealing with the influence of non-spherical shape is as follows. First, it is noted that the correlation time for rotational diffusion of a particle is of the same order as the timescale for diffusion over a distance corresponding to a particle diameter [32]. Because the model concerns long range hydrodynamic interactions at high dilution, it is reasonable to surmise complete reorientation of pairs of macromolecules over the time scale of their interaction. The ellipsoid can therefore be treated as an equivalent sphere. In the simplest possible case, the equivalent sphere size might be taken to be the ellipsoid major dimension. Under this assumption the equivalent volume fraction ϕ (and hence k_{DS}) is enhanced by the volume ratio $(a^3/a^2b = a/b)$ for the oblate ellipsoid and $(a^3/ab^2 = a^2/b^2)$ for the prolate ellipsoid. It is preferable, however, to take some account of the nature of the interaction.

A slightly more sophisticated approach, therefore, involves an average of the hydrodynamic interaction taken over all ellipsoid orientations, presumed uncorrelated. The details of $(U_1/U_{10})_{\perp,\parallel}$ are unknown for ellipsoids. For point interactions, the Oseen tensor scalar dependence is r^{-1}. Such a point approach is inappropriate for the restricted-draining sphere or ellipsoid, although it may be noted that the macroscopic hydrodynamic terms $(U_1/U_{10})_\parallel$ also depend on the surface separation as approximately x^{-1} [33]. The approach here, therefore, is to perform an average appropriate to the longitudinal term $(U_1/U_{10})_\parallel$ by finding the average value of r^{-1} between all points on the surface of two spheres of radius a and separation R. The same calculation is done for ellipsoids averaged over all orientations, and an equivalent spherical

size is found by comparison. A procedure for expanding x^{-1} in a power series to fourth order and considering the limit $(a/R) \ll 1$ is outlined in the Appendix.

The oblate and prolate ellipsoids can be further approximated by using respectively a reorienting disc of radius a and a reorienting rod of radius a. This simplification is appropriate when $(a/b) \gg 1$ and leads to equivalent spherical radii: $a_{\text{eff}} = 1/2^{1/2}\ a$ for the oblate ellipsoid and $a_{\text{eff}} = 1/3^{1/2}\ a$ for the prolate ellipsoid. In consequence, the effective volume fraction and hence k_{DS} is enhanced in the Anderson and Reed model by 0.35 (a/b) for oblate and 0.19 $(a/b)^2$ for prolate ellipsoids.

It must be emphasised that the model used here is elementary. A form for the hydrodynamic interaction is assumed which is applicable for head-on motion of a macroparticle pair and in addition, a rapid uncorrelated rotational reorientation of each particle. A more sophisticated approach would incorporate the orientation dependence of the $(U_1/U_{10})_{\perp,\parallel}$ terms corresponding to a pair of ellipsoids, and then perform the appropriate orientational average. However, the approach is not possible because these terms are unknown. The present model has the virtue of simplicity whilst retaining much of the essential physics. The significant influence of macroparticle shape on k_{DS} is clearly illustrated.

Theories which predict the concentration dependence of macroparticle friction are formulated in terms of volume fraction ϕ. The interpretation of experimental data thus requires modelling of the polymer mass/volume ratio, $N_{\text{A}}\ v_{\text{m}}/M$, where v_{m} is the "molecular volume". However, $N_{\text{A}}\ v_{\text{m}}/M$ should not be taken as simply the polymer specific volume. Indeed, the Pyun-Fixman, Yamakawa and Akcasu models applicable to random coils specifically require that v_{m} be regarded as the hydrodynamic volume, $4/3\ \pi R_{\text{H}}^3$ and in consequence

$$k_{\text{DS}}^c = k_{\text{DS}}^\phi\ 4/3\ \pi\ R_{\text{H}}^3\ N_{\text{A}} M^{-1} \tag{6}$$

where k_{DS}^c and k_{DS}^ϕ are coefficients of concentration in w/v and v/v units, respectively. Given $R_{\text{H}} \approx M^\nu$, the Akcasu model predicts a molar mass dependence of k_{DS}^c between $M^{0.5}$ and $M^{0.8}$ for theta and good solvents, respectively. Some molar mass dependence of k_{DS}^c has been observed for polystyrene random coil diffusion [34] in the good solvent, carbon tetrachloride at (28°C), although below 10^5 daltons, k_{DS}^c was largely independent of M.

For branched polymers, the identity of the hard sphere and hydrodynamic radius is more obvious. Given $R_{\text{H}} \approx M^{1/3}$, it is reasonable to expect that k_{DS}^c is independent of M for these polymers. As with the random coil, however, the polymer specific volume to be used in relating k_{DS}^c and k_{DS}^ϕ must incorporate solvent included within the hydrodynamic radius. While k_{DS}^ϕ values are similar for random coils (≈ 1; Akcasu [24]) and hard spheres (≈ 2; Anderson and Reed [29]), the more compact structure of spherical branched polymers suggests considerably lower k_{DS}^c values than observed for the random coil.

Solvent diffusion

Muhr and Blanshard [35] have extensively reviewed the factors relating to solvent diffusion in gels. The present work is concerned with the dilute regime in which the macromolecules present randomly distributed separated influences on the solvent motion. In this context, it is useful to make a clear distinction between models adopting macroscopic and microscopic viewpoints. In the macroscopic view, the medium in which diffusion occurs is treated as a continuum which contains immobile, impenetrable objects. The diffusive version of this problem was first solved by Wang [36] although the obstructive effects are essentially those obtained much earlier by Fricke [37] for electrical conductivity. In the Wang model, only two parameters are needed to describe the solvent diffusion. First, there is the macroparticle shape factor, $\bar{\alpha}$, arising from the obstruction effect in which the solvent molecules are obliged to divert tortuously around the obstruction presented by the macroparticle. Secondly, there is the solvation parameter, h, describing the fraction of solvent immobilized at any instant by association with the "stationary" macroparticles. The latter aspect of the model includes, in addition, the effect of increased macroparticle size arising from the bound solvent layer.

It is important to note that Wang's original paper expresses the solvent diffusive attenuation in terms of a reduced cross-sectional area for the particle flux. This has led to widespread confusion in the literature. Any properly averaged measurement of diffusion will compensate for the effect of volume exclusion on both the flux cross-section and the concentration gradient with Wang's equation altered accordingly. This change has been indicated by several authors [38—41] and leads to the appropriate first-order diffusive reduction equation

$$D^{solv} = D_0^{solv} \left[1 - \omega (\bar{\alpha} - 1) (V_p d_0 + h) + h\right] \tag{7}$$

where ω is the macroparticle weight fraction, V_p the apparent macroparticle specific volume, d_0 the density of the pure solvent, h the solvation coefficient (g solvent per g solute) and D_0^{solv} is the pure solvent self-diffusion coefficient. The shape factor $\bar{\alpha}$ can be defined in terms of the ellipsoidal parameter $\rho = a/b$. For an oblate ellipsoid,

$$\bar{\alpha} = \frac{1}{3}\left[1 - \frac{\rho}{1-\rho^2}\left\{(1-\rho^2)^{-1/2}\left(\tan^{-1}\left(\frac{\rho}{(1-\rho^2)^{1/2}}\right) - \frac{\pi}{2}\right) + \frac{1}{\rho}\right\}\right]^{-1}$$

$$+ \frac{4}{3}\left[\frac{2-\rho^2}{1-\rho^2} - \frac{\rho}{(1-\rho^2)^{3/2}}\left\{\frac{\pi}{2} - \tan^{-1}\left(\frac{\rho}{(1-\rho^2)^{1/2}}\right)\right\}\right]^{-1} \tag{8}$$

For a prolate ellipsoid, $\bar{\alpha}$ varies between the limits 1.5 and 1.667 over the range $1 \leqslant \rho \leqslant \infty$.

The Wang equation thus appears to offer a direct indication of macroparticle shape once the solvation factor h has been determined. Unfortunately, h is an ambiguous parameter, difficult to measure directly and in some cases

the dominant influence on D^{solv}/D_0^{solv}, as is demonstrated in this paper. One simple estimate of h may be obtained by n.m.r. methods in which the temperature of the solution is reduced below the solvent freezing point, and the remaining fraction of "unfrozen" signal is observed. This unfrozen component is manifested as an n.m.r. signal with long relaxation time and may be ascribed to solvent molecules experiencing altered intermolecular structure and, by implication, close association with the macromolecular surface.

The difficulty in assigning an appropriate value to h in the Wang procedure is associated with the complex behaviour of solvent molecules in close proximity to the polymer. The simplistic nature of the two class assumption of bound and unbound water is inadequate and it is necessary to become concerned with the microscopic details of the molecular interactions. For example, can the macromolecule be regarded as a particle which excludes solvent macroscopically, and therefore handled by continuum methods, or does the exclusion occur on a microscopic level, monomer by monomer? The macroscopic interpretation of h is least appropriate in the random coil case where solvent is closely associated with the polymer throughout its volume. While stochastic [42, 43] and free-volume [44—46] microscopic models have been applied by various authors with varying degrees of success, each fails to include long-range (hydrodynamic) effects which may, in fact, provide the largest perturbation to solvent motion. It is useful in this regard to reflect on the hydrodynamic properties of the random coil. In this case, the polymer friction is considerably reduced below that of the sum of monomeric contributions, because of severe disturbances of solvent motion within the coil. The similarity of coil hydrodynamic and structural radii gives rise to the restricted-draining picture in which the relative motion of monomer and local solvent is severely reduced. A simple consideration of the coil geometry [47] indicates that each solvent molecule within the coil radius of gyration is, on average, separated from its nearest polymer segment by no more than a few segment diameters. In view of the restrictions on shear imposed by viscous forces, the solvent may be regarded as being hydrodynamically trapped. Beyond R_G the solvent diffusion is expected to become progressively more independent of the polymer. This longer-range hydrodynamic influence must be contrasted with the localized solvent structural disturbance in the one or two monolayers adjacent to the polymer chain. It is clear that in the case of the random coil the "immobilized solvent" appropriate to the Wang expression may greatly exceed the "unfrozen solvent" apparent in the n.m.r. freezing experiment.

For highly branched polymers, the solvent fraction included within the gyration radius is clearly considerably smaller and it is reasonable to expect correspondingly lower values of h. The freezing experiment may give a closer estimate here. The degree to which the Wang approach is effective in elucidating branched poly-D-glucose shape factors will depend on the relative magnitudes of $(\bar{\alpha} - 1)$ and h. Freezing n.m.r. experiments in poly-D-glucoses suggest $h \leqslant 0.5$ gg^{-1} which is comparable with $(\bar{\alpha} - 1)$ for spherical macro-

molecules. Equation 7 is therefore likely to be conclusive only for severely oblate ellipsoids pertaining to large values of $(\bar{\alpha} - 1)$.

Recently, Altenberger and Tirrell [48] published a microscopic model for self-diffusion through a system of randomly distributed obstacles, in which hydrodynamic effects are incorporated by the continuum method of the Oseen tensor. Their model neglects connections between the fixed obstacles, and these authors regard their model as only a first step to understanding solvent diffusion in gels. They derive

$$D^{solv}/D_0^{solv} = 1 - 0.5\,(a_b/a_0)\,(4.5\,\phi)^{1/2}\,F\,[(1 + a_b/a_0)\,(4.5\,\phi)^{1/2}] - (1 + a_b/a_0)^3\,\phi \quad (9)$$

where a_0 and a_b are respectively the excluded volume interaction ranges of the obstacle (polymer segment) and Brownian particle (solvent molecule). An interesting feature of Altenberger and Tirrell's model is the existence of a weak $\phi^{1/2}$ term which implies a curvature at low volume fractions. For $\phi > 0.01$, the plots of D^{solv}/D_0^{solv} vs. ϕ appear linear, extrapolating to between 0.9 and 1.0 as $\phi \to 0$. The linear section of the data is strongly dependent on a_b/a_0 and by implication the local solvent and solute chemical structure.

Pulsed-field-gradient n.m.r.

The PFG/n.m.r. method has been extensively reviewed elsewhere [1–3]. In the case of Brownian movement, Stejskal and Tanner [49] have shown that for a molecular ensemble with self-diffusion coefficient, D, the normalized spin-echo amplitude in the presence of magnetic field gradients of magnitude G, duration δ and separation Δ is given by $A(G)/A(0) = \exp(-kD)$, where $k = \gamma^2\delta^2G^2(\Delta - \delta/3)$ and γ is the nuclear gyromagnetic ratio. Naturally occurring polysaccharides tend to have a wide range of molar masses and the standard PFG/n.m.r. experiment must be corrected to take this into account [50]. A simple polydispersity model [6, 51] in which polydispersity is represented by a log normal probability distribution, can be formulated in terms of a dependence of self-diffusion on molar mass as $D(M) \approx M^{\alpha}$. This scaling approach is appropriate for dilute random coils ($\alpha = -0.6$), semi-dilute random coils ($\alpha = -2$), and dilute, restricted-draining ellipsoid ($\alpha = -0.33$). Expanding $\exp[-kD(M)]$ in a power series and retaining the leading linear term gives an effective diffusion coefficient appropriate for small attenuations (i.e., $A(G)/A(0) > 0.5$):

$$D^{eff} = D(M_0)\exp[\alpha(\alpha + 2)\,\sigma^2/4] \quad (10)$$

where $M_0 = M_w\,\exp(-3\sigma^2/4)$

EXPERIMENTAL

Amylopectin was isolated, as described previously [6], from starch that had been extracted from wheat grain *cv. Aotea.* Potentiometric titration with iodine solution showed the polymer to be of high purity, with an iodine-binding capacity of 0.3% [52].

Glycogen that had been extracted from rat liver using the standard phenol–water procedure [53] was supplied by Prof. Roy Geddes. The sample had been treated with the enzyme protease K, a general protease which digests the protein backbone of the glycogen. The distribution of sedimentation coefficients of the resultant material indicated that it consisted largely of β particles. Fractionated dextran samples (Pharmacia Fine Chemicals) were checked by using column chromatography [15]. The resultant well-defined fractions were characterized by a M_w/M_n ratio as indicated in Table 1. When required, the water and any hydroxyl protons on the above polysaccharide samples were exchanged by dissolving the polymer in deuterium oxide, freeze-drying and repeating this sequence several times. Solutions of amylopectin in dimethyl sulphoxide (DMSO) were allowed to equilibrate for about 10 days by slowly stirring the solution in a nitrogen atmosphere before n.m.r. measurements were made. Glycogen and dextran dissolved more readily in both water and DMSO and only required equilibration overnight.

The self-diffusion experiments were done with 60-MHz proton spin echoes from a JEOL FX60 n.m.r. spectrometer interfaced to a pulsed-field gradient unit [1]. Measurements were made at 25°C unless otherwise stated.

RESULTS AND DISCUSSION

Random coil self-diffusion: dextran in D_2O and DMSO

In previous work [15] on the concentration dependence of dextran self-diffusion in D_2O, the polymer friction was found to exhibit a linear variation with concentration. The k^c_{DS} and extrapolated D_0 values that were so obtained are summarized in Table 1. Furthermore, measurement of D_0 vs. M suggested a power law relationship, $D_0 \approx M^{-0.57}$ [2], characteristic of random coils in a good solvent.

TABLE 1

The dextrans discussed, with their molar masses, polydispersity, self-diffusion coefficients, hydrodynamic radii and self-diffusion concentration dependence

Dextran	M_w (daltons)	M_w/M_n	D_0 (10^{-11} m^2 s^{-1})	R_H (nm)	k^c_{DS} (m^3 kg^{-1})
In D_2O					
Pharmacia T40	40 100	1.35	5.4(2)[a]	4.6(1)	0.032(1)
Pharmacia T70	75 800	1.60	4.0(4)[a]	6.2(3)	0.038(3)
Sigma 170	170 000	1.25	2.4(2)[a]	10(1)	0.042(2)
Pharmacia T500	461 000	1.50	1.35(8)[a]	18(1)	0.038(2)
Pharmacia F104	19 100	1.10	8.3(4)[b]	3.0(2)	—
Pharmacia F108	153 700	1.50	2.4(2)[b]	10(1)	—
In DMSO					
Pharmacia T40	40 100	1.35	2.6(1)	4.4(2)	0.029(4)
Pharmacia T500	461 000	1.50	0.9(1)	13(1)	0.033(1)

[a]Data from [15]. [b]Data from [13].

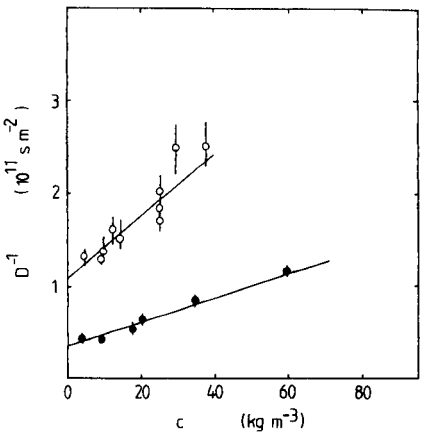

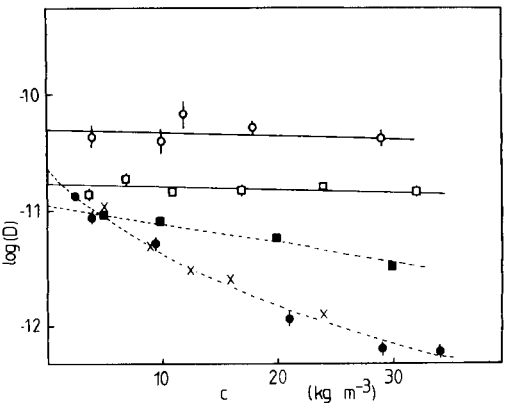

Fig. 1. Dependence of polymer self-diffusion on concentration, c, for dilute dextran in DMSO (28°C). The data are used to obtain the k^c_{DS} and D_0 values indicated in Table 1. Molar masses (daltons): (○) 461 000; (●) 40 100.

Fig. 2. Amylopectin and glycogen self-diffusion vs. concentration for D_2O (□, ■) and DMSO (○, ●, ×) solutions. (○, □) Glycogen; (●, ×, ■) amylopectin. Source of amylopectin: (●) *cv. Aotea*; (■, ×) *cv. Gamenya.* The data are plotted as log (D) vs. c, and D_0 values are found by extrapolation.

The present work extends the data shown in Table 1 by obtaining D vs. c in DMSO at 28°C, for the lowest (40 100 dalton) and highest (461 000 dalton) molar mass dextrans used in the previous study. These new data are plotted in Fig. 1. The resultant k^c_{DS} and D_0 values for dextran in DMSO are given in the last two rows of Table 1. The highest molar mass dextran in the DMSO solvent exhibits anomalous variations and some of the difficulty apparent in working with this system is indicated by the large scatter in the data. A possible explanation is that DMSO at 28°C is nearly a theta solvent for dextran and the polymer is experiencing fluctuations in dissolution. That theta behaviour should be more evident at higher molar mass is consistent with the known dependence of solvent quality on polymer size [54]. It is noteworthy that the ratio of D_0 values for 461 000- and 40 000-dalton dextran in DMSO indicates $D_0 \approx M^{0.43}$ [7], closer to the exponent of 1/2 expected for Gaussian behaviour in a theta solvent. The dextran apparently adopts a more compact coil in DMSO than in water.

The k^c_{DS} values shown in Table 1 can be compared with the predictions of the Akcasu model. This model gives a maximum, or theta solvent, k^c_{DS} of the order 10^{-2} m^3 kg^{-3} for dextran in D_2O and DMSO when the observed hydrodynamic radii are incorporated. While the predicted order of magnitude of k^c_{DS} is in broad agreement with the data, the details of the theory are not well represented. It is clear from Table 1 that k^c_{DS} is largely independent of molar mass, a result which is consistent with previous studies [34] of synthetic polystyrene in organic solvents, but not in agreement with

Akcasu's work. A weak solvent-dependence is apparent, with k^c_{DS} somewhat lower in DMSO. If DMSO is regarded as the poorer solvent, as indicated earlier, then the lower k^c_{DS} values are consistent with similar reduction of polystyrene k^c_{DS} in the theta solvent, cyclohexane (37°C) [55]. Again this is at variance with Akcasu's work. The suggestion that DMSO is a poorer solvent than water stands in sharp contrast with measurements of solution enthalpy [56]. These give interaction parameters, χ, an order of magnitude larger in DMSO than in water, making DMSO the better thermodynamic solvent.

It is interesting to note that other polysaccharides exhibit such anomalous behaviour. Chemical shift measurements [57, 58] with ^{13}C-n.m.r. indicate that amylose also adopts a more compact coil in DMSO than in water. In flexible random coil theory, the solvent influence acts via the effective monomer-monomer interaction, χ. In polysaccharides, however, allowance must be made for a change in flexible subunit size (Kuhn statistical length) as the solvent is varied. This is particularly so because of the significance of hydrogen bonding. Szejtli and Augustat [59] have suggested that for amylose in aqueous solutions, the rotation about D-glycosidic bonds is hindered by steric factors and only the helical or interrupted helical structure can exist. In contrast, amylose behaves as a random coil in DMSO [60]. It is likely that a similar, although more localized, behaviour occurs for dextran solutions in which the larger DMSO molecule and different hydrogen-bonding organisation prevents the formation of local helices. The existence of local ordered structures in aqueous solution would imply that the Kuhn length is larger in water leading to an expanded coil conformation despite the lower value of χ. The experimental data presented here suggest that not only is the dextran coil size smaller in DMSO, but that DMSO behaves as if it were the poorer solvent. At higher concentrations, a clearly defined semidilute regime was found for 170 000-dalton dextran with a concentration-dependence consistent with the predictions of reptation theory and, along with the D_0 vs. M scaling data, suggests that dextran B512 is indeed a linear random coil with limited side chains. The apparent reptational behaviour can be used to establish a branch length upper limit of 10 glucose units [15], because these branches must be less than an interentanglement length [61] over the semidilute regime.

Branched polymer self-diffusion: amylopectin and glycogen in D_2O and DMSO

The D vs. concentration data for glycogen and amylopectin are shown in Fig. 2. They are similar in that each exhibits a faster diffusion at infinite dilution in DMSO than in water, a trend opposite to that suggested by the solvent viscosity ratio. However, the concentration dependence of D is dramatically different for the two branched polymers. In both DMSO and water, the glycogen self-diffusion is practically independent of concentration. A similar concentration-independence has been observed for glycogen sedimentation [62] and ascribed to "hydrodynamic ideality".

The contrasting behaviour of amylopectin is evident. Not only is the concentration dependence several orders of magnitude larger but the D vs. c behaviour in DMSO and D_2O are sharply distinguished. Figure 2 clearly shows that the self-diffusion behaviour for amylopectin from the *Aotea cultivar* is consistent with the previous work on the *Gamenya cultivar* [6]. The log D vs. c plots of Fig. 2 were used to obtain extrapolated D_0 values which are incorporated in the D^{-1} vs. c plots of Fig. 3. The region of linear behaviour is small for amylopectin in contrast with that observed for dextran random

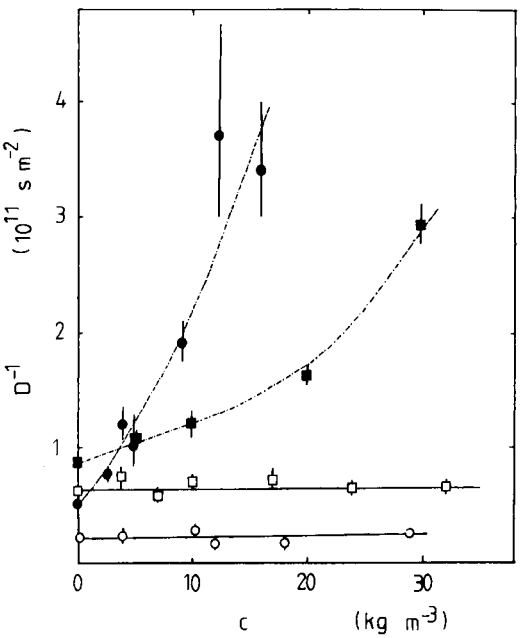

Fig. 3. Amylopectin and glycogen self-diffusion data from Fig. 2 plotted as D^{-1} vs. c, in order to obtain estimates of k^c_{DS}. (Symbols as in Fig. 2.)

TABLE 2

Data for amylopectin and glycogen, as given for dextran in Table 1. Both raw D_0^{eff} and polydispersity-corrected $D_0(M_w)$ values are given. The hydrodynamic radius is calculated from $D_0(M_w)$

Polymer	M_w (daltons)	M_w/M_n	D_0^{eff} (10^{-11} m^2 s^{-1})	$D_0(M_w)$ (10^{-11} m^2 s^{-1})	R_H (nm)	k^c_{DS} (m^3 kg^{-1})
In D_2O						
Amylopectin	$10^5 \sim 10^8$	~300	1.0(2)	0.28(6)	80(20)	0.030(5)
Glycogen	~10^7	~3	1.9(1)	1.4(1)	18(1)	⩽0.001
In DMSO						
Amylopectin	$10^5 \sim 10^8$	~300	2.8(7)	0.7(1)	22(3)	0.27(6)
Glycogen	~10^7	~3	4.8(3)	3.8(2)	4.1(2)	⩽0.005

coils; k^c_{DS} values obtained from initial slopes along with corresponding D_0 data are summarized in Table 2. The weight-averaged diffusion coefficients in Table 2 were calculated from Eqn. 10 which predicts

$$D_0(M_w) = D_0^{eff} \exp\{(\sigma^2/4)[3\alpha - \alpha(\alpha + 2)]\} \quad (11)$$

For highly branched polymer, $\alpha = -0.33$ and σ values of 3.34 and 1.48 are used, corresponding to amylopectin and glycogen polydispersities of 300 and 3, respectively.

Several features are apparent in the data in Table 2. Glycogen in aqueous solution has been the subject of previous D_0 studies using quasi-elastic light scattering (QELS) [63]. The $D_0(M_w)$ value obtained here by PFG/n.m.r. is $1.4(1) \times 10^{-11}$ m^2 s^{-1}; QELS data for a similar molar mass fraction gives $D_0(M_z) = 2.6 \times 10^{-12}$ m^2 s^{-1}. Allowing for the dependence of D_0 on M, a $D_0(M_z)/D_0(M_w)$ ratio of 1.4 is expected rather than 5 as observed here. Independent confirmation of the PFG/n.m.r. result is given by the implied glycogen hydrodynamic radius in D_2O of 18 nm. This radius is consistent with the β-particle radius of 13 nm obtained by electron microscopy [64]. The light-scattering experiments were of course done on a different glycogen preparation and it is possible, given the sensitivity of light scattering to particle size, that these data were weighted by the presence of additional larger components in the fraction.

The faster diffusion of glycogen in DMSO is quite unexpected because the viscosity of DMSO is approximately twice that of water at 28° C. Indeed, the data suggest a glycogen hydrodynamic radius some five times smaller in DMSO than in water. A similar discrepancy is also apparent for amylopectin where the favoured explanation is polymer aggregation in the aqueous solvent [6]. It is clear that the DMSO/D_2O discrepancy for glycogen could be explained by cleavage of the β-particle in DMSO. This suggests that the glycogen β-particle which exists in aqueous solution is not a single molecule but an aggregate. However, DMSO may cause depolymerization of glycogen.

The concentration dependence of glycogen self-diffusion is quite consistent with the predictions of Anderson and Reed [29] for hard spheres. Assuming a compact branched structure [8], it is reasonable to assign to the hydrodynamic specific volume, $N_{AV}\, v_m/M$, a value close to the dry glycogen specific value of 6.3×10^{-4} m^3 kg^{-1}. For the weak long-range force (theta solvent) limit, the Anderson and Reed model predicts $k^c_{DS} = 1.1 \times 10^{-3}$ m^2 kg^{-1} with lower values for good solvents. The glycogen data presented here are compatible with those expected from such a spherical macroparticle.

The k^c_{DS} data for amylopectin stand in sharp contrast. Using the simple ellipsoidal model proposed in this paper, the implied axial ratio is several hundred (whether oblate or prolate) in DMSO, and a ratio of roughly one order of magnitude smaller in water. It is also clear by comparison with glycogen that amylopectin in water is manifestly non-spherical. The shape of amylopectin in DMSO may be independently estimated by using solvent diffusion data (see below) and, consequently, detailed discussion of the

effective hydrodynamic radius given in Table 2 is postponed. However, the implication of the differing effective R_H value in DMSO and water is that amylopectin forms a molecular aggregate in the aqueous environment. The more spherical shape evidenced by a lower k^c_{DS} value in water, and the time-dependence of the amylopectin water spin-echo data, independently point to this conclusion.

Solvent diffusion

Figure 4 shows an echo attenuation plot for proton signals arising from DMSO molecules in a 2.4% solution of glycogen in DMSO at 28° C. Such data enable D values to be obtained to a precision of order 1%. The results of both the DMSO and water self-diffusion measurements for dextran solutions are shown in Fig. 5 where D^{solv}/D_0^{solv} is plotted against concentration in w/w units. The glycogen and amylopectin data are shown in Fig. 6. Each set of data has been fitted by linear regression and plotted with a normalized intercept. In fact, the random-coil data exhibit a small (≈ 0.97) intercept in D^{solv}/D_0^{solv} as $c \to 0$ which is consistent with the inclusion of a $c^{1/2}$ term according to the Altenberger and Tirrell model [48]. No such intercept is observed for glycogen although a smaller offset, just on the limit of experimental error, may be present for amylopectin. These low concentration effects are difficult to measure but may be used to indicate "structural openness" in the polymer under examination.

The D^{solv}/D_0^{solv} data can be analysed in terms of the macroscopic Wang hypothesis. To do this, attention is focussed on the value of solvation parameter to be used. Table 3 shows the h values obtained by means of the n.m.r. freezing experiment described earlier. The results are remarkably independent of polymer, and strongly dependent on solvent, which suggests that the

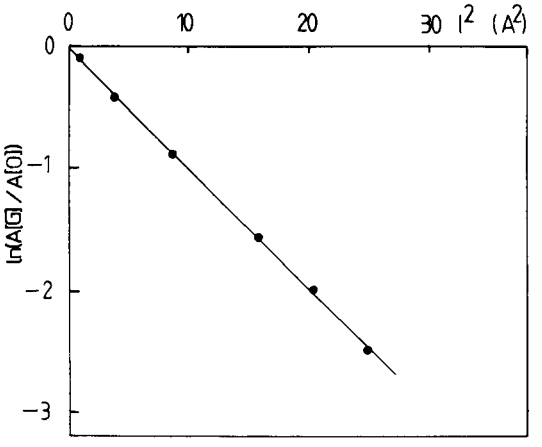

Fig. 4. Spin-echo attenuation plot for DMSO protons in a solution of 2.4% glycogen in DMSO at 28°C (Δ = 10 ms and δ = 3 ms).

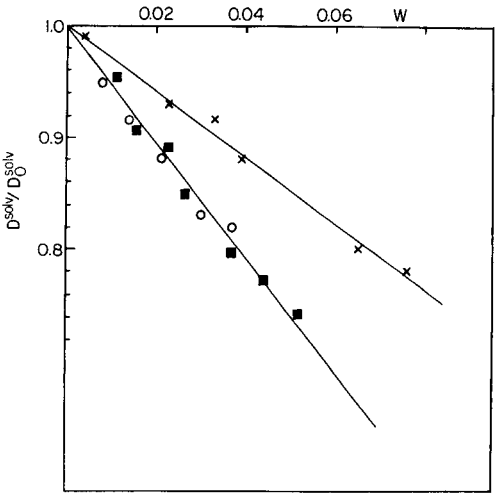

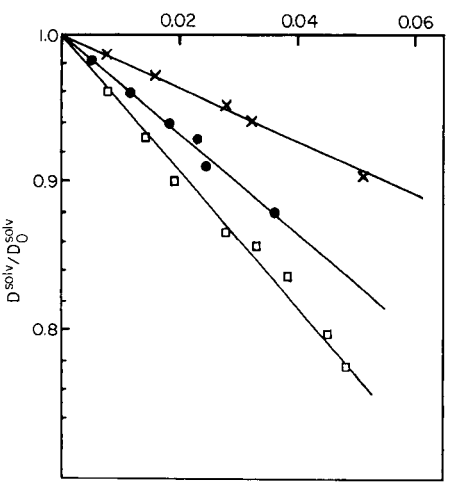

Fig. 5. Dependence of solvent self-diffusion on dextran concentrations $w(gg^{-1})$ for T40 dextran in water (×), T40 in DMSO (▪) and T500 dextran in DMSO (○).

Fig. 6. Dependence of solvent self-diffusion on concentration: (×) glycogen in water; (•) glycogen in DMSO; (□) amylopectin in DMSO. The different slopes apparent for amylopectin and glycogen indicates the different shape factors appropriate in DMSO solution.

TABLE 3

Solvation parameters (grams of solvent per gram of solute) obtained by the n.m.r. freezing method

Polymer	$h(D_2O)$	h(DMSO)
Dextran	0.28	0.55
Glycogen	0.26	
Amylopectin	0.25(4)	0.6(2)

freezing experiment measures a value of h related to local monomer/solvent interactions uncorrelated with polymer structure. The similarity of h values within a given solvent reflects the chemical similarity of the monomer units in each polysaccharide.

The random coil experiment provides a useful indication that the h values of Table 3 are smaller than those appropriate to the Wang analysis. Surmising a spherical shape for the dextran coil implies $\bar{\alpha} = 1.5$ in the fit to Eqn. 7 and hence yields h values of 1.8 gg^{-1} and 3.3 gg^{-1} for H_2O and DMSO, respectively. It may be noted that no molar mass dependence is apparent in these data. It is interesting to compare the values of the implied "solvation sphere", r_s, with the coil hydrodynamic radii, R_H. For 40 100-dalton dextran, the data give $r_s/R_H = 0.7$ in water and 0.8 in DMSO. Samples of 40 100-dalton

dextran were prepared in both solvents at concentrations corresponding to the ratio of solvent to polymer equal to the Wang h values. The solvent diffusive attenuations are 0.36 and 0.25 in water and DMSO, respectively. Clearly the "solvation sphere" does not consist of immobilized solvent, but instead reflects an average over graduated solvent diffusion which presumably increases in rapidity with distance from the coil centre. The dextran data provide a useful reference for the solvent diffusion experiments with the highly branched polymers in which the associated solvent is expected to be considerably smaller. A third estimate of h may be obtained from the glycogen data.

Taking a spherical shape for glycogen in both solvents, the data in Fig. 6 give $h = 0.95$ in water and $h = 2.0$ in DMSO. While h is, as expected, lower than for dextran, the ratio of hydration between the two solvents is again a factor of 2. It is an interesting feature of the freezing experiment that the h values so obtained in the two solvents are related by a similar factor of about 2 for each of the three polymers investigated.

There exist, therefore, three independent sets of data which suggest that the solvation value for each polysaccharide in DMSO should be approximately double that in water. Given this conclusion, the D^{solv}/D_0^{solv} data for amylopectin can be analysed. It is useful to estimate the smallest possible value of the axial ratio a/b for amylopectin in DMSO. This corresponds to the amylopectin/water conformation possessing the minimum value of $\bar{\alpha}$ (i.e., maximum h), equal to the spherical shape factor of 1.5. In this case, $h = 0.95$ in water, exactly as for glycogen. In consequence, h is assigned the value 2.0 in DMSO and this determines the lowest possible value of the shape factor for amylopectin in DMSO. Hence, for amylopectin (*Aotea*) in DMSO $\bar{\alpha} \geqslant 2.0 \Rightarrow a/b \geqslant 4.5$ (oblate ellipsoid), and for amylopectin (*Gamenya*) in DMSO, $\bar{\alpha} \geqslant 2.2 \Rightarrow a/b \geqslant 6$ (oblate ellipsoid). It is clear that evaluation of the D^{solv}/D_0^{solv} data indicates that amylopectin in DMSO has the shape of an oblate ellipsoid (a prolate ellipsoid cannot exceed $\bar{\alpha} = 1.67$). The suggested axial ratio is in fact the minimum consistent with evaluation of the data based on the Wang model.

The data for the dependence of amylopectin self-diffusion on concentration in water [6] suggest a distortion from ideal spherical behaviour, albeit less dramatic than that evidenced by amylopectin in DMSO. Of course, a presumption of $\bar{\alpha}$ larger than the spherical minimum leads to even greater estimates for (a/b) in DMSO. An explanation for the finding that amylopectin and the spherical glycogen exhibit the same diffusive attenuation for the aqueous solvent is that amylopectin possesses the larger $\bar{\alpha}$ and glycogen the larger h. It is reasonable to believe that the glycogen sphere, which is known to possess an empty core [8], will incorporate more solvent than the planar amylopectin molecule.

The dimensions of amylopectin

The size of amylopectin in DMSO and water can now be estimated by using the hydrodynamic radius deduced from the infinite dilution self-diffusion

coefficient $D_0(M_w)$. The calculation of $D_0(M_w)$ from D_0^{eff} requires some knowledge of the polydispersity. In this regard, it should be noted that the value of $M_w/M_n = 300$ used here predicts a $D_0(M_z)/D_0(M_w)$ ratio of 0.14 and hence, from PFG/n.m.r., $D_0(M_z) = 10(3) \times 10^{-13}$ m^2 s^{-1}. The QELS value at 24°C is $9(2) \times 10^{-13}$ m^2 s^{-1} and the excellent agreement may be taken as support for the value of M_w/M_n used in this evaluation. Taking the minimum (a/b) ratio of ca. 5 implied by the "Wang analysis" of the solvent-diffusion experiment, it is straightforward to estimate the amylopectin dimensions. Using the dependence of R_H on (a/b), $a = 21$ nm and $b = 4.3$ nm for amylopectin in DMSO. It is also clear that the molecular volume for amylopectin in water is about 100 times that in DMSO.

Provided that the amylopectin is taken to be densely packed with monomer, one may use the dry specific volume 0.62 cm^3 g^{-1} and the molecular volume $4/3\ \pi(a^2b)$ to estimate the molar mass as 8×10^6 daltons. The assumption of dense packing leads to an upper limit estimate. Another measure of M has been obtained [6] by relating c^* to the molecular spacing at the onset of entanglement. Using a comparison with c^* defined empirically in the same way (i.e., $c^* = 120$ kg m^{-2}) for 170 000-dalton dextran for which the radius of gyration is 9.2 nm, and scaling by $c^* = MN_{Av}^{-1}(2a)^{-3}$ for amylopectin, this approach yields $M_w = 2 \times 10^6$ daltons.

CONCLUSION

Despite the presence of the same monomer unit, and in the case of glycogen and amylopectin the same linkages between monomers, the polymers studied herein have very different conformations. Dextran, which serves as a reference macromolecule in the context of the present study, is shown by PFG/n.m.r. to be a random coil in both water and DMSO. This is apparent from the dependence of D on concentration in the semidilute regime and from the D_0 vs. M scaling data. Water appears to be the better solvent for this polymer, as judged by the dependence of D_0 on molar mass although this result stands in contrast with thermodynamic data. The plot of D^{solv}/D_0^{solv} vs. concentration in w/w units intercepts the ordinate below 1.0 as concentration → 0, and this is consistent with the theory of Altenberger and Tirrell [48]. Interpretation of this plot by means of the Wang hypothesis demonstrates the difficulty of evaluating the solvation parameters employed. Clearly, with random coils the n.m.r. freezing experiment underestimates the appropriate h values for the Wang treatment.

Glycogen is shown by PFG/n.m.r. to be a spherical molecule, and this is in accord with the evidence from other techniques. Thus, the concentration dependence of glycogen self-diffusion agrees with Anderson and Reed's equation for hard spheres. The unexpected finding is that glycogen diffuses more rapidly in DMSO than water. This may reflect intermolecular aggregation of the relatively long outermost chains of glycogen β-particles, possibly by the type of double-helix formation characteristic of $\alpha(1 \rightarrow 4)$ poly-D-

glucose chains. However, the possibility of depolymerization effects cannot be excluded at present.

With the amylopectin samples, the solvent diffusion data demonstrate that in DMSO these polysaccharides are highly planar, irrespective of whether the hydration coefficient used is that obtained directly by n.m.r. or by estimates from known h values of related molecules. The polymer diffusion measurements also indicate a planar molecule, though there is some discrepancy concerning the exact a/b ratio measured by the n.m.r. methods. Analytical ultracentrifugation techniques [7] suggest an a/b value of around 20. Such discrepancies would not be unexpected because each technique is sensitive to different facets of polymer behaviour. According to n.m.r., the molar mass of amylopectin in DMSO is of the order of 5×10^6 daltons and this agrees well with ultracentrifugation studies [7]. In water, amylopectin aggregates, as evidenced by the more spherical shape in the Wang experiment and the lower self-diffusion coefficient [6].

Banks and Greenwood [52] suggested that amylopectin is synthesized in the amyloplast in a two-dimensional form. During synthesis, the arrangement of chains within amylopectin is therefore constrained so as to produce a plate-like structure, a constraint lacking in glycogen. The present study is consistent with this suggestion and indicates that at least some of the two-dimensional character of amylopectin existing at the point of biosynthesis remains in solution. For amylopectin to be planar in solution, some factor preventing other conformations must operate. This factor could be stiffness associated with the bonds between monomers, steric hindrance, or the presence of traces of bonds other than α-D(1→4) or α-D(1→6) which cross-link glucose monomers in place. However, such linkages, if they do exist, have not been found and would be difficult to detect [65].

The difference in conformation of amylopectin and glycogen may reflect the different roles these molecules have as storage carbohydrates. The branched 3-dimensional structure of glycogen would tend to prevent the polymer crystallizing and so becoming relatively resistant to degradation. Thus stores of glycogen could be metabolized in animal tissue relatively quickly when needed. However, the requirement for rapid metabolism of carbohydrate stores does not occur in plants and therefore 2-dimensional branching is favoured. Such branching permits a greater quantity of carbohydrate to be stored per unit volume of tissue than would be possible in the 3-dimensional case. Furthermore, the presence of aggregates of 2-dimensional molecules in starch granules makes the particles rigid and limits swelling, which is to the advantage of the plant.

The authors are grateful to Prof. Roy Geddes and Mr Philip Calder of the Biochemistry Department, University of Auckland, for providing the glycogen samples. We also acknowledge technical assistance from June Husbands and Diane Bourn.

APPENDIX

Consider two identical ellipsoids with centres separated by distance R along the z-axis. The distance between two points on the surfaces labelled by (ellipsoid centred) polar coordinates (r_1, θ_1, ϕ_1) and (r_2, θ_2, ϕ_2) is given by

$$r_{12} = [(r_1 \sin\theta_1 \cos\phi_1 - r_2 \sin\theta_2 \cos\phi_2)^2 + (r_1 \sin\theta_1 \sin\phi_1 - r_2 \sin\theta_2 \sin\phi_2)^2 + (R + r_1 \cos\theta_1 - r_2 \cos\theta_2)^2]^{1/2}$$
$$= R\{1 + (2/R)(r_1 \cos\theta_1 - r_2 \cos\theta_2) + (1/R^2)[(r_1^2 + r_2^2) - 2r_1 r_2 [\sin\theta_1 \sin\theta_2 \cos(\phi_1 - \phi_2) + \cos\theta_1 \cos\phi_2]]\}^{1/2} \quad \text{(A1)}$$

The aim is to evaluate $\langle r_{12}^{-1} \rangle$ where the average is taken over the distribution of ellipsoid surface coordinates. This distribution is presumed to possess orientational isotropy because of the rapid rotational diffusion assumption. A simple approximation for the surface distribution of highly ellipsoidal objects is given, respectively, by the disc of radius a and rod of half length a for oblate and prolate structures, where a is the semi-major axis. Hence these distributions are written as

oblate ellipsoid: $P(r) = r/2\pi a^2$

prolate ellipsoid: $P(r) = 1/4\pi a$

sphere: $P(r) = (1/4\pi)\delta(a)$

To find $\langle r_{12}^{-1} \rangle$, a binomial expansion is used for r_{12}^{-1} to fourth order and integrated:

$$\langle r_{12}^{-1} \rangle = \int_0^{2\pi}\int_1^{-1}\int_0^{a} P(r_1)P(r_2)r_{12}^{-1}\, dr_1\, dr_2\, d(\cos\theta_1)\, d(\cos\theta_2)\, d\phi_1\, d\phi_2 \quad \text{(A2)}$$

The following relations are thus found:

oblate ellipsoid: $\langle r_{12}^{-1} \rangle = (1/R)[1 + a^4/24R^4]$ (A3)

prolate ellipsoid: $\langle r_{12}^{-1} \rangle = (1/R)[1 + a^4/54R^4]$ (A4)

sphere: $\langle r_{12}^{-1} \rangle = (1/R)[1 + a^4/6R^4]$ (A5)

Comparing Eqns. A3—A5, it is evident that the equivalent "effective sphere" radii for oblate and prolate ellipsoids are $1/2^{1/2}\, a$ and $1/3^{1/2}\, a$, respectively.

REFERENCES

1 P. T. Callaghan, Aust. J. Phys., 37 (1984) 359.
2 E. Von Meerwall, Adv. Polym. Sci., 54 (1984) 1.
3 E. Von Meerwall, Rubber Chem. Technol., 58 (1985) 527.
4 C. J. Stacy and J. F. Foster, J. Polym. Sci., 25 (1957) 39.
5 S. R. Erlander and D. French, J. Polym. Sci., 20 (1956) 7.
6 P. T. Callaghan and J. Lelievre, Biopolymers, 24 (1985) 441.
7 J. Lelievre, J. A. Lewis and K. Marsden, Carbohydr. Res., (1986) in press.
8 R. Geddes, in G. O. Aspinall (Ed.), The Polysaccharides, Academic Press, New York, 1985.
9 P. Drochmans and E. Dantan, in W. J. Whelan (Ed.), Control of Glycogen Metabolism, Proc. FEBS Meet., 1967, pp. 187—201.
10 O. Larm, B. Lindberg and S. Svenson, Carbohydr. Res., 20 (1971) 39.
11 W. D. Comper, M. I. Van Damme and B. N . Preston, J. Chem. Soc. Faraday Trans., 78 (1982) 3369.
12 B. N. Preston, W. D. Comper, A. E. Hughes, I. Snook and W. Van Megen, J. Chem. Soc. Faraday Trans., 78 (1982) 1209.

13 T. C. Laurent, L. O. Sundelof, K. V. Wik and B. Warmegard, Eur. J. Biochem., 68 (1976) 95.
14 W. Brown and P. Stilbs, Polymer, 23 (1982) 1870.
15 P. T. Callaghan and D. N. Pinder, Macromolecules, 16 (1983) 968.
16 H. Yamakawa, Modern Theory of Polymer Solutions, Harper and Row, New York, 1971, p. 23.
17 P. J. Flory, J. Chem. Phys., 17 (1949) 303.
18 J. G. Kirkwood and J. Riseman, J. Chem. Phys., 16 (1948) 565.
19 H. Yamakawa, Modern Theory of Polymer Solutions, Harper and Row, New York, 1971, p. 253.
20 G. Weill and J. des Cloizeaux, J. Phys. (Paris), 40 (1979) 99.
21 C. Tanford, Physical Chemistry of Macromolecules, Wiley, New York, 1961, p. 327.
22 H. Yamakawa, J. Chem. Phys., 36 (1962) 2995.
23 C. W. Pyun and M. Fixman, J. Chem. Phys., 41 (1964) 937.
24 A. Z. Akcasu, Polymer, 22 (1981) 1169.
25 J. L. Aquirre and T. J. Murphy, J. Chem. Phys., 59 (1973) 1833.
26 G. K. Batchelor, J. Fluid Mech., 74 (1976) 1.
27 K. F. Freed and M. Muthukumar, J. Chem. Phys., 78 (1983) 511.
28 G. J. Evans and C. P. James, J. Chem. Phys., 79 (1983) 5553.
29 J. C. Anderson and C. C. Reed, J. Chem. Phys., 64 (1976) 3240.
30 E. Rushton and G. A. Davies, Appl. Sci. Res., 28 (1973) 37.
31 M. H. Davis, Chem. Eng. Sci., 24 (1969) 1769.
32 A. Abragam, Principles of Nuclear Magnetism, Oxford University Press, London, 1961, p. 299.
33 G. D. Phillies, J. Chem. Phys., 81 (1984) 1487.
34 P. T. Callaghan and D. N. Pinder, Macromolecules, 14 (1981) 1334.
35 A. H. Muhr and J. M. V. Blanshard, Polymer, 23 (1982) 1012.
36 J. H. Wang, J. Am. Chem. Soc., 76 (1954) 4755.
37 H. Fricke, Phys. Rev., 24 (1924) 575.
38 M. E. Clark, E. E. Burnell, N. R. Chapman and J. A. M. Hinke, Biophys. J., 39 (1982) 289.
39 G. G. Cleveland, D. C. Chang, C. F. Hazlewood and H. E. Rorschack, Biophys. J., 16 (1976) 1043.
40 B. Lindman, N. Kamenka, M. Puyal, B. Brun and B. Jonsson, J. Phys. Chem., 88 (1984) 53.
41 A. G. Ogston, B. N. Preston and J. D. Wells, Proc. R. Soc. London, Ser. A, 333 (1973) 297.
42 J. S. Mackie and P. Meares, Proc. R. Soc. London, Ser. B, 232 (1955) 498.
43 A. G. Ogston, Trans. Faraday Soc., 54 (1958) 1754.
44 M. H. Cohen and D. Turnbull, J. Chem. Phys., 31 (1959) 1164.
45 H. Fujita, in J. Crank and G. S. Park (Eds.), Diffusion in Polymers, Academic Press, London, 1968, p. 98.
46 J. S. Vrentas and J. L. Duda, J. Polym. Sci., A2, 15 (1977) 403.
47 C. Tanford, Physical Chemistry of Macromolecules, Wiley, New York, 1961, p. 343.
48 A. R. Altenberger and M. Tirrell, J. Chem. Phys., 80 (1984) 2208.
49 E. O. Stejskal and J. E. Tanner, J. Chem. Phys., 42 (1965) 288.
50 P. T. Callaghan and D. N. Pinder, Macromolecules, 18 (1985) 373.
51 E. Von Meerwall, J. Magn. Reson., 50 (1982) 409.
52 W. Banks and C. T. Greenwood, Starch and its Components, Edinburgh University Press, Edinburgh, 1975.
53 R. Geddes and G. C. Stratton, Carbohydr. Res., 52 (1977) 291.
54 F. W. Billmeyer, Textbook of Polymer Science, 2nd edn., Wiley International, New York, 1971, p. 42.
55 P. J. Daivis, private communication.

56 A. M. Basedow, K. H. Ebert and W. Feigenbutz, Makromol. Chem., 181 (1980) 1071.
57 K. Takeo, K. Hiroge and T. Kuge, Chem. Lett., 1233 (1973).
58 P. Colson, H. J. Jennings and I. C. P. Smith, J. Am. Chem. Soc., 96 (1974) 8081.
59 J. Szejtli and S. Augustat, Staerke, 18 (1966) 38.
60 W. Banks and C. T. Greenwood, Carbohydr. Res., 7 (1968) 414.
61 See for example P. G. de Gennes, Scaling Concepts in Polymer Physics, Cornell University Press, Ithaca, NY, 1979.
62 W. Banks, R. Geddes, C. T. Greenwood and I. G. Jones, Staerke, 8 (1972) 245.
63 R. Geddes, J. D. Harvey and P. R. Wills, Biochem. J., 163 (1977) 201.
64 R. L. Whister and J. N. BeMiller, Arch. Biochem. Biophys., 98 (1962) 120.
65 D. French, in R. L. Whistler, J. N. Be Miller and E. F. Paschall (Eds.), Starch, Chemistry and Technology, Academic Press, New York, 1984.

Analytica Chimica Acta, 189 (1986) 167—181
Elsevier Science Publishers B.V., Amsterdam — Printed in The Netherlands

FURTHER STUDIES OF MULTIPLE NUCLEAR SPIN RELAXATION AND LOCAL MOTIONS IN DISSOLVED 1,1-DICHLORO-2,2-BIS(4-HYDROXYPHENYL)ETHYLENE POLYFORMAL

CHI-CHENG HUNG, JOHN H. SHIBATA, MICHAEL F. TARPEY and ALAN A. JONES*
Jeppson Laboratory, Department of Chemistry, Clark University, Worcester, MA 01610 (U.S.A.)
JOHN A. PORCO and PAUL T. INGLEFIELD
Department of Chemistry, College of the Holy Cross, Worcester, MA 01610 (U.S.A.)
(Received 6th March 1986)

SUMMARY

Deuterium, carbon-13 and proton spin-lattice relaxation times at two fields are reported for dilute solutions of 1,1-dichloro-2,2-bis(4-hydroxyphenyl)ethylene polyformal. The carbon-13 and proton relaxation measurements were made at a concentration of 10% (w/w) in deuterated s-tetrachloroethane and as a function of temperature. A partially deuterated analog with deuterated methylene groups was used in order to remove cross-relaxation effects from the phenylene proton relaxation. In addition, deuterium relaxation measurements were made on this sample at a concentration of 10% (w/w) in tetrachloroethane as a function of temperature. The data are interpreted in terms of segmental motion arising within the bisphenol units and anisotropic internal rotations of the other structural components. Motions of the phenylene groups in the backbone are described by the Hall-Helfand segmental correlation function plus the Woessner anisotropic internal-rotation correlation function. Motions of the formal linkage are described by the same segmental correlation function plus an internal correlation function based on restricted double rotation about the two carbon/oxygen bonds. The local motion of the formal group is discussed in terms of conformational transitions that are likely in a polyformal in view of the conformational energy surface. A Helfand Type II motion of the formal group corresponding to a transition from *gg'* to *tg* is identified as the most plausible rearrangement of this unit.

Spin relaxation in dilute solution has been used to characterize local chain motion in several polymers with aromatic backbone units [1–5]. One notable type is aromatic polycarbonates which are common high-impact-resistant engineering plastics. The polymer examined here, 1,1-dichloro-2,2-bis(4-hydroxyphenyl)ethylene polyformal, shown in Fig. 1 and abbreviated Chloral-PF, is a structural analog of a well studied polycarbonate, Chloral-PC [4, 5]. The only difference in the structure of Chloral-PF relative to Chloral-PC is the replacement of the carbonate units by formal units. The formal unit presents an opportunity to monitor chain motion at a site inaccessible in polycarbonates because the carbonate unit contains no protons and thus cannot be probed by the usual approach. Additional motivation for study

0003-2670/86/$03.50

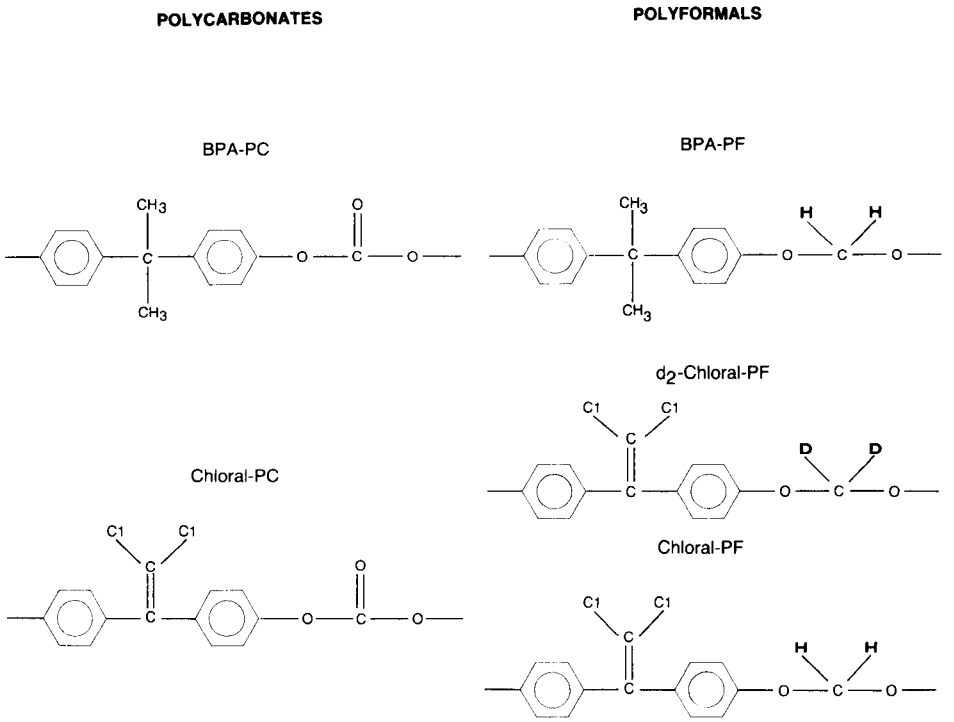

Fig. 1. Structure of the repeat units and the associated abbreviations.

arises because this polymer has a dynamic mechanical spectrum similar to the impact-resistant polycarbonates [6].

An early report of spin relaxation and local motion of dissolved Chloral-PF has already been presented [7]. In the present paper, an expanded data base is presented to verify and extend the previous interpretation. On the basis of the earlier data, the formal group was viewed as undergoing segmental motion originating in the bisphenol unit plus restricted rotational diffusion about an axis between the oxygens of the formal group. As discussed in the previous study, the choice of the O—O rotation axis is an approximation, leading to the conclusion that the formal group rotates freely about the O—O axis at high temperature. With an enlarged experimental data base, it is now possible to consider a more detailed and realistic model for the formal group motion. This model consists of simultaneous, restricted rotations about the C—O bonds in the formal linkage. The Szabo convention [8, 9] is adopted to describe simultaneous trans—gauche two-site jumps about the C—O bonds. This picture is consistent with solid-state deuterium n.m.r. studies on several polymers in which the methylene units in the backbone of the polymer chain undergo trans—gauche isomerization [10—12]. In the earlier study, it was also assumed that formal group rotation has no effect on the phenylene group motion. In the interpretation to be presented here, this assumption of

localized independent formal group motion continues to yield the best simulation of the data.

The deuterium magnetic resonance data reported here provide an independent probe of chain motion because the relaxation mechanism stems from the quadrupolar interaction. This mechanism is entirely different from the source of proton and carbon-13 relaxation which results from modulation of the dipole/dipole interaction. Also, certain complexities present in dipolar relaxation such as cross-relaxation and cross-correlation are absent from quadrupolar relaxation. The deuterium spin-relaxation times in this report are measured at two field strengths in the deuterated Chloral-PF analog shown in Fig. 1. The combination of deuterium, proton and carbon-13 relaxation measurements each at different field strengths provides an unusually extensive frequency probe (13.8—250 MHz) yielding a critical data base for quantifying the dynamics.

EXPERIMENTAL

High-molecular-weight samples of the polyformal were kindly supplied by General Electric. The structure of the repeat unit is shown in Fig. 1 as well as the structure of a partially deuterated form which was synthesized here [13]. Based on instrinsic viscosity, the weight-average molecular weight of the polyformal is 3.7×10^4 Daltons and that of the deuterated analogue is 2.9×10^4 Daltons. A 10% (w/w) solution of the polyformal in $C_2D_2Cl_4$ was prepared for proton and carbon-13 spin relaxation measurements. Another 10% (w/w) solution of the partially deuterated polymer in tetrachloroethane was also prepared for deuterium spin-relaxation measurements. These two samples were subjected to five freeze/pump/thaw cycles before sealing.

Two spectrometers were used. The 30- and 90-MHz proton measurements, the 22.6-MHz carbon-13 measurement and 13.815-MHz deuterium measurement were obtained on a Bruker SXP 20-100. The 250-MHz proton, 62.9-MHz carbon-13 and 38.397-MHz deuterium measurements were obtained on a Bruker WM-250. Temperature control was maintained to ±2 K with a Bruker B-ST 100/700 variable-temperature accessory calibrated against a thermocouple placed in a sample tube. All T_1 measurements were made with a standard $180°—\tau—90°$ sequence and are reported with an experimental uncertainty of 10%. Typical $\pi/2$ pulse widths for all nuclei are in the range 10—25 μs. The 10% error reported for T_1 includes errors arising from sample preparation, temperature control, pulse sequence and the fitting of the recovery of magnetization to equilibrium.

RESULTS

The recovery of magnetization to equilibrium monitored in the $180°—\tau—90°$ sequence follows a simple exponential dependence on delay time, τ. The data were fitted both with the standard linear least-squares form and non-

linear least-squares form. The two treatments yielded relaxation times (T_1) within 10% of each other and average values are reported. No evidence of cross-relaxation or cross-correlation were observed in the decay curve of the recovery of magnetization. The presence of cross-relaxation in the proton data was further checked by comparing the phenylene T_1 value in the fully protonated polymer to the phenylene T_1 value in the deuterated polymer. The phenylene proton T_1 is about 10% longer in the deuterated polymer indicating a small amount of cross-relaxation though the 10% change is essentially the same as the experimental uncertainty. Table 1 contains proton, carbon-13 and deuterium T_1 values as a function of temperature and Larmor frequency.

Interpretation

The standard relationships between T_1 values and spectral densities, J, are used for carbon-13, the expressions are:

$$1/T_1 = W_0 + 2W_{1c} + W_2$$

$$W_0 = \sum_j \gamma_C^2 \gamma_H^2 \hbar^2 J_1(\omega_0)/20 r_j^6$$

TABLE 1

Spin-lattice relaxation times of Chloral-PF

Temp. (°C)	Relaxation time (ms)			
	Phenylene proton		Phenylene carbon	
	90 MHz	30 MHz	62.9 MHz	22.6 MHz
0	548	153	137	72
20	499	189	174	106
40	522	274	243	156
60	628	412	377	349
80	794	553	543	448
100	1168	763	798	679
120	1411	939	1113	936

Temp. (°C)	Relaxation time (ms)					
	Formal proton		Formal carbon		Formal deuterium	
	250 MHz	90 MHz	62.9 MHz	22.6 MHz	38.4 MHz	13.8 MHz
−20					3.15	1.09
0	335	129	81	36	3.09	1.55
20	282	114	91	52	3.97	2.70
40	268	133	115	82	6.21	5.44
60	295	198	158	123	11.92	10.65
80	350	258	229	193	17.95	17.00
100	467	320	339	275	28.86	27.40
120	628	433	403	377	41.08	40.57

$$W_{1c} = \sum_j 3\gamma_C^2\gamma_H^2\hbar^2 J_1(\omega_C)/40r_j^6 \tag{1a}$$

$$W_2 = \sum_j 3\gamma_C^2\gamma_H^2\hbar^2 J_2(\omega_2)/10r_j^6$$

$$\omega_0 = \omega_H - \omega_C \quad \omega_2 = \omega_H + \omega_C$$

and for protons the relationship is

$$1/T_1 = \sum_j (9/8)\gamma^4\hbar^2 r_j^{-6}[(2/15)J_1(\omega_H) + (8/15)J_2(2\omega_H)] \tag{1b}$$

For deuterium quadrupole relaxation in liquids, the expression [14] is

$$1/T_1 = (3/80)(1 + \eta^2/3)(e^2qQ/\hbar)^2 [J(\omega_D) + 4J(2\omega_D)] \tag{1c}$$

where $e^2qQ/\hbar$ is the quadrupole coupling constant. The asymmetry parameter, η, is negligibly small for deuterium [11, 14].

The internuclear distances used are 1.09 Å for the phenylene C—H distance, 1.135 Å for the formal C—H distance, 2.36 Å for the 2—3 phenylene proton distance, and 1.79 Å for the formal proton—proton distance. The internuclear distance between the 2 and 3 phenylene protons is small but it is consistent with x-ray results on a similar low-molecular-weight molecule, dimethyl terephthalate [15]. The quadrupolar relaxation expression requires knowledge of the quadrupole coupling constant. For polymethylene oxide, the methylene quadrupole coupling constant is 154 ± 2 kHz [11]. For the polymethylene chains, the coupling constant is 167 kHz [12]. The coupling constant used here, 160 kHz, is in reasonable agreement with these values.

The expressions for the spectral densities can be developed from models for local motion in randomly coiled chains. The local motions to be considered here are segmental rearrangements, phenylene group rotation and formal group rotation. Segmental motion is described by a model developed by Helfand and coworkers [16, 17], based on computer simulations of chain dynamics. The correlation function for segmental motion involves two motional processes and is given by

$$\phi(t) = \exp(-t/\tau_0)\exp(-t/\tau_1) I_0(t/\tau_1) \tag{2}$$

where τ_1 is the correlation time for cooperative conformational transitions involving several bonds, τ_0 is the correlation time for single-bond conformational transitions, and I_0 is a modified Bessel function of order zero. This correlation function has been successfully applied to the solution study of polycarbonates [5]. Single bond and cooperative transitions occur in the bisphenol units of the backbone. Segmental motions about the bonds of this unit, depicted in Fig. 2, affect the dynamics of both the phenylene and formal groups. The correlation function can be Fourier-transformed to yield the following spectral density required for calculation of spin relaxation.

$$J(\omega) = 2\{[(\tau_0^{-1})(\tau_0^{-1} + 2\tau_1^{-1}) - \omega^2]^2 + [2(\tau_0^{-1} + \tau_1^{-1})\omega]^2\}^{-1/4}$$
$$\cos\{1/2 \arctan 2(\tau_0^{-1} + \tau_1^{-1})\omega/[\tau_0^{-1}(\tau_0^{-1} + 2\tau_1^{-1}) - \omega^2]\} \tag{3}$$

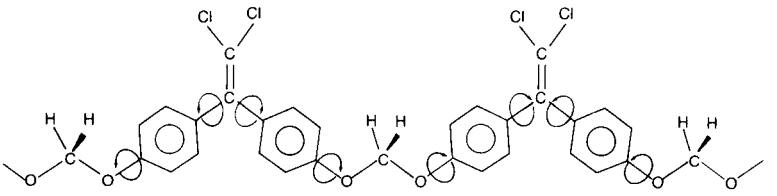

Fig. 2. The physical picture of segmental motion within the bisphenol unit. The arrows indicate those bonds in the bisphenol unit, the reorientation of which is included in the description of segmental motion.

Local phenylene and formal group rotation can be described by anisotropic internal rotation [18]. The correlation function for a trans–gauche two-site jump in the formal group can be calculated by using the Jones two-site jump model [19]. For two rotational equilibrium positions, the time-dependent probabilities can be calculated:

$$P(\phi_i, 0) = 1/2$$

$$P(\phi_j, t \mid \phi_i 0) = 1/2\ [1 + \exp(-t/\tau)]\ (\text{for } i = j) \tag{4}$$

$$P(\phi_j, t \mid \phi_i, 0) = 1/2\ [1 - \exp(-t/\tau)]\ (\text{for } i \neq j)$$

where $P(\phi_i, 0)$ is the probability of finding the internuclear vector at angle ϕ_i; $P(\phi_j, t \mid \phi_i, 0)$ is the time-dependent probability of finding the internuclear vector at angle ϕ_j given ϕ_i at time $t = 0$. The correlation function can thus be calculated by using those probabilities:

$$\begin{aligned} g_{mp}(t) &= \exp[im\phi_i(0)]\ \exp[-ip\phi_j(t)] \\ &= \sum_i P(\phi_i, 0)\ \exp(im\phi_i)\ [\sum_j \exp(-ip\phi_j)\ P(\phi_j, t \mid \phi_i, 0)] \end{aligned} \tag{5}$$

Assuming that the correlation function is independent of the initial position, $\phi_i(0)$, which is dependent on the choice of the coordinate system, then

$$g_{mm}(t) = 1/2[1 + \exp(-t/\tau_{irf})] + 1/2[1 - \exp(-t/\tau_{irf})]\ (\cos m\phi) \tag{6}$$

When $m \neq p$, $g_{mp}(t) = 0$. Here, ϕ is the jump angle, and τ_{irf} is the jump relaxation time. For the trans–gauche conformational change, $\phi = 120°$, and thus

$$g_{00}(t) = 1; g_{\pm1\pm1}(t) = g_{\pm2\pm2}(t) = 1/4 + 3/4\ \exp(-t/\tau_{irf}) \tag{7a}$$

For $\phi = 180°$, referred to as a π flip,

$$g_{00}(t) = 1; g_{\pm1\pm1}(t) = \exp(-t/\tau_{irf}); g_{\pm2\pm2}(t) = 1 \tag{7b}$$

The Szabo formula is used next to express the internal correlation function for double rotations as

$$G(t) = \sum_{mn} \sum_{p} \mathbf{d}^2_{mo}[\Delta]\ \mathbf{d}^2_{no}[\Delta] * \mathbf{d}^2_{pn}(\beta_{21})\ \mathbf{d}^2_{pm}(\beta_{21})\ g^{(1)}_{mn}(t) g^{(2)}_{pp}(t) \tag{8}$$

where $\mathbf{d}^2_{mo}[\Delta]$, $\mathbf{d}^2_{no}[\Delta]$, $\mathbf{d}^2_{pn}[\beta_{21}]$ and $\mathbf{d}^2_{pm}[\beta_{21}]$ are reduced Wigner rotation matrices. A frame 1 is defined such that the rotation axis, Z_1, is along the Z axis of frame 1. The internuclear vector I rotates about the Z_1 axis, as shown in Fig. 3. Similarly, the Z_1 axis rotates about the Z axis of frame 2. Here, Δ is the angle between the internuclear vector and the rotation axis Z_1; β_{21} is the Euler angle between the two rotation axes Z_1 and Z_2; and $g^{(1)}_{mn}(t)$ and $g^{(2)}_{pp}(t)$ are the correlation functions describing rotation of the internuclear vector about the Z_1 axis, and the rotation of frame 1 about the Z axis of frame 2, respectively. Equation 8 can be simplified when the correlation function is independent of initial states. For this case, $m = n$, and $G(t)$ becomes,

$$G(t) = \sum_{mp} [\mathbf{d}^2_{mo}(\Delta)]^2 \, [\mathbf{d}^2_{pm}(\beta_{21})]^2 \, g^{(1)}_{mm}(t) g^{(2)}_{pp}(t) \tag{9}$$

By using this equation, several types of anisotropic motion can be introduced including jumps between two minima, jumps between three minima or stochastic diffusion.

In the case of one internal rotation axis, the correlation function in Eqn. 8 reduces to

$$G(t) = \sum_{mn} \mathbf{d}^2_{mo}[\Delta] \, \mathbf{d}^2_{no}[\Delta] * g_{mn}(t) = \sum_{m} \{\mathbf{d}^2_{mo}[\Delta]\}^2 g_m(t) \tag{10}$$

where $g_m(t)$ is the correlation function described by Woessner [18]. For stochastic diffusion of phenylene group rotation about the C_1—C_4 axis, the correlation function is

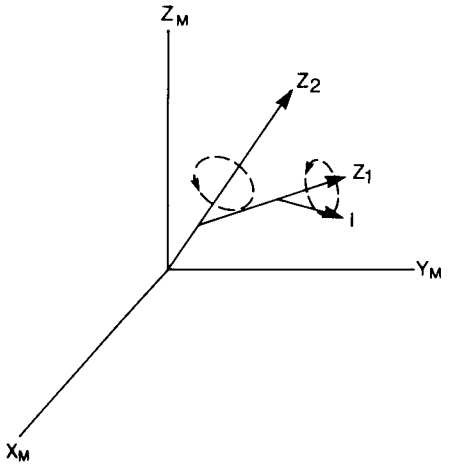

Fig. 3. The coordinate systems for double internal rotations of the formal group. The internuclear vector, I, rotates about the Z_1 axis. Z_1 rotates about the Z_2 axis which is the Z axis of frame 2. The axes of the molecular frame (Z_m, Y_m, X_m) are arbitrarily chosen to coincide with those of frame 2 (cf. [20]).

$$G(t) = A + B\exp(-t/\tau_{irp}) + C\exp(-4t/\tau_{irp}) \tag{11}$$

where $A = (3\cos^2\Delta - 1)^2/4$, $B = 3(\sin^2 2\Delta)/4$, and $C = 3(\sin^4\Delta)/4$.

The correlation function for segmental motion can be combined with formal group rotation and phenylene group rotation to yield a composite correlation function when each of the three local motions is considered to be independent. By using Eqns. 2 and 9, this composite correlation function can be Fourier-transformed to yield the following spectra density:

$$\begin{aligned} J(\omega) &= 2\,Re\int_0^\infty \phi(t)\,G(t)\exp(i\omega t)dt \\ &= 2\,Re\int_0^\infty \sum_{mp} [\mathbf{d}^2_{mo}(\Delta)]^2\,[\mathbf{d}^2_{pm}(\beta_{21})]^2\exp(-t/\tau_0)\exp(-t/\tau_1)\,I_0(t/\tau_1) \\ &\quad g^{(1)}_{mm}(t)g^{(2)}_{pp}(t)\exp(i\omega t)dt \end{aligned} \tag{12}$$

By inserting the internal correlation function for formal group motion described by Eqn. 7(a) and integrating, the spectra density becomes

$$\begin{aligned} J(\omega) &= J_a(\tau_0,\tau_1,\omega)\,[\mathbf{d}^2_{00}(\Delta)]^2\,[\mathbf{d}^2_{00}(\beta_{21})]^2 \\ &\quad + [1/16\,J_a(\tau_0,\tau_1,\omega) + 3/8\,J_b(\tau_{b0},\tau_1,\omega) + 9/16\,J_c(\tau_{c0},\tau_1,\omega)] \\ &\quad < 2[\mathbf{d}^2_{20}(\Delta)]^2\ \{[\mathbf{d}^2_{22}(\beta_{21})]^2 + [\mathbf{d}^2_{22}(\beta_{21})]^2\} \\ &\quad + 2[^2_{10}(\Delta)]^2\ \{[\mathbf{d}^2_{11}(\beta_{21})]^2 + [\mathbf{d}^2_{1\text{-}1}(\beta_{21})]^2\} \\ &\quad + 2\{[\mathbf{d}^2_{10}(\Delta)]^2 + [\mathbf{d}^2_{20}(\Delta)]^2\}\ \{[\mathbf{d}^2_{21}(\beta_{21})]^2 + [\mathbf{d}^2_{2\text{-}1}(\beta_{21})]^2\} > \\ &\quad + [1/4\,J_a(\tau_0,\tau_1,\omega) + 3/4\,J_b(\tau_{b0},\tau_1,\omega)] \\ &\quad < 2\{[\mathbf{d}^2_{00}(\Delta)]^2 + [\mathbf{d}^2_{20}(\Delta)]^2\}\ [\mathbf{d}^2_{20}(\beta_{21})]^2 \\ &\quad + 2\{[\mathbf{d}^2_{00}(\Delta)]^2 + [\mathbf{d}^2_{10}(\Delta)]^2\}\ [\mathbf{d}^2_{10}(\beta_{21})]^2 > \end{aligned} \tag{13}$$

with $\tau^{-1}_{b0} = \tau^{-1}_0 + \tau^{-1}_{irf}$ and $\tau^{-1}_{c0} = \tau^{-1}_0 + (\tau_{irf}/2)^{-1}$

Here, $J_a(\tau_0, \tau_1, \omega)$, $J_b(\tau_{b0}, \tau_1, \omega)$ and $J_c(\tau_{c0}, \tau_1, \omega)$ have the same form as Eqn. 3 with τ_0 replaced by τ_0, τ_{b0} and τ_{c0}, respectively. A correlation time, τ_{irf}, is set for the time scale of formal rotation about the C—O axes.

For phenylene group motion, two approaches were considered. The first approach allows no effect from formal group rotation and the second approach allows for the effect of rotation of formal group. In the first case, simply substituting Eqn. 11 for $G(t)$ into Eqn. 12 yields the spectral density

$$J(\omega) = AJ_x(\tau_0,\tau_1,\omega) + BJ_y(\tau_{y0},\tau_1,\omega) + CJ_z(\tau_{z0},\tau_1,\omega) \tag{14}$$

For stochastic diffusion,

$$\tau^{-1}_{y0} = \tau^{-1}_0 + \tau^{-1}_{irp};\ \tau^{-1}_{z0} = \tau^{-1}_0 + (\tau_{irp}/4)^{-1} \tag{15}$$

The form of J_x, J_y and J_z is the same as in Eqn. 3 with τ_0 replaced by τ_0, τ_{y0} and τ_{z0}, respectively. A correlation time, τ_{irp}, is set for the time scale of phenylene rotation. In the second case, the correlation function for phenylene group motion is obtained by multiplying the correlation function for stochastic diffusion given by Eqn. 11 with a correlation function given by Eqn. 7(a). Following the same calculation as in the derivation of Eqn. 13, then yields a lengthy but very similar result to Eqn. 13.

Because of the simple form for segmental motion in the Hall-Helfand correlation function [16], Eqns. 13 and 14 can be used in a nonlinear least-squares program to fit the data as a function of temperature if an Arrhenius dependence is assumed for τ_0, τ_1 and τ_{irf}. Two frequencies of phenylene proton data and six more frequencies, two each for formal proton, carbon and deuterium data, are simulated by three parameters: τ_0, τ_1 and τ_{irf}. Because both the formal group and phenylene group are in the backbone, it is required that the same τ_0 and τ_1 parameters for segmental motion are used in fitting the formal and phenylene group motion. After the segmental and formal motion parameters have been measured, the correlation time, τ_{irp}, for phenylene group rotation is determined from the phenylene carbon data. All experimental relaxation times can be simulated to about 10%, which is within experimental error. Correlation times and Arrhenius parameters are compiled in Table 2.

Because the phenylene proton/proton dipole interaction is parallel to the C_1—C_4 axis of the ring, proton T_1 values of the phenylene group measured at two frequencies can conceivably be affected by both segmental motion and formal group motion. If the effect of formal group rotation is included in the simulation as discussed above, the phenylene group would rotate 120° about the C—O axis. This leads to deviations from the experimental phenylene T_1 values, producing high T_1 predictions for the entire temperature

TABLE 2

Simulation parameters for Chloral-PF using the Hall-Helfand model

Temp. (°C)	τ_1(ns)	τ_0(ns)	τ_{irp}(ns)	τ_{irf}(ns)
−20	3.40	25.0	—	15.0
0	2.38	11.0	2.15	4.5
20	1.14	6.5	1.19	2.5
40	0.60	4.14	0.81	0.99
60	0.34	2.77	0.37	0.57
80	0.21	1.94	0.26	0.34
100	0.13	1.41	0.18	0.21
120	0.088	1.06	0.126	0.149
E_a (kJ mol^{-1})	24.5	17.4	21.0	26.1
τ_∞ (fs)	48.9	5160.0	188.4	77.4
Correlation coefficient	0.99	0.99	0.99	0.99

range. Inclusion of the formal motion in the calculation of the phenylene group relaxation simply leads to too much motion. If the phenylene group rotation is considered over smaller angles, e.g., 60° or less, about the C—O axis, it is possible to simulate the proton and carbon data by re-adjusting the simulation parameters (τ_1, τ_0 and τ_{irf}). However, the deuterium data cannot be simulated well with this set of parameters. This difficulty indicates the utility of a large data base in discriminating between various motional possibilities. The only consistent interpretation found restricts formal group internal rotation to the formal group with no associated motion of the phenylene group. It is possible that very small amplitude motion of the phenylene group resulting from formal motion exists but major reorientation is unlikely to view of the present simulation results.

DISCUSSION

The results for formal group motion differ from the earlier study on this system. The current interpretation involves trans—gauche isomerization within the formal unit and this motion does not extend beyond the formal unit. By applying the double internal rotation concept to the formal group and including two deuterium frequency measurements, it is possible to obtain

TABLE 3

Comparisons of simulation parameters of polycarbonates and polyformal

Polymer	Segmental motion				Ref.
	Apparent activation energy (kJ mol^{-1})		Arrhenius prefactor τ_∞ (fs)		
	Cooperative segmental	Single backbone rotation	Cooperative segmental	Single backbone rotation	
	T_g(°C) (τ_1)	(τ_0)	(τ_1)	(τ_0)	
BPA-PC	150 19	16	280	10030	4
Chloral-PC	164 17	18	940	4090	4
Chloral-PF	108 25	17	50	5160	This work

		Phenylene ring motion			
	T_γ(°C)[a]	Type	E_a (kJ mol^{-1})	τ_∞ (fs)	
BPA-PC	−100	Stochastic diffusion	22	60	4
Chloral-PC	−100	Stochastic diffusion	18	400	4
Chloral-PF	−100	Stochastic diffusion	21	190	This work

[a]The temperature of the main sub-glass transition loss peak measured at 1 Hz [6].

reasonable time scales and activation energies for segmental motion and internal rotation which can be compared to the corresponding values obtained for the polycarbonates [3–5]. Table 3 contains those comparisons. The similarity of the segmental motion is apparent and reasonable because the segmental description reflects motions within the bisphenol unit as shown in Fig. 2 and is not associated with the formal or carbonate groups. One interesting difference between the Hall-Helfand interpretation of Chloral-PF and the polycarbonates is the relative apparent activation energies for τ_1 and τ_0. For the polycarbonates, the activation energies for cooperative segmental motion and single backbone bond rotation are found to be similar. This can only occur if cooperative segmental motions occur sequentially as opposed to simultaneously [21–23]. For the Chloral-PF, the activation energy for the cooperative process is somewhat higher than for the single transitions which may be indicative of more nearly simultaneous cooperative transitions such as those produced by crankshaft motions. The same result was also found in another solution study of a related system, Bisphenol A polyformal (BPA-PF) [24]. The difference in activation energy for the above two processes in BPA-PF is smaller but still significant. The single transitions are minor processes in both the polycarbonates and polyformals, primarily because of the larger prefactor as opposed to a larger activation energy.

Phenylene group rotation in the Chloral-PF can also be compared to that of Chloral-PC. Phenylene group rotation in Chloral-PF is a factor of 1.5 to 2.0 slower at a given temperature relative to Chloral-PC but the activation energy for phenylene group rotation in both polymers are quite similar [5]. This suggests that phenylene group rotation is dominated by the local potential energy surface and is not greatly affected by the change from a formal link to a carbonate link. The phenylene group rotation in solution is best modeled by stochastic diffusion while it is modeled by π flips in glassy polycarbonates [20, 25, 26]. Calculations by Tonelli [27] suggest a low barrier to phenylene group reaction for an isolated polycarbonate chain. MNDO calculations on the dichloroethylene unit indicate a high barrier, 42 kJ mol^{-1}, to phenylene group rotation [28]. The discrepancy between these solution results and the calculation is not resolved but the similarity of the experimental data between the Chloral unit and the Bisphenol A unit is indicative of comparable mobility.

The best simulation for formal group rotation is obtained by applying double internal rotations about the C—O bonds while not allowing these motions to contribute to phenylene relaxation. This motion is described as a product form of two single exponential correlation functions. A physical representation of formal group motion that is consistent with the simulation results, particularly the lack of influence on the phenylene group, is a challenging task. The conformational states of the formal group are not known with certainty but can be inferred from similar small-molecule structures and for this purpose the conformational energy map of dimethoxymethane is important [29, 30]. The lowest conformational states of the formal group in dimethoxymethane are gg' and $g'g$. This unusual situation relative to poly-

ethylene chains is commonly called the anomeric effect [31, 32]. Corresponding to each of these conformations, there are two conformations which are only 4 kJ higher in energy. The tg' and gt conformations are energetically near the gg' conformation while the tg and $g't$ conformations are energetically near the $g'g$ conformation. The $g'g'$, gg and tt states are higher in energy. Because of the similarity of conformational changes for gg' and $g'g$ and for simplicity, only the gg' case is illustrated. The most facile conformational changes from the lowest states can be represented by

$$gg' \leftrightharpoons (tg') \leftrightharpoons tg \tag{16}$$

$$gg' \leftrightharpoons (gt) \leftrightharpoons g't \tag{17}$$

These conformational changes can be applied to the formal groups of polymer chain. Figure 4 illustrates local formal group motion resulting from conformational state changes in a repeat unit. The lowest conformational state is gg' as shown in Fig. 4(1). In Eqn. 16, gg' undergoes trans–gauche rotation to form tg' in Fig. 4(2). This simple trans–gauche isomerization leads to rotation of the chain end but this dislocation can be avoided by allowing a second reorientation, tg' to tg. Here the chain end is translated but not reorientated which corresponds to a Helfand Type II motion [21].

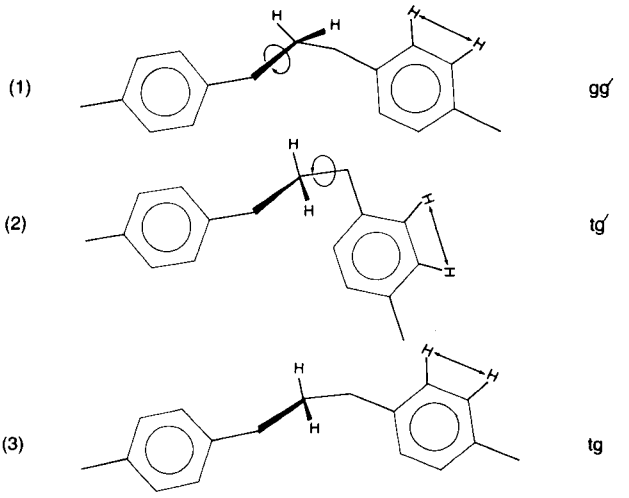

Fig. 4. Likely conformational transitions of the formal group. The motional process associated with Eqn. 16 is shown (see text) with arrows indicating the rotations of the conformational changes from (1) to (3). The overall conformational process is gg' to tg with the intermediate state of tg' shown only to indicate the two conformational changes involved in the overall process. The intermediate state, tg', is an unlikely transition state because it involves a large rotation of the chain end and some other pathway avoiding the tg' intermediate is likely. Nevertheless, the conformations of two bonds change, which is the point made by the inclusion of the tg' state. The proton/proton dipolar interaction of the phenylene group is only translated and not reoriented. This is a Helfand Type II motion thought to be a generally plausible form of segmental motion [21].

Thus the net conformational change is gg' to tg but for calculational purposes, it can be produced in two steps: gg' to tg' and then tg' to tg. However, the state tg' is not proposed as a real intermediate but rather as calculational intermediate. The process, gg' to tg, is not observed in the computer simulations of Helfand which were used to verify the importance of Type II processes. This gg' conformation is rare in an alkane backbone but important in polyethers such as polymethylene oxide where the dynamic process gg' to tg could be quite significant.

Returning to the aromatic polyformal of this study, the motion proposed in Fig. 4 does not reorientate the proton/proton interaction in the phenylene group and thus this formal motion will not cause phenylene group relaxation, which is consistent with experimental results. An exactly analogous process involving the other C—O bond can occur as noted in Eqn. 17. In this case, gg' undergoes two 120° bond rotations to form $g't$. If one combines both processes in Eqns. 16 and 17, there are two possible isomerization mechanisms to cause reorientation in a formal group. This picture is consistent with the mathematical interpretation of double trans—gauche rotations on the formal group developed in the context of the Szabo formulae.

Because the formal group motion may be coupled with other formal groups across the bisphenol group and undergo cooperative transitions, the orientation correlation function describing these cooperative transitions was examined. In general, these correlation functions are not exponential [33]. Helfand derived the orientation correlation function given in Eqn. 2, which includes a Bessel function to describe cooperative transitions. This correlation function has been applied in the present treatment of formal group motion in place of a single exponential function. However, this correlation function does not simulate the data throughout the entire temperature and frequency range, which is not surprising because a distribution of correlation times would increase the breadth of the T_1 minimum whereas the experimental T_1 curves are quite narrow. Other types of correlation functions corresponding to crankshaft and the three-bond-jump motion also involve a distribution of correlation times and would similarly increase the breadth of the T_1 minimum. Skinner and Budimir [34] have presented a treatment of cooperative sequential motions which leads to a single exponential form but no simple identification was found between the Skinner treatment and the polyformal conformational transitions.

The interpretation described here has been successfully tested by another solution T_1 study of BPA-PF which includes data as a function of field, temperature and concentration [24].

The trans—gauche isomerization in Chloral-PF is also under study in the glassy state by solid-state deuterium n.m.r. experiments; the simulation of these experimental results are still in progress. It would be interesting to know whether the local chain dynamics model proposed here for formal and phenylene group internal rotation still persists in the glassy state. Recently, Jones [35] proposed a model for the chain dynamics of polycarbonates which

involves trans—cis conformational changes of the carbonate unit. The polycarbonate chain is mainly composed of trans—trans carbonate units with occasional cis—trans or trans—cis carbonate units. The phenylene rings undergo flips in association with the C—O bond rotations. The neighboring carbonate would undergo counter-rotation from the trans—cis state to the trans—trans state. The C_1—C_4 axes of the phenylene rings between these two rotating carbonate units only reorient by 11° or less. Over a period of time, all phenylene rings would be flipped as the cis—trans and trans—cis conformations diffuse along the chain. This dynamic model is somewhat different than the formal group model discussed above though they are related. In the formal motional description, there is no cooperative reorientation of a neighboring formal unit which could compensate the translational motion whereas such a compensatory process is proposed in glassy polycarbonates. The results of relaxation studies on glassy polyformal will help sharpen the similarities and differences between the two systems.

The ability of multinuclear, multifrequency n.m.r. to distinguish complex dynamic possibilities existing in high-molecular-weight polymer solutions is encouraging and suggests that n.m.r. with its ability to probe different atomic sites in the repeat unit and differing motional timescales offers real potential for testing the various chain dynamic models based on repeat unit structure and conformation.

This research was done with the financial support of the National Science Foundation Grant DMR-790677, of National Science Foundation Equipment Grant No. CHE 77-09059, of National Science Foundation Grant No. DMR-8108679, and of U.S. Army Research Office Grants DAAG 29-82-G-0001, and DAAG 29 85-K0126. We thank the Worcester Consortium NMR Facility for use of the SXP90 and WM250 spectrometers, and Mr. Frank Shea for his assistance.

REFERENCES

1 A. A. Jones and R. P. Lubianez, Macromolecules, 11 (1978) 126.
2 R. P. Lubianez, A. A. Jones and M. Bisceglia, Macromolecules, 12 (1980) 1141.
3 A. A. Jones and M. Bisceglia, Macromolecules, 12 (1979) 1136.
4 J. F. O'Gara, S. G. Dejardins and A. A. Jones, Macromolecules, 14 (1981) 64.
5 J. J. Connolly, E. Gordon and A. A. Jones, Macromolecules, 17 (1984) 722.
6 A. F. Yee and S. A. Smith, Macromolecules, 14 (1981) 54.
7 M. F. Tarpey, Y.-Y. Lin, A. A. Jones and P. T. Inglefield, in J. C. Randall (Ed.), NMR and Macromolecules, American Chemical Society, Washington, DC, 1984; Am. Chem. Soc. Symp. Ser., No. 247, 1984, p. 67.
8 A. Szabo, J. Chem. Phys., 81 (1984) 1.
9 R. J. Wittebort and A. Szabo, J. Chem. Phys., 69 (1978) 1722.
10 L. W. Jelinski, J. J. Dumais and A. K. Engel, Macromolecules, 16 (1983) 492.
11 D. Hentschel, H. Sillescu, H. Spiess, H. Voelkel and R. Willenberg, XIX Congress Ampere, Heidelberg 1976, p. 381.
12 T. H. Huang, R. P. Skarjune, R. J. Wittebort, R. G. Griffin and E. J. Oldfield, J. Am. Chem. Soc., 102 (1980) 7377.

13 A. S. Hay, F. J. Williams, G. M. Loucks, H. M. Relles, B. M. Boulette, P. E. Donabue and D. S. Johnson, Polym. Prepr. Am. Chem. Soc. Div. Polym. Chem., 23(2) (1982) 117.
14 A. Abragam, The Principles of Nuclear Magnetism, Oxford University Press, Clarendon, 1961, p. 347.
15 P. F. Brisse and S. Perez, Acta Crystallogr., 1332 (1976) 2110.
16 C. K. Hall and E. Helfand, J. Chem. Phys., 77 (1982) 3275.
17 T. A. Weber and E. Helfand, J. Phys. Chem., 87 (1983) 2881.
18 D. E. Woessner, J. Chem. Phys., 36 (1962) 1.
19 A. A. Jones, J. Polym. Sci., Polym. Phys. Ed., 15 (1977) 863.
20 H. W. Spiess, Colloid Polym. Sci., 261 (1983) 193.
21 E. Helfand, J. Chem. Phys., 54 (1971) 4651.
22 E. Helfand, Z. R. Wasserman and T. A. Weber, Macromolecules, 13 (1980) 526.
23 J. Skolnik and E. Helfand, J. Chem. Phys., 72 (1980) 5489.
24 C.-C. Hung, J. H. Shibata, A. A. Jones and P. T. Inglefield, Polymer, in press.
25 P. T. Inglefield, R. M. Amici, J. F. O'Gara, C.-C. Hung and A. A. Jones, Macromolecules, 16 (1983) 1552.
26 J. F. O'Gara, A. A. Jones, C.-C. Hung and P. T. Inglefield, Macromolecules, 18 (1985) 1117.
27 A. E. Tonelli, Macromolecules, 5 (1972) 558; 6 (1973) 503.
28 A. A. Jones, J. F. O'Gara, P. T. Inglefield, J. T. Bendler, A. F. Yee and K. L. Ngai, Macromolecules, 16 (1983) 658.
29 I. Tvaroska and T. Bleha, J. Mol. Struct., 24 (1975) 249.
30 G. A. Jeffrey and R. Taylor, J. Comput. Chem., 1 (1980) 99.
31 S. Wolfe, Acc. Chem. Res., 5 (1972) 102.
32 E. L. Ehel, Angew. Chem., 84 (1972) 779.
33 J. L. Skinner, J. Chem. Phys., 79 (1983) 1955.
34 J. L. Skinner and J. Budimir, J. Chem. Phys., 82 (1985) 5232.
35 A. A. Jones, Macromolecules, 18 (1985) 902.

Analytica Chimica Acta, 189 (1986) 183—197
Elsevier Science Publishers B.V., Amsterdam — Printed in The Netherlands

AN INSTRUMENT FOR MEASURING THE OSCILLATORY ELECTRIC BIREFRINGENCE PROPERTIES OF POLYMER SOLUTIONS

R. L. MORRIS and T. P. LODGE*
Department of Chemistry, University of Minnesota, Minneapolis, MN 55455 (U.S.A.)
(Received 14th April 1986)

SUMMARY

An instrument for measuring the oscillatory electric birefringence properties of synthetic polymers dissolved in organic solvents has been designed and constructed. Novel features of the design include an in situ variable inter-electrode spacing Kerr cell and a double-beam optical train. The accessible frequency range extends from below 1 Hz to at least 100 kHz, with electric fields variable up to approximately 6000 V cm^{-1} (peak-to-peak). Measurements are made with a powerful computerized data acquisition and processing system, based on an approach previously used for viscoelastic and oscillatory flow birefringence experiments. Preliminary results on a viscous liquid, Aroclor-1248, indicate that time-temperature superposition holds up to reduced frequencies of at least 100 MHz. Comparison with theoretical predictions for rigid rod suspensions suggests that this liquid exhibits relaxation behavior with a time constant of ca. 6 ns at 25.00°C.

The dynamics of conformational change of flexible polymers in solution have long been recognized as a powerful means for characterization, and as an important route to elucidating the complex relationships between detailed chemical structure and macroscopic physical properties of macromolecular systems [1—3]. Conformational rearrangements, which may be thermally driven or induced by the application of external fields, are not only revealing of polymer properties, but also in many cases their direct cause, e.g., flexibility and elasticity. From an experimental viewpoint, a crucial feature of these molecular motions is the wide range of time scales involved. A typical high-molecular-weight polymer may exhibit conformational rearrangements with characteristic times ranging from nanoseconds to seconds. There is a natural correspondence between time scale and length scale; for instance, relaxation times in the nanosecond range would be associated with motions involving characteristic repeat units containing only a few monomers, while the longest relaxation times reflect rearrangements of the entire molecule. It is a continuing challenge to design experiments that can probe as much of this time range as possible, while simultaneously maintaining the sensitivity necessary to extract single chain information.

One class of experiments which has demonstrated great potential in this area involves the measurement of the optical birefringence induced in a polymer solution by the action of a sinusoidally time-varying external

0003-2670/86/$03.50

orientating field. Three kinds of field have been considered: hydrodynamic, electric, and magnetic, corresponding to the physical phenomena known as the Maxwell, Kerr, and Cotton-Mouton effects, respectively. Of these three, the hydrodynamic approach in the form of oscillatory flow birefringence (OFB) has been developed to the greatest extent [4—9], while oscillatory electric birefringence (OEB) is the subject of this paper. The OFB and OEB approaches may be thought of as optical analogs to the more familiar linear viscoelastic and dielectric relaxation experiments. Indeed, under many circumstances, OFB and viscoelastic experiments yield equivalent information [7, 10—13], as may also be expected for OEB and dielectric relaxation measurements. However, there are important differences in both principle and practice, which underscore the potential value of the optical approach. For example, in OFB and OEB, the measured properties are uncoupled from the applied field, in the sense that it is not necessary to account for the dynamic mechanical or electrical impedance of the apparatus, as is required in the viscoelastic or dielectric relaxation experiments. This can be particularly important in dilute solutions, where the polymer contribution to the measured response is already small. At a fundamental level, OFB and OEB sense molecular orientation, while viscoelastic and dielectric properties reflect energy loss and storage; thus it is certainly not required in principle that the information content be equivalent. On a practical level, the optical experiments allow some measure of spatial resolution within the sample solution, by appropriate placement of the light beam, whereas viscoelastic and dielectric relaxation measurements are inherently integrated over the entire sample. This can be crucial when the state of the applied field within the sample is in question [14—16]. Lastly, for certain polymer systems, the optical response will inevitably differ from the mechanical or electrical. As an example, in the case of block copolymers, the optical signal contribution from each block will be weighted by the optical anisotropy of the respective monomer units, while the viscoelastic and dielectric relaxation signals will reflect the relative hydrodynamic and dipolar properties, respectively.

Electric birefringence has been used extensively over the past forty years for the investigation of macromolecular dynamics, with particular emphasis on the rotational diffusion of relatively rigid biopolymers [17, 18]. The applied electric field is typically a square wave or pulse, and the measured quantities of interest are the rise and decay of the birefringence on application and removal of the field, respectively, and also the value of the steady-state birefringence achieved. The OEB approach has also been used successfully, albeit sparingly [19—23]. There are several possible explanations for this, which include the facts that: (i) for rigid polymers, there is usually only one predominant relaxation process, and the frequency dependence is of less interest; (ii) for ionic systems, such as biopolymers, the field can only be applied for short times, because of the inevitable heating effects when current is passed; (iii) to obtain adequate signals, very large field strengths are often needed (e.g., in excess of 10^4 V cm^{-1}), which may be difficult in the

sinusoidal case; (iv) only relatively recently has it been convenient to use digital lock-in detection schemes which take advantage of the periodic nature of the OEB signal. For the systems of interest here, namely uncharged, flexible polymers in organic solvents, points (i) and (ii) are of less significance; points (iii) and (iv) are addressed in the experimental section.

The OEB and OFB techniques are closely related, yet there are important differences which render them complementary rather than redundant. The most fundamental of these lies in the orientation mechanisms involved. For OFB, the sinusoidally time-varying shear flow will excite many relaxation modes simultaneously; in OEB, the situation is more complex. Orientation of both permanent and induced dipole moments, and polarization of counterion atmospheres in ionic systems, may all contribute to the induced anisotropy. For flexible polymers with a substantial permanent moment in the monomer unit, three possible dipole geometries have been classified [24]. Type A dipoles lie along the chain backbone direction, and thus the entire molecule possesses a net moment directly correlated to the chain end-to-end vector. Type B dipoles lie perpendicular to the backbone, and thus possess no correlation with the end-to-end vector for polymers with sufficiently high molecular weight. Type C dipoles are on flexible side chains, and also show no correlation with the end-to-end vector. In principle, a given polymer may possess components of any one, two, or all three classes, although Type B dipoles predominate for vinyl polymers. These various possibilities imbue OEB with a degree of selectivity; for example, OEB measurements on a pure Type A polymer will reflect long-range motions, while for a Type B polymer more local modes of motion will be probed. Two other differences between OFB and OEB are particularly significant. The frequency range achievable with current OFB instrumentation is typically 0.01 to 2000 Hz [6]; in order to extend this range, viscous solvents (1—1000 Poise) and time-temperature superposition are used [1, 4—8]. But in OEB, real-time frequencies above 100 kHz are attainable. In OFB, even at relatively low frequencies, rather viscous solvents are required to establish the correct shear flow ("gap-loading") conditions if thin fluid layer geometry is employed [1, 14], while in OEB no analogous restrictions apply. Thus with OEB there is access to a greater range of solvents, and questions involving the role of solvent quality and chemical structure in polymer dynamics may be addressed.

This paper describes an OEB apparatus designed particularly for measurements on solutions of flexible polymers. Novel features of this approach, relative to OEB instrumentation described in the literature [21—23], include a double-beam configuration, a Kerr cell with in situ variable electrode separation, and the use of a powerful computerized data acquisition and processing system (DAPS) based on that used for OFB and viscoelastic measurements [7, 13, 25—27]. Preliminary results on simple systems are also presented.

EXPERIMENTAL

Apparatus for OEB measurements

A block diagram of the oscillatory electric birefringence apparatus is shown in Fig. 1. Light from a 5 mW helium-neon laser (Uniphase 1105P) passes through a converging lens, a Glan-Thompson polarizer, and a mica quarter-wave plate (Karl Lambrecht) before entering the Kerr cell. The emerging elliptically-polarized light is split into two orthogonally-polarized beams by a Rochon beam-splitting prism polarizer (Karl Lambrecht); each beam is then detected by a separate photodiode (Hamamatsu S1723-01) after passing through 633-nm line filters. The current from each photodiode, consisting of a small a.c. component superposed on a large d.c. offset, is converted to a voltage and amplified before being digitized by the data acquisition system described below. Immediately prior to the current-to-voltage conversion, the d.c. component is almost completely balanced by the addition of a precisely selectable current of opposite sign. In order to avoid introducing large phase or amplitude errors into the high-frequency a.c. signals, both current-to-voltage and amplification stages are designed around ultrafast FET amplifiers (Analog Devices 46J).

The sinusoidally time-varying electric field is produced by a frequency synthesizer and high-voltage amplifier in series. The synthesizer (Hewlett-Packard 3325A) has a frequency range of 1 μHz to 21 MHz, with amplitudes of up to 20 V p-p. The high voltage amplifier stage consists of either a circuit based on the Burr-Brown 3584JM, or on an extended range audio

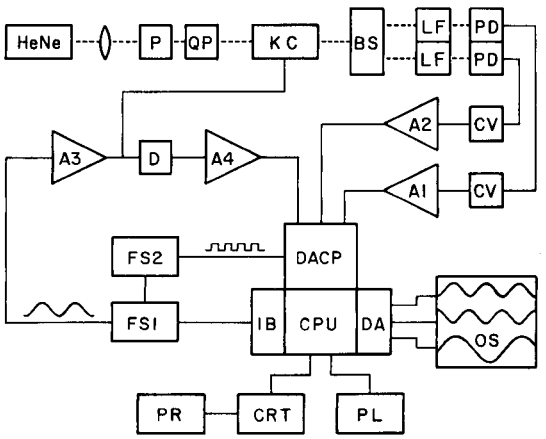

Fig. 1. Block diagram of OEB apparatus: HeNe, laser source; P, linear polarizer; QP, quarter-wave plate; KC, Kerr cell; BS, beam-splitting polarizer; LF, 633-nm line filter; PD, photodiode; CV, current-to-voltage converter; A1, A2, A4, FET amplifiers; A3, high-voltage amplifier; D, divider network; FS 1,2, frequency synthesizers; DACP, data-acquisition and control processor; CPU, central processing unit; IB, parallel interface; DA, digital-to-analog converter; OS, oscilloscope; PL, plotter; CRT, control terminal; PR, printer.

amplifier (Lasermetrics AF3). The former has a frequency range of 0 to 300 kHz (−3 dB) and an output voltage range of 290 V p-p, while the latter operates from 3 Hz to 260 kHz (−3 dB) at an output voltage of up to 650 V p-p. The amplitude and frequency of the synthesizer are under computer control. The electric field applied to the Kerr cell is also attenuated before passing to the data acquisition system through another FET amplifier.

In the general case, the birefringence signal induced by the application of a sinusoidally time-varying electric field can be written as

$$\Delta n = \Delta n_s \pm \Delta n_a \cos(2\omega t + \psi) \tag{1}$$

where ω is the frequency of the applied field, provided that the field is sufficiently small that the Kerr law is obeyed [17, 21]. The three quantities of interest are Δn_s, the steady component of the birefringence, and Δn_a and ψ, the magnitude and phase of the alternating component; all may be viewed individually as including contributions from the orientation of permanent and induced dipole moments. For the optical train used in this apparatus, the measured signal from each photodiode is proportional to the intensity incident on the diode, and may be written as:

$$I = I_0 \pm I_s \pm I_a \cos(2\omega t + \beta) \tag{2}$$

where I_0, I_s, I_a, and β, the measured photocurrents and phase angle, are directly related to Δn_s, Δn_a, and ψ [28]. The validity of Eqn. (2) also rests on the assumption that the optical phase retardation is very small compared to unity. Correction for the frequency response of all electrical components is made in the extraction of the desired quantities. The plus or minus possibility in Eqn. 2 reflects the phase difference between the two diode signals, and also the possibility of either positive or negative birefringence.

Two cross-sectional views of the Kerr cell are shown in Fig. 2. The novel feature of this design is the provision for straightforward in situ variation of the inter-electrode spacing. This in turn permits some means of assessing whether the electric field within the gap is homogeneous and unaffected by, for example, electrode polarization. Even under adverse circumstances, systematic variation of the inter-electrode spacing can in principle be used to account for these contributions, in the same manner as used in dielectric relaxation measurements [16]. The sample solution is contained in a titanium jacket (1). The electrodes (2), which are 5.08 cm long and 1.27 cm wide, are machined from copper, plated with platinum, and mounted in delrin holders (3, 4). The light beam enters and exits through windows (6) which are held in place by O-rings (5), to avoid both solution leakage and stress-induced birefringence. The lower holder is fixed, while the upper holder is translated and pivoted to vary the gap width and assure parallel surfaces. Electrical connection to the lower electrode is achieved via a hole in the base of the jacket, also sealed by an O-ring (5). The upper holder is attached to the rocker mount (7) by screws (not shown), and pivots about the light beam axis on two pyrex spheres (8). Once aligned, the orientation is maintained by

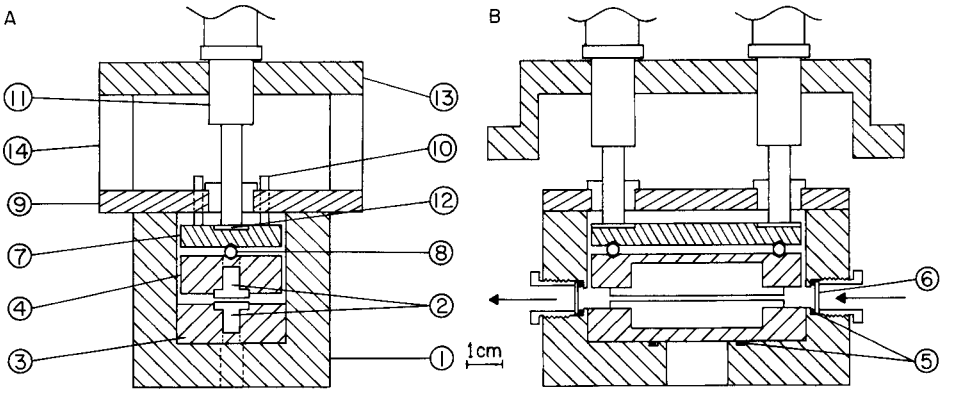

Fig. 2. Cross-sectional views of the Kerr cell: 1, titanium jacket; 2, platinum-plated electrodes; 3, lower electrode holder; 4, upper electrode holder; 5, O-ring seals; 6, windows; 7, rocker mount; 8, pyrex spheres; 9, cell cover; 10, guideposts; 11, micrometers; 12, glass plates; 13, mounting plate; 14, spacers.

adjusting the screws which are accessible through the cell cover (9). Vertical translation is achieved via two micrometers (11). The rocker mount is connected to the cell cover by springs (not shown). To ensure smooth uni-axial motion, stainless-steel guideposts (10) attached to the rocker mount ride in teflon sleeves through the cell cover. To avoid thermal contact between the rocker mount and the micrometers, each micrometer tip pushes on a thin glass plate embedded in the rocker mount. The micrometers are rigidly mounted on a plate (13) which is itself rigidly attached to an optical rail system. All the optical components are referenced to the same rail system, which rests on a vibration isolation table (Newport Research Corporation RS-48-12). The cell cover is attached to the plate through plexiglas spacers (14). Temperature control is achieved by passing fluid from a refrigerated bath/circulator (Neslab Instruments RTE-8) through channels in the titanium jacket. The temperature in the solution is monitored by a thermistor embedded in the upper electrode, and is routinely maintained to within $\pm 0.01^{\circ}C$. This also provides a sensitive indication of undesirable current passage in the cell. The thermistor was calibrated to better than $\pm 0.003^{\circ}C$ against a platinum resistance thermometer with a calibration traceable to NBS. The sample cell requires a solution volume of ca. 8 ml.

Data acquisition and processing system

The general function of the data acquisition and processing system (DAPS) is to extract the magnitudes and relative phases of a finite number of coherent periodic signals. For the OEB experiment, the desired quantities are the a.c. amplitudes, d.c. offsets, and relative phasing of the two photodiode signals, and the a.c. amplitude and relative phase of the applied electric field. The DAPS operates by sequentially sampling and digitizing the three signals,

performing real-time signal averaging, and subsequently applying a cross-correlation routine to discriminate against certain kinds of noise. At the heart of the DAPS is an algorithm, first developed by Stokich et al. [25] for OFB and viscoelastic experiments, which selects a data acquisition frequency for each desired applied field frequency; this algorithm was modified somewhat for the OEB experiment. A considerably more detailed discussion of the DAPS algorithm and its noise rejection capability has been presented [13, 26]; another application is discussed elsewhere in this volume [27]. The DAPS hardware includes two frequency synthesizers (Hewlett-Packard 3325A) operating from a single high-stability time base, and a computer system with suitable analog-to-digital conversion capability (Masscomp MCS-540).

In order to build a digital representation of each signal in computer memory, it is necessary to select the number of distinct sampled points to define one signal cycle. In this instance, 1000 points is a reasonable number in that it provides phase resolution at the 0.4° level for sinusoidally time-varying signals. However, the algorithm uses a prime number, 1013, to avoid the possibility of undesired redundant sampling. The sampling frequency, f_s, is then computed on the basis of the highest sampling rate the DAPS hardware can provide. For the MCS-540 as currently configured, this rate is approximately 100 kHz, although there is some evidence that this can be increased substantially in the future. For low frequency signals, f_s is calculated by multiplying the desired drive or signal frequency, f_d, by 1013, and then by 3 to account for the three distinct signals, each of which is passed to a different channel of a multiplexer. Thus a 1013-point digital representation of each signal is obtained over a single real-time cycle of the signal. When f_d exceeds approximately 33 Hz, this approach yields an f_s greater than 100 kHz. Therefore, it is necessary to acquire the 1013 points over more than one real-time signal cycle, and to fold these back into the correct order subsequently. The algorithm calculates the minimum number, L, of real-time signal cycles necessary to collect 1013 points for each of the three channels, and computes f_s as $(1013 \times 3 \times f_d/L)$. This process may produce a value of f_s which contains too many significant figures for the synthesizer, which has μHz resolution up to 100 kHz; however, in this event a very slight modification to f_d can be made which eliminates the problem, and which represents no significant loss in selectability of f_d.

A crucial feature of the above algorithm is that the 1014th, 2027th, etc., points collected on a given channel occur at exactly the same phase of the signal as the first point. In other words, after the initial 1013 points have been obtained, all later points are redundant, and each is summed directly into the corresponding memory location (i.e., modulo 1013) to achieve real-time signal averaging. Thus, only 3×1013 memory locations are required for data storage. In practice, it is this sum-to-memory step which is limiting in terms of the maximum f_s, rather than other hardware limitations such as the analog-to-digital conversion rate. Nevertheless, because it is frequently

desirable to have 10^4 or more signal averages for a given f_d, this approach is much more efficient than storing each point in a unique location and then averaging.

After signal averaging and folding into the correct order, the 1013-point digitized versions of each signal are cross-correlated with computer-generated sine and cosine waves of the same frequency. Essentially, this process involves no more than a numerical integration over one period. The six cross-correlation sums allow determination of the three a.c. magnitudes and phases; the d.c. offsets are obtained by adding the portion of the signal subtracted prior to the current-to-voltage conversion to the residual offset calculated by summing the 1013 stored points. The cross-correlation thus acts as a powerful digital lock-in detector. It can be shown that all noise components in the signals which are higher harmonics of f_d are completely eliminated. In addition, all noise frequencies which are expressable as $f_d(1 \pm n/L)$, where n is any positive integer, are also eliminated. Finally, noise components of other frequencies are attenuated to a considerable degree, as has been described in detail [13, 26]. It is important to note that the algorithm is in no way restricted to $f_d < f_s$. Application of the Nyquist criterion reveals that at high values of f_d there are aliasing frequencies which the cross-correlation will neither eliminate nor attenuate. However, because these aliasing frequencies depend on f_s, it should be possible to circumvent this problem if it occurs, by selecting alternative values of f_s for a given f_d.

Careful consideration of the algorithm described above reveals that in practice it is not completely efficient, in the sense that actual f_s values are often considerably lower than the maximum allowed. In order to keep f_s close to the maximum over as wide a range of f_d as possible, the OEB version of the algorithm divides values of f_d into four intervals, and applies a straightforward variant of the original algorithm in each interval. For f_d values greater than 33 kHz, the algorithm is used exactly as described above. In the interval 33 Hz $< f_d <$ 33 kHz, the number of points is increased from 1013 to a prime number between 1013 and 2011, once L is selected, to keep f_s as large as possible. Below 33 Hz, $L = 1$ and the number of points can be increased above 1013 and need not be a prime number. Essentially, f_s is maintained close to 100 kHz, and adjusted slightly to guarantee that signal averaging is performed correctly. In principle, this method could be extended to arbitrarily small values of f_d, but in practice the increased number of points increases the time needed for the cross-correlation to an unreasonable level. For this DAPS, a maximum number of points of 10 000 was selected, and thus for f_d below about 3.3 Hz, f_s must fall below 100 kHz. The floating-point processor in the MCS-540 brings the computation time for six 10 000-point cross-correlation sums below 10 s.

The specifications of the DAPS computer hardware are important in determining the speed and accuracy with which data can be obtained. The MCS-540 is a 68000-based 32-bit computer, with a Masscomp-enhanced UNIX operating system. In the configuration employed for OEB measure-

ments, there is a 27-MByte Winchester disk and 2 MByte of ECC memory, in which the data are stored as they are acquired. All control and calculation programs are written in C. The data acquisition hardware includes a separate processor. The signals pass through a multiplexer, sample-and-hold amplifier, and analog-to-digital converter sequentially. The converter has 12-bit resolution, and data can be acquired at rates up to 1 MHz. As discussed above, the summation step restricts the maximum f_s. However, if higher values of f_s are desirable, it is possible to acquire data at up to 1 MHz, store in ECC memory until the capacity is exhausted, and then perform the averaging. The two frequency synthesizers are controlled by the MCS-540 via the HP-IB bus, and are frequency-locked to a single time base. One synthesizer produces the sine wave at f_d while the second triggers the data acquisition with a square wave at f_s. The acquired data, signal-averaged and folded, are displayed on an oscilloscope via digital-to-analog converters operating at 30 kHz with 12-bit resolution.

Extraction of OEB properties

The DAPS outlined above allows determination of the quantities I_0, I_s, I_a, and β from the measured signals, and thus the quantities of interest Δn_s, Δn_a, and ψ. However, two important points have been ignored in the above discussion. The first is the fact that the electric field signal has frequency ω, while the two optical signals have a.c. components at frequency 2ω; this affects the way the cross-correlation is performed. The second is the fact that the ratio I_s/I_0 is determined with considerably less accuracy than I_a/I_0, even though of similar magnitude.

The difference in signal frequency is dealt with in a very straightforward manner; specifically, the two optical signals are simply cross-correlated against $\cos 2\omega t$ and $\sin 2\omega t$ rather than $\cos \omega t$ and $\sin \omega t$. The use of a common f_s for all three signals presents no problem; the folded optical signals actually have 1013 equally-spaced points over two full cycles, which may be folded again into one cycle. The phase angle ψ, which is ultimately extracted is in units of degrees relative to 2ω.

The inaccuracy in I_s/I_0 stems from the small magnitudes involved. For example, this ratio is typically in the range 10^{-4}—10^{-6}; thus, to obtain accuracy at the 1% level, with I_0 corresponding to signals between 10 and 100 V, it is necessary to measure voltages in the range of 10 μV to 10 mV corresponding to I_s, with accuracy down to 0.1 μV. This is difficult to achieve even with exceptional amplifier stability, given least-significant-bit error in the mV range from the analog-to-digital converter. The problem is less acute for I_a/I_0, because of the lock-in nature of the detection. This observation suggests a solution to the difficulty, namely modulation of the I_s signal, as suggested by Ookubo et al. [22]. Thus, to measure Δn_s, the applied electric field is amplitude-modulated at some (low) frequency:

$$E = E_0 \, (1 + \sin (\Omega t)) \sin (\omega t) \tag{3}$$

This results in a much more complicated observed optical response, with I_s appearing in the amplitude of an a.c. signal with frequency components at Ω and 2Ω. There are also components at 2ω, $2\omega \pm \Omega$, and $2\omega \pm 2\Omega$ involving I_a. Cross-correlation at Ω eliminates the 2Ω signal by definition, and if $\omega \gg \Omega$, the other terms average to zero. However, if ω is an integral multiple of Ω, all the other terms are rejected exactly. Thus, I_s can be extracted with an accuracy similar to that obtained for I_a. The electric field signal has components in ω and $\omega \pm \Omega$. The electric field amplitude, E_0, can be extracted by correlation against ω, and the $\omega \pm \Omega$ component rejected exactly, if ω, Ω, and L are chosen in such a way that $\omega \pm \Omega$ is expressable as $f_d(1 \pm n/L)$, where n is any positive integer. This is, in fact, straightforward given that ω is an integral multiple of Ω. Furthermore, when f_s is selected to provide 1013 equally-spaced points along one cycle of Ω, it automatically provides 1013 equally-spaced points over an integral number of cycles of ω. Thus, Δn_a and ψ can be evaluated from an experiment without amplitude modulation of the applied field, and Δn_s in a separate experiment with amplitude modulation. The modulation does require the use of an additional synthesizer.

Examination of the full expression for the resulting optical and electrical signals in the presence of modulation reveals a further possibility, whereby the necessity of separate experiments for obtaining Δn_s and Δn_a can be eliminated. The desired quantities E_0, I_s, and I_a occur as coefficients of a.c. terms with frequencies of ω, Ω, and 2ω, respectively, with interference from terms in $\omega \pm \Omega$, 2Ω, $2\omega \pm \Omega$, and $2\omega \pm 2\Omega$. Successful cross-correlation at any frequency requires only that the data be taken over integral numbers of cycles of the desired frequency; thus the various signals may each be cross-correlated with the appropriate cosine and sine terms on the same set of data, if ω and thus 2ω are higher harmonics of Ω. In addition, adjustment of the number of cycles over which data are acquired can guarantee that all the interfering cross-terms are exactly rejected, concurrently. This will place some restrictions on the choice of Ω, and on the length of time over which data should be acquired; neither constraint should be substantial. It should be noted, however, that Ω is only required to be sufficiently small that the solution response is frequency-independent at Ω, and $\Omega < \omega$; it is not required that $\Omega \ll \omega$ as is the case with more conventional lock-in approaches.

Samples

Nitrobenzene was obtained from the Baker Chemical Company, and was dried over alumina and filtered prior to use. It was also found necessary to store the samples in a desiccator to avoid developing significant conductivity over time. Aroclor-1248 (lot KM502) is a product of the Monsanto Chemical Company; it is a mixture of polychlorinated biphenyls, with an average degree of chlorination of about four. It was also filtered prior to use.

RESULTS AND DISCUSSION

Results for the steady and alternating components of the birefringence, Δn_s and Δn_a, measured for pure nitrobenzene are plotted against the r.m.s. electric field amplitude squared, in Fig. 3. The Kerr law is clearly obeyed, and the slopes of the regression lines are 1.00 in both cases. The data were mostly acquired with an applied field frequency of 1000 Hz. As nitrobenzene is a simple liquid with a rotational relaxation time in the sub-nanosecond region, no frequency dependence is expected; however, as a check some data points were repeated with an excitation frequency of 100 Hz. These data are indistinguishable from those obtained at 1000 Hz. Three different inter-electrode spacings were used: 1.00, 1.50, and 2.00 mm. As expected, the data form a unique master curve when the electric field in the solution is taken to be the ratio of the applied voltage to the measured gap. The values of the Kerr constants B_s and B_a, defined by $B_s = \Delta n_s/E^2\ \lambda_0$ and $B_a = \Delta n_a/E^2\ \lambda_0$, were obtained by regression on all points for which the measured birefringence exceeded 10^{-11}. They were identical within experimental error, with values of $B_s = 3.09 \times 10^{-10}$ and $B_a = 3.11 \times 10^{-10}$ cm V^{-2}. These are in good agreement with the value of $3.24 \pm 0.19 \times 10^{-10}$ determined by Misakian and Hebner [29] for $\lambda_0 = 632.8$ nm. Some scatter in the data becomes evident for values of the birefringence below 10^{-11}, and no measurements were obtained below 10^{-12} with the current instrumental configuration. In order to establish that the frequency dependence of all the electronic components has been accounted for correctly, B_s, B_a, and ψ were evaluated for nitrobenzene over the range 10 Hz to 100 kHz with an r.m.s. electric field of 275 V cm^{-1}; no frequency dependence in the birefringence properties was detected.

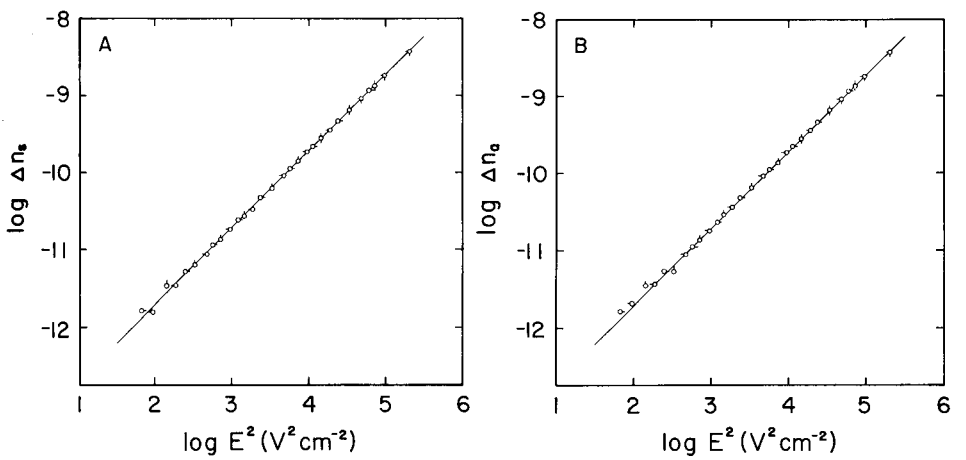

Fig. 3. The OEB properties of nitrobenzene at 25.0°C. With $f = 1000$ Hz: (—○) 1.00-mm gap; (♁) 1.50-mm gap; (○—) 2.00-mm gap. With $f = 100$ Hz: (♀) 1.00-mm gap.

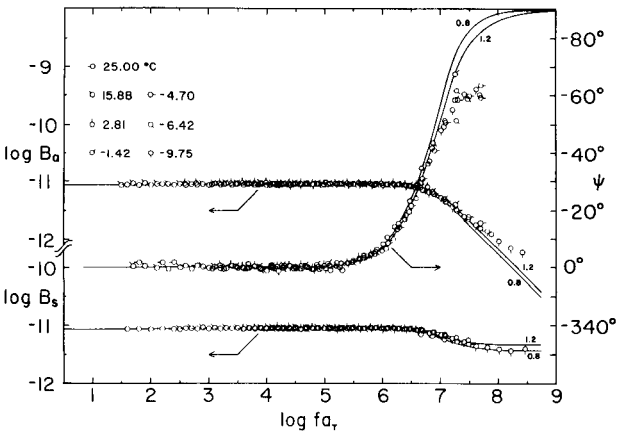

Fig. 4. The OEB properties of Aroclor-1248 as a function of reduced frequency, at a reference temperature of 25.00°C and an optical wavelength of 632.8 nm. Data were obtained at seven temperatures from 25.00°C to −9.75°C, as shown. Theoretical curves correspond to rigid rod theory with P equal to 0.8 (upper curve for ψ, lower curves for B_a and B_s) or 1.2 and τ = 6 ns.

The three OEB functions, B_s, B_a, and ψ, were measured for Aroclor-1248 over the frequency range 10 Hz to 100 kHz, at seven temperatures ranging from 25.00°C to −9.75°C; the solvent viscosity increases from 2.2 P to approximately 10^4 P over this interval. The results are plotted in Fig. 4, assuming time-temperature superposition, i.e., the reduced frequency axis, log fa_T, is determined by shifting the data horizontally by the factor a_T, which is the ratio of the solvent or solution relaxation time(s) at temperature T to the relaxation time(s) at a reference temperature T_0 (in this instance, 25.00°C) [1]. Time-temperature superposition is based on the recognition that in theoretical expressions for the dynamic response of a system to a sinusoidally time-varying perturbation, the applied frequency and the system relaxation times appear only as dimensionless products. Thus, if the relaxation time(s) is (are) scaled by a constant factor, such as a change in solvent viscosity, this factor can be incorporated into a new, effective frequency. Values of the shift factor, a_T, as a function of temperature for any particular system can be correlated via the two-parameter Williams-Landel-Ferry equation [1]. For Aroclor liquids, the shift factors are governed primarily, but not entirely, by the temperature dependence of the viscosity. It is known, for example, that shift factors for Aroclor-1248 obtained from viscosity and oscillatory flow birefringence measurements do not agree exactly [30]. The values used here were chosen to be identical to those reported for the OFB properties of Aroclor-1248 [30]; unlike the OFB case, the birefringence magnitude is not affected by the change in viscosity, and empirical a_T values are harder to extract directly, especially at the higher temperatures. Within the precision of the data, the superposition thus obtained is very good, for all three

quantities. The low-frequency limiting values of B_s and B_a, B_{so} and B_{ao}, do have a weak temperature dependence related to the relative contributions of permanent and induced dipoles [17]. These data have all been shifted vertically assuming a pure permanent dipole contribution, i.e., by $(T/T_0)^2$.

The three functions are each frequency-independent up to reduced frequencies of about 1 MHz, and the magnitudes of B_{so} and B_{ao} are identical. The average values of B_{so} and B_{ao} obtained in the plateau region at 25.00°C are 8.54×10^{-12} and 8.60×10^{-12}, respectively; this is quite consistent with the pulsed-field measurement of two other Aroclor fractions by Misakian and Hebner [29]. The phase angle ψ is also 0°, within experimental error, up to a reduced frequency of ca. 5.5 MHz. Above this frequency, there is evidence in all three functions of a solvent relaxation process. If the simple assumption is made to model the liquid as a suspension of rigid rods, the results of Peterlin and Stuart [31], Benoit [32], and Thurston and Bowling [21] can be compared with the data. To obtain theoretical predictions for the three functions, it is necessary to select a rotational relaxation time τ for the molecule, and also a value for the quantity P, defined by Thurston and Bowling [21] to be:

$$P = kT\,(g_1 - g_2)_e/\mu^2 \tag{4}$$

Here, k is Boltzmann's constant, T the absolute temperature, μ the permanent dipole moment, and $(g_1 - g_2)_e$ the polarizability anisotropy at the applied frequency. Thus P is a measure of the relative contribution of induced and permanent dipole moments to the observed response; it is 0 for a pure permanent dipole, and $\pm\,\infty$ for the pure induced case. In the rigid rod model, both the induced and the permanent contribution show a frequency dependence reflecting the molecular relaxation time, although the dependence itself differs between the two. Simply for illustration, theoretical curves for $P = 0.8$ and 1.2 are compared with the data, assuming a relaxation time of 6 ns; the agreement is reasonable. Better agreement might be found by considering this liquid as polydisperse, as it is a blend of different chemical species; although the relevant equations have been developed [21], these preliminary data probably do not justify such detailed examination. It is worth noting that polydispersity in τ, μ, $(g_1 - g_2)_e$, and the optical anisotropy can all contribute to the shapes of the resulting curves. The finite value of P implied by these data also means that the $(T/T_0)^2$ shift applied to B_s and B_a is not quite correct, but the magnitude of this effect is small. It is important to emphasize that this evaluation is performed only to obtain an estimate of the frequency at which solvent relaxation becomes important for Aroclor-1248. There is no justification for using the rigid rod theory other than to model the effect of a single relaxation time on the observed response.

CONCLUSIONS

A new instrument for measuring all three OEB functions for solutions of synthetic polymers has been described. The available frequency range extends

from below 1 Hz to at least 100 kHz, with electric fields variable up to about 6000 V cm^{-1} p-p. Novel features of the apparatus include the ability to vary the inter-electrode spacing rapidly, precisely, and reproducibly, in situ, and the use of a double-beam optical configuration. Data acquisition is done with a Masscomp computer and a modified version of a data-sampling algorithm used for viscoelastic and oscillatory flow birefringence experiments. Measurements on nitrobenzene demonstrate the reliability and range of the instrument. Preliminary results on Aroclor-1248 illustrate the potential power of the technique, extending the accessible reduced frequency range to almost 1 GHz in this solvent, which is at least two decades further than for OFB results reported previously [4—8, 30]. Time-temperature superposition appears to be obeyed over most of this range, and an average solvent relaxation time of approximately 6 ns at 25.00°C is obtained by comparing the data to predictions for a rigid rod suspension. This is in at least qualitative agreement with viscoelastic results on the same solvent [33, 34]. The relationship between the OEB properties of Aroclor liquids and the viscoelastic and OFB results already reported will be discussed in more detail at a later date.

Although the instrument as currently configured is suitable for many systems of interest, it is generally the case that flexible polymers have relatively small values of B. Thus, it is important to consider ways in which the performance of the apparatus can be enhanced, particularly with regard to the small signal case. At present, a crucial limitation is noise in the laser source. Although the double-beam configuration helps, the fact remains that fluctuations in I_0, with noise frequencies in the range of 1 to 100 kHz and amplitudes of approximately 0.005 to 0.01 I_0, are a constant problem. The typical values of I_s and I_a are 10^{-4} to 10^{-6} of I_0, and attempts to amplify these signals are thwarted by saturation of the amplifier by the laser noise. A more stable laser could thus extend the sensitivity of the apparatus substantially. Furthermore, the signal increases linearly with I_0, while the shot noise increases with $(I_0)^{1/2}$, and a more intense laser should also help in this regard. Other means of increasing the signal include larger applied voltages and smaller inter-electrode spacings, but neither of these is particularly appealing. In the former case, difficulties with small conductivities become substantial, while in the latter case it is difficult to pass an intense laser beam through a long gap less than 1-mm wide without generating substantial reflections off the electrodes. Increasing the length of the electrodes also offers a straightforward means to enhance the signal, but requires greater solution volumes. A Kerr Cell with 30.48-cm long electrodes is currently under construction.

The authors acknowledge helpful discussions with Dr. P. J. Barbara. We are grateful to Dr. J. L. Schrag for providing the Aroclor-1248, and to S. Amelar for the thermistor calibration. The work was supported by the National Science Foundation under grant DMR 8319291.

REFERENCES

1 J. D. Ferry, Viscoelastic Properties of Polymers, 3rd edn., Wiley, New York, 1980.
2 J. G. Kirkwood, in P. L. Auer (Ed.), Collected Works, Macromolecules, Gordon and Breach, New York, 1967.
3 H. Yamakawa, Modern Theory of Polymer Solutions, Harper and Row, New York, 1971.
4 G. B. Thurston and J. L. Schrag, J. Chem. Phys., 45 (1966) 3373.
5 G. B. Thurston and J. L. Schrag, J. Polym. Sci., Part A2, 6 (1968) 325.
6 J. W. Miller and J. L. Schrag, Macromolecules, 8 (1975) 361.
7 C. J. T. Martel, T. P. Lodge, M. G. Dibbs, T. M. Stokich, R. L. Sammler, C. J. Carriere and J. L. Schrag, J. Chem. Soc. Faraday Symp., 18 (1983) 173.
8 T. P. Lodge and J. L. Schrag, Macromolecules, 17 (1984) 352.
9 N. Ookubo, T. Abe, Y. Ooshima and Y. Wada, Prog. Polym. Phys. Jpn., 24 (1981) 439.
10 B. H. Zimm, J. Chem. Phys., 24 (1956) 269.
11 T. P. Lodge, Ph.D. Thesis, University of Wisconsin, 1980.
12 V. F. Man, Ph.D. Thesis, University of Wisconsin, 1984.
13 T. M. Stokich, Ph.D. Thesis, University of Wisconsin, 1986.
14 J. L. Schrag, Trans. Soc. Rheol., 21 (1977) 399.
15 J. L. Schrag, J. F. Guess and G. B. Thurston, J. Appl. Phys., 36 (1965) 1996.
16 D. Rosen, in P. Alexander and H. P. Lundgren (Eds.), Analytical Methods of Protein Chemistry, Vol. 4, Pergamon, New York, 1966.
17 C. T. O'Konski (Ed.), Molecular Electro-Optics, Part I, M. Dekker, New York, 1976.
18 E. Fredericq and C. Houssier, Electric Dichroism and Electric Birefringence, Clarendon Press, Oxford, 1973.
19 H. Benoit, J. Chim. Phys., 49 (1952) 517.
20 C. T. O'Konski and A. J. Haltner, J. Am. Chem. Soc., 79 (1957) 5634.
21 G. B. Thurston and D. I. Bowling, J. Colloid Interface Sci., 30 (1969) 34.
22 N. Ookubo, Y. Mori, R. Hayakawa and Y. Wada, Jpn. J. Appl. Phys., 19 (1980) 2271.
23 Y. Mori, N. Ookubo, R. Hayakawa and Y. Wada, J. Polym. Sci. Polym. Phys. Ed., 20 (1982) 2111.
24 W. H. Stockmayer, Pure Appl. Chem., 15 (1967) 539.
25 T. M. Stokich, M. G. Dibbs, T. P. Lodge and J. L. Schrag, unpublished results.
26 M. G. Dibbs, Ph.D. Thesis, University of Wisconsin, 1983.
27 E. J. Amis, C. J. Carriere, F. H. M. Nestler, J. L. Schrag and J. D. Ferry, Anal. Chim. Acta, 189 (1986) 199.
28 G. B. Thurston, Appl. Opt., 3 (1964) 755.
29 M. Misakian and R. E. Hebner, Jr., J. Appl. Phys., 47 (1976) 4052.
30 R. L. Sammler, Ph.D. Thesis, University of Wisconsin, 1985.
31 A. Peterlin and H. A. Stuart, Hand- und Jahrbuch Chem. Phys., 8 (1943) 1B.
32 H. Benoit, Ann. Phys. (Paris), 12 (1951) 36.
33 R. S. Moore, H. J. McSkimin, C. Gieniewski and P. Andreatch, Jr., J. Chem. Phys., 47 (1967) 4329.
34 P. Merchak and J. L. Schrag, private communication.

Analytica Chimica Acta, 189 (1986) 199—215
Elsevier Science Publishers B.V., Amsterdam — Printed in The Netherlands

AN IMPROVED SYSTEM FOR DATA ACQUISITION AND ANALYSIS FOR VISCOELASTIC MEASUREMENTS OF DILUTE MACROMOLECULAR SOLUTIONS WITH THE MODIFIED BIRNBOIM-SCHRAG MULTIPLE LUMPED RESONATOR

ERIC J. AMIS[a], CRAIG J. CARRIERE[b], F. HENRY M. NESTLER, JOHN L. SCHRAG and JOHN D. FERRY*

Department of Chemistry, University of Wisconsin-Madison, Madison, Wisconsin 53706 (U.S.A.)

(Received 27th February 1986)

SUMMARY

A new system of data acquisition and analysis has been developed for the modified Birnboim-Schrag multiple lumped resonator apparatus which is used to measure the viscoelastic properties of long-chain macromolecules in dilute solution. The modifications to the original apparatus include improved temperature control and vibration isolation. The original theory has been reworked so that each resonance mode can be characterized by a greater number of data points. The entire data acquisition/processing system is automated and placed under computer control; a correction for mode coupling is derived. The modifications result in improved precision in the measured viscoelastic moduli and increased instrumental reliability.

During the past several years various measurements of the frequency dependence of the viscoelastic properties of dilute solutions of long-chain macromolecules have been reported [1]. Of the various experimental techniques available, the Birnboim-Schrag multiple lumped resonator (MLR), first described in 1971 [2], remains unique in its capability to measure the viscoelastic properties of dilute solutions with low viscosity in the frequency range 100—8000 Hz. The properties are obtained by measuring the changes in frequency and bandwidth for the resonance modes of a cylindrical rod element undergoing torsional oscillations while surrounded by solvent or a dilute polymer solution. Values of the storage modulus, G', can be measured down to 1 ± 0.1 dyne cm^{-2}. In the viscosity range 0.005—0.50 P, the instrument has provided valuable experimental data on dilute solutions of random coil [3], branched [4], and rod-like [5] polymers. Many of these experiments provided rigorous tests of infinite dilution theories for the conformational dynamics of long-chain macromolecules in solution.

[a]Present address: Department of Chemistry, University of Southern California, Los Angeles, CA 90089, U.S.A.
[b]Present address: Materials Research Laboratory, University of Illinois, Urbana, IL 61801, U.S.A.

0003-2670/86/$03.50

Since the original report on the apparatus, there have been extensive modifications of the supporting instrumentation, particularly the electronics, data-acquisition hardware, and signal-averaging and data-reduction techniques, while the basic instrument has remained essentially unchanged. Some of these changes have been briefly mentioned in various papers [6, 7] presenting experimental results, but no comprehensive report of the current status of the MLR has appeared since 1971 [2]. This paper discusses the changes which have been made in the last few years in a major effort to improve operational reliability, precision of measurement, and ease of use. The computerized data-acquisition and signal-averaging approach as currently implemented provides high-precision analyses of periodic, noisy signals in general.

APPARATUS

The basic apparatus [2, 8] involves a resonator mounted in a rigid, thermostated housing as shown in Fig. 1. The resonator itself consists of five inertial lumps connected together by six torsional springs of different diameters machined from a single piece of low loss aluminum or titanium alloy; thus five resonant frequencies are exhibited. The resonator is rigidly clamped at top and bottom. A sinusoidally time-varying current is passed through drive coils on either side of a small permanent magnet which is press fit into the top of the resonator; the current produces an oscillating magnetic field perpendicular to the permanent magnet axis which drives the resonator in forced torsional oscillations at specific frequencies. The resonator response is monitored by reflecting a light beam off a small front surface mirror attached to the top of the resonator. The device is machined so that the five normal

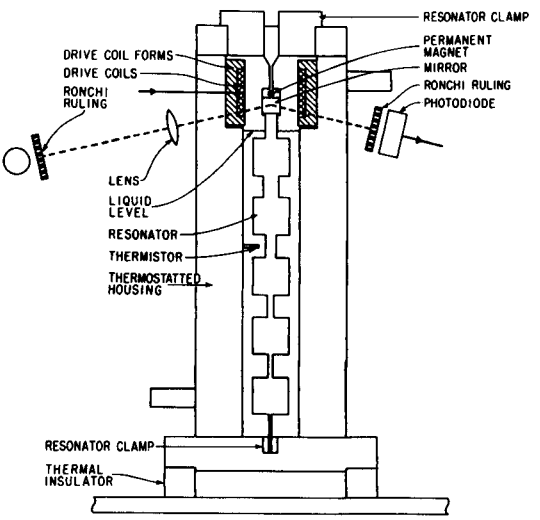

Fig. 1. Sketch of multiple-lumped resonator in temperature-controlled housing.

modes are well spaced in frequency and essentially uncoupled; the dimensions of the lumps are 1.59 cm (bottom four lumps) or 1.42 cm long (top lump) and 0.795 cm in radius while the springs are each 0.952 cm long and vary in diameter from 0.075 to 0.640 cm. In air the mechanical Q's of the resonators are typically 10^4 or better.

In order to measure the viscoelastic properties of a dilute solution of a sample, solvent and polymer solutions of various concentrations are successively placed in the thermostated volume (about 45 ml) surrounding the resonator. The filling is done through a small port in the bottom of the thermostated housing from an external reservoir. The filling process is observed through a full-length inspection window on the front of the housing with the aid of mirrors so that the experimentalist can ensure that no bubbles are trapped on or beneath the lumps. For solutions with viscosities in the range 0.005—0.50 P, the angular displacements of the resonator elements produce propagating shear waves (cylindrical shear waves from the side surfaces of the lumps and plane torsional waves from the top and bottom of the lumps) of sufficiently small wavelengths that the liquid can be treated as a medium of infinite extent (i.e., no reflected waves need be considered); thus the instrument is designated as a surface-loading device [9—11]. Angular displacements of the lumps are less than $\pm 0.001^\circ$ in order to avoid nonlinear spring effects. The angular displacements are monitored by a small light beam which reflects off a front surface mirror mounted on the top of the resonator and superimposes the image (1×1 magnification) of a Ronchi ruling (500 lines/inch) onto an identical ruling placed before a photodiode. The total time-dependent light flux on the photodiode provides a voltage signal which is amplified by two wide-band analog amplifiers before being passed to one channel of a data-acquisition module (ADAC Corporation Model 535-16PD-A-O). The analog phase-delay network which has previously been described as part of this circuit has been removed and the resulting higher but frequency-independent phase errors are determined and compensated with new computer software as discussed below. The drive signal supplied to the power amplifier that feeds the drive coils is provided by a programmable frequency synthesizer (Rockland Model 5100). The same signal is used as the high-stability ($\Delta f \cong 5 \times 10^{-6}$/year from an oven-stabilized 8-MHz master clock) sinusoidally time-varying reference signal, so that the measured phase angle is that of the resonator angular displacement relative to this reference drive signal. (Originally, the drive current was used as the reference because the actual torque exerted on the resonator was expected to be essentially in phase with this current. However, eddy current effects in the resonator housing give rise to significant deviations so that the time-varying magnetic field at the site of the resonator was not in phase with the drive current.) The reference drive signal is fed to the second channel of the data-acquisition module. The drive currents are produced by a clean, stable power amplifier (McIntosh 60 W).

Extreme temperature stabilization is required for this instrument because

the resonance frequency, calibration constant and bandwidth for each mode are all strongly dependent on temperature. In order to improve the temperature stability, several changes have been instituted. The basic control system consists of water passing from a circulating temperature bath (Lauda K4R) through channels in the housing and back to the bath. A sealed, insulated mixing chamber was added in the circulation line between the bath and the housing to combat temperature fluctuations in the circulating fluid caused by cycling of the thermostated bath. The entire instrument is now enclosed in a Plexiglas box which isolates it from air currents. The incandescent light source has been replaced by a tungsten-halogen lamp (12 W Sylvania ERB) which is housed outside the Plexiglas enclosure; the new lamp provides a beam of improved quality and much greater intensity. To make fine temperature adjustments easier, an additional fine control was added to the Lauda R20K platinum resistance thermometer control module. This was done by adding a 10—100-Ω variable resistor in parallel with the 0.7-Ω slide wire fine adjust. Although the control is nonlinear, changes of less than 0.001°C are possible at all settings. The temperature of the sample is monitored during a run with a thermistor probe (Fenwal GB32P3) in the solution. Its resistance is measured with a Wheatstone bridge (very low bridge current) and a d.c. null detector (Leeds & Northrup 2437). With these modifications, stability of ±0.002°C can be obtained with a resolution of ±0.0003°C.

In order to reduce mechanical noise contamination of resonator displacement signals, the MLR is mounted on a 500-lb. granite slab which is floated on highly damped air cushions. Vibration transmission from the temperature-control lines has been minimized by the mixing chamber mentioned above and by mass loading of the lines at several points between the resonator housing and the water bath.

DATA ACQUISITION

The major changes in the MLR apparatus have been in the computerized data acquisition, control and analysis procedures. Improvements have been made in three major areas: (1) extensive signal averaging is now performed through a specialized sampling scheme; (2) a control computer is used which automatically selects additional frequency points according to the data that have already been taken; and (3) frequency/phase points are analyzed by means of the general equations of motion which enables many more data points to be utilized in the evaluation of the experimental parameters and the sample viscoelasticity. The first of these improvements will be described next. Items 2 and 3 will require a discussion of MLR theory.

The present data-acquisition and processing system (DAPS) used for the MLR is a third-generation version of the original system for use with the modified Birnboim and MLR apparatuses [12]. The original system was based on cross-correlation combined with very limited signal-averaging capabilities.

Extensive signal averaging was not used because of limitations in computer memory size and the unavailability of a data-acquisition timing signal with high resolution, variable frequency and ultra-high stability, that could be synchronized with the transducer driving signal (at least 10^{-3} Hz resolution). Thus a fixed-frequency master timing signal was used, and data points were assigned to a narrow time "window" rather than a precisely known acquisition time. A second-generation system (DAPS II) was subsequently assembled that incorporated extensive signal averaging but still retained the time "window" approach, again because of the lack of an adequate timing signal source [13, 14]. Shortly after DAPS II was constructed, programmable frequency synthesizers with very high stability and 10^{-6} Hz resolution steps became available from Hewlett-Packard. Thus it became possible to abandon the time "window" approach by selecting appropriate transducer-drive signal and acquisition-timing signal frequencies such that a specific number of data points taken at very precisely known times could be obtained. Such a system (DAPS III) was subsequently developed by Stokich [15], Dibbs [16], and Lodge [17] for use with the modified Birnboim apparatus for viscoelasticity studies and the thin fluid layer apparatus for oscillatory flow birefringence measurements. The present data-acquisition system used with the MLR is an extension of a modification of DAPS III developed by Nestler; the modifications were necessary because of the incorporation of two programmable frequency synthesizers with substantially different frequency resolutions. The hardware consists of a computer (Data General Nova 4/S with dual floppy disks), a data-acquisition module (S/H, MPLX, ADC, control circuitry and interface), and two programmable frequency synthesizers (Rockland 5100 and Hewlett-Packard 3325A) along with appropriate interfaces. The input/output device for the system is either a Diablo 1620 terminal/printer or an Apple-IIe microcomputer with dual floppy disks and a Diablo 630 ECS printer. Figure 2 shows the present setup; the essence of the data-acquisition scheme is to represent digitally, with appropriate magnitudes and relative phasing, one folded (modulo 2π) cycle of each of the two analog input signals.

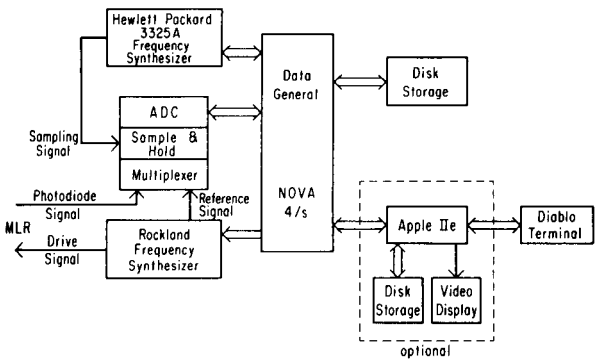

Fig. 2. Computerized data-acquisition and processing system.

Signal-averaging and cross-correlation techniques are applied to extract the amplitudes and relative phasing of these signals. (Complete descriptions of this process are available [15, 16].)

The Rockland frequency synthesizer, as noted above, provides a drive signal (1-mHz resolution) to the resonator drive coils and also to the reference channel of the data-acquisition module. The other channel receives as its signal the amplified voltage from the photodiode displacement detector. The second frequency synthesizer (Hewlett-Packard 3325A), with frequency settable to 1-μHz resolution, provides the ultra-stable sampling clock pulses to the sample-and-hold unit of the data-acquisition module at a rate which yields two sets of 1001 unique points along one folded cycle (modulo 2π) of the drive frequency. Signal averaging to any desired extent is readily obtained; after the system has sampled each point once, it adds in successive redundant points along the curves until the desired number of averages has been obtained.

The sampling method is shown schematically in Fig. 3 where, for purposes of this description, the collection of 11 points is shown rather than 1001 to represent one folded (modulo 2π) cycle. If the drive signal has a frequency ω, a sampling frequency is calculated as $\omega_s = \omega(11/i)$ such that 11 cycles of ω_s, each triggering one ADC sampling, will occur in some integer number, i, of cycles of ω. Figure 3 shows two cases of $i = 10$ and 6. The ultimate limitation on ω_s is the ADC throughput rate and i is therefore chosen to be an integer (1 or greater) to give ω_s less than 30 kHz for 2-channel acquisition. If i is an even factor of the number of points used to represent one folded modulo 2π cycle, the sampling scheme will produce redundant data points giving an

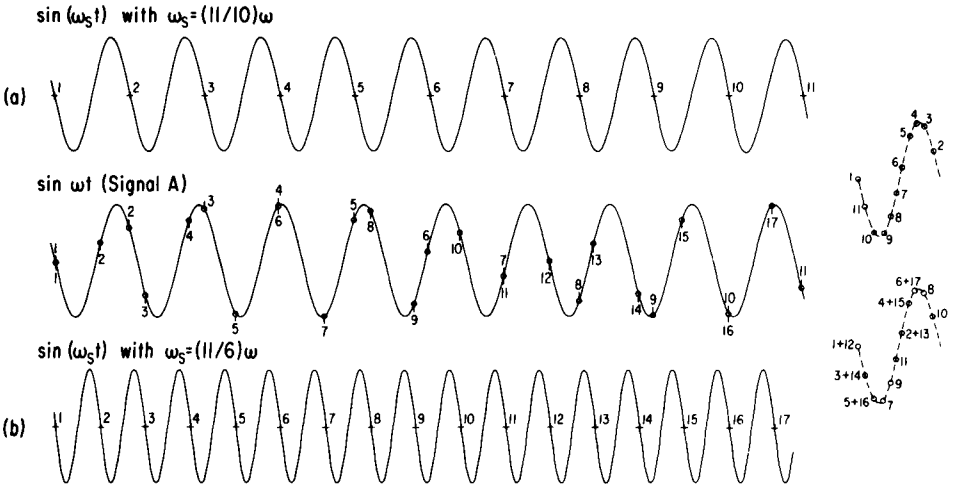

Fig. 3. Schematic representation of sampling technique where signal A with frequency ω is sampled at rate ω_s such that 11 data points, representing one cycle of A, are collected in (a) 10 or (b) 6 cycles of the signal A.

incorrect representation of the curves. This problem is circumvented by choosing the number of points to be a prime number or, as we do, by not allowing i to equal any factor of the number of points (for 1001 points, $i \neq 7, 11, 13$ or their products). (A complete discussion of this problem is available [15, 16].)

Signal averaging is thus a natural extension of the sampling technique as is shown in Fig. 3b. After 11 points have been collected, each additional point will be redundant and can be simply added to the current value in the appropriate position. Thus no. 12 adds to no. 1, no. 13 adds to no. 2, etc. The process can be extended to a very large number of averages (the present hardware limit is 32 767). This sampling technique, with its optimized sampling rate, allows efficient use of the data-acquisition module throughput to provide real-time continuous signal averaging; although the data are stored, modulo 2π, noise or extraneous signals are accumulated and folded back in a manner that permits quantitative prediction of the influence of these components on the signal-to-noise ratio as well as the error introduced in the subsequent data analysis procedures.

The amplitude of each signal and the relative phase between signals are calculated by a type of cross-correlation. The scheme used can be illustrated in terms of four numerical integrations actually performed as summations in the digitized representations, performed on the two signals A and B. Assuming noise-free signals for purposes of illustration, if $A = A_0 \cos(\omega t + a)$ and $B = B_0 \cos(\omega t + b)$, with frequency ω and arbitrary phases a and b, the integrations are:

$$\text{I:} \int_0^{2\pi} A \sin(\omega t) d(\omega t) = -\pi A_0 \sin a$$

$$\text{II:} \int_0^{2\pi} B \sin(\omega t) d(\omega t) = -\pi B_0 \sin b$$

$$\text{III:} \int_0^{2\pi} A \cos(\omega t) d(\omega t) = \pi A_0 \cos a$$

$$\text{IV:} \int_0^{2\pi} B \cos(\omega t) d(\omega t) = \pi B_0 \cos b$$

The amplitude of each signal could be obtained as

$$A_0 = [\text{I}^2 + \text{III}^2]^{1/2}/\pi \text{ and } B_0 = [\text{II}^2 + \text{IV}^2]^{1/2}/\pi$$

and, more importantly for our analysis, the phase difference between the drive and response signals would be given by

$$\theta = \arctan(-\text{I}/\text{III}) - \arctan(-\text{II}/\text{IV})$$

In actuality, the summations do not cover the $\omega t = 0$ to 2π range and the choice of the total time of data acquisition and the number of data points

per cycle will affect the degree of rejection of extraneous periodic "signals". In effect, the bandwidth and character of the digital filter can be adjusted rather arbitrarily to optimal conditions for a given application. The correlation technique is thus adjustably selective for the frequency ω and eliminates the influence of harmonics of ω as well as any d.c. bias; adjustable rejection of periodic but non-harmonic stray signals is obtained also. The final result for each chosen frequency point of the MLR run is therefore a single value of the phase difference.

The above is a highly simplified description of the actual data-acquisition scheme and the benefits obtainable via this approach. In particular, analytical expressions for noise and stray signal (non-harmonic frequencies) rejection are obtained for this method so that quantitative error estimates are provided. Complete descriptions of the basic method are available [15, 16, 18].

Two sets of computer programs for the Nova 4/s handle the data-acquisition and signal-averaging tasks. The main program, written in FORTRAN, accepts input through a serial (RS232) interface which specifies the drive frequency to be used and the number of signal averages required. After calculating the parameters for the frequency synthesizers, it calls machine-language subroutines which perform the functions of setting the synthesizers, clearing memory, sampling, adding to the memory accumulations, and performing the numerical integrations for the cross-correlation. Several diagnostic programs and subroutines are also available for testing the synthesizers, interfaces, and ADC's. The main Nova program calculates the amplitudes of the two input signals and their relative phase. This information is stored on the 8-in. floppy disk of the Nova computer and is output through the serial interface to the terminal device.

For manual operation, the terminal device is a Diablo 1620 printer/keyboard which the operator uses to enter the desired frequency and averaging variables, and which provides a hard-copy listing of the results. Under the new automated operation mode, the terminal is replaced with an Apple-IIe microcomputer running an MLR data-acquisition operating system. This set of program modules, written in the MODULA-2 programming language (Volition Systems, Del Mar, CA), allows the operator to specify starting parameters for a particular resonance mode and then proceeds with automated data collection. Because 8—12 digit accuracy is needed in the intermediate calculations, double precision arithmetic (machine language library written by Dr. Edwin Turner of this Department) is used extensively. The data-acquisition program communicates through the serial line of the Nova to search frequencies and acquire the optimum frequency/phase points throughout a given resonance. In practice, 16—20 points spaced symmetrically about the resonance frequency plus the resonance frequency are used. These data are automatically stored on floppy disk and printed for hard-copy backup. Additional program modules in the MLR operating system perform the data analysis described below and provide various data-output options including provision for a plotting module to be added at a later date. As will be shown

in the next sections, these sets of frequency and phase pairs are used for characterization of instrument constants and determination of viscoelastic properties.

THEORY

The basic theory of the MLR has been reported elsewhere [2, 8] and only a brief review is presented here. A complete description of the motions of the MLR would entail solving the general equations of motion for a system of coupled resonators. However, the resonators have been designed so that each resonance can be treated to a good approximation as decoupled from the rest; the lowest frequency resonance, where all five lumps twist in unison relative to the housing, corresponds to the resonance of a single moment of inertia and a single spring element, and the remaining four modes can be treated as simple dumbbell motions (two moments of inertia and a single connecting spring element). These dumbbell motions can also be approximated by that for a single moment of inertia and a single spring element if the mode exhibits low mechanical loss and the ratio of the moments of inertia on either side of the dumbbell equals the ratio of the impedances due to the surrounding liquid. Thus, each resonance mode for the MLR can, to a good approximation, be described in terms of a single moment of inertia, I, and a torsional spring constant, k, both of which will depend on the particular resonance being considered.

The viscoelastic properties of the liquid surrounding the resonator can be calculated from the measured torsional impedance Z_T. If end effects are neglected, the torsional impedance can be broken into two distinct parts, first a term $(Z_T)_{T,B}$ which is due to the plane torsional shear waves propagating away from the bottom and top of a lump and also a term $(Z_T)_S$ which is due to the cylindrical torsional shear waves propagating away from the sides of a lump. It is convenient to write Z_T in terms of the characteristic impedance at the resonator surface, $Z_M^S = R_M^S + iX_M^S$, which is defined as the ratio of the force per unit area to the linear velocity of the surface being considered. Thus the effective characteristic impedance is given by

$$Z_M^S = (Z_M^S)_S + (Z_M^S)_{T,B} = Z_T/\pi a^3(2l + a) \tag{1}$$

where a is the radius and l is the length of the lump being considered.

If the waves propagating from the spring elements and reflections between the ends of adjacent lumps can be ignored, then $(Z_M^S)_{T,B}$ is equivalent to $(Z_M^S)_{PL}$, which is the characteristic impedance for plane shear waves propagating into an infinite medium. This is related to the properties of the viscoelastic medium surrounding the resonator [19, 20] by

$$\begin{aligned}(Z_M^S)_{PL} &= (R_M^S)_{PL} + i(X_M^S)_{PL} \\ &= (\rho G^*)^{1/2} \\ &= (\rho/2)^{1/2}\,((G + G')^{1/2} + i(G - G')^{1/2})\end{aligned} \tag{2}$$

where $G^* = G' + iG''$ is the complex shear modulus of the liquid, $G = |G^*|$, and ρ is the liquid density; thus [2]

$$G' = [(R_M^S)_{PL}^2 - (X_M^S)_{PL}^2]/\rho \tag{3}$$

and

$$G'' = [2(R_M^S)_{PL}(X_M^S)_{PL}]/\rho \tag{4}$$

If the ratio of shear wavelength to lump radius is less than 0.04, then $(Z_M^S)_S$ is also essentially $(Z_M^S)_{PL}$. This condition is violated for fluid viscosities greater than 0.008 P; the typical working solution viscosity range is 0.01—0.50 P. Thus, in general, $(Z_M^S)_S$ must be corrected for the influence of the cylindrical character of the wave propagating from the side of the lump. The real and imaginary parts of the characteristic impedance for plane wave conditions can be calculated from R_M^S and X_M^S obtained for cylindrical wave conditions [2, 21]:

$$(R_M^S)_{PL} \cong R_M^S - [3l/a(2l + a)]\ G''/\omega \tag{5}$$

$$(X_M^S)_{PL} \cong X_M^S + [3l/a(2l + a)]\ G'/\omega \tag{6}$$

provided that $\eta' < 2$ P and $\eta' >> \eta''$.

MEASUREMENT TECHNIQUE

The complex characteristic impedance, Z_M^S, can be obtained by measuring either the displacement amplitude and the driving torque or the phase lag, θ, between the drive and displacement signals versus frequency across a resonance band [2]. In the MLR apparatus, θ is chosen as the quantity measured experimentally because the data-acquisition and processing system now employed is capable of measuring phases to $\pm 0.02°$ corresponding to an overall amplitude measurement accuracy of better than $\pm 0.0005\%$ which would place truly exceptional demands on the instrument and the auxiliary electronics. Once Z_M^S has been determined from θ and ω values, G' and G'' can be calculated from Eqns. 3 and 4. In the following paragraphs the current data-analysis approach is discussed and the changes that have been introduced over the past several years are indicated.

The phase angle is related [2] to the drive frequency ω through

$$\tan\theta = \omega(R_M^S + R_T^0)/\{K(\omega_r^{02} - \omega^2) - \omega X_M^S\} \tag{7}$$

where R_T^0 describes the energy loss of the resonator in vacuum, ω_r^0 is the resonance frequency of the resonator in vacuum and K is a geometric constant which is proportional to the moment of inertia of the top half of the dumbbell mode being considered and is defined elsewhere [2, 8].

The components of the characteristic impedance at resonance can be calculated from Eqn. 7. Previously, measurements were made at frequencies corresponding to the displacement resonance and two other symmetrically different phase angles, i.e., 90°, 45° and 135°. From these data, the visco-

elastic properties of the solution under investigation were calculated. Recently, the acquisition procedure has been generalized to allow the operator to collect a greater number of points (usually from 8 to 20 phase measurements at frequencies symmetrically spaced about the resonance frequency plus the resonance frequency are made) in order to improve the instrumental precision. The viscoelastic properties of the polymer sample are calculated as follows.

Equation 7 can be rewritten as

$$\{(R_M^S + R_T^0)/K\} \cot\theta + X_M^S/K = (\omega_r^{02} - \omega^2)/\omega \tag{8}$$

It should be noted that a plot of $1/\tan\theta$ versus $(\omega_r^{0\,2} - \omega^2)/\omega$ interpolated to $1/\tan\theta = 0$ is equivalent to interpolating θ to 90°. Therefore, the above equation allows the data obtained to be directly interpolated to displacement resonance. The intercept of Eqn. 8 is

$$(X_M^S)_{\omega_r} = K(\omega_r^{02} - \omega_r^2)/\omega_r \tag{9}$$

The real component of the complex impedance, R_M^S, can be calculated at frequencies other than displacement resonance from

$$R_M^S \cong -(X_M^S)_{\omega_r} \tan\theta\ (\omega_\theta/\omega_r)^{1/2} + K[(\omega_r^{02} - \omega_\theta^2)/\omega_\theta]\ \tan\theta - R_T^0 \tag{10}$$

where ω_θ is the frequency associated with phase angle θ and ω_r is the displacement resonance frequency for a particular mode. The term $(\omega_\theta/\omega_r)^{1/2}$ corrects approximately for the frequency dependence of X_M^S which is measured at ω_r.

In order to utilize Eqns. 8–10 to obtain values of R_M^S and X_M^S at displacement resonance, the values of K, R_T^0 and ω_r^0 must be determined very precisely. This is done by measuring the displacement resonance frequency, ω_r^0, with air surrounding the resonator, along with the response curve for the solvent alone. If the resonator is surrounded with air, then Eqn. 8 becomes

$$(R_T^0/K) \cot\theta = (\omega_r^{02} - \omega_\theta^2)/\omega_\theta \tag{11}$$

since $Z_M \cong 0$. By applying Eqn. 11 for $\theta = 45°$ and 135°, it can be shown that

$$R_T^0 = K(\omega_{135} - \omega_{45}) \tag{12}$$

where ω_{135}, ω_{45} are the frequencies associated with phase delays at 135° and 45° respectively. With a Newtonian solvent surrounding the resonator, $R_M^S = X_M^S$ and Eqn. 8 reduces to

$$[(X_M^S + R_T^0)/K]\ \cot\theta + (X_M^S/K) = (\omega_r^{02} - \omega_\theta^2)/\omega_\theta \tag{13}$$

Because the solvent is Newtonian, it can also be shown [2] that at displacement resonance

$$X_M^S = (\eta_s \rho \omega_r/2)^{1/2} \tag{14}$$

where ρ is the solvent density, η_s is the solvent viscosity, and ω_r is the displacement resonance frequency for the mode being examined.

To obtain K, R_T^0, and ω_r^0, experimental data consisting of measured phase delays at different frequencies across a particular displacement resonance band are obtained with both air and solvent surrounding the resonator. From the air data, the displacement resonance bandwidth, $\omega_{135} - \omega_{45}$, and an estimate of the vacuum displacement resonance frequency, ω_r^0, are obtained. Equation 13 can be applied to the solvent data, and from the linear interpolation to 90° ($1/\tan\theta = 0$) X_M^S at displacement resonance can be obtained. Equation 9 can then be solved for the displacement resonance frequency ω_r and by using this, along with Eqn. 12, R_M^S can be calculated for each data point from Eqn. 10. After a small correction for constant phase errors has been made to both R_M^S and X_M^S (to be discussed later), the value of G' for the solvent is calculated from Eqn. 3. If the estimate of ω_r^0 is correct, G' should be effectively zero because the solvent is a Newtonian liquid. However, if a nonzero G' is obtained, the vacuum displacement resonance frequency is corrected by using the equation

$$\omega_r^0 = \omega_r^{0'} + (G'\rho\omega_r/4X_M^S K\omega_r^{0'}) \tag{15}$$

where $\omega_r^{0'}$ is the initial estimated vacuum displacement resonance value, ρ is the solvent density and K is the cell constant. The above equation can be obtained by substituting $\omega_r^0 + \Delta\omega_r^0$ into Eqn. 9 and solving for $\Delta\omega_r^0$ (where $\Delta\omega_r^0$ represents the error in the vacuum displacement resonance frequency), making use of Eqn. 3. Using the new value for ω_r^0, the apparent solvent viscosity can be calculated from Eqn. 14 and a new cell constant can be obtained from

$$K = K'(\eta_s/\eta_1)^{1/2} \tag{16}$$

where K' is the old cell constant, η_s is the true solvent viscosity measured by capillary viscometry and η_1 is the solvent viscosity calculated from Eqn. 14, using the measured resonance frequency. The new cell constant and vacuum displacement resonance frequency values are then used in Eqn. 13 to recalculate X_M^S at resonance for the solvent and then the entire procedure is repeated. This process is iterated until successive vacuum displacement resonance frequency values agree to 0.1 mHz.

The calculation procedure outlined above assumes that the phases used are exact and that end effects are negligible. In truth, there exists a number of sources of small, but important, phase errors. Frequency-dependent phase shifts which occur in the amplifiers, the photodiode circuit, etc., are known and readily corrected for; however there are also small constant phase errors which are not well known. For example, for modes 2 through 5, a small phase error is produced by the unequal driving torques being applied to the two halves of the dumbbell. Although this error increases with increasing viscosity, it remains essentially constant across a displacement resonance bandwidth. Although the sources of other constant phase errors may not be well known, they are all corrected for quite easily. Constant phase errors will produce errors in the measured phase lag of equal amounts on both sides of

the displacement resonance frequency. If the resonance bandwidth is symmetric about the displacement resonance frequency and sufficiently narrow, then the correct values of R_M^S and X_M^S will be given by

$$(R_M^S)_{\omega_r} = \sum_{k=1}^{2N+1} (R_M^S)_k / (2N + 1) \tag{17}$$

and

$$(X_M^S)_{\omega_r} = (X_M^S)'_{\omega_r} + \left[\sum_{i=1}^{N} (R_M^S)_i - \sum_{j=1}^{N} (R_M^S)_j \right] \Big/ \left[\sum_{j=1}^{N} \cot\theta_j - \sum_{i=1}^{N} \cot\theta_i \right] \tag{18}$$

where N is the number of points on each side of resonance, and i sums R_M^S and $\cot\theta$ over all phase points below 90°, while j sums points above 90° and k sums over both sides; $(X_M^S)'_{\omega_r}$ is the initial value of $(X_M^S)_{\omega_r}$ calculated from the resonance frequency as described above.

The above equations are valid as long as the phase errors are small (less than 1°). To ensure that this condition is satisfied, the data are initially corrected for any large constant phase errors as follows.

Equation 7 can be recast as

$$[(R_M^S + R_T^0)/K] \cot\theta + (X_M^S/K) = (\omega_r^{02} - \omega^2)/\omega \tag{19}$$

If R_M^S and X_M^S vary negligibly within the bandwidth, a plot of $1/\tan\theta$ versus $(\omega_r^{02} - \omega^2)/\omega$ will be linear as illustrated in Fig. 4 for $\gamma = 0$. If the measured phase angle differs from the correct value of θ by a frequency-independent amount γ, however, a plot of $1/\tan(\theta + \gamma)$ versus $(\omega_r^{02} - \omega^2)/\omega$ will not be linear, as illustrated in Fig. 4. By using this criterion, all the experimental data are initially corrected for large constant phase errors by varying the value of γ until the plot of $1/\tan(\theta + \gamma)$ versus $(\omega_r^{02} - \omega^2)/\omega$ is linear. The resulting γ correction (determined to at least the 0.02° resolution of the θ values) is applied to the measured θ values across the resonance. Any remaining small constant phase errors are subsequently corrected with Eqns. 17 and 18.

As previously mentioned, no correction has yet been made for end effects; if the solution viscosity is above (approximately) 0.05 P, the error cannot be ignored. The corrections for end effects have been discussed before [2] and it has been shown that the equations obtained are similar to those found for the cylindrical wave corrections (Eqns. 5 and 6). The correction for end effects can be written as

$$(R_M^S)_{PL} = R_M^S - AG''/\omega \tag{20}$$

and

$$(X_M^S)_{PL} = X_M^S + AG'/\omega \tag{21}$$

where the constant A has been experimentally found to be 0.76. Since Eqns. 5 and 6 and Eqns. 20 and 21 have the same form, they can be combined,

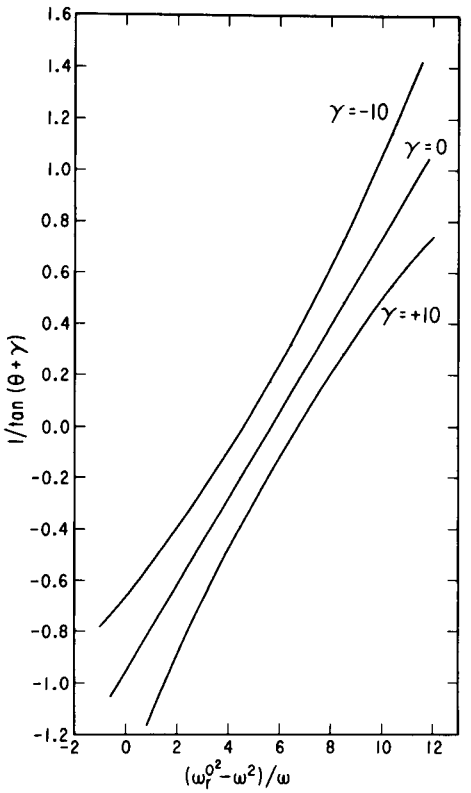

Fig. 4. Plot of experimental values of $1/\tan(\theta + \gamma)$ vs. $(\omega_r^{0\,2} - \omega^2)/\omega$ for water at 25.0°C to demonstrate the effect of small constant phase error γ in the measured phase value. The non-zero intercept refers to the term X_M^S/K in Eqn. 19.

with the constant A now equal [2] to 2.26 ± 0.15, in order to correct for end and cylindrical effects simultaneously.

The procedure used to obtain the solution viscoelastic properties, i.e., G' and G'', is summarized as follows. The measured phase angles for air, solvent and polymer data are initially corrected for constant phase errors with the experimentally determined γ values. The values of K, R_T^0, and ω_r^0 are then calculated from the air and solvent data as has been previously described. The experimental data for the polymer are then interpolated to displacement resonance using Eqn. 7 from which $(X_M^S)_{\omega_r}$ is obtained. The solution displacement resonance frequency is calculated using Eqn. 9 and the previously calculated value for the cell constant. The value of $R_M^S(\omega)$ is then calculated at each experimental frequency using Eqn. 10. Each of the values of $R_M^S(\omega)$ is corrected to displacement resonance by

$$(R_M^S)_{\omega_r} \cong R_M^S(\omega)\,(\omega_r/\omega_\theta)^{1/2} \tag{22}$$

where R_M^S is the real component of the complex characteristic impedance.

Small constant phase errors are corrected for using Eqns. 17 and 18. The values of G' and G'' are then obtained from Eqns. 3 and 4; these are used to obtain values for $(R_M^S)_{PL}$ and $(X_M^S)_{PL}$ corrected for cylindrical and end effects by using Eqns. 20 and 21. The new values of $(R_M^S)_{PL}$ and $(X_M^S)_{PL}$ are then used to calculate corrected values of G' and G''. This final step can be iterated for improved accuracy; however, the corrections are usually sufficiently small to make iteration unnecessary.

The resonators have been constructed so that coupling between the modes is minimized. Coupling is expected to cause errors in the measured phase lag which should increase as the viscosity increases and which should be particularly important for the fifth mode. The effect of mode coupling has been calculated [22] and was found to be given by

$$\tan\theta = \omega [R_T (1 + \delta_c) + R_T^0] / \{I[\omega_r^{02} - \omega^2(1 + \delta_c) - \omega(1 + \delta_c)X_T]\} \qquad (23)$$

where the constant δ_c will vary with mode number and will be a function of the solution viscosity. Coupling will therefore lead to an error in the values of R_T and X_T as well as the solution resonance frequency ω_r. Preliminary calculations and experimental evidence indicate that coupling will cause significant errors only in solutions with viscosities greater than 0.5 P. Further investigations of the magnitude of coupling errors for cases in the usual range of 0.005—0.25 P are underway.

RESULTS

The final results of the changes in design and operation of the MLR have met the original goals of improved operational reliability and precision of measurements. Specifically, it is now possible to make measurements of solvents and six polymer concentrations in one 12-h workday (double the previous rate); 9—21 data points are now acquired to characterize each resonance curve (the 3-point method was used before); random and systematic variations in the electronic phase error have been reduced 10-fold; temperature control is now stable to ±0.002°C although operator adjustments must still be made during the course of most experiments; the experimental uncertainty has been reduced and reproducibility is now very good.

Figure 5 shows an example of the infinite dilution extrapolation plots of $(G'M/cRT)^{1/2}$ and $(G'' - \omega\eta_s)M/cRT$ against concentration for a schizophyllan polysaccharide. Here M is molecular weight and c is concentration (g ml^{-1}). As these plots indicate, the data for G' show very little scatter and it may be possible to observe changes in the concentration-dependence which have previously been inaccessible. The data for G'' extrapolate satisfactorily at the lower frequencies, though for this polymer there is non-linearity at higher concentrations. At higher frequencies, especially for the fifth mode, data are usually less reliable and the lines drawn for extrapolation are somewhat uncertain. However, the intercepts, which are the most important results, are determined within a few percent. The intercepts provide the

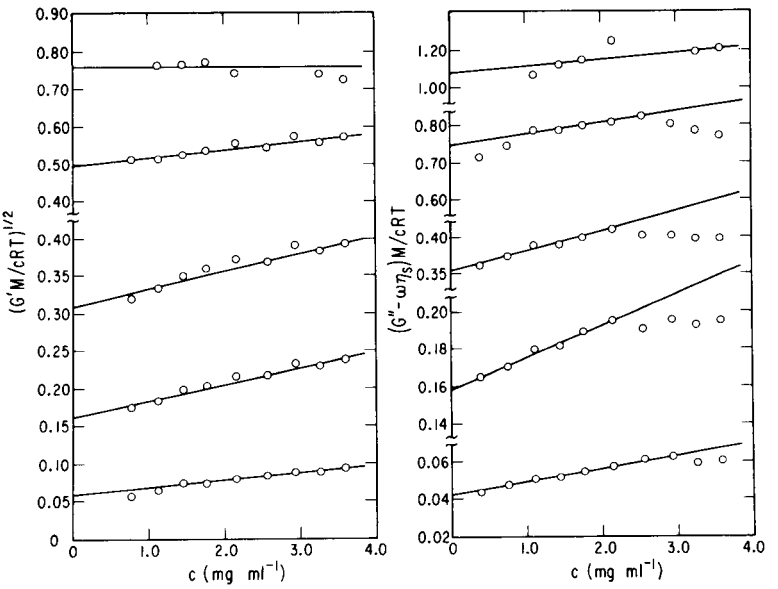

Fig. 5. Reduced storage $(G'M/cRT)^{1/2}$ and loss $(G'' - \omega\eta_s)M/cRT$ moduli plotted against concentration for five resonance mode frequencies: from bottom to top, 102, 393, 984, 2372, and 5811 Hz. The sample is schizophyllan polysaccharide in water [23].

reduced intrinsic storage and loss moduli, $[G']_R$ and $[G'']_R$, which for these measurements are in agreement with the best values using the old data-analysis scheme.

Measurements made since the instrument has been upgraded continue to confirm the intrinsic capability of the MLR for viscoelastic measurements in dilute solution and the benefits of the latest modifications.

FUTURE PLANS

Three areas are currently under consideration for future developments. First, difficulties with temperature stability and the necessity of continual manual adjustment remain a major operational problem. It should be possible to solve this problem with a better temperature controller and further improvements in the insulation of the instrument. Secondly, there is mode coupling, in which one resonance mode is perturbed by the presence of other modes, and the resulting error is thought to be small and was neglected in the original mathematical treatment [2]. The result of one method of assessing this error has been given in this paper; and while mode coupling appears to be negligible for solutions with low viscosity (<0.30 P), it does become important for solutions with higher viscosity. The effects of mode coupling are presently being explored. Thirdly, we continue to explore new designs and modifications which will extend the frequency range beyond the five-mode limit of the MLR. Because of the extreme sensitivity required to make

these measurements on dilute solutions, it seems clear that use of some type of resonance device will continue to be essential.

This work was supported in part by Grant 21652 from the National Institutes of Health and Grant DMR-8115462 from the Polymers Program, National Science Foundation.

NOTE ADDED IN PROOF

A new implementation of the MLR has recently been completed, with improved temperature control and data acquisition (E. J. Amis and D. W. Hair, Polymer Preprints ACS, 27(2) (1986) 273).

REFERENCES

1 J. D. Ferry, Viscoelastic Properties of Polymers, 3rd edn., Wiley, New York, 1980.
2 J. L. Schrag and R. M. Johnson, Rev. Sci. Instrum., 42 (1971) 224.
3 K. Osaki, J. L. Schrag and J. D. Ferry, Macromolecules, 5 (1972) 144.
4 Y. Mitsuda, K. Osaki, J. L. Schrag and J. D. Ferry, Polym. J., 4 (1972) 24.
5 N. Nemoto, J. L. Schrag, J. D. Ferry and R. W. Fulton, Biopolymers, 14 (1975) 409.
6 S. Hvidt, F. H. M. Nestler, M. L. Greaser and J. D. Ferry, Biochemistry, 21 (1982) 4064.
7 E. J. Amis, C. J. Carriere and J. D. Ferry, Int. J. Biol. Macromol., 7 (1985) 130.
8 R. M. Johnson, Ph.D. Thesis, University of Wisconsin, 1970.
9 G. B. Thurston and J. L. Schrag, J. Appl. Phys., 35 (1964) 144.
10 J. L. Schrag, J. F. Guess and G. B. Thurston, J. Appl. Phys., 36 (1965) 1996.
11 J. L. Schrag, Trans. Soc. Rheol., 21 (1977) 399.
12 D. J. Massa and J. L. Schrag, J. Polym. Sci., A2, 10 (1972) 71.
13 A. L. Soli and J. L. Schrag, Macromolecules, 12 (1979) 1159.
14 A. L. Soli, Ph.D. Thesis, University of Wisconsin, 1978.
15 T. M. Stokich, Ph.D. Thesis, University of Wisconsin, 1986.
16 M. G. Dibbs, Ph.D. Thesis, University of Wisconsin, 1983.
17 T. P. Lodge, Ph.D. Thesis, University of Wisconsin, 1980.
18 R. L. Sammler, Ph.D. Thesis, University of Wisconsin, 1985.
19 R. B. Lindsay, Mechanical Radiation, McGraw-Hill, New York, 1960.
20 W. P. Mason, Trans. Am. Soc. Mech. Eng., 69 (1947) 369.
21 H. J. McSkimin, J. Acoust. Soc. Am., 24 (1952) 335.
22 C. J. Carriere, Ph.D. Thesis, University of Wisconsin, 1985.
23 C. J. Carriere, E. J. Amis, J. L. Schrag and J. D. Ferry, Macromolecules, 18 (1985) 2019.

END OF PAPERS ON POLYMER CHARACTERIZATION

0003-2670/86/$03.50

rinted in The Netherlands

CONTENTS

(Abstracted, Indexed in: Anal. Abstr.; Biol. Abstr.; Chem. Abstr.; Curr. Contents Phys. Chem. Earth Sci.; Life Sci.; Index Med.; Mass Spectrom. Bull.; Sci. Citation Index; Excerpta Med.)

Special Issue on Modern Methods of Polymer Characterization